bias

Bremer Institut für
angewandte Strahltechnik

STRAHLTECHNIK BAND 75

Sandro Eckert

Laser-Induced Thermochemical Polishing of Metals

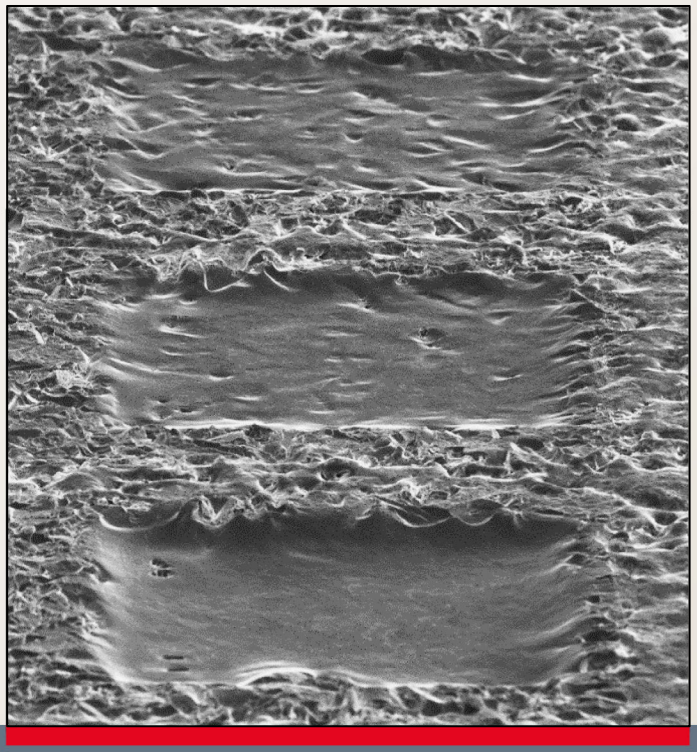

Wissen schafft Wirtschaft

Eckert, Sandro – Laser-Induced Thermochemical Polishing of Metals

Strahltechnik Band 75, BIAS Verlag, 2022.

Herausgeber der Reihe: F. Vollertsen, R. Bergmann

ISBN 978-3-933762-69-6

BIAS Verlag, Bremen, 2022

Laser-Induced Thermochemical Polishing of Metals

Vom Fachbereich Produktionstechnik
der
UNIVERSITÄT BREMEN

zur Erlangung des Grades
Doktor-Ingenieur
genehmigte

Dissertation

von
M. Sc. Sandro Benjamin Eckert

Gutachter:
Prof. Dr.-Ing. Frank Vollertsen (Universität Bremen)
Prof. Dr.-Ing. Andreas Ostendorf (Ruhr-Universität Bochum)

Tag der mündlichen Prüfung: 21.01.2022

Eckert, Sandro:

Laser-Induced Thermochemical Polishing of Metals

Strahltechnik, Bd. 75, Bremen; BIAS Verlag, 2022. Hrsg.: F. Vollertsen, R. Bergmann

Zugl.: Bremen, Univ., Diss., 2022.

ISBN 978-3-933762-69-6

Keywords: laser thermochemistry, micropolishing, surface roughness, geometric levelling

This work investigates material removal by laser-induced thermochemical machining (LCM) as a method for selectively polishing passive metals in applications where conventional finishing technologies induce unacceptable mechanical or thermal stresses. The main objectives are to identify reliable process conditions, to understand the effects of various process parameters on polishing and the corresponding mechanisms of action and to develop a model to predict surface roughness. A multipass LCM method is developed, which allows controlled polishing of different materials by adjusting laser power, spot diameter, scan passes, line spacing and scan velocity. The results show that polishing characteristics are determined by the laser-induced average thermal load and exposure time. Polishing can be understood as a geometric levelling process and can be predicted by a model based on local differences of the thermal gradient. The stable lower limit of roughness of the finished surface is mainly defined at the microstructural level by inhomogeneous etching between the face and boundaries of the grains. These findings present opportunities for flexible and selective adjustment of LCM process parameters to achieve the desired roughness level for surfaces of micro- and macroscopic dimensions.

Laserinduziertes thermochemisches Polieren von Metallen

Schlüsselwörter: Laserchemie, Polieren, Oberflächenrauheit, Geometrische Einebnung

Die vorliegende Arbeit befasst sich mit der Oberflächenbeschaffenheit beim laserinduzierten thermochemischen Materialabtrag von passiven Metallen, um ein neuartiges Verfahren zum selektiven Polieren zu ermöglichen. Schwerpunkte der Untersuchung sind die Identifizierung der Einflussgrößen und Ursachen der Oberflächenglättung, sowie die Entwicklung eines Vorhersagemodells. Dazu wird ein neuartiges Verfahren zum laserthermochemischen Polieren entwickelt, welches eine kontrollierte Oberflächenglättung verschiedener Materialien durch das gezielte Einstellen von Laserleistung, Spotdurchmesser, Scanwiederholungen, Linienabstand und Scangeschwindigkeit ermöglicht. Die Ergebnisse belegen, dass sich der Glättungsprozess mit Hilfe der laserinduzierten thermischen Beanspruchung und Belichtungsdauer beschreiben lässt. Die Oberflächenglättung wird durch geometrische Einebnung verursacht und lässt sich anhand des thermischen Gradienten vorhersagen. Die untere Grenze der Rauheit wird hauptsächlich durch Auflösungseffekte auf Gefügeebene bestimmt. Die gewonnen Erkenntnissen bilden die Grundlage, um gezielt die Rauheit von metallischen Bauteilen einzustellen.

Danksagung

Die vorliegende Arbeit entstand neben meiner Tätigkeit als wissenschaftlicher Mitarbeiter am BIAS – Bremer Institut für angewandte Strahltechnik, unter anderem im Rahmen der Projekte “Selektives Laserchemisches Polieren“ und “Prozesse mit thermochemischer Wirkung” (Transregio TRR136), die von der Deutschen Forschungsgemeinschaft (DFG) gefördert wurden.

Meinen besonderen Dank möchte ich Herrn Professor Dr.-Ing. habil. Frank Vollertsen aussprechen, der als Betreuer der Doktorarbeit und Institutsleiter des BIAS die Erstellung dieser Arbeit ermöglichte und mich durch konstruktive wissenschaftliche Diskussionen stets im inhaltlichen Fortschritt unterstützte. Für das entgegengebrachte Vertrauen, die hervorragenden Arbeitsbedingungen und den notwendigen Freiraum um komplexe Fragestellungen anzugehen, bin ich äußerst dankbar.

Für die Übernahme des Koreferats gilt mein herzlicher Dank Herrn Professor Dr.-Ing. Andreas Ostendorf (Ruhr-Universität Hamburg). Herrn Professor Dr.-Ing. Lutz Mädler (Universität Bremen), Frau Professor Dr.-Ing. Maren Petersen (Universität Bremen), sowie den Herren Marcel Simons (Universität Bremen) und Timon Ahlers (Universität Bremen) danke ich für die Mitarbeit im Prüfungsausschuss des Promotionskolloquiums.

Meinen ehemaligen Kollegen und Kolleginnen am BIAS sowie meinen ehemaligen Studierenden danke ich für die stets gute Zusammenarbeit und den hervorragenden Teamgeist. Insbesonders danke ich Hamza Messaoudi und Hans Fenske für ihre unermüdliche Bereitschaft und Geduld zu fachlichen Diskussion, sowie Andreas Klett für seine pragmatische Unterstützung bei der Realisierung von Versuchsaufbauten. Darüber hinaus danke ich allen Lauffreunden am BIAS für die unzähligen gemeinsamen Laufstunden, die einen fantastischen Ausgleich nach langen Tagen im Labor und am Schreibtisch boten.

Abschließend möchte ich meiner Familie von ganzem Herzen danken, allen voran meiner Frau Laura und meiner Schwester Angelina für ihre ausnahmslose Unterstützung und mentalen Rückhalt.

Bremen, März 2022 Sandro Eckert

Contents

Symbols and Abbreviations

Symbol	Unit	Definition
A	m^2	Surface area
A_a	m/s	Pre-exponential factor in the Arrhenius equation
A_r	m^2	Laser spot area
b	m	Line spacing
c	mol/m^3	Concentration of reactants
c_a	--	Proportionality constant in the LCP model
c_{bulk}	mol/m^3	Bulk electrolyte concentration
c_D	m/s	Average material dissolution velocity in the original geometric levelling model (Equation (2.9)) [Wag54]
c_L	K/m	Thermal geometric levelling process parameters, $\frac{\Delta T}{d_f}$
c_M	$m^2/(K \cdot s)$	Thermal geometric levelling material parameters, $c_M = \frac{m_M K}{\rho E_a}$
c_p	$J/(K \cdot kg)$	Specific heat capacity
c_{sat}	mol/m^3	Saturation concentration at the material-electrolyte interface
c_T	m/s	Average material dissolution velocity describing the linear decrease of the average surface plane (Equation (7.11))
D_c	m^2/s	Diffusion coefficient
d_f	m	Laser spot diameter
$d_{j,i}$	m	Spot cavity diameter along the major (subscript *j*) and minor (subscript *i*) axes
D_T	m^2/s	Thermal diffusivity
E_a	J/mol	Activation energy
f	1/m	Spatial frequency
$f(z)$	--	Attenuation of the laser intensity in the *z*-direction
f_M	--	Functional correlation of the modification *M*

f_{Sa}	--	Functional correlation of the average roughness S_a
G	--	Green function of the heat equation
h_c	m	Depth of cavity center
h_m	m	Maximum cavity depth
h_s	m	Depth of the current surface plane S below the initial surface plane S_I, i.e., average depth of material removal
$I(x,y)$	W/m^2	Laser beam intensity distribution on the surface
I_0	W/m^2	Intensity at the laser beam center
I_a	W/m^2	Absorbed laser beam intensity
J	A/m^2	Current density
J_c	mol/(m^2·s)	Diffusion flux
J_T	J/(m^2·s)	Heat flux
K	W/(m·K)	Thermal conductivity
k	m/s	Reaction rate constant
$k_{x,y}$	1/m	Wave vectors
L	--	Material loading
L_c	m	Line cavity length
$L_{x,y}$	m	Lateral lengths of the polishing area
L_z	m	Sample thickness (perpendicular to the surface)
M	--	Material modification
m_M	kg	Atomic mass
M_{Sa}	--	Material modification in roughness after one scan pass
$\widetilde{M}_{Sa}$	--	N-fold material modification in roughness
N	--	Number of scan passes
n	mol	Amount of substance
n_d	--	Refractive index of the surrounding medium

P_L	W	Laser power
$P_{L,dist}$	W	Power threshold for disturbed material removal
$P_{L,th}$	W	Power threshold for material removal
Q	W/m^2	Heat source power density
$q(t)$	--	Temporal dependency (for modulated laser radiation)
R	J/(K·mol)	Universal gas constant
R^2	--	Coefficient of determination
R_a	m	Arithmetical mean height of a profile line
S	m	Current surface plane (at time t)
$s(x,y)$	m	Surface-height data with regard to S_R
$s(x,y)^*$	m	Surface-height data with regard to S_I
$s^+(k_x,k_y)$	1/m	Fourier transformed surface-height data
S_a	m	Arithmetical mean height of the surface
$S_{a,f}$	m	Minimum (lower limit)/residual surface roughness
$S_{a,i}$	m	Initial surface roughness
$S_{a,\lambda}$	m	Spectral roughness (within wavelength band)
s_{avg}	m	Distance between current surface plane S and reference surface plane S_R
S_I	m	Initial surface plane (at time t = 0 s)
S_R	m	Reference surface plane
t	s	Time variable
$T(x,y,z)$	°C	Temperature distribution
t_A	s	Total processing time for the treated surface area
T_c	°C	Center temperature rise
T_L	°C	Thermal load
t_N	s	Single-pass exposure time

t_p	s	Polishing time (time required to achieve the stable lower limit of the finished surface)
t_r	s	Average exposure time
T_{th}	°C	Thermal threshold (material removal)
$T_{th,dist}$	°C	Thermal threshold (disturbances)
u	%	Line overlap
U	V	Electrode potential
U_b	V	Transpassive potential
U_c	V	Active dissolution potential
U_p	V	Passivation potential
V	m^3	Dissolved material volume
v	m/s	Scan velocity
V_c	m^3	Cavity volume
v_f	m/s	Flow velocity
w_0	m	Beam radius defined by I_0/e
w_c	m	Line cavity width
w_r	m	Beam radius defined by I_0/e^2
x,y,z	m	Cartesian coordinates
$z(x)$	m	Distance from the current surface plane S to a point on the surface
α	%	Absorptivity
δ_c	m	Diffusion layer thickness
δ_{th}	m	Thermal boundary layer thickness
θ	°	Rotation angle between scan trajectories
θ_L	°	Angle of incidence
Λ	m	Spacing of the laser-induced ripple structures
λ	µm	Wavelength

$\lambda_{c,max}$, $\lambda_{c,min}$	µm	Cutoff wavelengths
λ_S	m	Average (roughness) wavelength
$\lambda_{S,i}$	m	Initial average (roughness) wavelength
ρ	kg/m^3	Density
τ_{Sa}	s	Mean lifetime of the average roughness
Φ	V	Electric potential
ψ	m	Amplitude of the sine-wave profile
ψ_0	m	Amplitude of the sine-wave profile at the time t = 0 s

Abbreviation	**Definition**
B1, …, B4	Labels for rolled and abrasive-blasted samples
CCD	Charge-coupled device
EDX	Energy-dispersive X-ray spectroscopy
FFT	Fast Fourier transformation
H_3PO_4	Phosphoric acid
ISO	International Organization for Standardization
LCM	Laser-induced thermochemical machining
LCP	Laser-induced thermochemical polishing
SEM	Scanning electron microscopy
SSR	Sum of squared residuals
SST	Total sum of squares
T1, …, T4	Labels for turned samples
Ti6Al4V	Alpha-beta titanium alloy

1 Introduction

Surface finishing methods have been applied as additional processing steps since the Neolithic period, when simple prehistoric flint hand axes, which had been the prevailing technology for thousands of years, were suddenly replaced by polished stone axes. With their improved functionality, increased durability and better resistance to corrosion, polished stone axes became the signature tool of the period. Polishing brought out qualities in the form and appearance of axes that enhanced the appreciation of those who held them [Dav11]. The ability to improve these two fundamental attributes, functionality and aesthetics, continues to motivate every polishing process today.

Now more than ever, surface finishing technologies have become essential to improving the performance of parts and products, increasing usability and reliability and prolonging life span. Conventional finishing technologies based on abrasive methods are difficult to apply to machine-shaped surfaces, free-form surfaces and the interior surfaces of cavities, all of which are increasingly in demand because of the new design freedom provided by additive manufacturing. Additional challenges arise with the continuing miniaturization of components, which require low tolerances for form deviations and cannot accommodate deformation by mechanical or thermal stresses. These challenges are further complicated when the components should have functional surface finishes or are used in automated applications. In order to overcome these application limitations, many studies have aimed to surpass conventional methods by developing entirely new finishing technologies, including combined finishing technologies that draw on the complementary strengths of electric, magnetic, acoustic, chemical or thermal energies [Yan18]. These combined technologies integrate the advantages of different machining methods to achieve the desired surface finish.

Laser-induced thermochemical machining is one such innovative processing technology. In this approach, laser radiation selectively removes material from passive metals by heating the surface and generating a local electric cell, which results in localized anodic dissolution that leaves a residue-free surface finish within a small range of process parameters. Guiding the laser beam across the surface allows precise, gentle and direct microscale structuring [Bäu11], which supports two-dimensional cutting and structuring applications, as well as three-dimensional material removal to produce microparts.

The present work is dedicated to the subject of whether laser-induced thermochemical material removal can be applied as an innovative surface finishing method for passive metal parts in selective micropolishing applications.

2 State of Research

2.1 Overview of technological opportunities

Conventional mechanical polishing and vibratory finishing methods for deburring, cleaning and brightening complex three-dimensional (3D) metallic parts are often unsuitable or uneconomical for micro-applications. These processes induce mechanical and thermal stresses that can damage the part, and therefore electrochemical polishing is often used for such applications. Electrochemical polishing is a subtractive machining method that dissolves a few µm of material between the anodically polarized workpiece and a cathodic counter electrode, both of which are placed in an electrolyte solution under an external power supply. This approach does not induce noticeable mechanical or thermal stress and is used for controlled surface brightening, smoothing, cleaning and deburring of metallic parts.

Electrochemical polishing was first systematically developed in the 1930s [Jac36]. Since then, the approach has been applied to a broad range of applications in microelectronics [Huo03], and to medical [Oli07], turbomachine, aerospace [Klo14], automobile, pharmaceutical, architectural and food and beverage products [Swa10]. In many industrial applications, among others, the technique is deployed to produce low roughness and high gloss values. Electropolished surfaces show good corrosion resistance [Sha08], fatigue strength and biocompatibility [Bar07], and also low friction [Alv12]. However, only certain material-electrolyte combinations can produce a surface finish of optical quality and with an average roughness of $S_a < 0.08$ µm. Common materials include stainless steel, nickel-chromium-based superalloys and titanium, in combination with phosphoric- and sulphuric-acid-based electrolytes [Gab72]. Furthermore, electrochemical polishing is of limited use for selective or functional surface finishing, because the processing result depends on the electric potential near the surface, which is difficult to confine in selective polishing applications, or to keep constant when working on complex part geometries.

Fluid-jet-based electrochemical machining (**Figure 2.1a**) [Hac12] and electrochemical micromachining were developed for these purposes [Dat00]. In the jet-based approach, a submillimeter nozzle confines the material dissolution, and electrochemical micromachining achieves this aim by using a cathode of only a few micrometers in size [Spi13]. These processes can be used for selective surface texturing [Kaw14], and the machined surfaces show low roughnesses of $S_a < 0.02$ µm (titanium) for small roughness wavelengths (< 100 µm) [Lan03]. Under specific process parameters, jet-based electrochemical machining can be used for polishing: using a slit nozzle of

9.5 mm × 0.2 mm, mirror-like surface finishing with R_a = 0.25 µm can be obtained on stainless steel [Kaw15] with an inter-electrode gap of 1 mm and a translating speed of 0.5 mm/s, as shown in **Figure 2.1b**. Laser-assisted jet-based electrochemical machining methods have been developed to increase the removal volume and accuracy [Des04]. The laser irradiation induces a potential shift that breaks the oxide layer by local heating and increases the current density [Paj06]. The induced temperature must be monitored carefully to avoid heat-affected zones or spark damage due to electrolyte boiling. Surface textures with a roughness of S_a = 0.03 µm (nickel alloy) have been reported [Sil11].

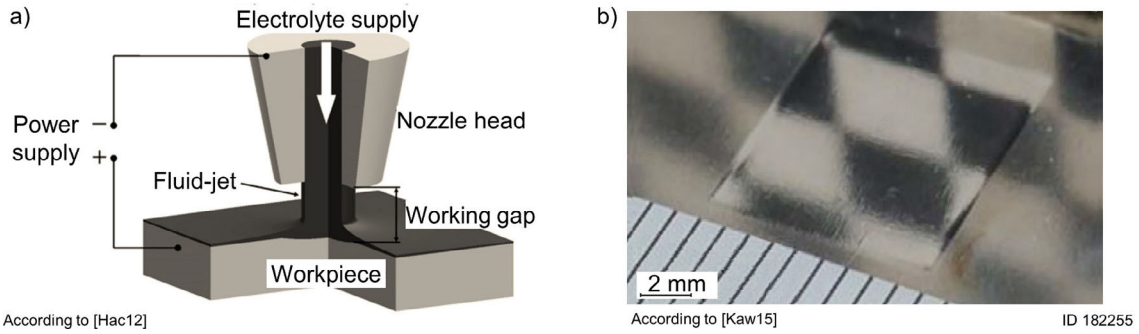

Figure 2.1: (a) Illustration of jet-based electrochemical machining setup [Hac12] and (b) example of mirror-like surface finish achieved using a slit nozzel on stainless steel [Kaw15].

For some material-electrolyte combinations, the laser-induced potential shift can be large enough to support processing without an external electrode. Selective laser-induced etching without an external electrode was first demonstrated in the late 1980s as the reverse of a plating process [Dat87], [Gut88]. In the mid-1990s, this concept was further developed into laser-induced thermochemical machining (LCM) using a closed, wet-etching chamber [Now95] or a jet-based setup [Ste04]. Extensive research was conducted to enable model-based control [Mor05] of scan trajectories [Zha15] for reliable 3D material removal. LCM has since been applied to cutting thin foils [Now95], microstructuring [Ste02] and producing microforming tools [Ste11] and microforming dies [Mes18]. Most of the electrochemical micromachining and LCM studies to date have focused on reliable 3D material removal of certain shapes with prescribed tolerance.

In recent decades, polishing with laser radiation, as illustrated in **Figure 2.2a**, has been proposed as a new method for obtaining a high-quality selective finish. Smoothing can be achieved by melting a thin surface layer. In the molten phase, the changed surface tension leads to material relocation, flowing from the peaks to the valleys and resulting in a smoothed surface once the material solidifies. The result depends decisively on the process parameters. **Figure 2.2b** shows a milled steel surface after polishing with (1) continuous wave laser radiation and (2) pulsed laser radiation. The former type is often unsuitable for micro-applications because of its high thermal impact and melting depth of 20 to 80 µm [Wil06]. Pulsed (ns) laser micropolishing is a more suitable method for

selectively polishing metallic microparts. Pulsed laser radiation reduces the thermal impact and melting depth relative to continuous wave radiation and still effectively reduces microroughness [Wil03]. By controlling the pulse duration, melt pool oscillations can be suppressed and the roughness reduced to S_a = 0.05 µm (Ti6Al4V) with a melt depth of 3 µm [Pfe13]. However, the temperature must be controlled and an inert gas must be used to avoid crack formation [Per09]. The use of adaptive scan trajectories can minimize surface anisotropies [Vad13]. Although the use of pulsed laser radiation allows more precise thermal energy deposition, this method still induces thermal stress and microstructural changes.

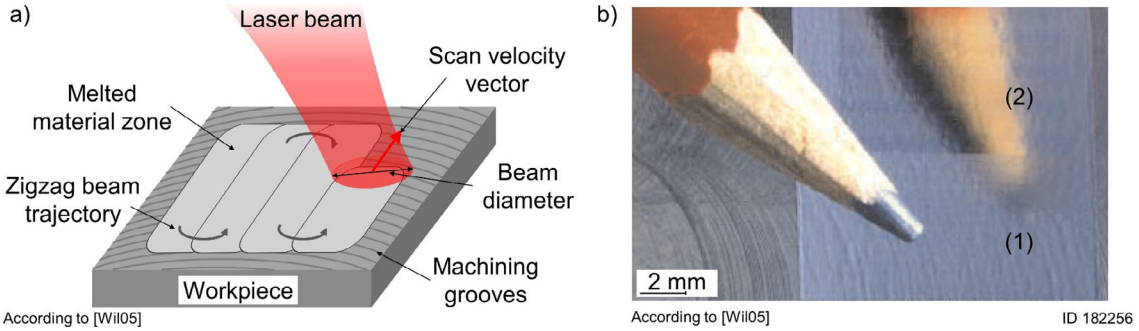

Figure 2.2: (a) Laser radiation over the surface and (b) example of a selective laser polished milled steel surface with (1) continuous wave and (2) pulsed laser radiation [Wil06].

Thus, selective and gentle polishing of metallic microparts remains challenging. In order to overcome technical limitations, increasing interest and effort were made to develop selective, nonconventional surface finishing methods. LCM in a wet-etching setup is considered a promising option for micropolishing for the following reasons.

- Guiding the laser radiation across the surface enables selective processing.
- The laser spot size and thereby lateral polishing dimensions can range from a few micrometers to millimeter scales.
- The laser process can be readily automated and integrated into 3D applications.
- The laser is a non-contact and wear-free tool.
- Chemical material removal produces surfaces with favorable corrosion resistance and biocompatibility and low roughness.
- The bulk material is exposed to negligible thermal or mechanical stress.
- Minimal material removal of only a few micrometers in depth are necessary.

2.2 Electrochemical polishing

In general, electrochemical polishing is performed in an electrochemical cell, where two electrodes are conductively connected and immersed in an electrolyte. Material is dissolved during a charge exchange between the metallic workpiece and the (acid) electrolyte, which generates an electric current to the cathode. The review papers of Landolt [Lan87] and Yang et al. [Yan17] describe the various mechanisms and models

that have been proposed for this process, such as geometric levelling, resistance theory, diffusion phenomena, passivation and acceptor theory. These models aim to explain why elevated surface regions (roughness peaks) are removed faster than lower regions (roughness valleys). Faster removal of peaks is essential for smoothing and brightening.

Smoothing is based on the mass transport limitations of reactants or products as shown by a horizontal plateau in the current density-potential profile, which marks the so-called passivation potential. Such a plateau is found whenever the diffusion of one reactant consumed by an electrode process is the controlling factor, i.e., the concentration of the reactant at the surface of the electrode is much lower than its bulk concentration. Brightening is based on the reduction of micro-roughness (surface features with short roughness wavelengths of 0.8 µm to 10 µm), whereas smoothing depends more on the reduction of meso- and macro-roughnesses at longer wavelengths (10 µm to 80 µm) [Lan87]. The following subsections describe the mechanisms by which electrochemical smoothing acts at atomic, micro- and mesoscopic length scales on the material-electrolyte interface: the formation of the electric double layer, mass transport and the limiting current density, geometric levelling and anodic brightening.

2.2.1 Electric double layer

From the electrochemical perspective, material removal results from a redox reaction, whereby reduction and oxidation occur at the cathode and anode, respectively. If a metal is immersed in an electrolyte, charge neutrality is maintained by charge separation near the metal-electrolyte interface, in the so-called electric double layer (0.2 nm to 10 nm), as illustrated in **Figure 2.3a**. The charge distribution at the interface depends on the applied potential and numerous other factors: the electric properties of the solid, the adsorption of water molecules and hydrated cations and the chemisorption of anions. Near the surface, the dipolar water molecules are aligned to form a double layer. Metal atoms can dissolve into the double layer by losing valence electrons through multiple oxidation processes that depend on the exact chemical reactions that occur between the available species, and these exact reactions are often unknown. However, the dissolved cations are generally hydrated in the aqueous solution [Lan07], and certain anions, such as chloride, can chemisorb onto the surface, replacing adsorbed water molecules and participating in corrosion processes. In addition, solid metal surfaces contain numerous defects and inhomogeneities, such as atomic steps, point defects, dislocations and grain boundaries, that influence the double layer properties.

This atomistic view of the double layer is often approximated by a less complex electric analog, the classical Stern model [Del07]. The Stern model describes the potential difference between the metal and the solution as shown in **Figure 2.3b**. The model combines aspects of the Helmholtz model, which assumes a linear decrease of the

potential as a function of the distance, and the Gouy-Chapman model, which assumes an exponential decrease of the potential as a function of the distance. Within the Helmholtz layer, the ions are assumed to be governed purely by electrostatic forces and thereby take stable positions. Negative and positive charges are separated, such that the layer acts like a planar capacitor. This model provides a good approximation of the potential close (0.2 nm to 0.3 nm) to the surface. The inner and outer Helmholtz planes are differentiated by the chemisorption of some ion types from the inner layer onto the surface. The outer Helmholtz plane defines the edge of the diffuse double layer that is farthest from the metal surface. At that distance, the ion positions are no longer stable.

In addition to the electrostatic forces, the thermal motion of the ions given by the Boltzmann distribution must be considered [Del07]. This distribution describes the potential depending on the ion concentration and explains why the potential decreases exponentially with the distance from the surface. With typical values for an aqueous electrolyte at room temperature and a concentration of 10^{-4} mol/L, the thickness of the diffuse double layer will be 30 nm, which is significantly larger than the thickness of the outer Helmholtz layer alone [Lan07]. Nevertheless, this thickness is still small compared to the scale of the surface roughness to be processed.

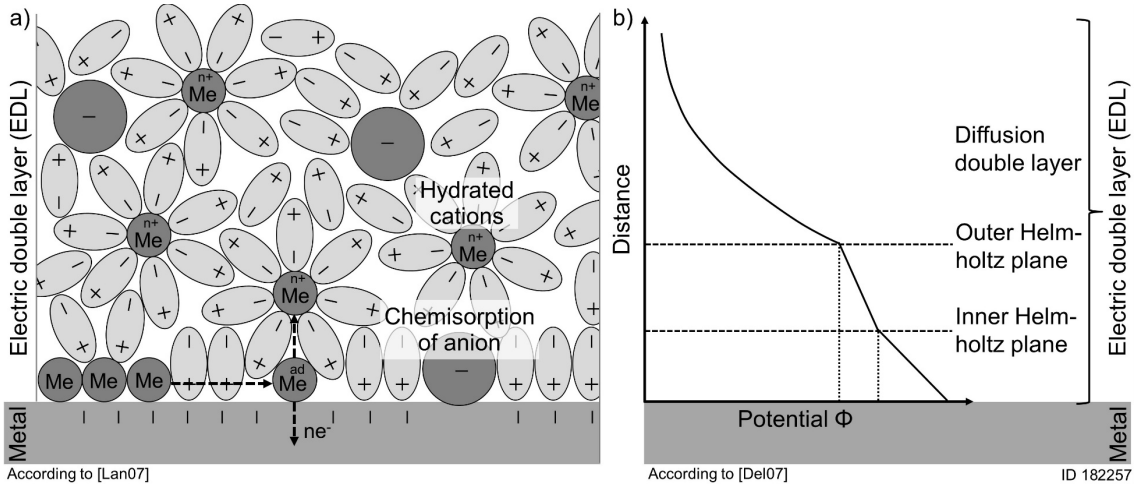

Figure 2.3: Illustrations of the electric double layer from (a) an atomistic perspective, with hydrated cations, and (b) an electrical perspective, with the potential difference between the metal and different layers of the solution according to the Stern model.

2.2.2 Mass transport

Once the hydrated cations are beyond the reach of the electrostatic forces of the double layer, their further transport in the electrolyte is governed by diffusion through a concentration gradient in the solution, migration by proton transfer [Mar99] and convection due to fluid currents. The last two processes become increasingly important in systems with high electrolyte concentrations and high Reynolds numbers [Buh15], but are of minor importance in conventional electrochemical polishing and process conditions

that are the focus of this work. This section focuses on mass transport by diffusion phenomena, described by Fick's second law of diffusion.

The velocity of the diluted electrolyte is assumed to be zero at the metal electrode-electrolyte interface. Because of the chemical reactions described in the previous section, the concentrations of reactants and products near the metal electrode surface (beyond the double layer) are higher than in the bulk electrolyte. This concentration gradient results in diffusion, with net movement of species from the material surface to the bulk electrolyte, as shown in **Figure 2.4**. The region between the electric double layer and the bulk electrolyte concentration is called the diffusion layer. The effective thickness of this diffusion layer δ_c can be defined as the distance between the intersection of the line tangent to the concentration curve at $y = 0$ and the extrapolated plateau of the bulk concentration c_{bulk}. Although the real diffusion layer may be thicker, this definition helps to distinguish between diffusion inside the layer ($y < \delta_c$) and the lack of diffusion outside the layer ($y > \delta_c$). The thickness of the diffusion layer depends on the prevailing convection and is typically between 1 µm and 100 µm, which is orders of magnitude thicker than the electric double layer [Lan07].

Diffusion can limit the material dissolution rate because the dissolution rate is a function of the concentration of reactants or products near the electrode surface. **Figure 2.4** shows typical concentration profiles of a reactant (**Figure 2.4a**) and a product (**Figure 2.4b**). In the first case, the maximum dissolution rate at the surface would be limited by an oxidizing agent, such as dissolved molecular oxygen, the concentration of which drops to zero at the interface. The dissolution rate may also be limited by the transport of corrosion products involved in an electrode reaction. The concentration of products near the surface can reach its saturation value and prevent a further increase of the dissolution rate. In both cases, the concentration of the rate limiting species is either zero or at its saturation value at the surface, depending on whether the reactants or the products are the limiting species.

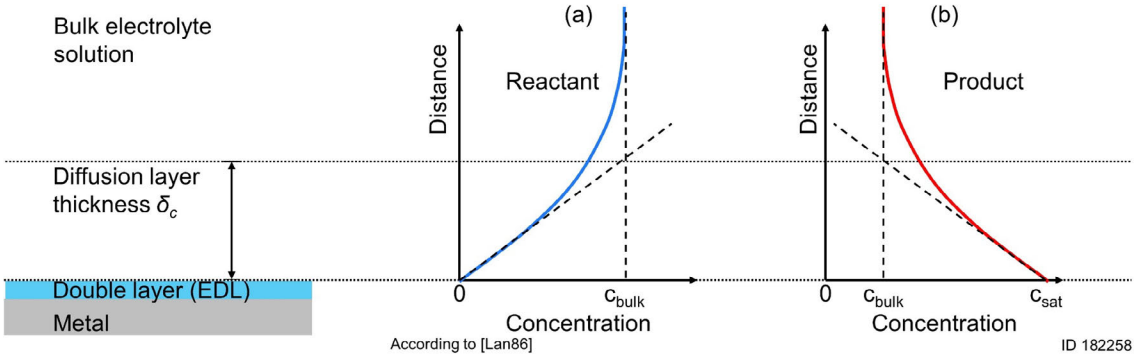

Figure 2.4: Schematics of (a) reactant and (b) product concentrations near the metal electrode surface as a function of the distance from the surface.

Although the exact chemical reactions and limiting species are often unknown, different transport-limiting mechanisms have been proposed in the literature. Proposed mechanisms include a salt precipitation of the dissolving metal, limited diffusion of acceptor anions by the formation of complexes and a water-based limitation caused by the formation of hydrated metal ions [Lan87]. Which mechanism dominates depend decisively on the material-electrolyte combination and the applied external potential.

2.2.3 Limiting current density

According to Faraday's law, the current density that flows through the metal electrode-electrolyte interface is proportional to the material dissolution rate. The application of an external potential changes the reaction kinetics of the dissolved metal ions in ways that depend on the polarization and migration through the double and diffusion layers into the bulk electrolyte. Measuring all anodic and cathodic partial currents as a function of the applied potential provides insight into the chemical reactions, the polarization in the electric double layer and the diffusion layer formation. Electrochemical polishing is achieved by applying the specific potential that adjusts the chemical processes on the surface in the desired manner.

Figure 2.5 shows the current density J as a function of the applied potential U for iron, nickel, chromium [Oka73] and titanium [Liu15]. The dashed lines in the figure distinguish the three different characteristic potential regimes for iron (black line): (1) the active (anodic) material dissolution U_c, (2) the passivation potential U_p and (3) the transpassive potential U_b. For the other species, the dashed lines would be shifted such that the initial peak is contained in the active (anodic) material dissolution U_c, the subsequent valley in the passivation potential U_p, and the final rise in the transpassive potential U_b. To obtain a glossy finish, electrochemical polishing is conducted at potentials in the range of the passivation regime.

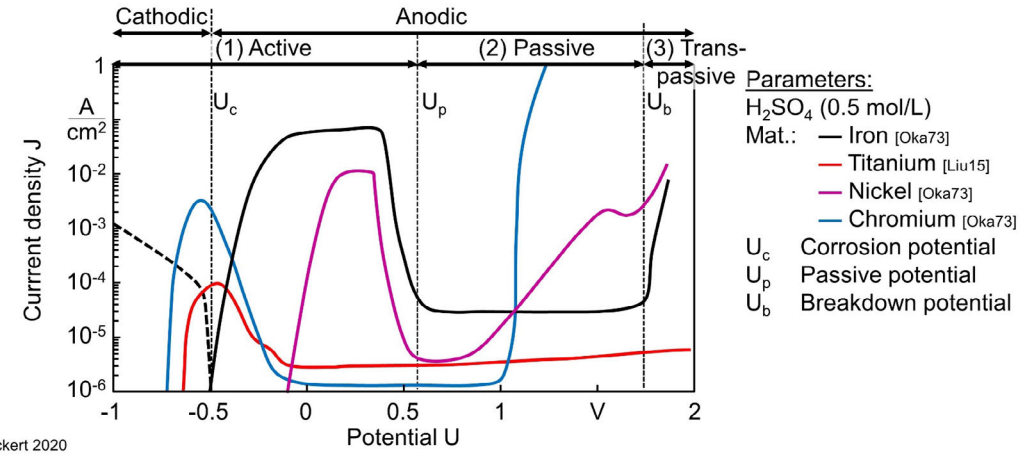

Figure 2.5: Current-potential curves showing the polarization regimes for different materials. The dashed lines separating the potential regimes apply only to iron.

During passivation, the current density and dissolution rate abruptly decrease because of the transport limitation caused by the formation of the diffusion layer. The passivation regime favors electrochemical polishing because in this regime, the thickness of the diffusion layer increases with the applied potential, and the diffusion layer effectively suppresses anisotropic etching, resulting in a very low microroughness and high brightness [Lan07]. If transport is not so limited, as in the other regimes, anisotropic etching can cause significant residual roughness on the surface. Anisotropic etching removes single layers of atoms and has been described by theories of crystal growth and dissolution. The transport limitation in the passivation regime results in a very low material dissolution rate, and polishing can take several minutes to hours.

In contrast, the material dissolution rate increases abruptly at the breakdown potential U_b, where the transpassive regime starts. This regime is frequently used for electrochemical machining because of the high material removal rates of several mm/min [Klo12]. Massive oxygen formation during processing causes heterogeneous material removal and pitting corrosion. Materials that show a higher breakdown potential U_b are associated with better corrosion resistance. In general, materials with a high corrosion resistance exhibit a low U_p and a high U_b [Lan07]. For instance, **Figure 2.5** shows that compared to iron (black line), the passive regime of titanium (red line) starts at lower potentials, has a lower current density within the passive regime and a higher breakdown potential. Therefore, titanium has a larger passivation potential range (nobility) and a much higher corrosion resistance. Furthermore, alloying a less noble material like iron with chromium can significantly improve iron's chemical resistance, as is the case in stainless steel.

In summary, the polarization of the electric double layer and the formation of a diffusion layer depends strongly on the material-electrolyte combination and the applied external potential. Analysis of the current-potential curve informs the determination of the ideal process parameters for electrochemical polishing. The result of the polishing process is further influenced by free and forced convection [Buh05], temperature and pressure, in addition to the characteristics of the material-electrolyte system.

2.2.4 Geometric levelling

Electrochemical polishing under anodic current conditions was systematically investigated by Edwards [Edw51], who showed that for geometric reasons, a grooved spaced surface is levelled, regardless of whether the local current density is in the active or passive regime. This process is termed "geometric levelling" and explains the smoothing on a macroscopic level. This section presents the geometric levelling approach according to Wagner [Wag54], which is based on a sine-wave profile of the material surface with amplitude ψ and wavelength λ, as depicted in **Figure 2.6**. A formula is derived for the decrease of the amplitude ψ as a function of the displacement h_s of the

receding average surface plane S from the initial surface plane S_I, i.e., h_s describes the material removal depth of the surface after a specific time t.

Geometric levelling is based on local differences in the dissolution rates of roughness peaks and valleys. These differences can be caused either by transport limitation of e.g., reactants, illustrated by the blue color gradient in **Figure 2.6**, or by an electric potential gradient on the surface, depicted by the orange color gradient in the figure. An ideal electropolishing process (without forced convection) is assumed, where the concentration of reactants c would be zero at the electrode surface, such that the boundary condition can be defined as follows.

$$c = 0 \qquad \text{at} \qquad z = \psi \cdot sin(2\pi x/\lambda) \tag{2.1}$$

Here, z is the distance of a point on the sine-wave profile from the current average surface plane S of the anode at the x-coordinate, as shown in **Figure 2.6**. The diffusion layer thickness δ_c is assumed to be much larger than the amplitude ψ. Thus, the reactant concentration in the bulk electrolyte is considered to be uniform, in contrast to the nonuniform concentration inside the diffusion layer, which causes differences in the dissolution rate that depend on the surface topography. Roughness peaks are exposed to higher concentrations of reactants and therefore dissolve at higher rates. The concentration in the z-direction is described by the diffusion equation given by Fick's second law, applying stationary conditions without any electrolyte flows:

$$\frac{\partial c}{\partial t} = D_c \nabla^2 c = 0 \tag{2.2}$$

where D_c is the diffusion coefficient, c is the concentration of the limiting specie and t is the time.

An alternative ideal electropolishing process can be assumed in which the electric potential at the surface is zero. This is the case if polarization at the surface is negligible, and the cathode is parallel to the average surface plane at a distance much larger than the amplitude ψ. For stationary conditions, the electric potential Φ inside the electrolyte is described by Laplace's equation:

$$\nabla^2 \Phi = 0 \tag{2.3}$$

and solving this equation yields the electric potential at the surface of the anode. The electric potential is higher at roughness peaks than in even regions or in valleys. According to Ohm's law, the electric potential is proportional to the current density J, and therefore elevated surface parts dissolve at higher rates.

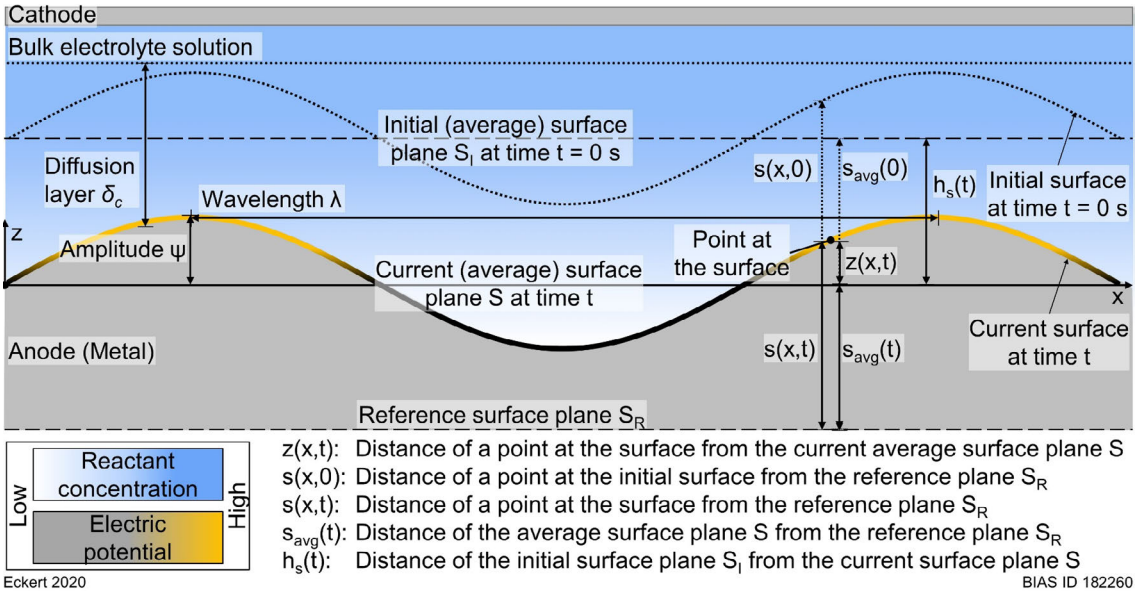

Figure 2.6: Illustration of the reactant concentration and electric potential over a sine-wave surface profile.

Both approaches to describing the differences between the dissolution rates of roughness peaks and valleys have the same mathematical form. Thus, the solutions produced by Equation (2.2) and Equation (2.3) are similar, as shown by Wagner [Wag54]. However, Wagner concluded that polarization causes a more uniform effective potential than calculated by Equation (2.3), i.e., the current density-potential curve has almost the same value at all points along the sine-wave anode and thus cannot cause geometric levelling [Wag51].

The following recapitulation of Wagner's model of geometric levelling based on the diffusion equation [Wag54] given by Equation (2.2) provides a basis for understanding smoothing during laser-induced thermochemical polishing as discussed in Chapter 7. One particular solution to Equation (2.2) reads [Ewd53]:

$$c(x,z) = B\left(z - \psi \cdot e^{-2\pi z/\lambda} \cdot \sin(2\pi x/\lambda)\right) \tag{2.4}$$

where B is a constant. For a surface profile with $\psi \ll \lambda$ and $\psi \ll \delta_c$, Equation (2.4) satisfies the boundary condition of Equation (2.1). Differentiating Equation (2.4) as follows yields the concentration gradient:

$$\frac{\partial c}{\partial z} = B\left(1 - (2\pi\psi/\lambda) \cdot e^{-2\pi z/\lambda} \cdot sin(2\pi x/\lambda)\right) \tag{2.5}$$

For $z \gg \lambda$, the gradient is supposed to be constant and becomes independent of x and z. The constant B is then equal to the average value of the concentration gradient at the surface, $(\partial c/\partial z)_{avg}$. This approximation of a linear dependence of the concentration on the distance holds only inside the diffusion layer, as shown in **Figure 2.4a**. Thus, a necessary

condition for Equations (2.4) and (2.5) is that the effective thickness of the diffusion layer must be much greater than the wavelength: $\lambda \ll \delta_c$. Substituting Equation (2.1) in Equation (2.5), expanding the exponential function, and neglecting terms of higher powers than the first, yields the concentration gradient:

$$\frac{\partial c}{\partial z} \cong \left(\frac{\partial c}{\partial z}\right)_{avg} \cdot \left(1 + \frac{2\pi\psi}{\lambda} \cdot \sin(2\pi x/\lambda)\right) \tag{2.6}$$

In the *x*-direction, the concentration gradient follows the sinusoidal profile given by Equation (2.1); in the *z*-direction, the gradient takes a constant average value $(\partial c/\partial z)_{avg}$.

The change in the shape of the surface profile as a function of the time interval can be derived by Fick's first law:

$$J_c = -D_c \frac{\partial c}{\partial z} = \frac{dn}{dAdt} \tag{2.7}$$

Here, D_c is the diffusion coefficient, and J_c is the diffusion flux, which measures the amount of substance n that will flow through a unit area A during a unit time interval t. Equation (2.7) describes the dissolution rate as proportional to the concentration gradient of the reactants. The amount of substance n that dissolves from the surface is determined by:

$$dn = \frac{\rho}{m_M} dV = \frac{\rho}{m_M} dAds \tag{2.8}$$

Here, ρ is the density, m_M is the atomic mass and V is the dissolved volume, which is determined by the dissolved material per unit area dA and the decrease ds of each point of the surface, as shown in **Figure 2.6**. Equation (2.8) can be substituted into Equation (2.7) and then into Equation (2.6) as follows.

$$\frac{ds(x,t)}{dt} = -\underbrace{\frac{m_M D_c}{\rho}\left(\frac{\partial c}{\partial z}\right)_{avg}}_{:=c_D} \cdot \left(1 + \frac{2\pi\psi}{\lambda} \cdot sin(2\pi x/\lambda)\right) \tag{2.9}$$

Here, the constant c_D is the average material dissolution velocity, equal to the product of the average concentration gradient, the diffusion coefficient, and the volume of metal reacting with one mole of the reactants.

The distance $s(x,t)$ of a point at the surface from the reference plane S_R, is equal to the distance s_{avg} of the average surface plane S from the reference plane S_R plus the distance $z(x)$ of a point at the surface from the current average surface plane S, as follows.

$$s(x) = s_{avg} + z(x) \tag{2.10}$$

$$z(x) = \psi \cdot sin(2\pi x/\lambda) \tag{2.11}$$

Thus, using these definitions in conjunction with Equation (2.9) yields:

$$\frac{ds_{avg}}{dt} + \frac{dz(x)}{dt} = -c_D - c_D \frac{2\pi\psi}{\lambda} \cdot sin(2\pi x/\lambda) \tag{2.12}$$

The decrease of the distances s_{avg} and $z(x)$ per unit time are linearly independent of each other, and therefore Equation (2.12) can be separated into:

$$\frac{ds_{avg}}{dt} = -c_D \qquad \text{and} \tag{2.13}$$

$$\frac{dz(x)}{dt} = -c_D \frac{2\pi\psi}{\lambda} \cdot sin(2\pi x/\lambda) \tag{2.14}$$

By substituting Equation (2.13) and the differentiation of Equation (2.11) with respect to ψ into Equation (2.14), one obtains:

$$\frac{d\psi}{ds_{avg}} = \frac{2\pi\psi}{\lambda} \tag{2.15}$$

The recess of the distance s_{avg} of the average surface plane S from the reference plane S_R is equal to the displacement of the initial surface plane S_I from the average surface plane S according to $dh_s = - ds_{avg}$ (see **Figure 2.6**). Therefore, integrating Equation (2.15) shows that:

$$\psi = \psi_0 e^{-(2\pi/\lambda)\cdot h_s} \tag{2.16}$$

where ψ_0 is the amplitude of the sine-wave surface profile at the time $t = 0$ s, and ψ is the amplitude at time t, corresponding to the displacement h_s, which describes the material removal depth from the initial surface plane. Equation (2.16) indicates that the amplitudes of short sine waves will decrease faster than the amplitudes of long sine waves. Thus, microroughness will disappear faster than meso- and macroroughness [Wag54].

Wagner's geometric levelling model described most of the experimental investigations that had been reported at that time, as long as the model's boundary conditions and simplifications were appropriate. The approach can be extended to more complex surface profiles by a mathematical Fourier analysis [Pet80], which requires expanding the diffusion layer by a Fourier series and solving the boundary value problem numerically, e.g., with the finite element method [Cle84]. Geometric levelling explains polishing solely based on the geometric properties of the surface. Although the model accurately describes dissolution rates and smoothing for many process conditions, certain phenomena can cause significant deviations from the predicted dissolution rate and

surface finish; such cases include anisotropic etching, pitting corrosion, convection-induced surface patterns [Buh15], gas bubble patterns [Ger02] and phenomena associated with different rates of removal of alloy species. In this work, the analytical approach of Equation (2.16) will be used to compare the smoothing dynamic of electrochemical polishing to laser-induced thermochemical polishing.

2.2.5 Anodic brightening

Electrochemical smoothing processes are often classified as one of two types, based on process conditions: anodic/geometric levelling (removing meso- and macroroughness) and anodic brightening (removing microroughness) [Jac56]. **Figure 2.7** shows scanning electron microscope (SEM) images of a triangular surface profile after anodic levelling and after the combination of anodic levelling and brightening. Anodic levelling refers to the elimination of roughness at heights greater than 1 µm. Levelling is the result of the potential and concentration differences between the roughness peaks and valleys, as described in Section 2.2.4. Anodic brightening refers to the elimination of microroughness at heights lower than 1 µm. Brightening is the result of suppressed anisotropic etching, which is caused by the response of the electrochemical material dissolution to the crystallographic orientation of the metal. Unless this etching behavior is suppressed, the surface finish can show the formation of crystallographic etch patterns, revealing distinct crystal planes. This phenomena is explained by classic theories of crystal growth and dissolution, which postulate the removal of atoms from energetically favored kink sites on monoatomic steps [Lan87]. The resulting surface finish depends on many factors, such as the electrolyte and the material composition. As a first reference, anodic brightening is often considered to occur under process conditions that include transport limitation and the formation of a compact or viscous surface layer. In other words, the occurrence of etching patterns indicates dissolution in the active or transpassive regimes in the absence of mass transport limitation.

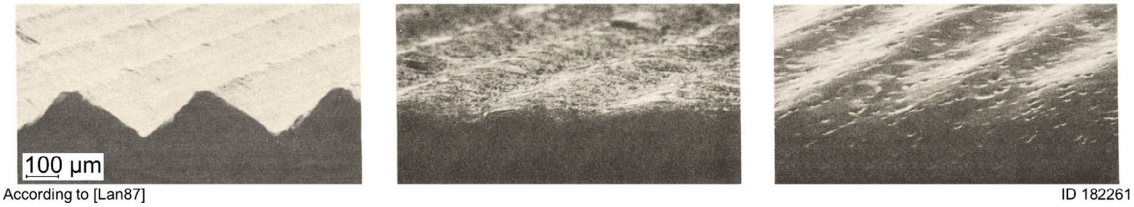

Figure 2.7: Scanning electron microscope (SEM) images of the triangular surface profile of a copper sample before treatment (left), after anodic levelling (middle) and after anodic levelling and brightening (right).

2.3 Laser-induced thermochemical material removal

2.3.1 Fundamentals

The material removal process fundamentals that are the focus of this work are based on laser-induced thermochemical machining in liquid electrolytes. This is a selective subtractive material removal method that can be used without applying an external potential and is based on the dependence of the electrochemical potential on the temperature. The laser-induced temperature increase on the surface can shift the electrochemical potential enough to initiate material dissolution.

Laser-enhanced material deposition and etching were first studied by Gutfeld et al., who investigated the influence of laser radiation on the polarization of the surface by means of potential measurements. An increase in temperature was found to shift the electrochemical (corrosion) potential in the laser-induced plating of copper in a sulfuric acid [Pui81]. For plating, the potential must shift to positive values in the center and negative values at the periphery. In general, the potential shift is determined by the negative value of the entropy change due to the laser-induced heating of the workpiece [Pui81]. Typical values for the potential shift in the plating of titanium in phosphoric acid are of some $5 \cdot 10^{-3}$ V/K. Laser etching has also been reported as the reverse of a plating process, with a negative shift of the electrochemical potential, on nickel [Dat87], molybdenum [Gut88], titanium [Now95] and stainless steel [Gut87].

Pippe et al. postulated two zones of different potentials on the surface, where the zones are electrically connected by the electrolyte. In the laser-irradiated center, the potential shifts to negative values $\partial\Phi/\partial T < 0$, creating an anodic area, while the colder periphery acts as the cathode, where the reduction occurs. This generates a local electric cell on the interface between the metal and electrolyte, the so-called “thermobattery” as shown in **Figure 2.8b**. As a result, an electric current can flow at the metal-electrolyte interface between the center and the periphery. Because of the very small cell dimensions of the battery, the electric field strengths are very high, and a potential shift with typical values of some 100 mV can be generated [Bäu11]. Investigations on the potential shift as a function of the temperature were performed on stainless steel and titanium by Rabbow and Stephen. They determined the activation temperature of the etching reaction to be 70°C for stainless steel [Rab07] and 90°C for titanium [Ste10]. A mathematical description of the laser-induced potential shift and the associated material removal has not yet been reported. Nonetheless, the thermobattery model offers a qualitative approach to explaining experimental observations.

2.3.2 Micromachining

Gutfeld et al. investigated laser-enhanced material deposition in the late 1970s and early 1980s with the aim of repairing conductor tracks for microelectronic applications by direct, maskless electroplating [Gut79]. The reverse process, laser-induced etching, was further developed in the mid-1990s by Nowak et al., who demonstrated the production of micro-antennae by direct and maskless etching. The antennae were cut from stainless steel foils with etching rates of up to 10 µm/s. The modification threshold was determined to be 0.2 W for an estimated focus diameter of 1.2 µm and 1 W for a focus diameter of 25 µm. During laser irradiation, a significant current increase was observed [Now96]. The authors proposed that laser radiation thermally activates the chemical reaction by breaking through the passivation layer, i.e., above a certain threshold temperature, the passivation layer can no longer be formed.

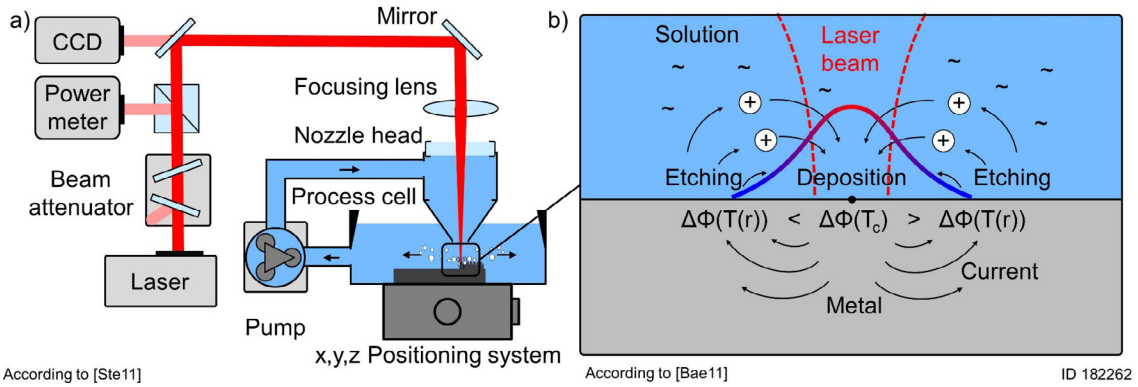

Figure 2.8: (a) Experimental setup based on an axial electrolyte jet [Ste11a]. (b) Depiction of the thermobattery model without external electric field [Bäu11].

Stephen and Rabbow investigated the influence of the flow velocity with the jet-based setup shown in **Figure 2.8a**. They showed that the aspect ratio of a removal cavity is limited by diffusion. Increasing the flow rate resulted in a decreased removal rate but higher cutting-edge quality and aspect ratio [Ste04]. These observations were attributed to a cooling effect of the electrolyte jet and reduced diffusion limitations inside the cavity. Furthermore, the material-removal rate was demonstrated to correlate with the peak temperature, regardless of the laser wavelength. Focus diameters of 7.8 µm and 13.0 µm with laser powers of 2.4 W and 16 W were used [Ste10]. Depending on the laser power, disturbances of the removal cavity due to periodic width fluctuations occurred, as shown in **Figure 2.9a** [Rab07]. Their formation was discussed as the result of a pulsating etching front due to gas formation [Mor05]. Any geometric form deviation from a Gaussian-like removal cavity (**Figure 2.9b**, Class A) is considered a material removal disturbance.

Mehrafsun showed that removal disturbances occur in the cavity center by fluctuations in depth (with a 12 W laser power and 24 µm focus diameter), as shown in **Figure 2.9b**. Disturbance-free material removal was found with a laser power of 6 W, an etchant flow

velocity of 1.8 m/s and a feed velocity of 5 µm/s [Meh13]. Emerging process gases were later shown to have a decisive influence on the formation of these disturbances [Meh18]. Disturbances can also be caused by laser-induced convection and material melting, and the latter may be a problem for high laser intensities above 0.5 MW/cm^2. Messaoudi et al. presented a temperature model for calculating the laser-induced temperature on the surface and reported activation temperatures of > 70 °C for visible material removal after irradiation for 1 s [Mes17].

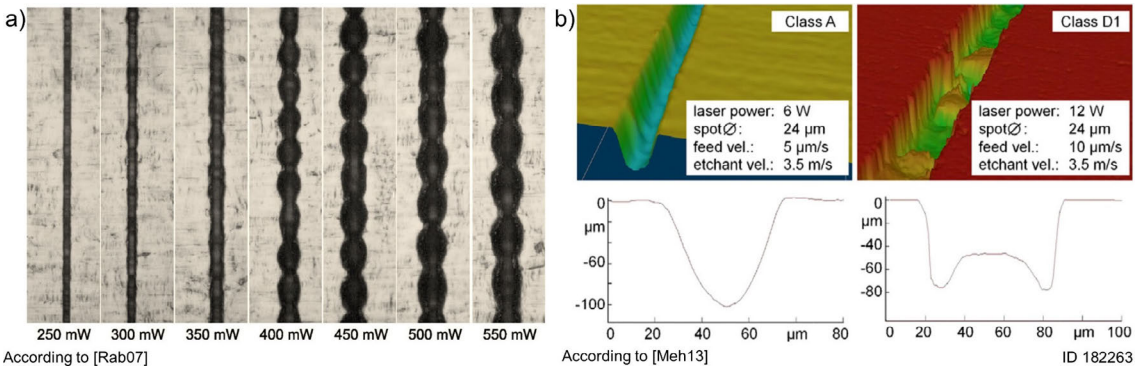

Figure 2.9: (a) Reflected-light images of a series of cavities structured with increasing laser powers on stainless steel [Rab07] and (b) surface-height data from disturbance-free and disturbed line cavities on Stellite 21 [Meh13].

Most previous studies have focused on the removal rate, aspect ratio, formation of disturbances and shape deviations in micromachining processes, with the aims of increasing process efficiency and avoiding disturbances. To date, no systematic investigations of the surface roughness and the mechanisms involved in the process of undisturbed material removal have been reported. Furthermore, the interactions of relevant process parameters are unknown. An overview of important influencing factors is given in **Figure 2.10**.

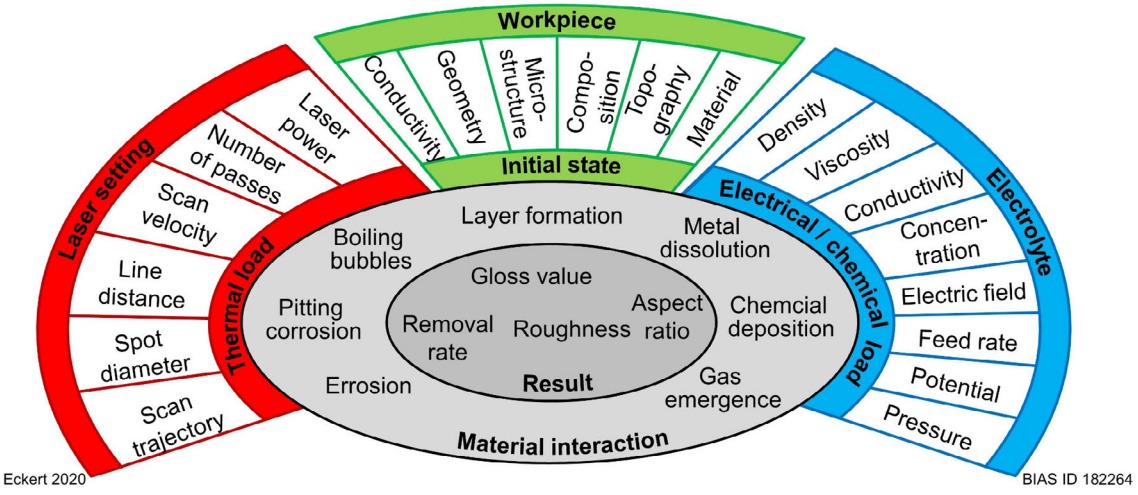

Figure 2.10: Overview of important process parameters in laser-induced thermochemical machining.

2.4 Laser-induced periodic surface structures

Materials modified with laser radiation frequently exhibit "laser-induced periodic surface structures". Since their first discovery in 1965 [Bir65], their emergence has often been discussed as resulting from the interaction between the incident laser radiation and a surface scattering wave, or from the excitation of surface plasmon polaritons [Sip83]. The shape and characteristics of the periodic structures depend on process conditions, such as the surface material and laser wavelength, energy, pulse duration and so forth. During material processing with continuous wave radiation, parallel grooves with depths of a few dozen nanometers, so-called ripples, can often be observed. The ripples are oriented perpendicular to the polarization of the laser radiation and show a spacing Λ, calculated by [Guo82]:

$$\Lambda = \frac{\lambda}{n_d \cdot (1 - sin\,\theta_L)} \tag{2.17}$$

where θ_L is the angle of incidence measured from the surface normal, and n_d is the refractive index of the surrounding medium.

2.5 Concept of process signatures

Controlling and adjusting surface integrity is a major challenge in manufacturing technology. One approach to surface integrity control, the concept of process signatures, was first presented by Eppinger et al. [Epp95] in the 1990s. This approach is based on process monitoring and recording of attributes, such as vibrations during turning [Sch01], forces during stamping [Kar89], defects during additive manufacturing [Fan98] or acoustic emissions during precision machining [Lee06]. The collected data are analyzed to find statistical correlations between those attributes and surface integrity properties to achieve a specific result [Sea16].

Correlations between the material modification and the process parameter (Correlation A in **Figure 2.11**), or external process quantities such as the intensity (Correlation B), are commonly sought in order to characterize certain process impacts. Such correlations can be used to choose suitable process parameters on empirical [Wan17] or numerical bases [Ste13]. Although those models and correlations are sufficient for their specific machining application, in modern manufacturing, most parts pass through a chain of different processing operations from initial production to final assembly. These chains motivate the development of more process-independent and generalized correlations and models. Therefore, Brinksmeier et al. defined process signatures as the correlation between material loads and material modifications, such as hardness, residual stress and roughness [Bri11], as depicted in **Figure 2.11**.

This approach considers the material loads (e.g., stress, strain and temperature) to predict observable material modifications and surface integrity properties across different machining processes [Bri18b], under the assumption that similar internal loads will lead to similar material modifications. The process signature should be expressed as a matrix with several process signature components, which are represented by functional correlations between the material modification M and the material loads L [Bri18a]:

$$M = f_M(L) \tag{2.18}$$

Such correlations were identified for processes such as hardening [Fre18], hard milling [Sea16], mechanical metal cutting [Buc17], deep rolling [Mey16] and electrochemical machining [Klo18]. In order to formulate suitable equations for process signature components and to determine the required process parameters, a physics-based knowledge of the material loads is necessary.

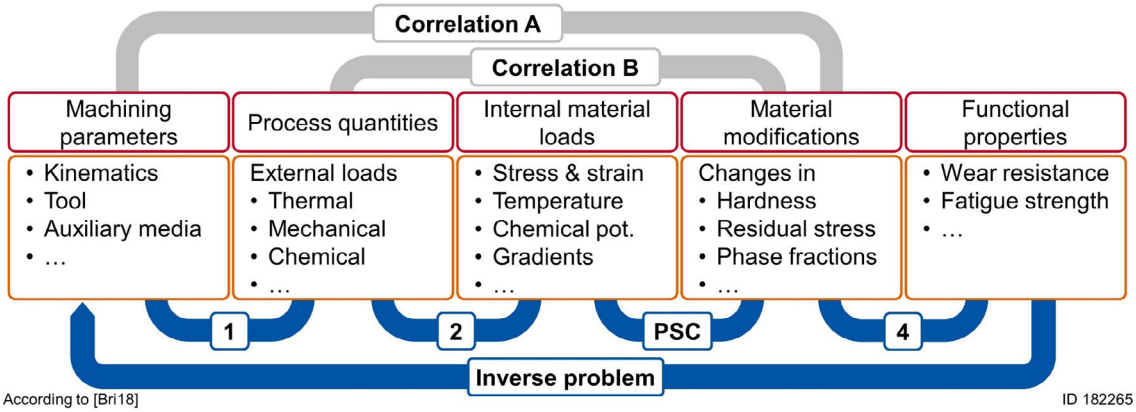

Figure 2.11: Causal sequences in manufacturing processes [Bri18]; PSC: process signature components.

However, the machining impacts are often highly multiphysical, and material modification is the result of complex internal material interactions and mechanisms. In many cases, identifying, calculating, or measuring the relevant internal load is either not possible or very challenging. Furthermore, the exact mechanisms are often unknown.

In laser-induced thermochemical machining, material removal results from the complex interactions among the laser-induced heating, changes in the electrochemical potential, anodic material dissolution and local convective and forced fluid dynamics. To date, only limited aspects of these interactions have been investigated and modelled. Single-spot experiments have shown [Mes17] that the removal geometry correlates with the temperature distribution. The extent to which the laser-induced thermal load can be correlated with roughness changes has not yet been reported and is subject of this work.

3 Objective

As presented in Chapter 2, laser-induced thermochemical machining (LCM) offers several interesting properties that could be leveraged to advance micropolishing processes for passive metals. These properties motivate the investigation of LCM for improving surface finishing characteristics, including brightening, smoothing, cleaning and deburring. The present work aims to develop the experimental and theoretical knowledge on this topic to harness LCM for selective micropolishing applications. The use of LCM for these purposes is referred to as laser-induced thermochemical polishing (LCP).

The objectives of the present work are to identify relevant influences on and deduce suitable conditions for laser-induced thermochemical surface smoothing, to develop a selective polishing process, and to identify the mechanisms involved. For this purpose, the interactions of various process parameters and their impacts on the surface finish must be clarified. The following central research hypotheses guide the investigation.

- During LCP, material removal and surface roughness can be described by the fundamental parameters of thermal load and exposure time.
- The mechanism of geometric levelling governs the different removal rates at surface peaks and valleys and leads to polishing.
- The surface finish is limited by material composition and microstructure, regardless of the initial roughness.

A scanner-based multipass LCM method, which allows controlled millisecond exposure of the surface to laser radiation, is developed to investigate these phenomena. In order to identify reliable process conditions for smoothing, process parameters such as laser power, scan velocity, spot diameter, line spacing and number of passes are systematically varied. The surface finish is analyzed by reflected-light images, surface-height data, average roughness S_a, as well as micro- and mesoroughness and waviness. The first hypothesis is tested by evaluating the material removal in terms of the thermal load and exposure time. Therefore, different sets of process parameters but equal thermal load, should result in similar modifications. The second hypothesis is tested by correlating the material removal depth with the average roughness. If geometric levelling occurs, the amplitude of a surface profile should decrease exponentially as a function of the removal depth and profile wavelength. Furthermore, a formula is derived and tested for the decrease of the average roughness as a function of the thermal load and exposure time. For the third hypothesis, the polishing of different preprocessed samples and materials is analyzed to determine the extent to which the surface finish shows material-specific etching patterns and inhomogeneous etching of distinct alloy elements.

4 Method

4.1 Experimental setup

The laser setup shown in **Figure 4.1** was developed for the experimental investigations. The setup consists of a laser source, optical components, a two-dimensional laser scanner, and a closed wet-etching chamber where the samples are mounted. The single-mode fiber laser (SPI Lasers JK400FL) emits continuous-wave laser radiation with a wavelength of 1080 nm in TEM_{00} mode and with a beam quality factor of 1.3 and a laser power of P_L = 15 W to 400 W. The emitted intensity distribution I is almost Gaussian-shaped. The spot diameter d_f is defined by $P_L = \pi d_f^2 I_0/8$ according to Equation (A.4) in the appendix, and as summarized in **Figure 4.1**. The laser power can be reduced down to 0.1 W by changing the transmission of a variable edge filter. To adjust and monitor the laser power, the radiation is partly reflected to a power meter (Coherent PM150-50C) by a 50:50 beam splitter. The beam diameter can be reduced to a third by an inversely mounted telescope (Sill Optics S6EXZ5310). This allows the spot diameter to be incrementally increased from d_f = 31 µm to 156 µm. Furthermore, the beam diameter can be adjusted between 156 µm and 950 µm by defocusing the Gaussian beam, whereby the entire scan head and thus the beam waist are moved relative to the sample in the z-direction. Several spot diameters and z-positions were verified with a beam profile camera (Ophir Spiricon SP920G).

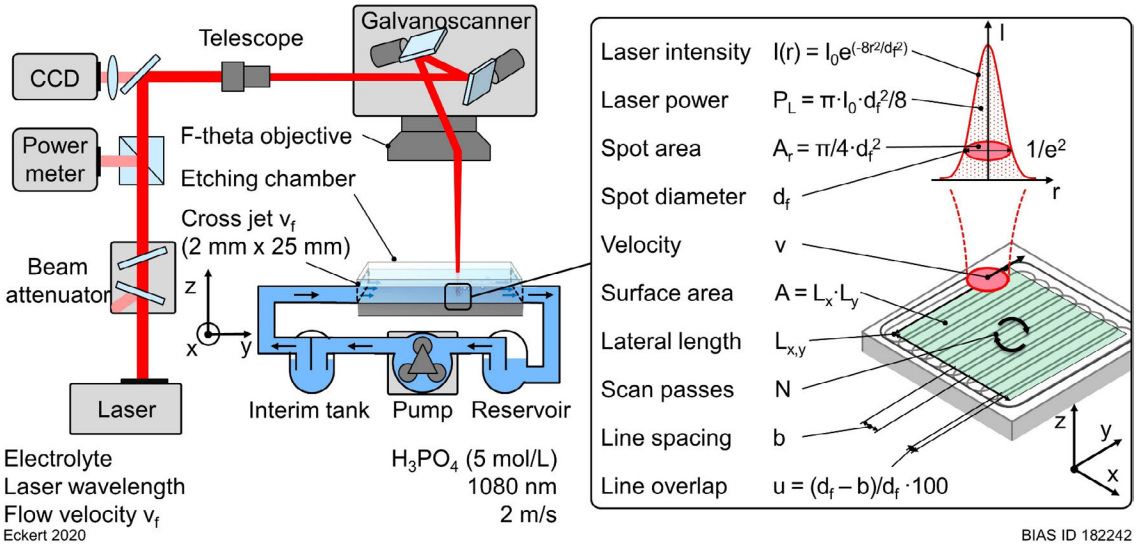

Figure 4.1: Schematics of the experimental setup for the laser-induced thermochemical polishing process and the relevant process settings and definitions.

The laser radiation is focused by a telecentric f-theta optic (Sill Optics S4LFT3162) with a focus length of 163.5 mm and guided across the sample surface using a two-dimensional scanner system (Raylase Superscan III-15) with velocities between v = 2 mm/s and

10 m/s. The size of the scan field is 120 mm × 120 mm. The exact spot position on the sample is adjusted by a linear axis (Newport MTN-50PP) and monitored with a CCD camera. The reflected light is bandpass-filtered and magnified by a 200-mm convex lens. The linear axis and the scanner are controlled by the Weldmark 3 software (Raylase).

The samples were polished in a closed wet-etching chamber through which an electrolyte was circulated. The sample materials were first cut into 20 mm × 20 mm (x- and y-dimensions) samples and hot-mounted in an epoxy thermosetting polymer. The mounted samples were inserted into the etching chamber by means of a sealing ring. The electrolyte was pumped at 1 L/min through an interim tank to the etching chamber to minimize pulsation from the peristaltic pump. The electrolyte flow velocity v_f was 2 m/s, introduced as a cross jet over the surface of the samples in a 25 mm × 2 mm (x- and z-dimensions) flat channel. This ensured faster removal of emerging process gases from the spot area. This experimental setup enabled the investigation of the influence of a wide range of laser powers P_L, spot diameters d_f, line spacings b, scan velocities v and numbers of passes N on the surface finish, as illustrated in **Figure 4.1**.

4.2 Materials and electrolyte

This study tested metals with a strong tendency to form a stable oxide layer on their surfaces (passive metals), even in highly acidic environments. In all experiments, 5.0 M (28.7 vol. %) phosphoric acid solution (H_3PO_4) was used as the electrolyte. Titanium Grade 1, titanium Grade 2, titanium alloy Ti6Al4V (Grade 5), nickel titanium (Nitinol), cobalt-chrome-based alloy (Stellite 21) and bulk metallic glass on a zirconium basis were investigated. Rolled sheets with thicknesses of L_z = 0.8 mm were used for the titanium-based samples. The cast metallic glass sample had a thickness of 5 mm, and the cobalt-chrome-based samples had thicknesses of 4 mm. Table 1 summarizes the material's element compositions, properties and labels.

Table 1: Sample materials and their physical properties under standard temperature and pressure conditions.

Material	**Titanium (Grade 1)** [Boy94]	**Titanium (Grade 2)** [Boy94]	**Ti6Al4V (Grade 5)** [Boy94]	**Nitinol** [Boy94]	**Metallic Glass** [Mat18]	**Stellite 21** [Del07]
Elements [%]	Ti: 99.5	Ti: 99.3	Ti: 89.4 Al: 6.1 V: 4.0	Ni: 55.8 Ti: 44.2	Zr: 62.5 Cu: 31.0 Al: 3.3	Co:62.3 Cr: 27.0 Mo: 5.5
Density ρ [kg/m^3]	4510	4510	4430	6500	6900	8360
Thermal conductivity K [W/(m·K)]	25	25	7	10	13	15
Spec. heat capacity c_p [J/(K·kg)]	523	523	560	320	419	404
Absorptivity α [%] [Rak98]	39	39	37	30	26	27
Avg atomic mass m_M [1.7·10^{-27}·kg]	47.9	47.9	46.5	53.9	77.6	56.0
Sample thickness L_z [mm]	0.8	0.8	0.8	0.8	5	4

Commercially available materials may contain traces of iron (Fe), carbon (C), nitrogen (N), hydrogen (H) and oxygen (O). Although their concentrations are in most cases negligibly low (< 0.1 %), they can nonetheless have a significant influence on a chemical reaction. Here, the average atomic mass was calculated by summing the products of each atomic mass and the corresponding element ratio, neglecting trace elements. As another consideration, the absorptance of a polished surface varies between 26 % and 39 %, depending on the material. Therefore, prior to polishing, the materials were cut into samples, hot-mounted and cleaned with ethanol, and the microstructures of the materials were initially characterized through metallographic microsection images, shown in **Figure 4.2**. The rolled titanium (Grade 1) samples serve as the reference material.

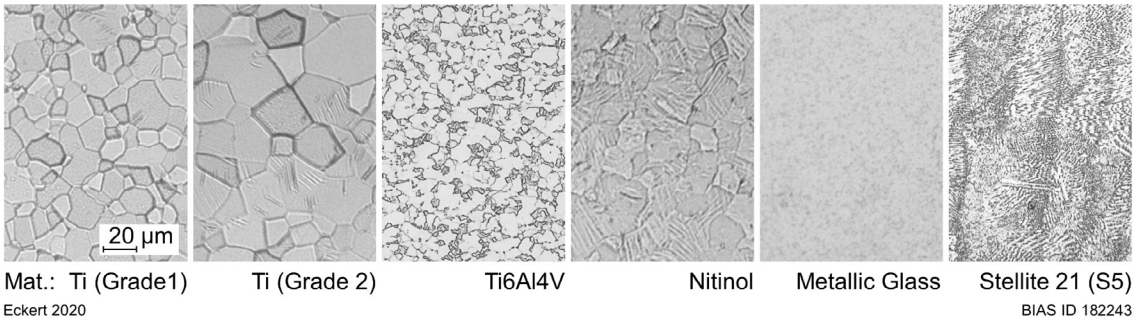

Figure 4.2: Initial microstructures of the investigated materials.

In order to investigate the influence of the material's microstructure on the polishing results, five variously manufactured cobalt-chrome-based Stellite 21 samples were investigated. Table 2 gives an overview of the different manufacturing processes used to produce these samples.

Table 2: Overview of the variously manufactured Stellite 21 samples.

Material	Label	Generation process
Stellite 21	S1	Spray formed
	S2	Cast
	S3	Additively manufactured (annealed for 10 h at 1100 °C)
	S4	Additively manufactured (unannealed)
	S5	Laser sintered

4.3 Measurement methodology

4.3.1 Removal depth

The surface was characterized with a confocal laser scanning microscope (Keyence VK9710) using a 50× objective (1 pixel = 0.139 µm). The measurement data cover a surface area of 285 µm × 215 µm and represent three-dimensional coordinates of the surface topography. These measurement data describe the surface as coordinate points of distance $s(x,y)$ (primary surface-height data) to a reference plane S_R (in accordance as depictured in **Figure 2.6**). The acquired data sets are suitable for roughness measurements

and analysis of the modification depth. Depth measurements were performed with the VK-Analyzer software (Keyence) and MATLAB (MathWorks).

Figure 4.3 illustrates the analysis of the three different types of modifications: spot cavities, line cavities and area structuring. In order to characterize surface modifications, such as the spot or line cavity depth h_c, and the material removal depth h_s, the primary surface-height data $s(x,y)$ were analyzed with respect to the initial unmodified surface area. The unmodified surface area (black crosshatched area in **Figure 4.3**) was used to define the initial surface plane S_I by averaging the height data $s(x,y)$ (in x- and y-dimension), which describes the average height of the initial surface $s_{avg}(0)$ to the reference plane at time $t = 0$ s (see **Figure 2.6**). Next the entire primary surface-height data $s(x,y)$ were offset by this averaged value $s_{avg}(0)$ so that the initial surface plane defines the zero-line ($z = 0$) of the new transformed surface-height data $s(x,y)^*$. The transformed height data describe the surface as coordinate points of distance $s(x,y)^* = s_{avg}(0) - s(x,y)$ to the initial (unmodified) surface plane S_I. So that the removal depth values were always measured in relation to the initial surface plane (zero-line).

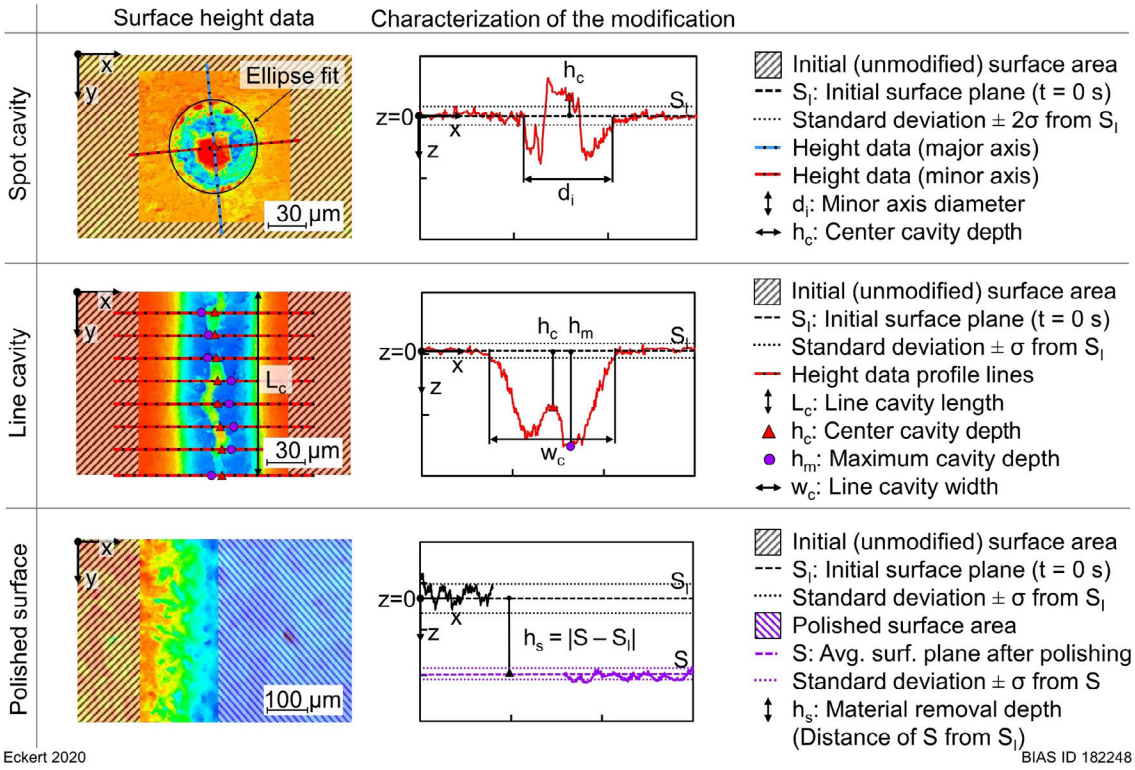

Figure 4.3: Schematics of the removal depth measurements for spot and line cavities and the surface.

In particular, the depth of the spot cavity was determined based on the two-dimensional height profile along the major and minor axes of a least-squares ellipse fit. As the criterion for defining the cavity diameter along the major axis d_j and minor axis d_i, height data below a threshold of two-standard deviations from the initial surface plane were considered. The depth h_c was measured in the center at $d_{j,i}/2$ and averaged over six

different cavities. The uncertainty of the depth measurement was determined by the standard deviation.

In a similar manner, the average center depth h_c of a line cavity of length L_c was determined based on eight two-dimensional height profiles oriented perpendicular to the scan direction along the y-axis. The profile lines were separated from each other by 20 µm. The threshold of the material removal was again defined by the intersection of the height data with the straight line representing data points more than two-standard deviations below the initial surface plane. The distance between the two intersection points defined the width w_c of the line cavity at a specific y-position. The average width was measured by averaging the cavity widths of all profile lines, and the maximum removal depths h_m were likewise measured and averaged. If process disturbances occur, the maximum depth is not necessarily equal to the depth in the cavity center at $w_c/2$. The center depth can even rise above the zero-line and show positive values. For both the maximum depth and the center depth, the uncertainty was determined by their standard deviations. The cavity volume V_c was measured following the same pattern, by integrating all height data from the cavity below two standard deviations from the average surface plane in the x- and y-directions.

The material removal depth h_s describes the displacement of the initial average surface plane S_I to the current average surface plane S after processing for a specific time t and can be determined using the transformed surface-height data $s(x,y)^*$. For this purpose, the surface-height data within the polished surface area were averaged in the x- and y-directions (purple crosshatched area in **Figure 4.3**). The average value describes the depth of the polished surface plane S in relation to the initial surface plane S_I (zero-line). The material removal depth h_s depends on the time t, since the depth increases with further processing. The uncertainty of h_s was calculated by propagating the uncertainties of the standard deviations of S_I and S. Note, that h_s is defined as the absolute value $|S - S_I|$ and therefore has positive numerical values, although the material removal increases in depth.

4.3.2 Surface roughness

As stated in the previous section, the surface-height data were measured with the confocal laser scanning microscope (Keyence VK9710) using a 50× objective (1 pixel = 0.139 µm) and covered a surface area of 285 µm × 215 µm. The surface can be generally categorized into small to large surface features and differentiated into micro-, meso- and waviness contributions to the roughness. Smaller surface features typically have a more significant influence on the surface brightness, whereas larger, process-related deviations increase the waviness. Many surface processes generate characteristic, often periodic patterns, resulting in a nonuniform surface finish. In this thesis, the analysis of the surface finish focuses on the characterization of:

- The average surface roughness S_a according to ISO 25178 [ISO12]
- The average roughness wavelength λ_S according to ISO 4287 [ISO97]
- The average spectral roughness $S_{a,\lambda}$, which describes the roughness separated into multiple wavelength bands, according to Willenborg [Wil06].

The average surface roughness S_a is the arithmetical mean height of the surface. This value is determined with the VK-Analyzer software (Keyence) using SL-filtered surface-height data, as follows. According to ISO 25178, the lower cutoff wavelength is set to $\lambda_{c,min}$ = 0.8 µm (S-filter) and the upper cutoff wavelength is $\lambda_{c,max}$ = 250 µm (L-filter). No additional filters are applied. The S-filter removes most of the noise from the signal because these wavelengths are below the diffraction limit of the microscope. The L-filter removes long wavelengths that contribute to form and shape deviations rather than roughness. The uncertainty of the average roughness is calculated based on the standard deviation of the roughness values in the four quadrants of the surface-height data.

The average roughness wavelength λ_S can be understood as the mean spacing between peaks. This value is determined with the VK-Analyzer software (Keyence) according to ISO 4287. Thus, the λ_S values of 30 profile lines in the x- and y-directions, separated by 7 µm from each other, were determined and averaged. The individual profile lines were filtered with cutoff wavelengths of $\lambda_{c,min}$ = 0.8 µm and $\lambda_{c,max}$ = 250 µm to remove noise and waviness.

The spectral analysis of the roughness $S_{a,\lambda}$ aims to visualize and quantify the influence of the machining process on the different length scales of the surface finish. Analyzing changes across different wavelengths provides additional information about process-related characteristics of the surface finish. A schematic of the calculation procedure is shown in **Figure 4.4**. First, a fast Fourier transform (FFT) was applied to the primary data, $s(x,y) \rightarrow s^+(k_x,k_y)$, to determine the spatial frequencies using the FFTW library in MATLAB (Version 9.5, R2018b) [Fri98], and the surface features were classified according to their spatial frequencies. This spatial decomposition was achieved by applying a two-dimensional Gaussian bandpass filter to $s^+(k_x,k_y)$, with upper $k_{c,max} = 2\pi/\lambda_{c,max}$ and lower $k_{c,min} = 2\pi/\lambda_{c,min}$ cutoff wavelengths. A set of cutoff wavelengths (0.8 – 1.25 – 2.5 – 5 – 10 – 20 – 40 – 80 – 160 – 320 µm) defined the wavelength intervals into which the data were separated. The filter intervals correspond to different surface feature categories: microstructures, process-related ridges and grooves, and geometric positioning or vibrational distortions. By inverse FFT of the nine filtered frequency data sets, nine filtered surface topographies were obtained, reflecting the origin and contribution of the surface features to the roughness. The surface roughness of these topographies is calculated by:

$$S_{a,\lambda} = \frac{1}{A}\iint_{A} |z(x,y)|\, dxdy \tag{4.1}$$

Each $S_{a,\lambda}$ value represents the roughness of a particular two-dimensional spectral wavelength band. In this context, $S_{a,\lambda}$ is referred to as spectral roughness, which can be interpreted as the roughness caused by surface features of a specific wavelength. Note that the roughness value contains no directional information because of the integration in the x- and y-directions. The roughness spectrum shows the $S_{a,\lambda}$ values on a logarithmic scale as a function of the wavelength bands (**Figure 4.4**). The uncertainty of the spectral roughness $S_{a,\lambda}$ results from the standard deviation of the four quadrants of each data set.

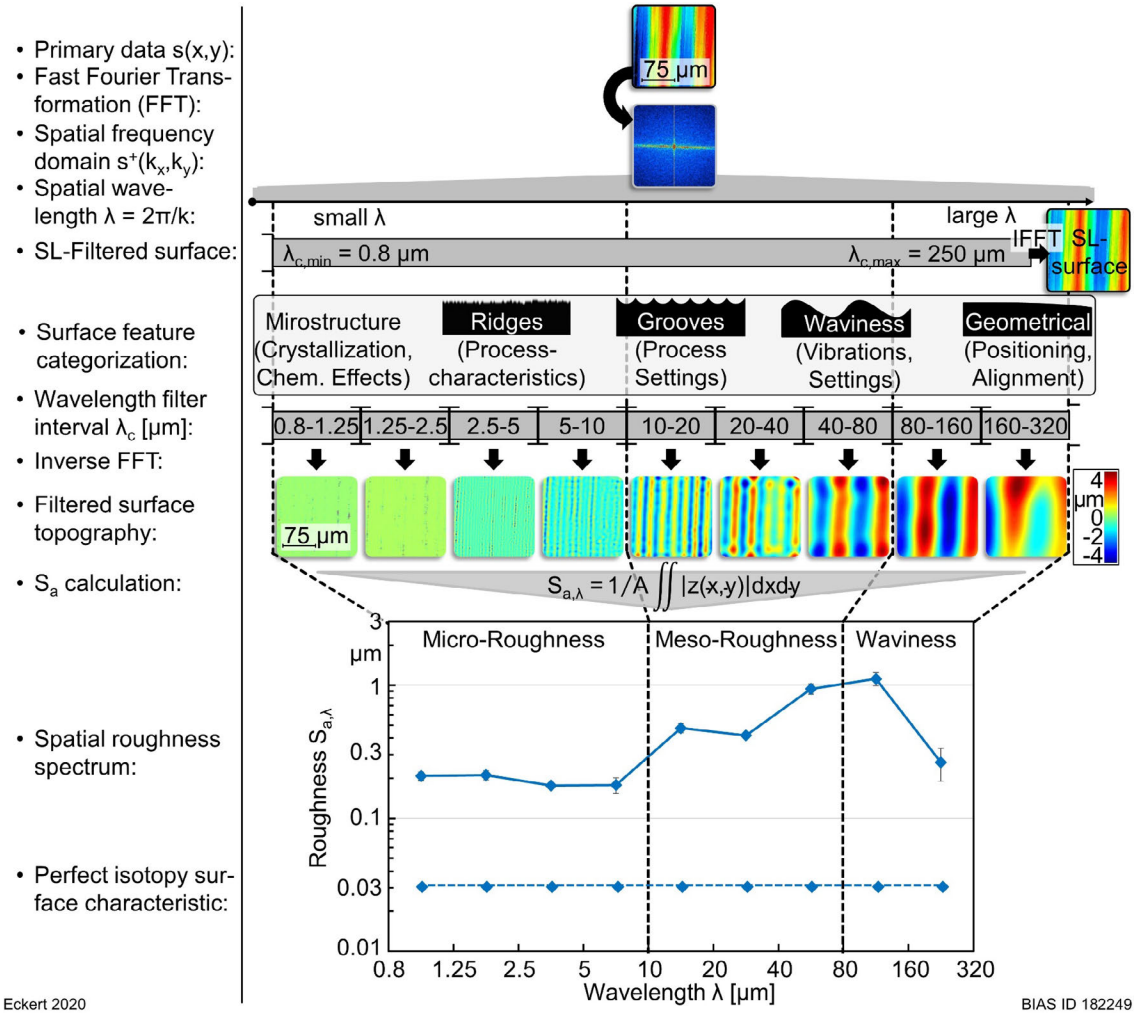

Figure 4.4: Procedure for calculating the spectral roughness. The wavelengths are associated with surface features, as illustrated for the spectrum of a turned surface (blue line). The dashed line shows an idealized uniform surface finish over multiple wavelengths.

The wavelengths are grouped into microroughness (0.8 µm to 10 µm), mesoroughness (10 µm to 80 µm) and waviness (80 µm to 320 µm) regimes. The turned surface shown in **Figure 4.4** has a small spectral roughness of approximately 0.2 µm within the microroughness regime. Because of this low microroughness, the surface finish appears

to be relatively bright. The maximum at a wavelength of 80 µm correlates with the spacing between turning grooves. Thus, the turning process generates a characteristic surface finish with distinct features. The roughness spectrum integrates the directional dependency and categorizes surface features in a two-dimensional diagram. Distinctive surface patterns, such as periodic grooves, increase roughness in the corresponding wavelength band. The roughness spectrum thus describes uniformity over multiple wavelength bands and the impact of a finishing process on different length scales of surface features. A polishing process that generates an ideal smooth and uniform surface finish should result in a roughness spectrum with a horizontal progression (the dashed blue line at the bottom of **Figure 4.4**).

4.4 Surface preparation

The samples were preprocessed by abrasive blasting, turning and grinding to investigate the influence of the initial topography on the surface finish. The titanium samples had an as-delivered rolled surface with an average roughness of 0.5 µm and average wavelength of 8.0 µm. Some of these samples were abrasive-blasted (samples B2, B3, B4) with a garnet-type mineral (grain size: 70 µm, 5 bar) for 1 s, 3 s and 6 s. Other titanium samples were turned (samples T2, T3, T4) at three different process settings or ground (sample T1) with an abrasive paper (grain size: P320) to produce isotropic and anisotropic surface topographies. **Figure 4.5** shows reflected-light images, surface-height data and the height distribution, average roughnesses and average wavelengths of the rolled or abrasive-blasted titanium (Grade 1) surfaces, labeled by the preprocessing B1 through B4. The height distributions show the percentage of the surface-height data on a logarithmic scale on the z-axis. Abrasive blasting induced an initial roughness between $S_{a,i}$ = 1.4 µm and 3.4 µm and initial average wavelength between $\lambda_{S,i}$ = 14.5 µm and 21.0 µm, and also changed the symmetry of the height distribution. The first second of abrasive blasting (B2) produced deep indentations ($\Delta z < -4$ µm) that led to an asymmetric distribution. After six seconds (B4), the distribution was symmetric again, with the peak-to-valley distance increasing from 4 µm to 16 µm.

Figure 4.6 shows the results for the pre-ground and pre-turned surfaces, labeled T1 through T4. The turning tool was oriented at different angles to produce spaced grooves with roughnesses between $S_{a,i}$ = 0.5 µm and 2.2 µm and average wavelengths between $\lambda_{S,i}$ = 4.8 µm and 50.6 µm. Symmetrical distributions with peak-to-valley distances between 4 µm and 12 µm were produced, with distances depending on the process setting.

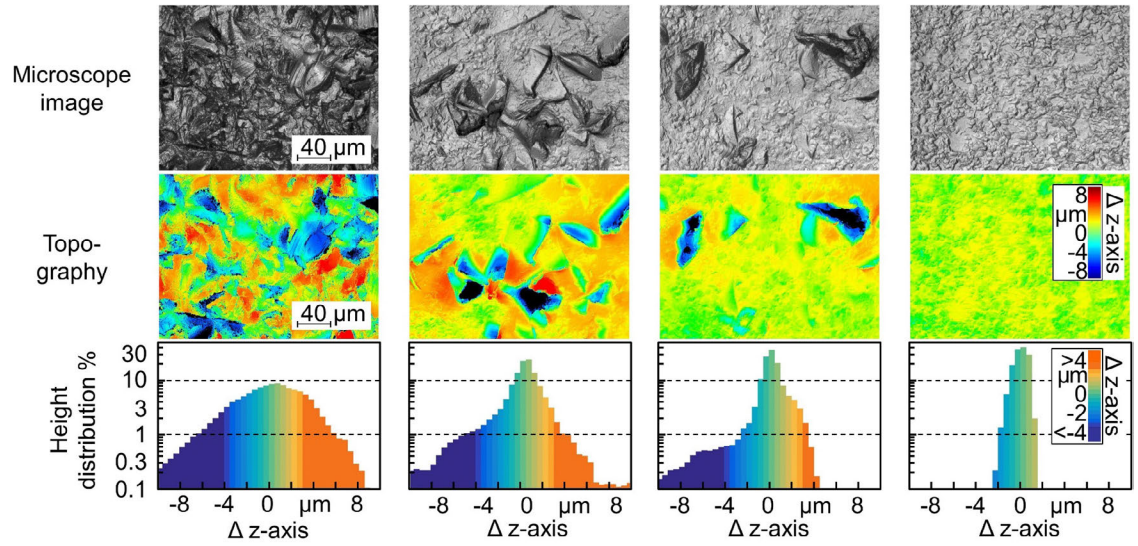

Material:	Ti (Grade 1)	Ti (Grade 1)	Ti (Grade 1)	Ti (Grade 1)
Label:	B4	B3	B2	B1
Initial surface:	Abr. bla. 6 s	Abr. bla. 3 s	Abr. bla. 1 s	Rolled
Initial rough. $S_{a,i}$:	3.4 µm	2.2 µm	1.4 µm	0.5 µm
Initial rough. λ_S:	19.0 µm	21.0 µm	14.5 µm	8.0 µm

Eckert 2020 BIAS ID 182244

Figure 4.5: Reflected-light images, surface-height data and height distribution of rolled and abrasive-blasted surfaces. The average roughness is determined according to ISO 25178.

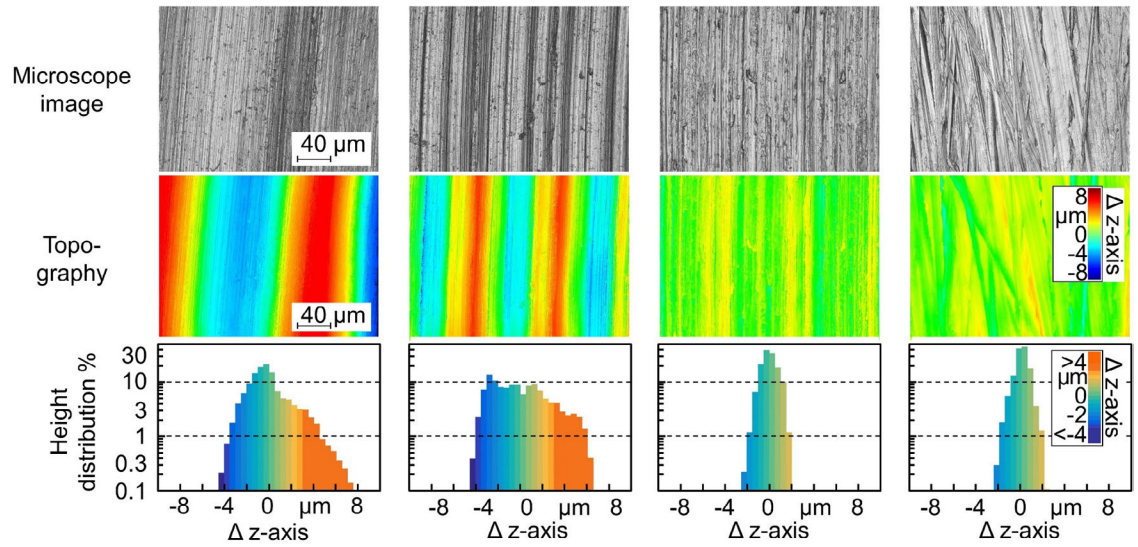

Material:	Ti (Grade 1)	Ti (Grade 1)	Ti (Grade 1)	Ti (Grade 1)
Label:	T4	T3	T2	T1
Initial surface:	Turned (650 $\frac{U}{min}$, 4 $\frac{mm}{min}$)	Turned (650 $\frac{U}{min}$, 6 $\frac{mm}{min}$)	Turned (330 $\frac{U}{min}$, 4 $\frac{mm}{min}$)	Ground (P320)
Initial rough. $S_{a,i}$:	2.0 µm	2.2 µm	0.6 µm	0.5 µm
Initial rough. λ_S:	50.6 µm	22.8 µm	4.8 µm	6.8 µm

Eckert 2020 BIAS ID 182245

Figure 4.6: Reflected-light images, surface-height data and height distribution of ground and turned surfaces. The average roughness is determined according to ISO 25178.

All other materials such a titanium (Grade 2), Ti6Al4V, Nitinol, Stellite 21 (S1 through S5) and metallic glass samples were only subjected to 6 s of abrasive blasting. Their resulting initial roughnesses varied from 2.5 µm to 3.4 µm. Table 3 summarizes the initial

surface preparations, average roughnesses, average wavelengths and absorptivity of each material/surface combination.

Table 3: Overview of the surface preparation, average roughness, wavelength and absorptivity.

Material	Label	Surface preparation	Initial rough. $S_{a,i}$ [µm]	Avg. wavel. λ_S [µm]	Absorptivity α [%]
Titanium (Grade 1)	B1	Rolled (as-delivered)	0.5	8.0	43
	B2	Abrasive blasted 1 s	1.4	14.5	45
	B3	Abrasive blasted 3 s	2.2	21.0	55
	B4	Abrasive blasted 6 s	3.4	19.0	63
	T1	Ground (P320)	0.5	6.8	43
	T2	Turned (330 U/min, 4 mm/min)	0.6	4.8	44
	T3	Turned (650 U/min, 6 mm/min)	2.2	22.8	49
	T4	Turned (650 U/min, 4 mm/min)	2.0	50.6	47
Titanium (Grade 2)	B4	Abrasive blasted 6 s	3.2	22.6	65
Ti6Al4V (Grade 5)			3.4	18.8	68
Nitinol			2.7	18.5	59
Metallic Glass			2.7	16.6	49
Stellite 21 (S1 to S5)			2.5	2	44

After the surface treatment, the absorptance α of the materials was measured with an integrating sphere at a wavelength of 808 nm, as described by Kügler [Küg19]. The laser radiation was focused with a numerical aperture of 0.5, resulting in a spot diameter of 0.38 mm on the sample surface. In order to determine the measurement uncertainty, the absorptance of the five titanium samples that were abrasive blasted for 6 s were averaged, and the measurement uncertainty was determined to be 1.7 % by the standard deviation. The abrasive-blasted surfaces tended toward higher absorptance with higher roughness, whereas the absorptance of the turned surfaces was almost constant.

4.5 Experimental parameters and procedure

Three types of experiments were performed: structuring individual spot cavities, structuring line cavities and area polishing. The area polishing experiments were subdivided into those for determining suitable process parameters and those for investigating the influences of the material and initial topography. Laser-induced thermochemical polishing (LCP) was performed as a multicycle process with up to some hundreds of accumulated scan passes. The reason for the high number of passes was that one laser pass with velocities of millimeters per second removes material at the nanometer scale, with typical laser-induced thermochemical material (LCM) removal rates in the range of several micrometers per second.

In the first set of experiments, single spots were structured on rolled titanium (Grade 1) samples with an irradiation time of 1 s and laser powers increasing from 0.5 W to 8.0 W. In the second set of experiments, individual 0.8 mm long lines were structured using various laser powers, spot diameters, scan velocities and numbers of passes. The cavities were separated 400 µm from each other. Table 4 summarizes the parameters employed

for these experiments. The cavities were topologically characterized with the laser scanning microscope. The depths of the cavity center h_c and maximum h_m were measured. The removal depth was examined as a function of laser power, number of passes and spot diameter. Furthermore, cross-sectional images and scanning electron microscopy (SEM, Zeiss EVO MA10) and energy-dispersive X-ray spectroscopy (EDX, Bruker XFlash 6) images were taken from selected cavities (integration time: 210 s) to determine the material modifications. The SEM images were taken under a tilt angle of 65° and a voltage of 20 kV.

In the third set of experiments, the influence of the process parameters on the surface finish was investigated. On the rolled (B1) and ground (T1) samples, areas of 1000 µm × 1000 µm were polished. A zigzag laser beam trajectory with a defined line spacing was used for area polishing. First, the influences of process parameters were studied, including overlap, spot diameter, scan velocity, rotation angle, laser power and number of passes on the surface finish. Second, to investigate the influence of the initial topography, areas were polished on the different prepared initial topographies listed in Table 3, and experiments were conducted varying only the laser power and number of passes and holding other parameters constant. Third, to investigate the influence of materials, the materials listed in Table 1 and 2 were area-polished and investigated with regard to laser power and number of passes, holding all other process parameters constant. Table 4 presents the process parameters for each of these sets of experiments.

Table 4: Overview of the conducted experiments and process parameters.

	First and Second Step: Spot and line cavities	**Third Step: Area polishing**		
		Process parameters	**Initial topography**	**Influence of materials**
Material	Titanium	Titanium	Titanium	Table 1, Table 2
Initial surface	B1	B1	B1 to B4, T1 to T4	B4
Laser power P_L [W]	0.5, …, 8.0	0.5, …, 4.5	2, …, 3	1, …, 3
Spot diameter d_f [µm]	31, …, 260	31, …, 950	110	110
Line spacing b [µm]	-	2,…, 70 7,…, 250	35	35
Scan passes N [1]	1, …, 600	50, 200, …, 100k	1, …, 400	1, …, 400
Scan velocity v [mm/s]	2, 4, 8, 16, 200	2, 20, 200	2	2
Section	**5.1**	**5.2**	**5.3**	**5.3**

All polished surfaces were topographically measured using the laser scanning microscope as shown in **Figure 4.7**. Each surface was analyzed with regard to its average roughness S_a, average wavelength λ_S and spectral roughness $S_{a,\lambda}$ (as defined in Section 4.3.2).

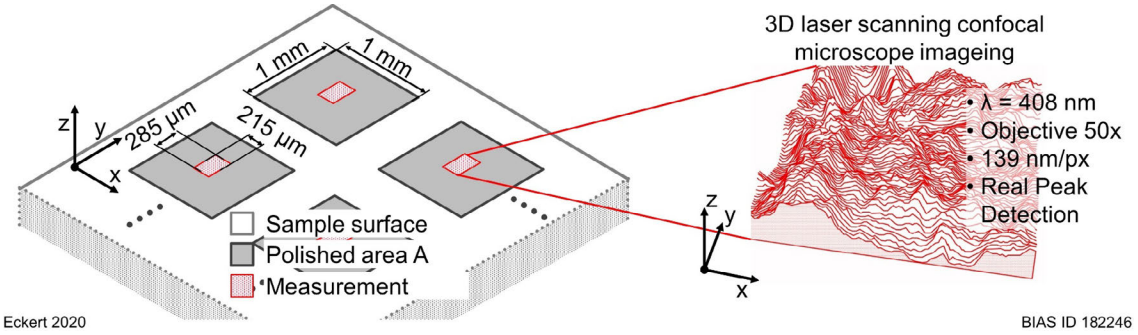

Figure 4.7: Schematic of the polished test areas positioned in a matrix and illustration of the automated surface measurement.

In addition, an experiment was designed to image the continuous smoothing between the passes. Reference lines were used to measure the same region before and after several passes, allowing the tracking and visualization of changes in individual surface features and the surface finish over time. The process parameters were kept constant while the number of passes was incrementally increased from 5 to 1000. Using MATLAB, all reflected-light images and surface-height data were assembled and stacked by matching features of an unmodified reference area. The surface finish was further analyzed with respect to average roughness S_a, material removal depth h_s and spectral roughness $S_{a,\lambda}$. The procedure is shown in **Figure 4.8**.

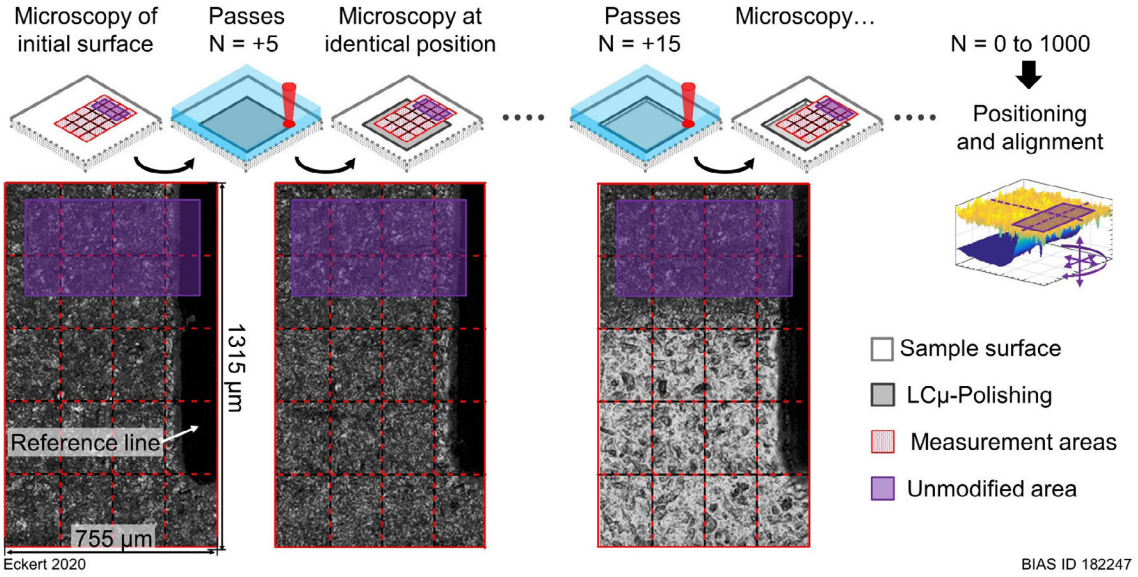

Figure 4.8: Schematic of the experimental procedure for investigating the surface evolution over time.

4.6 Definition of load

In the application of LCM as a two-dimensional polishing process, the focused laser radiation was guided in a zigzag beam trajectory across the area A. Because modification of the surface occurs only during exposure to laser radiation, surface roughness and uniformity of the surface finish are significantly influenced by the geometric parameters

of the scan trajectory. These include the line spacing b, spot area A_r and scan velocity v as shown in **Figure 4.9**. In this work, the zigzag trajectory was traced N times by the laser beam until the desired surface finish was achieved. The time required for this is described by the process time t_A. If the processing area is given by $A = L_x \cdot L_y$, the processing time can easily be calculated as:

$$t_A = \frac{A}{b \cdot v} \cdot N = \frac{L_x L_y}{b \cdot v} \cdot N \tag{4.2}$$

with L_x and L_y are the lateral lengths in the x- and y-directions of the processed area.

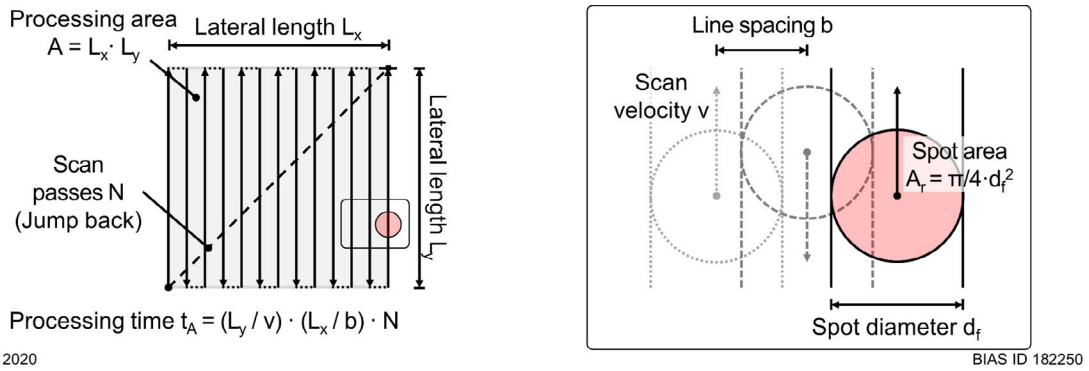

Figure 4.9: Schematic of the laser beam's zigzag scan trajectory and its parameters.

The geometric path of the laser beam along the surface defines how long each part of the surface was irradiated. Because of the circular spot shape, each surface element was irradiated for a different length of time. However, with sufficient line overlap and scan passes, each surface element was irradiated for an average exposure time t_r. The exposure time describes the time of irradiation per unit spot area A_r. Therefore, the average exposure time t_r can be calculated from the ratio of the processing area A to the laser spot area A_r, which is equal to the ratio of the processing time t_A to the average exposure time t_r:

$$\frac{A}{A_r} = \frac{t_A}{t_r} \tag{4.3}$$

Substitution of Equation (4.2) in Equation (4.3), gives the formula for the average exposure time t_r according to:

$$t_r = t_N \cdot N = \frac{\pi}{4} \frac{d_f^2}{b \cdot v} \cdot N \tag{4.4}$$

with the spot area $A_r = \pi/4 \cdot d_f^2$, the single-pass exposure time t_N, line spacing b, scan velocity v, and number of passes N. By substituting $A_r = \pi/4 \cdot d_f^2$ into Equation (4.3), the processing time is given by:

$$t_A = \frac{A}{\frac{\pi}{4} d_f^2} \cdot t_r \tag{4.5}$$

In addition to the geometric process parameters, the induced temperature distribution also has a major impact on the modification. Previous works have shown that the geometry of the removal cavity can be correlated with the temperature distribution [Mes17]. Each pixel on the surface is affected by a different temperature because of the Gaussian beam characteristic. Thus, the material removal at the center is deeper than at the periphery. However, for LCP, the zigzag scan trajectory and multiple passes are assumed to expose each part of the surface to an average thermal load. This is even more evident if the inter-pass rotation angle is also changed. In the following, the thermal load T_L and the thermal gradient ($\partial T_L/\partial z$) are defined as the $1/e$ component of the calculated laser-induced center temperature increase and gradient. These parameters are interpreted as average values to describe the thermal laser impact on the workpiece and the thermal influence on the surface during LCP.

In general, the induced temperature $T(x,y,z,t)$ of a Gaussian beam has a three-dimensional distribution in x-, y- and z-directions in time t, where the xy-plane is the substrate surface and the positive z-axis points into the material. The temperature distribution can be calculated by solving the heat equation:

$$\rho c_p \frac{\partial T}{\partial t} = K \nabla^2 T + Q \tag{4.6}$$

with the heat source power density Q, density ρ, specific heat capacity c_p and thermal conductivity K. Because mostly the laser spot was small compared with the sample size, this work assumed a semi-infinite substrate with constant material parameters and a heat source defined by the absorbed intensity. A detailed presentation of the boundary value problem (**Figure A.1**), including the formula derivations and individual calculation steps, can be found in Appendix A.1.

A solution for the boundary value problem is obtained analytically by the Green function technique, Equation (A.8) [Car59]. This leads to a complex integral expression, Equation (A.10), which is evaluated by FFT [Röm10]. An example of the obtained temperature distribution $T(x,y,0)$ is shown in **Figure 4.10** for a velocity of $v = 2$ mm/s, laser power of $P_L = 0.7$ W and spot diameter of $d_f = 31$ µm. An analytical solution for this problem is given for the center temperature rise $T_c = T(0,0,0)$ of a static laser beam with $v = 0$ mm/s. The thermal load is defined based on Equation (A.15) as the $1/e$ component of the calculated center temperature value, according to:

$$T_L = T_c e^{-1} = \frac{\sqrt{2} \cdot \alpha \cdot P_L}{\sqrt{\pi} \cdot K \cdot d_f} e^{-1} \tag{4.7}$$

with the absorptance α. The thermal loads as a function of the laser power calculated with Equation (4.7) and the material properties given in Table 1 are shown in **Figure 4.10** for a spot diameter of 110 µm. The thermal loads vary by a factor of four. Higher thermal loads are correlated with lower thermal conductivity K.

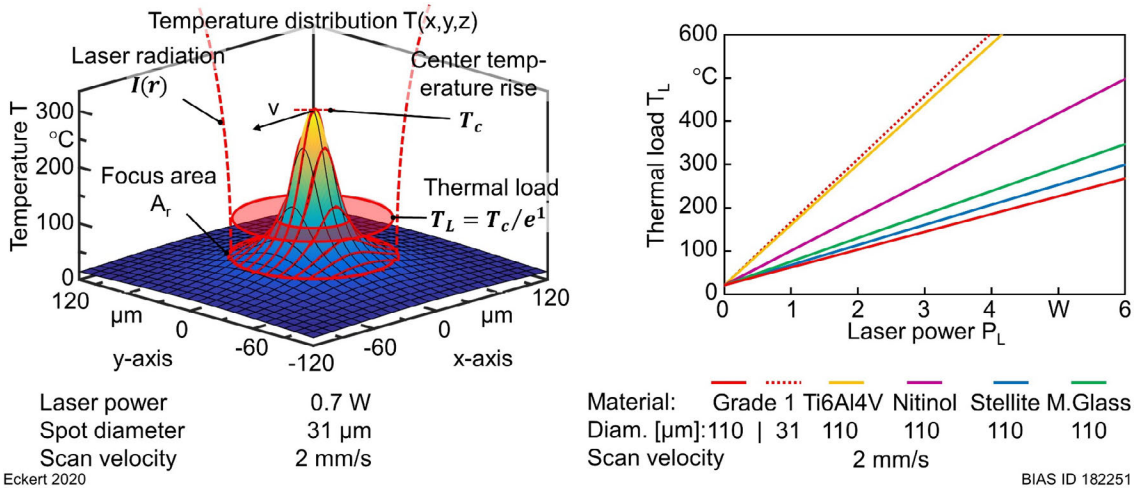

Figure 4.10: On the left side, calculated surface temperature rise [Röm10] and the right side, thermal loads for different materials according to Equation (4.7).

Furthermore, the general solution of Equation (A.10) is evaluated in the z-direction for a stationary solution, with $v = 0$ mm/s. An example of the resulting center temperature rise $T(0,0,z)$ as a function of the z-position is shown in **Figure 4.11** for a laser power of 3.1 W and a spot diameter of 110 µm for titanium (straight red line). For small values of z, the temperature in the z-direction can be approximated by a linear dependency (dashed black line). In this case, the center temperature rise in the z-direction $T(0,0,z)$ can be calculated by an analytical expression according to Equation (A.18), as shown by the dashed black tangent line. The thermal gradient is defined based on Equation (A.19) as the $1/e$ component of the approximated center temperature gradient at the surface, according to:

$$\left(\frac{\partial T_L}{\partial z}\right) = \frac{dT_c}{dz} e^{-1} = \frac{8 \cdot \alpha \cdot P_L}{\pi \cdot K \cdot d_f^2} e^{-1} \tag{4.8}$$

Substituting Equation (4.7) into Equation (4.8) yields:

$$\left(\frac{\partial T_L}{\partial z}\right) = \frac{4\sqrt{2}}{e\sqrt{\pi}} \frac{T_c}{d_f} \approx \frac{T_c}{d_f} \tag{4.9}$$

This approximation holds only in a boundary layer close to the surface. The intersection of the tangent line with the z-axis can be used to define a boundary layer thickness δ_{th} within which Equation (4.9) is an acceptable approximation. By setting Equation (A.18) to zero and rearranging to z, the boundary layer thickness δ_{th} is as follows.

$$\delta_{th} = \frac{\sqrt{\pi}}{4 \cdot \sqrt{2}} d_f \approx \frac{1}{3} d_f \tag{4.10}$$

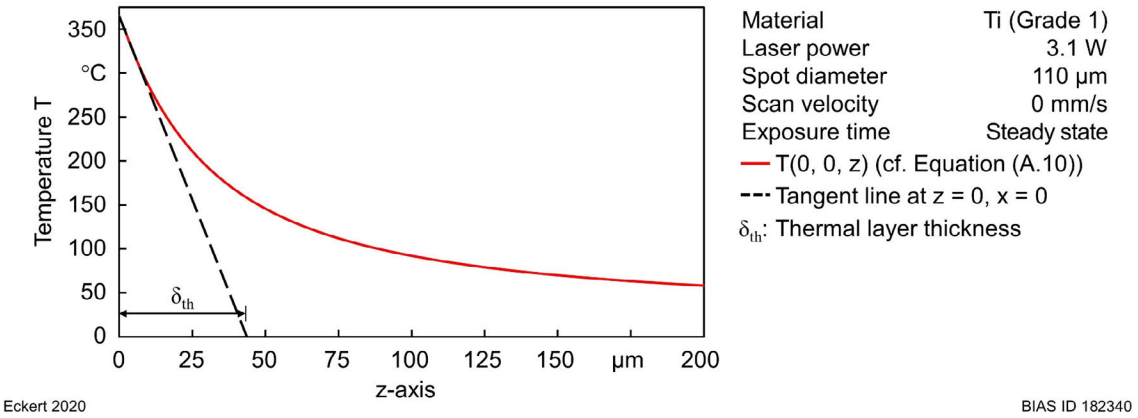

Figure 4.11: Comparison of different calculations of the center temperature as a function of the depth in the z-direction.

5 Results

5.1 Material modifications

5.1.1 Single-spot irradiation

For the initial rolled titanium sample (B1), **Figure 5.1** shows the removal depth at the cavity center h_c as a function of the laser power P_L, along with three SEM images of the cavities. The laser power varied from 0.2 W to 3.5 W. The material removal starts at a threshold power $P_{L,th} = 0.6$ W and increases linearly. The SEM images at right in **Figure 5.1** show that in the center, removal depths of 10 µm occurred within 1 s of laser exposure. At a laser power of $P_{L,dist} = 1.1$ W the depth decreased abruptly, and structures rising up to 10 µm above the initial surface occurred in the cavity center. With increasing power, these structures became wider and more flattened. In accordance with Mehrafsun et al. (**Figure 2.9b**), such deviations from a Gaussian cavity shape can be considered disturbances of the material removal process. Note, that the maximum removal depth h_m did not change as much as the center cavity depth h_c.

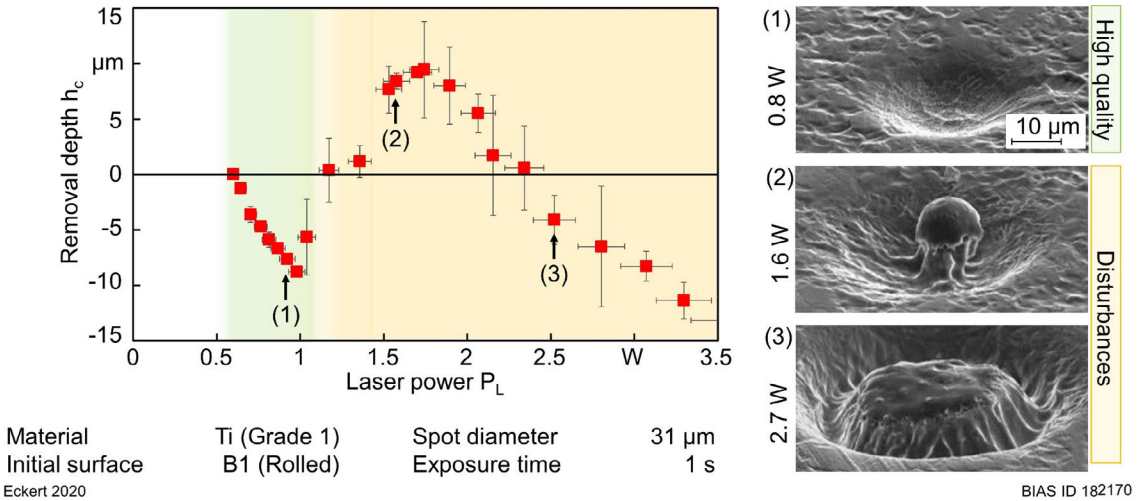

Figure 5.1: Depth of structured cavities in Ti (Grade 1) obtained in 5.0 M H_3PO_4 as a function of laser power. At right, SEM images show cavities (1) within 1 s of laser exposure, (2) at a laser power of $P_{L,dist} = 1.1$ W and (3) with increasing power.

The chemical compositions of these cavities were characterized with EDX measurements, as shown in **Figure 5.2**. The EDX spectrum of the disturbed cavity obtained in H_3PO_4 (red line) shows a significant phosphor peak at 2 keV and an oxygen peak at 0.6 keV. In the undisturbed cavity (black line), only titanium was detected. The material disturbance filled half of the spherical etched cavity, as shown in the cross-sectional image. Titanium, titanium-phosphate-oxygen, and titanium-oxygen compounds were identified in the disturbance (blue line). The titanium-phosphate-oxygen compound appears as a white

layer in the cross-sectional image. The material modifications were classified into three regimes according to their chemical compositions:

1. No material modification (< 0.6 W, up to 1 s exposure)
2. Undisturbed modification (0.6 W to 1.1 W, no chemical change)
3. Disturbed material removal (> 1.1 W, white layer formation)

Only the undisturbed cavities without any material deposition are suitable for polishing.

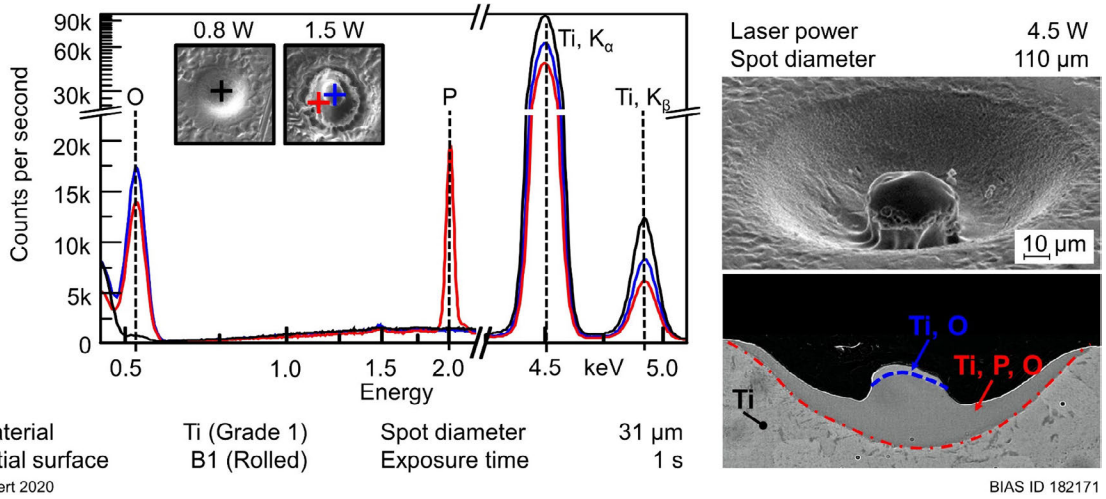

Figure 5.2: EDX spectra of undisturbed and disturbed cavities and SEM and cross-sectional images of a semispherical cavity with material accummulation.

5.1.2 Multipass line scans: Laser power and spot diameter

The three modification regimes that were observed for spot cavities were also observed for line cavities that were passed multiple times. Each sample was passed 50 times, corresponding to a total exposure time of 0.8 s, with a particular laser power between 0.6 W and 4.5 W. **Figure 5.3** shows reflected-light images and surface-height data of undisturbed and disturbed line cavities from top and cross-sectional views. Material removal and disturbances occurred in multipass cavities at similar laser powers as for single-spot cavities. In the disturbed material removal regime, piled accumulations appeared irregularly along the middle of the line cavity and showed a white layer in the cross-section. The undisturbed modification formed at 0.9 W and had a flat surface. These results showed that disturbances in the cavity center occurred over multiple short exposures much as in single-scanned line cavities with a slower scan velocity [Meh12].

Figure 5.4 shows reflected-light images and surface-height data of undisturbed line cavities that were structured by multiple passes with spot diameters of 31, 65, 109, 157 and 209 µm, at laser powers of 1.0, 1.9, 3.3, 4.9 and 6.3 W, respectively. The surface-height data show similar approximately Gaussian-shaped removal cavities, with increasing depth and width under higher spot diameters. These results can be expected because the average exposure time for each line cavity increased because of the larger

spot diameter, even though the number of passes and scan velocity were kept constant. With further increased laser power, removal disturbances occurred in the cavity center, causing deviations from the Gaussian removal shape.

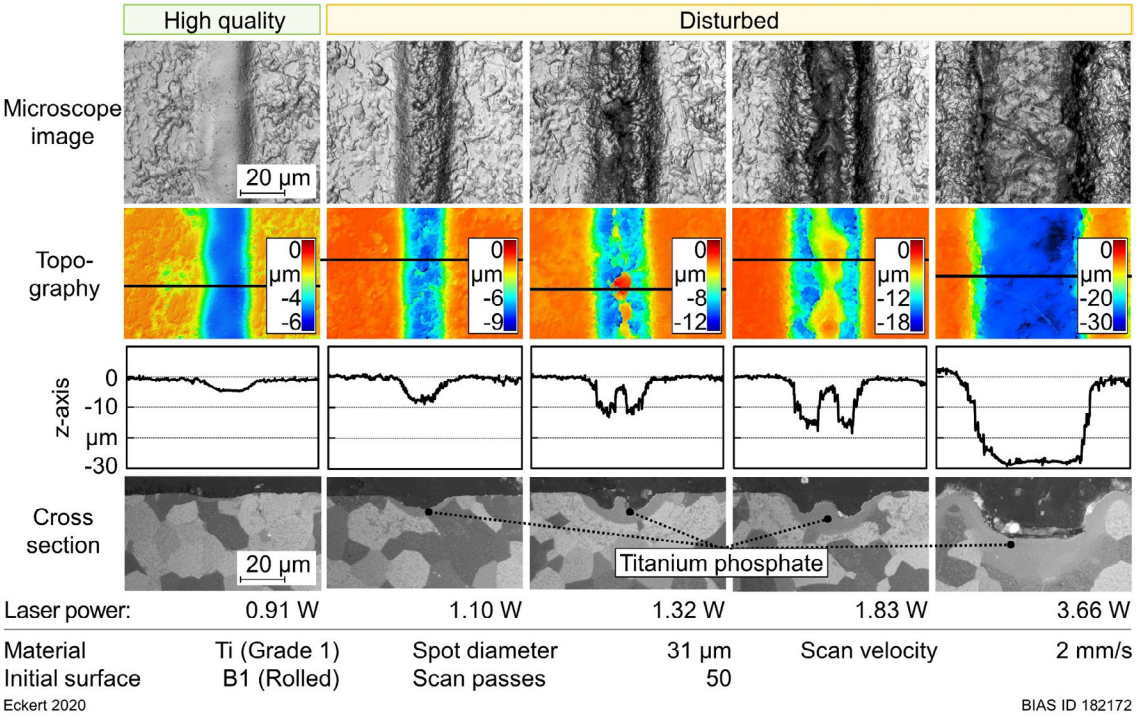

Figure 5.3: Reflected-light images, surface-height data and cross-sectional images of undisturbed and disturbed multipass cavities with increasing laser powers.

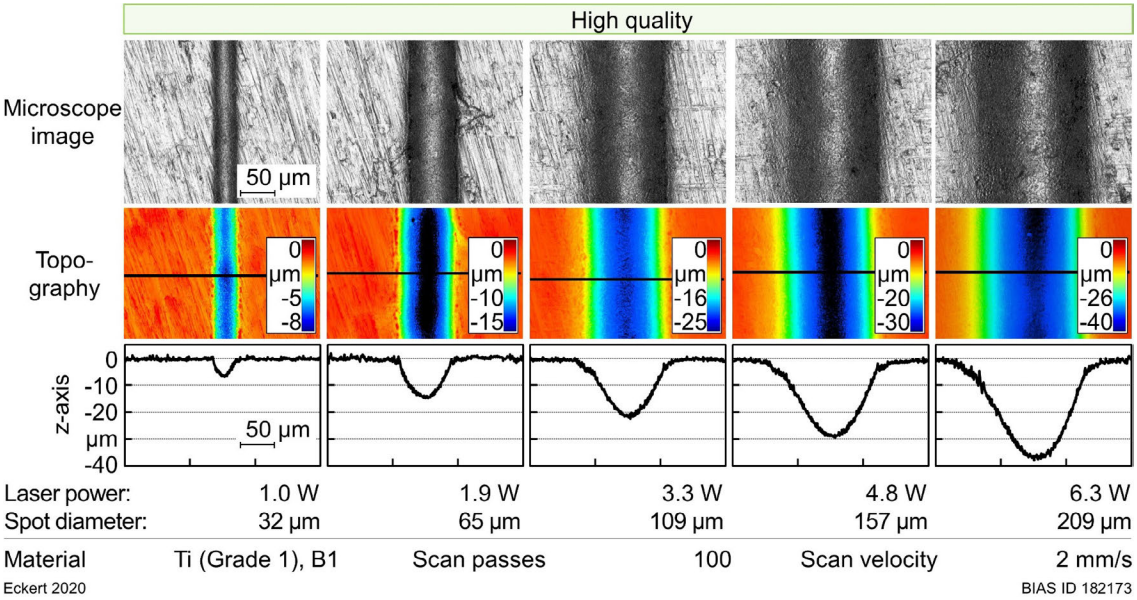

Figure 5.4: Reflected-light images and surface-height data of undisturbed multipass cavities with increasing spot diameters and laser powers.

Figure 5.5 shows the resulting cavity depths h_c structured with spot diameters of 31, 65, 109, 157, 209 and 260 µm as a function of the laser power. The number of passes was either kept constant at 100 (marked with circles in the figure) or reduced from 50 to 30,

20 and 15 (marked with diamonds). This process ensured a constant exposure time of 0.8 s, according to Equation (4.4). The material removal started at a characteristic threshold power $P_{L,th}$, and the removal depth increased linearly until disturbances occurred in the cavity center at laser power $P_{L,dist}$. These thresholds depended on the spot diameter and were determined by the intersection of a linear regression with the x-axis. This procedure resulted in threshold values of 0.7, 1.3, 2.2, 3.2, 4.0 and 5.1 W for $P_{L,th}$. These thresholds correspond to increases proportional to the spot diameter and indicate an invariance with respect to the thermal load, which can be expected from Equation (4.7), where T_L is proportional to P_L/d_f, as further discussed in Chapter 6.

Disturbances cause an abrupt decrease in removal depth and were observed at laser powers $P_{L,dist}$ of 1.3, 2.8, 4.5 and 6.2 W. For spot diameters of 209 µm and 260 µm, disturbances can be expected to occur above the maximum of 8 W investigated here. The slope of the linear regression, i.e., the increase of the removal depth per unit power, is independent of the spot diameter if the number of scan passes is kept constant (circles in **Figure 5.5**). In contrast, with a constant exposure time (diamonds), the slope decreases with increasing spot diameter. The material removal threshold starts at the same laser power independent of the number of passes and exposure time.

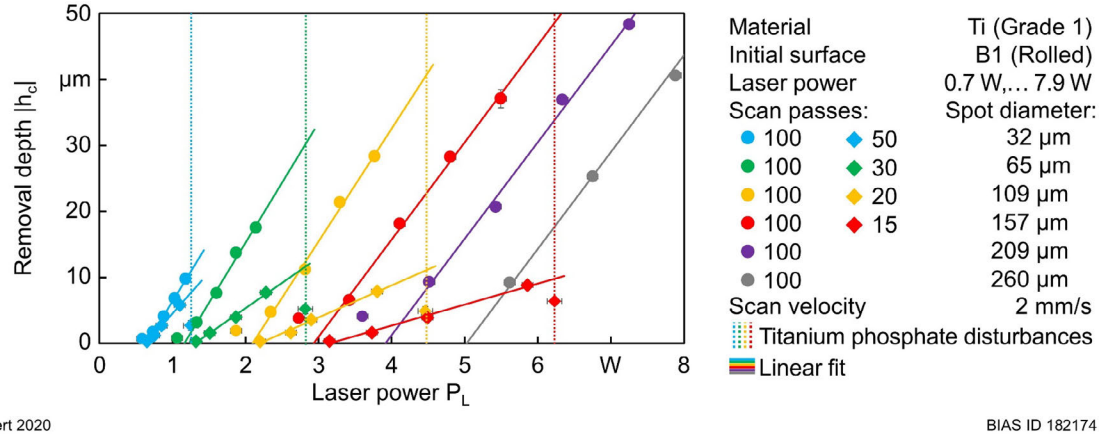

Figure 5.5: Removal depth as a function of laser power for selected spot diameters.

In addition to the removal depth, the width of the line cavities also increased. **Figure 5.6** shows the resulting cavity width as a function of the laser power after 100 scan passes (marked with circles). These line cavities were in the undisturbed regime. Data points for each spot diameter were fitted by a linear regression, which showed that the line cavity width increased linearly with the laser power, with the slope of the linear fit flattening as the spot diameter increased.

For completeness, **Figure 5.7** shows the line cavity volume V_c (determined for a cavity length L_c of 704 µm) as a function of the laser power for spot diameters from 32 µm to 260 µm. The cavity volume increased with the laser power and the spot diameter.

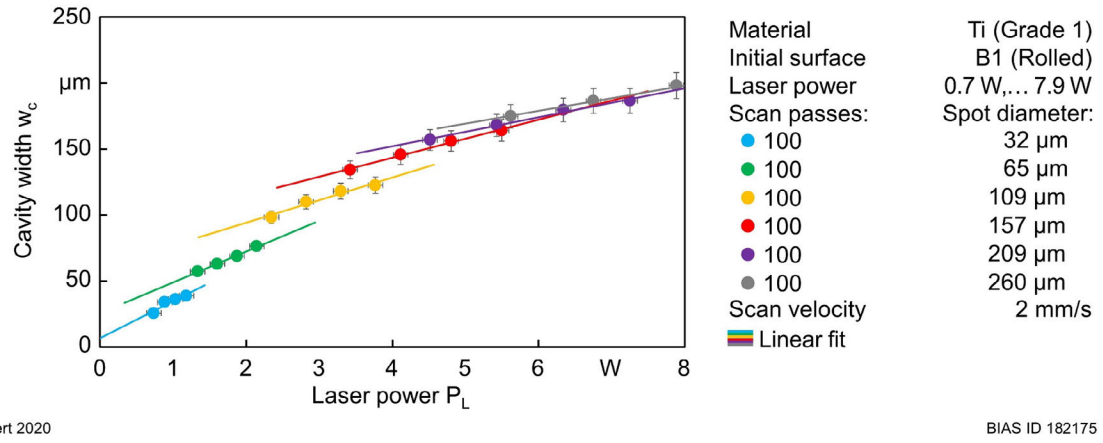

Figure 5.6: Line cavity width as a function of laser power for different spot diameters.

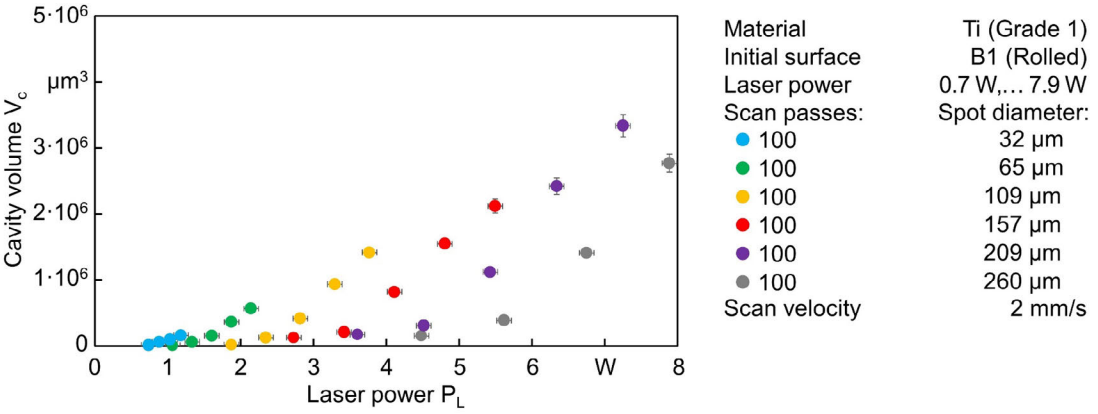

Figure 5.7: Cavity volume as a function of laser power for different spot diameters.

5.1.3 Multipass line scans: Scan passes and velocity

Figure 5.8 presents reflected-light images, surface-height data and cross-sectional images of line cavities structured under a constant laser power of 1.3 W but with an increasing number of passes, from 10 to 150. These numbers correspond to increasing exposure time from 0.14 s to 1.76 s, with more than 1 s elapsing between passes before the surface is irradiated again. The figure shows disturbed line cavities with white layer formation and piled accumulations of material in the center. The accumulations in the center grew with the number of passes increasing from 10 to 50. With additional passes, to 75 and then 150, the material accumulated at the bottom of the deepening line cavity.

Keeping the number of passes constant at 50 and increasing the scan velocity shortens the exposure time. Scan velocities of 2, 4, 8, 16 and 200 mm/s were investigated. **Figure 5.9** shows the reflected-light images and surface-height data of line cavities resulting from this irradiation procedure. The exposure time was reduced from 0.6 s to 0.2 ms, and the depths of the line cavities decreased significantly. However, the formation of the white layer was independent of the scan velocity or exposure time, as shown in the cross-sectional images.

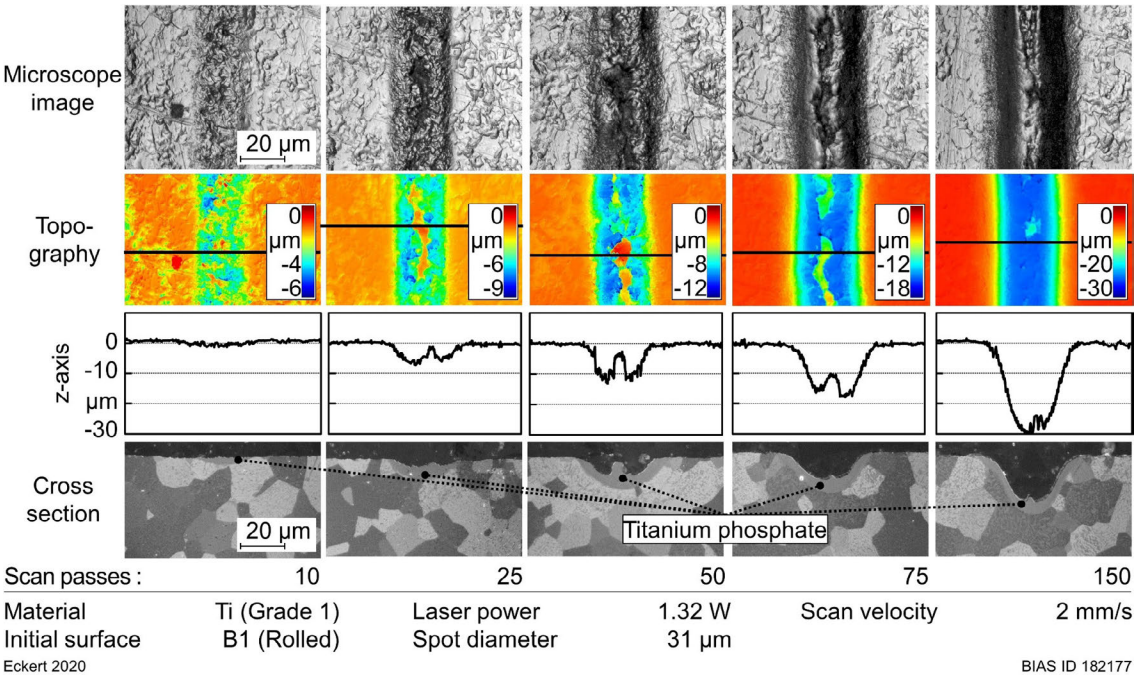

Figure 5.8: Reflected-light images, surface-height data and cross-sectional images of disturbed multipass cavities with increasing passes, corresponding to increasing exposure times.

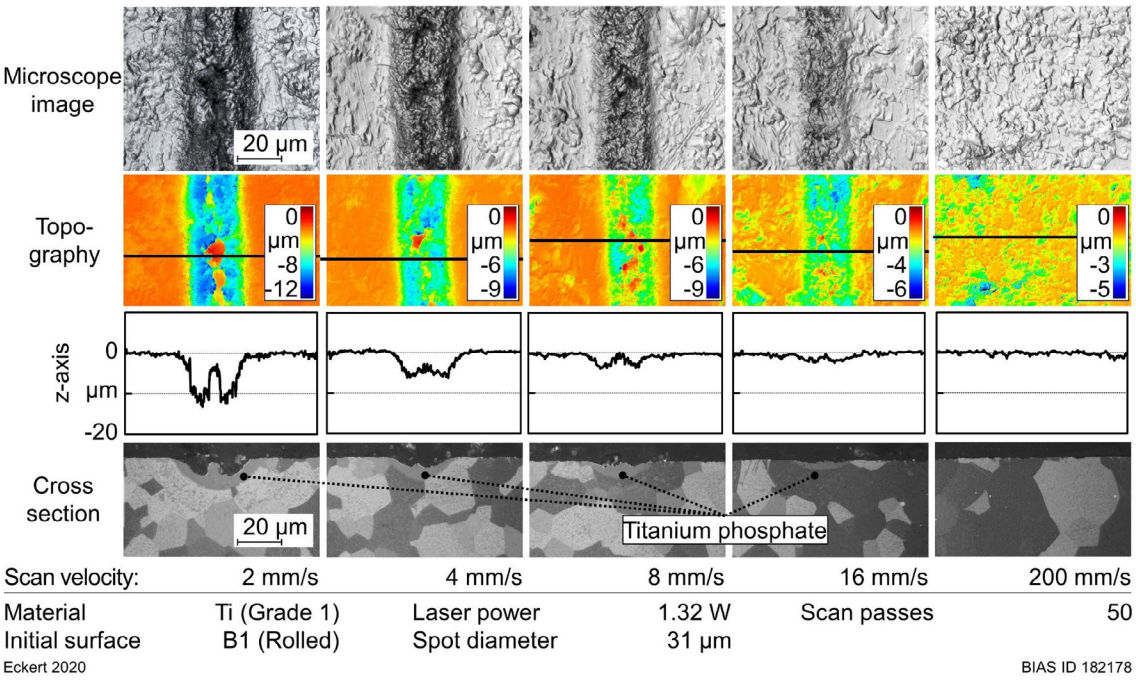

Figure 5.9: Reflected-light images, surface-height data and cross-sectional images with increasing scan velocities, corresponding to decreasing exposure times.

The white layer corresponded to the material accumulation in the center of the line cavity and consisted of titanium, phosphate and oxygen (as shown in **Figure 5.2**). That this feature occurred independently of the number of scan passes and scan velocity indicates that the white layer was mainly influenced by the thermal load, as further discussed in Chapter 6. The change in chemical composition indicated that additional chemical reactions occurred.

Figure 5.10 shows the maximum removal depths h_m as a function of the number of passes N for four scan velocities. The removal depth increased linearly with the number of passes, with a decreasing gradient as the scan velocity increased. Therefore, for a higher scan velocity, the surface must be scanned significantly more times to achieve the same removal depth. Cavities structured with increasing scan velocities attained the same depth after a proportionally increased number of passes. These results demonstrate that the removal depth achieved by multiple passes is the result of N-fold superposition of small nanometer-scaled material removals. Increasing the scan velocity leads to a lower gradient, i.e., less material is removed with each pass. These results indicate that the average exposure time of the surface is significant, as further discussed in Chapter 6.

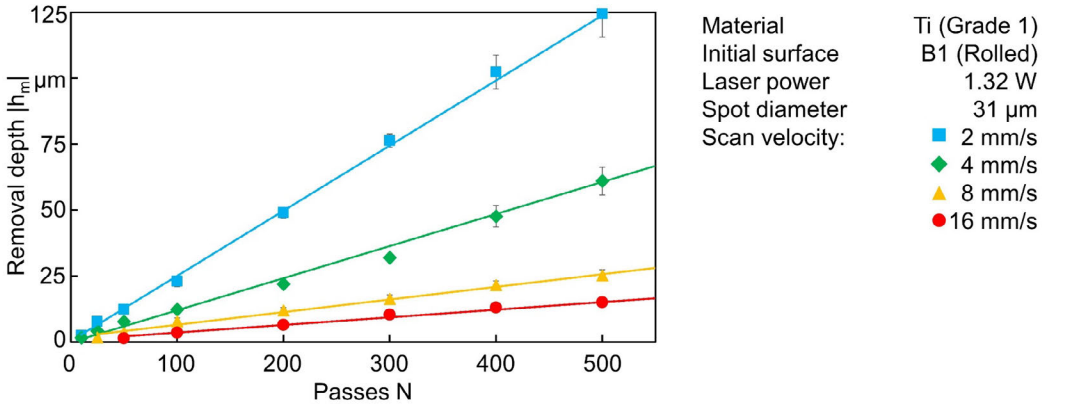

Figure 5.10: Removal depth as a function of the number of passes for four selected scan velocities.

5.2 Process parameter influences on polishing

5.2.1 Line spacing and spot diameter

The line spacing b and spot diameter d_f were varied to evaluate their influence on surface roughness and uniformity. **Figure 5.11** shows reflected-light images of the initial ground surface (T1) and of the surface finish produced with a zigzag scan trajectory after 50 passes with line spacings decreasing from 28 µm to 4 µm. The spot diameter was set to 31 µm and the laser power to 0.85 W. The line overlap $u = (d_f - b)/d_f \cdot 100$ was calculated from the spot diameter and line spacing. For small line overlaps between 0 % and 50 %, parallel line cavities appeared on the surface because less material was removed from the periphery of the beam spot than from its center, due to the Gaussian intensity distribution of the laser beam.

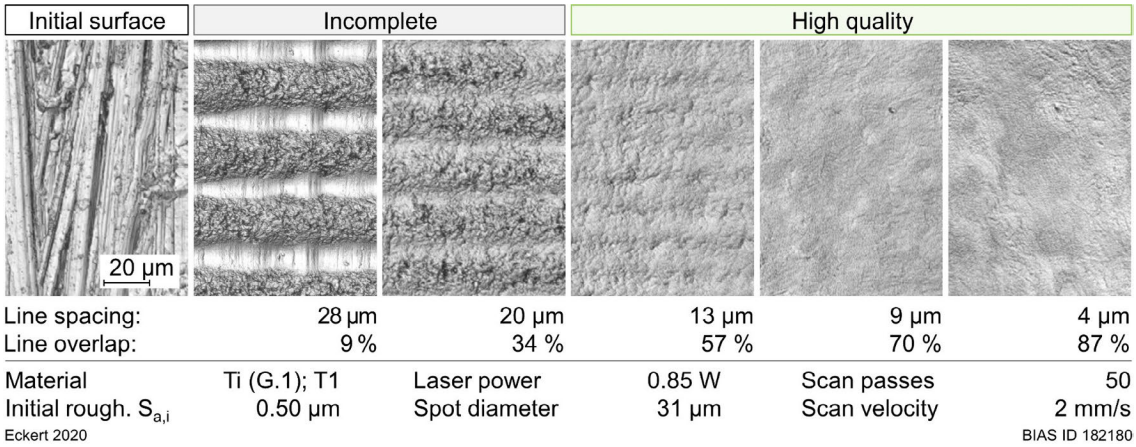

Figure 5.11: Surface finishes produced with a zigzag scan trajectory with different line spacings.

The resulting elevations between the lines produced a maximum in the spectral roughness at a wavelength that approximately corresponded to the line spacing, as shown in **Figure 5.12**, where the spectral roughness is plotted on a semi-logarithmic scale as a function of the wavelength. These cases with small line overlaps resulted in a spectral roughness that exceeded the initial roughness (dashed black line). This pattern disappeared with increasing line overlap, resulting in a more uniform surface finish, where the influence of the scan trajectory can no longer be visually distinguished in the surface finish. For a line spacing of 9 µm, equating to an overlap of 70 %, the roughness was lower than 0.05 µm over all wavelengths (blue line). For large line overlap of 87 % (purple line), an increase in waviness was observed. In general, the spectral roughness followed an s-curve with a minimum in the micro- and a maximum in the mesoroughness regimes.

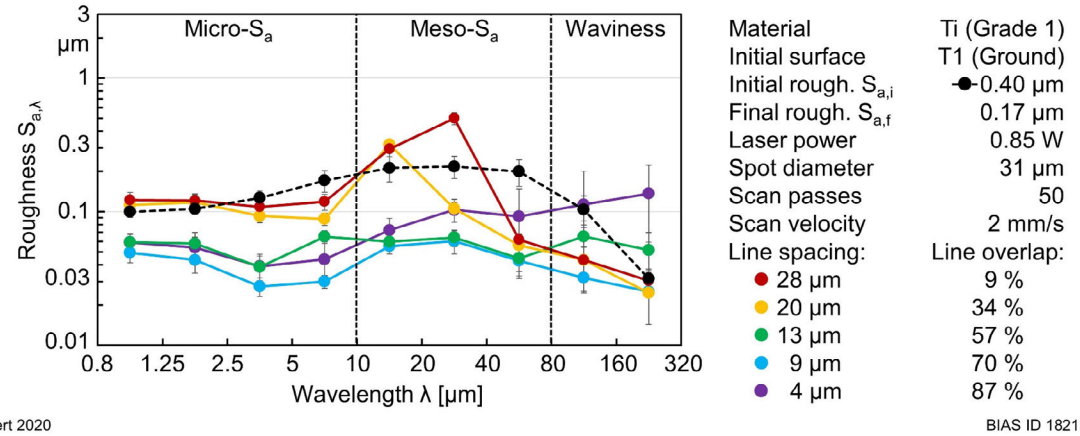

Figure 5.12: Roughness as a function of the wavelength on a semi-logarithmic scale for various line spacings and a spot diameter of 31 µm.

Figure 5.13 shows the roughness spectra for surfaces structured with a spot diameter of 110 µm and a laser power of 2.9 W. According to Equation (4.5), the processing time in this case is 12.5 times shorter compared with the 31 µm spot. The line spacing varied between 99 µm and 15 µm, resulting in the same line overlap as with the smaller spot.

Because of the larger spot diameter, the spectral roughness maxima appeared at larger wavelengths. For a line spacing of 35 µm, corresponding to an overlap of 67 %, the surface roughness was reduced to less than 0.05 µm with a minimum in the micro- and a maximum in the mesoroughness regimes. With very large line overlaps, above 80 %, the mesoroughness and waviness increase. In general, the spectral roughness again followed an s-curve with a minimum-maximum distance related to the larger spot diameter.

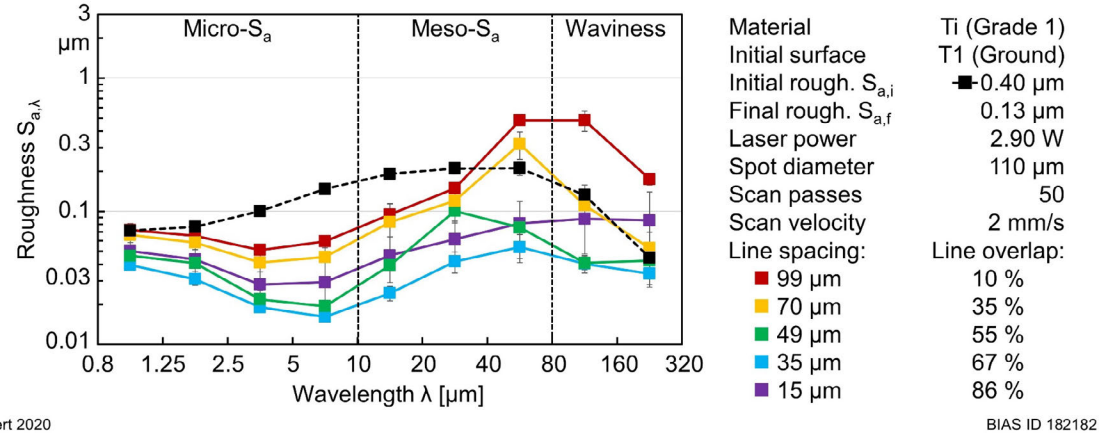

Figure 5.13: Roughness spectra for various line spacings and a spot diameter of 110 µm.

A comparison of the average roughnesses S_a for the 31 µm and 110 µm spot diameters is shown in **Figure 5.14** as a function of line overlap. The initial roughness was 0.5 µm. Small line overlaps below 30 % resulted in increased roughness caused by the elevations between the lines. Above 30 % overlap, the roughness first decreased, remaining at a low level for overlaps between 50 % and 75 %, and then increased again for overlaps above 75 % because of the induced waviness. For both diameters, a minimum of approximately 0.2 µm occurred at a line overlap of 70 %.

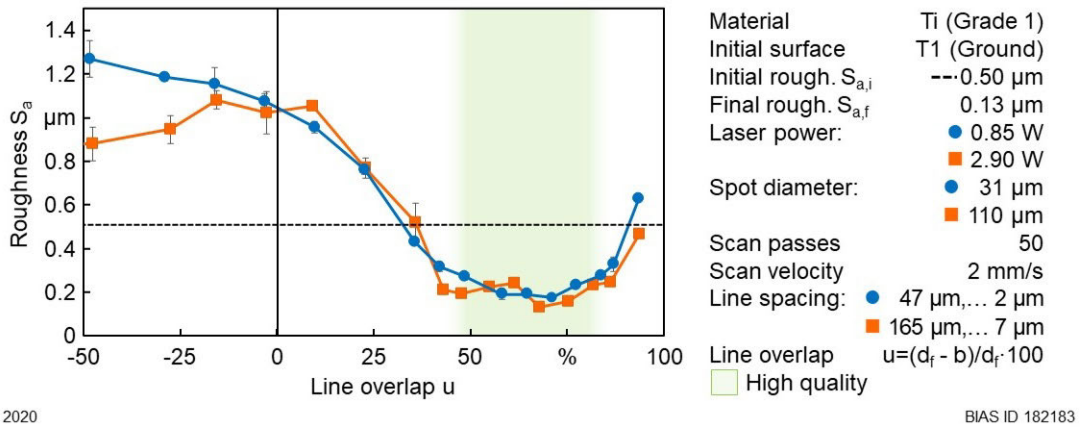

Figure 5.14: Roughness as a function of line overlap for 31 µm and 110 µm spot diameters.

Regardless of the spot diameter, a uniform surface finish of high quality (spectral roughness < 0.05 µm) requires a line overlap in a range between:

$$d_f/2 > b > d_f/5 \Rightarrow 50\,\% < u < 80\,\% \tag{5.1}$$

5.2.2 Scan trajectory

Further optimization of the surface finish was investigated by varying the rotation angle θ between each laser pass from 180° (zigzag trajectory) to 90° (cross zigzag), 45° and 30°. **Figure 5.15** shows reflected-light images, height data and the corresponding Fourier transformations for each surface finish. The surface texture of the initial rolled (B1) titanium sheet had a roughness of 0.45 µm, and the FFT image was point-symmetric without any directional dependency. The roughness of the polished surface was reduced to less than 0.15 µm for all scan trajectories. Although the reflected-light images appear much the same, the Fourier spectra show a strong directional dependency originating from the rotation of the zigzag scan trajectory. Rotating the zigzag trajectory by approximately 90° between subsequent passes produced a checked pattern in the FFT image. With smaller rotation angles of 45° and 30°, the directional dependency decreased, and the associated FFT images appeared almost point-symmetric without any obvious directional influences.

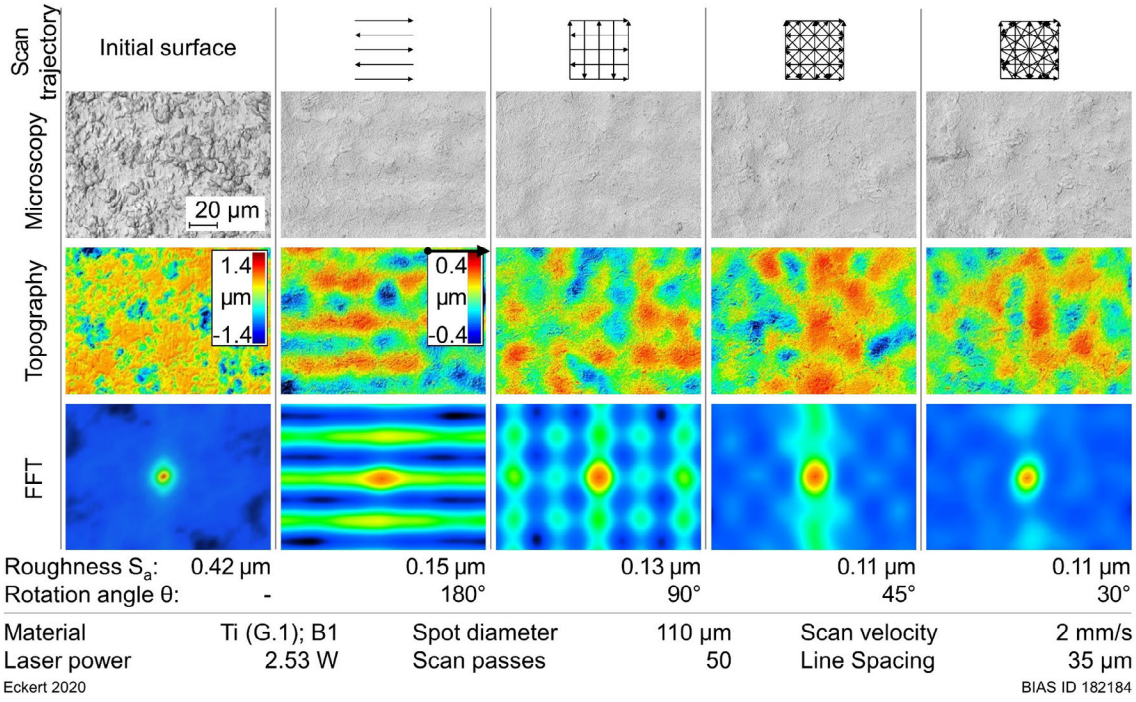

Figure 5.15: Reflected-light images, surface-height data and Fourier transformations of polished samples for different rotation angles θ between subsequent passes.

Figure 5.16 shows the corresponding roughness spectra, with a linear scale on the *y*-axis. The initial surface (dashed line) shows a maximum in the mesoroughness regime of 0.17 µm for wavelength between 10 µm and 40 µm. In contrast, the roughnesses of the polished surfaces (after 50 passes) followed s-curves with minima and maxima, but significantly reduced roughness $S_{a,\lambda}$ for all wavelength bands up to 160 µm. At smaller

rotation angles between subsequent passes, the s-curve characteristic of the roughness spectrum flattens and both the minimum and maximum decreased in magnitude. A very uniform surface finish would show a horizontal line.

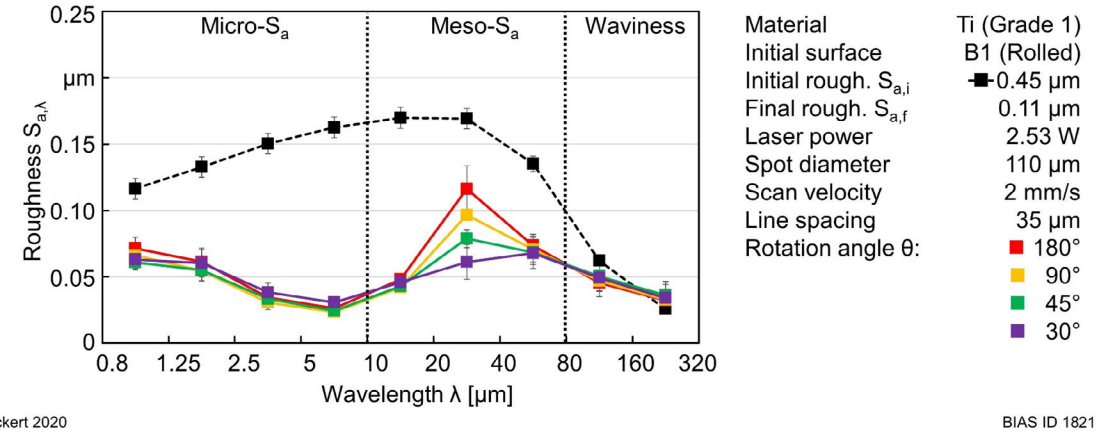

Figure 5.16: Roughness spectra of polished surfaces for different rotation angles θ between subsequent passes.

In summary, a smaller rotation angle θ between scan passes resulted in a more uniform surface finish. However, the uniformity that can be achieved by reducing the rotation angle is limited. The applicable rotation angle θ and the number of passes can be linked according to:

$$\theta = 180°/N \tag{5.2}$$

Reducing the rotation angle between scan passes is only a first approach to increasing the uniformity. In order to minimize the influence of individual tracks, an irregular adaptive scan strategy could be used [Vad13].

5.2.3 Laser power and scan passes

Figure 5.17 shows reflected-light images and surface-height data of the initial rolled surface (B1) and of the surface finishes processed with increasing laser power and a constant number of passes. Each surface measurement was taken at a different position on the sample. The surface finishes showed high-quality globular α-titanium microstructures for laser powers of 2.3 W and 2.5 W. For higher laser powers, at or above 2.9 W, the surface finish was increasingly covered with disturbances in the form of nanoporous cavities.

Figure 5.18a shows the roughness S_a as a function of laser power. With increasing laser power, the roughness decreased rapidly from the initial 0.53 µm to 0.2 µm, once the power threshold of $P_{L,th}$ = 2.2 W was exceeded. The average roughness remained at the low level of 0.2 µm for laser powers between 2.2 W and 2.8 W and increased slightly for powers above 2.8 W.

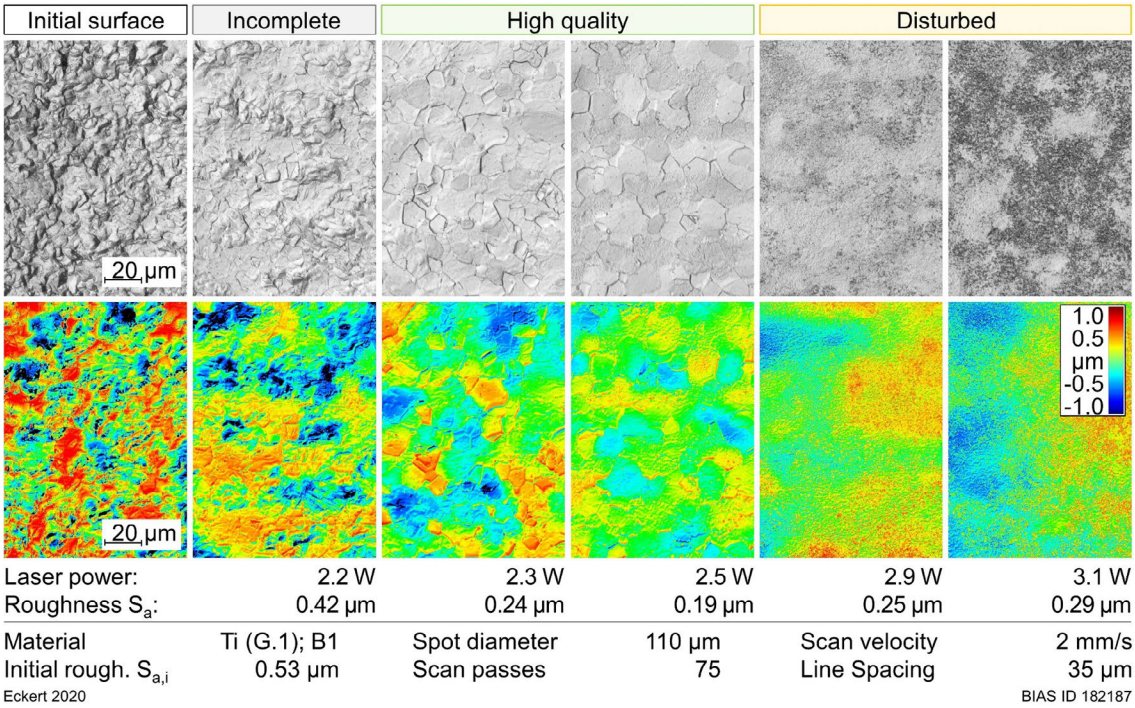

Figure 5.17: Reflected-light images and surface-height data of the surface finish of the initial rolled Ti after polishing with increasing laser power.

Figure 5.18b shows the corresponding spectral roughness as a function of the wavelength, with a linear scale on the *y*-axis. For laser powers between 2.2 W and 2.9 W, the roughness $S_{a,\lambda}$ was smaller than 0.15 µm for all wavelengths. For higher laser powers above $P_{L,dist} = 2.9$ W, the removal depth increased, resulting in surface recesses that contributed to an uneven surface, and the microroughness and waviness increased. This could be attributed to the observed disturbances, which might be caused by corrosion [Kou12] or laser-induced periodic surface structures [Bon17]. However, the roughness with the higher powers was still lower than the initial roughness, although the nanoporous cavities caused strong light scattering and abruptly decreased brightness.

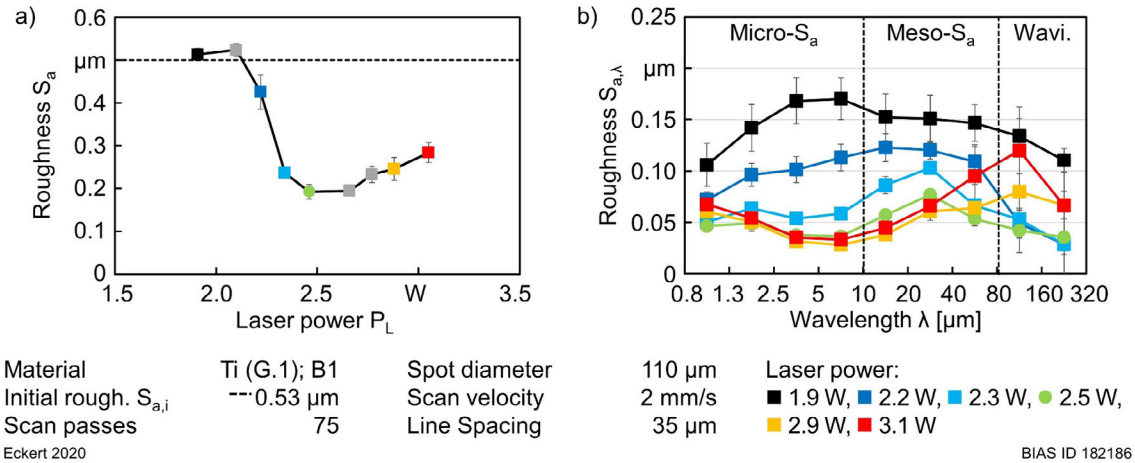

Figure 5.18: (a) Roughness S_a as a function of the laser power after 75 passes and (b) corresponding roughness spectra.

Figure 5.19 shows reflected-light images and height data for surface finishes structured with a laser power of 2.46 W and an increasing number of passes. After 75 passes, the surface was visually smoothed, showing the globular titanium (Grade 1) microstructure. Further processing did not further improve the surface quality. On the contrary, after 200 and 400 passes, the roughness increased significantly to 0.22 µm and 0.33 µm, respectively. The grain boundaries were less pronounced, but still visible.

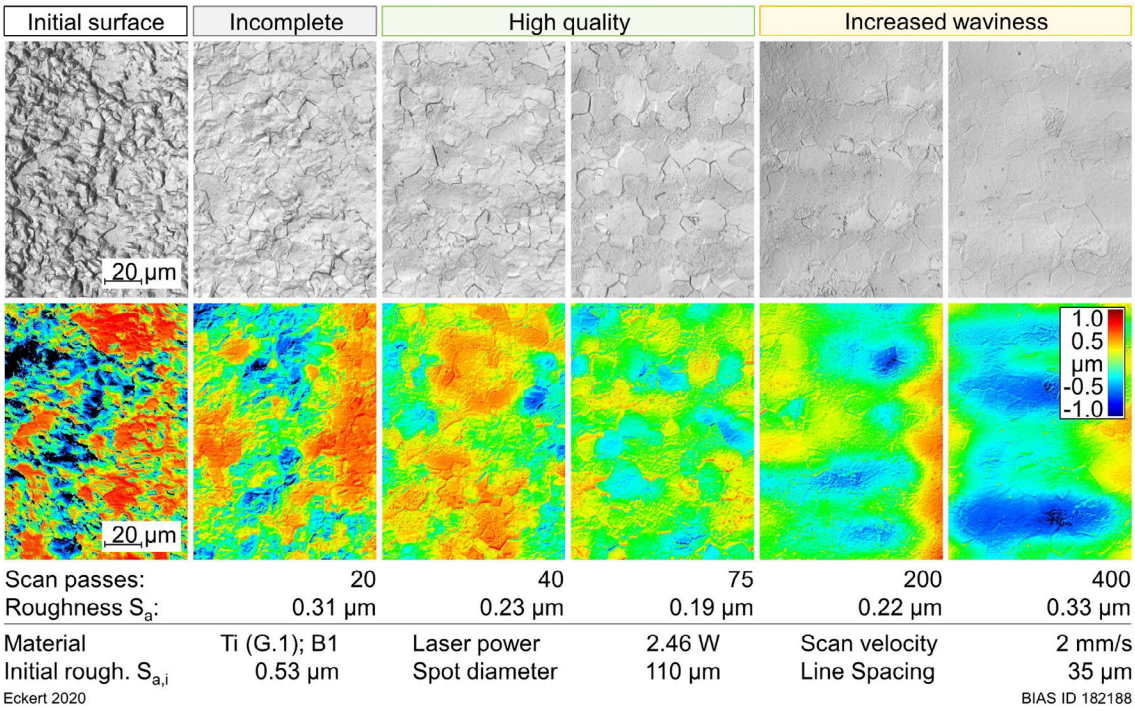

Figure 5.19: Reflected-light images and surface-height data the initial rolled Ti processed with an increasing number of scan passes.

Figure 5.20a shows the roughness S_a as a function of the number of passes. During the first 30 passes, the average roughness decreased rapidly from 0.53 µm down to 0.23 µm (light blue data point) and improved further to 0.18 µm after 100 passes (dark green data point). Further processing slightly increased the roughness to 0.33 µm after 400 passes.

Figure 5.20b shows the roughness spectra with a linear scale on the *y*-axis. For up to 100 passes, the roughness decreased steadily over all wavelengths. Further processing up to 400 passes (yellow and red lines) significantly increased the mesoroughness and waviness for wavelengths above 20 µm, and the microroughness remained low, with roughnesses $S_{a,\lambda} < 0.03$ µm. The roughness spectra in the microroughness regime essentially reached a stable lower limit with respect to the number of passes at approximately 30 passes.

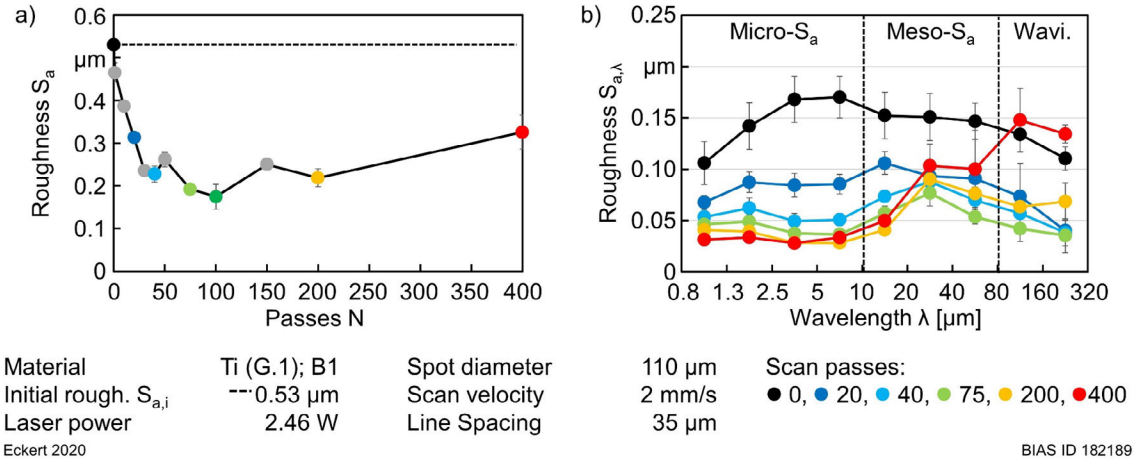

Figure 5.20: (a) Roughness S_a as a function of the number of passes and (b) the roughness spectra for selected numbers of passes.

The average roughness as a function of the laser power and the number of passes is shown in a two-dimensional plot in **Figure 5.21**. The average roughness is color-coded, from green (< 0.2 µm, minimum of roughness) to yellow (0.5 µm, initial roughness) up to red (0.7 µm, increased). The lowest average roughness of S_a = 0.11 µm was achieved with a laser power of 2.7 W and 150 scan passes.

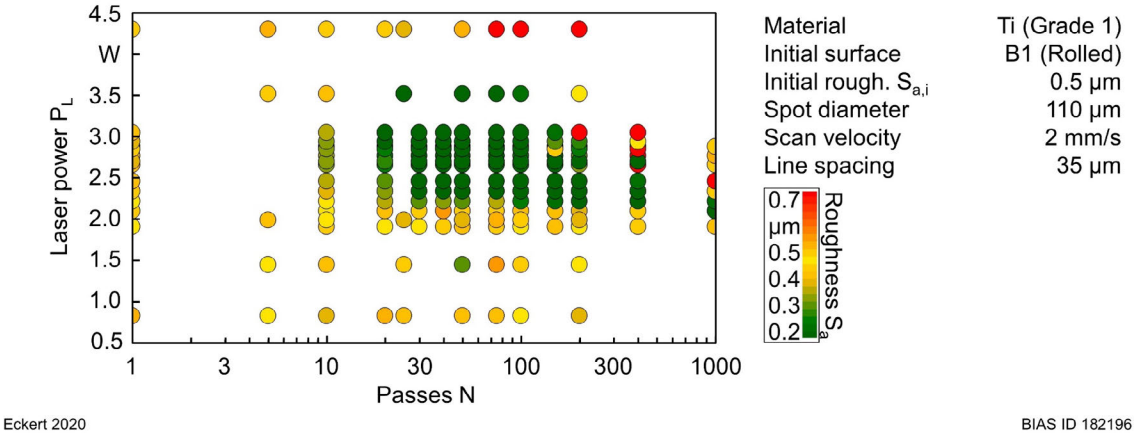

Figure 5.21: Average roughness as a function of laser power and number of passes.

For titanium (Grade 1) and a spot diameter of 110 µm, the best surface finishes with a significantly reduced roughness were achieved for laser powers in the range between:

$$P_{L,th} = 2.2\,W < P_L < P_{L,dist} = 2.9\,W \tag{5.3}$$

Considering this power range in conjunction with the results shown in **Figure 5.21**, a minimum of 30 scan passes is necessary to optimize the surface finish. For scan passes above 200 and laser powers above 3 W, the roughness increased and can exceed the initial roughness of 0.5 µm. However, the value for the power and disturbance thresholds in Equation (5.3) depend not only on the spot diameter (Section 5.1.2) but also on influences such as the material and electrolyte (Section 5.3.2).

Figure 5.22 shows surface roughnesses separated into the micro- and mesoroughness and waviness regimes. The increase in mesoroughness and waviness observed for high numbers of passes and laser powers can be linked to the increasing removal depth (aspect ratio) of the processed surface, as shown in the following section. For laser powers above 3 W, the microroughness increased because of induced surface disturbances, including the observed nanoporous cavities.

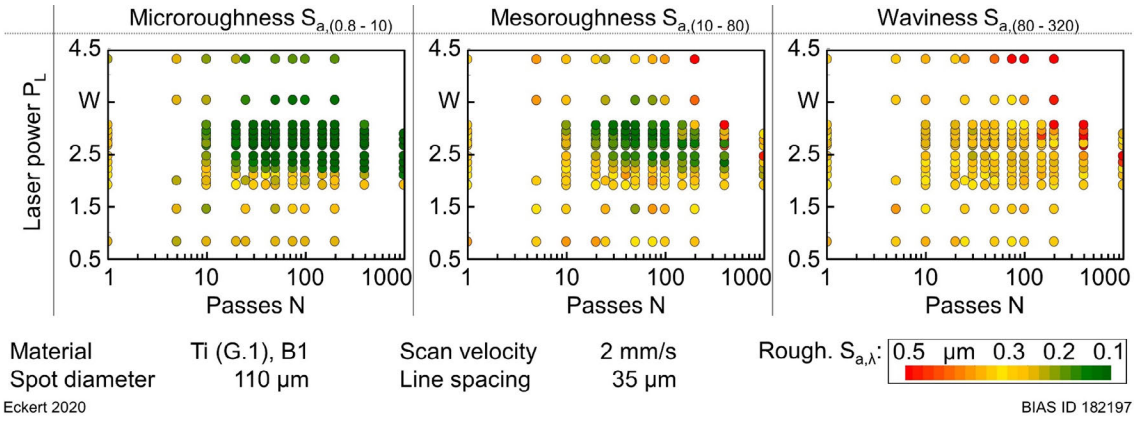

Figure 5.22: Surface roughness as a function of laser power and number of passes separated into the micro- and mesoroughness and waviness regimes.

5.2.4 Removal depth and aspect ratio

Smoothing during LCM is achieved by removing material from the surface and is thereby related to the recess of the average surface plane caused by processing, i.e., increases in the removal depth. **Figure 5.23** shows the removal depth h_s as a function of the number of scan passes during smoothing on a double logarithmic scale for a laser power of 2.46 W (data points corresponding to **Figure 5.20**). The experimental data were fitted by a linear regression (blue line), which showed that the removal depth of the surface increased linearly with the number of passes. The minimum roughness of 0.18 µm was achieved after 100 scan passes, corresponding to 7.6 µm of material removal. After 1000 passes, the removal depth reached 75 µm. The linear increase of the removal depth showed that no electrolyte saturation occurred. Therefore, the time between each scan pass was long enough for a complete exchange of the local electrolyte. Because of the subtractive finishing approach of LCP, which is based on material dissolution from the surface, the roughness reduction and the recess of the average surface plane are mutually dependent. For further reference, Appendix A.2 presents additional surface finish and removal depth results, including the polishing and removal depth as a function of the number of passes of initially ground (T1) (**Figure A.4**), and abrasive-blasted (B2) (**Figure A.6**) surfaces, where spot diameters of 31 µm and 336 µm, with respective laser powers of 1.05 W and 10.2 W, were used.

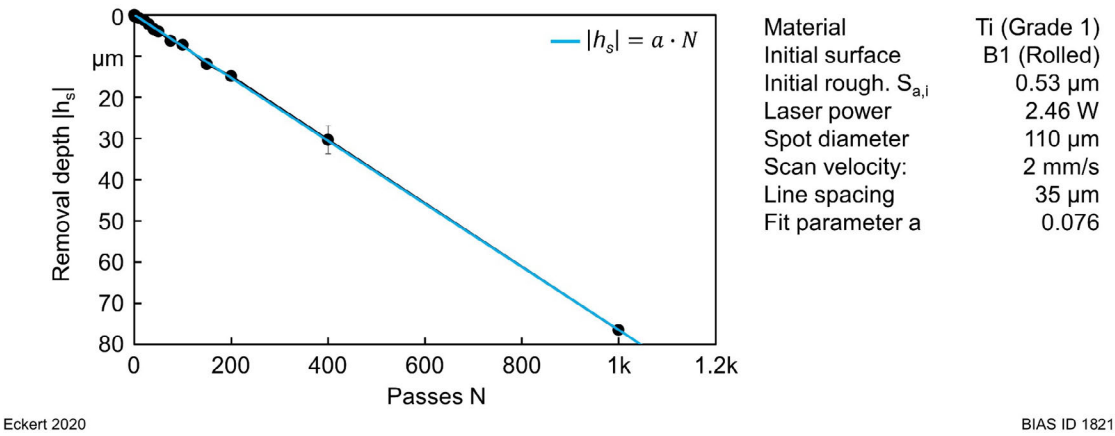

Figure 5.23: Removal depth h_s as a function of the number of passes. The minimum roughness of 0.18 µm was achieved after 100 scan passes.

As shown in Section 5.2.3, the waviness of the surface finish increased with the number of passes and thus with the removal depth. The increasing material removal caused a more uneven surface finish. **Figure 5.24** shows reflected-light images and surface-height data of the entire 800 µm × 800 µm polished surface area after 20, 50, 100, 200 and 1000 scan passes. For aspect ratios $|h_s|/L_x$ greater than 0.03 (corresponding to 200 passes), shape deviations of the polished area from the initially flat surface can be observed.

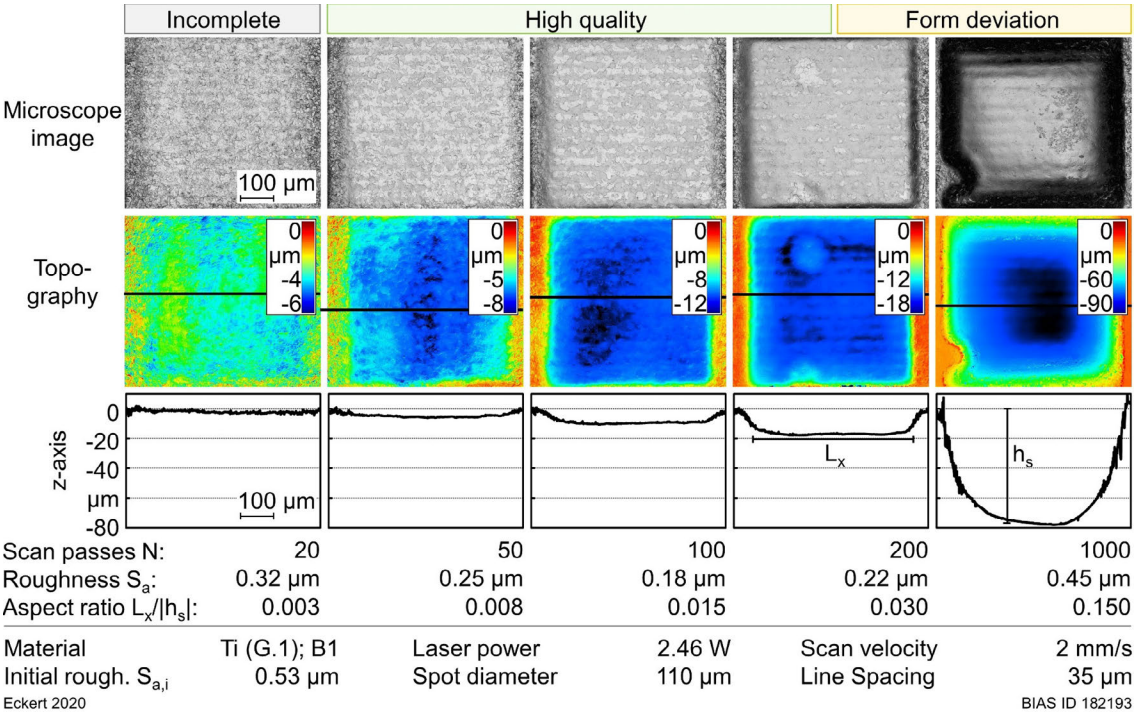

Figure 5.24: Reflected-light images and surface-height data for the polished surface with an increasing number of scan passes.

The progressive recess of the average surface plane leads to a 3D structuring in depth with an uneven surface at the bottom. This explains the increased waviness observed in **Figure 5.20**, while the microroughness remains unaffected. The shape deviation is

proposed to result from changing thermal conditions due to the increasing removal depth and the Gaussian intensity distribution. The underlying cause is that the edge of the surface is never processed with the maximum intensity.

These results showed that the aspect ratio $|h_s|/L_x$ should be less than 0.03 for LCM to be a reliable surface finishing process. The induced waviness and shape deviation at the edge are then minimal. This condition corresponds to the surface finish that has reached a stable lower limit on roughness with regard to the number of passes and removal depth, i.e., with further processing the average surface plane recedes in depth without any further improvements. The removal depth that achieves this surface finish limits the minimum lateral x- and y-dimensions of the polished area $A = L_x \cdot L_y$ because the aspect ratio should remain less than 0.03. The material removal $|h_s|$ required to achieve minimum average roughness depends on the initial roughness, as discussed in more detail in Chapter 7.

5.2.5 Scan velocity and passes

Figure 5.25 shows the roughness for three different scan velocities and an increasing number of passes. The roughness was evaluated for 200 to 100,000 passes and scan velocities of 2, 20 and 200 mm/s. The roughness continuously decreased from the initial value of 0.5 µm to its minimum between 0.1 µm and 0.2 µm. The faster the scan velocity, the more passes were necessary to decrease the roughness. The relationships among the scan velocity, line spacing, scan passes and average exposure time are further discussed in Chapter 6.

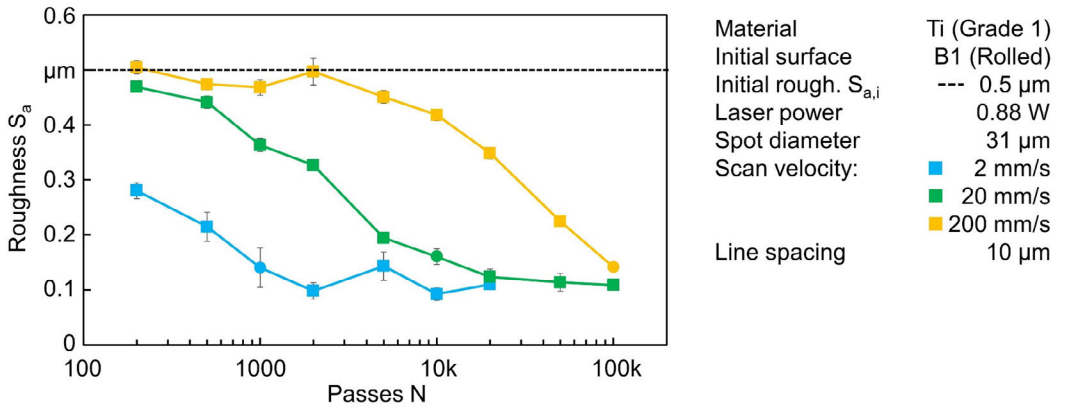

Figure 5.25: Roughness as a function of the number of passes for three different scan velocities.

5.2.6 Spot diameter and laser power

As shown in Sections 5.1.2 and 5.2.1, in order to achieve similar processing results with different spot diameters, both the laser power and the line spacing must be increased proportionally to the spot diameter. **Figure 5.26** shows the average roughness as a function of the number of passes for 10 different spot diameters from 34 µm to 950 µm, with proportionally increased line spacing from 9 µm to 238 µm and laser powers from

1.0 W to 28.8 W. In order to keep the line overlap constant at 75 %, the line spacing b was adjusted, depending on the spot diameter, to $d_f/4$. The investigated set of spot diameters was designed such that each increment was separated by the square root of two according to the pattern 60 µm·$\sqrt{2}^{9}$ = 59 µm·$\sqrt{2}^{8}$ = … = 672 µm·$\sqrt{2}^{1}$ = 950 µm (except for 34 µm), so that the processing time was halved by each step. This design was selected because the processing time is inversely proportional to the square of the spot diameter, according to Equation (4.5). However, this does not imply a constant exposure time during one scan pass for different spot diameters. The exact spot diameters and laser powers are listed in the parameters of **Figure 5.26**. With increasing numbers of passes, the roughness decreased rapidly from 1.7 µm down to the lower limit of approximately 0.25 µm. Reaching this lower limit required 30 passes for spot diameters above 119 µm, and 75, 110 and 175 passes for spot diameters of 84 µm, 60 µm and 34 µm, respectively.

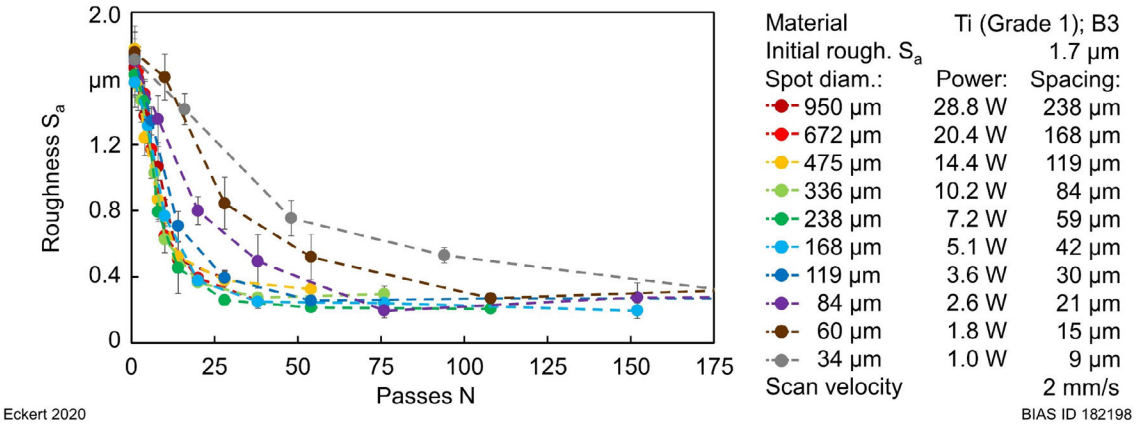

Figure 5.26: Average roughness S_a as a function of the number of passes for different spot diameters and propotionally increased line spacing and laser power.

Figure 5.27 shows the same data in a two-dimensional plot of the average roughness S_a as a function of the spot diameter and scan passes. The roughness is color-coded, from green (< 0.3 µm, minimum of roughness) to red (1.7 µm, initial roughness). In general, more scan passes were required to smooth the surface as the spot diameter decreased, although the largest spot diameters of 475, 672 and 950 µm were exceptions to this trend. For these three diameters, additional polishing would be necessary to reach the lower limit on roughness attained with the smaller spot diameters.

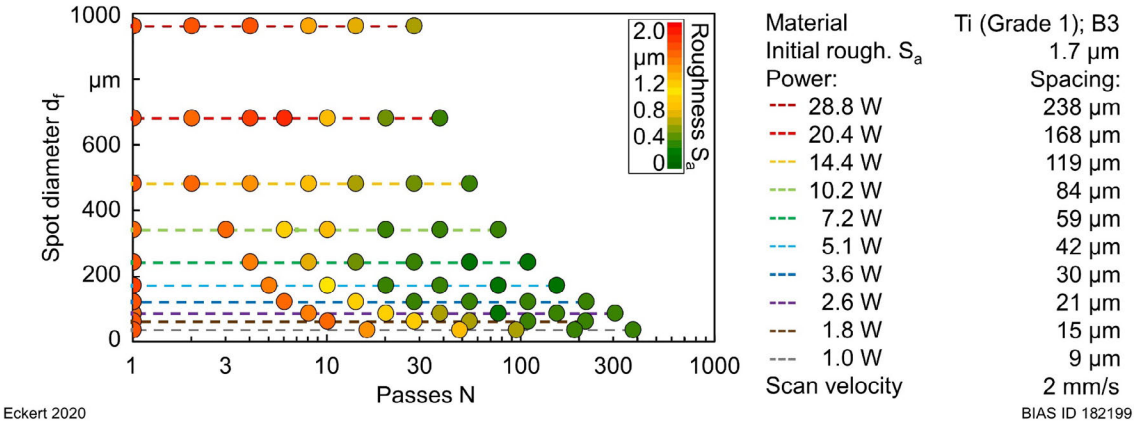

Figure 5.27: Average roughness S_a as a function of the spot diameter and number of passes.

Figure 5.28 shows typical reflected-light images and surface-height data for surfaces finished with spot diameters of 34, 119, 238, 336 and 672 µm and 188, 54, 28, 20 and 10 scan passes, respectively. These parameters were chosen so that the average exposure time was approximately 10 s. For spot diameters up to 336 µm, the roughness was significantly reduced to 15 % of the initial value. For the larger spot diameter of 672 µm, the surface roughness was reduced to 38 % of the initial value, and the surface showed remnants from the initial roughness in the surface-height data. Additional reflected-light images and surface-height data for the spot diameters not shown here are shown in Appendix A.2 (**Figure A.7**).

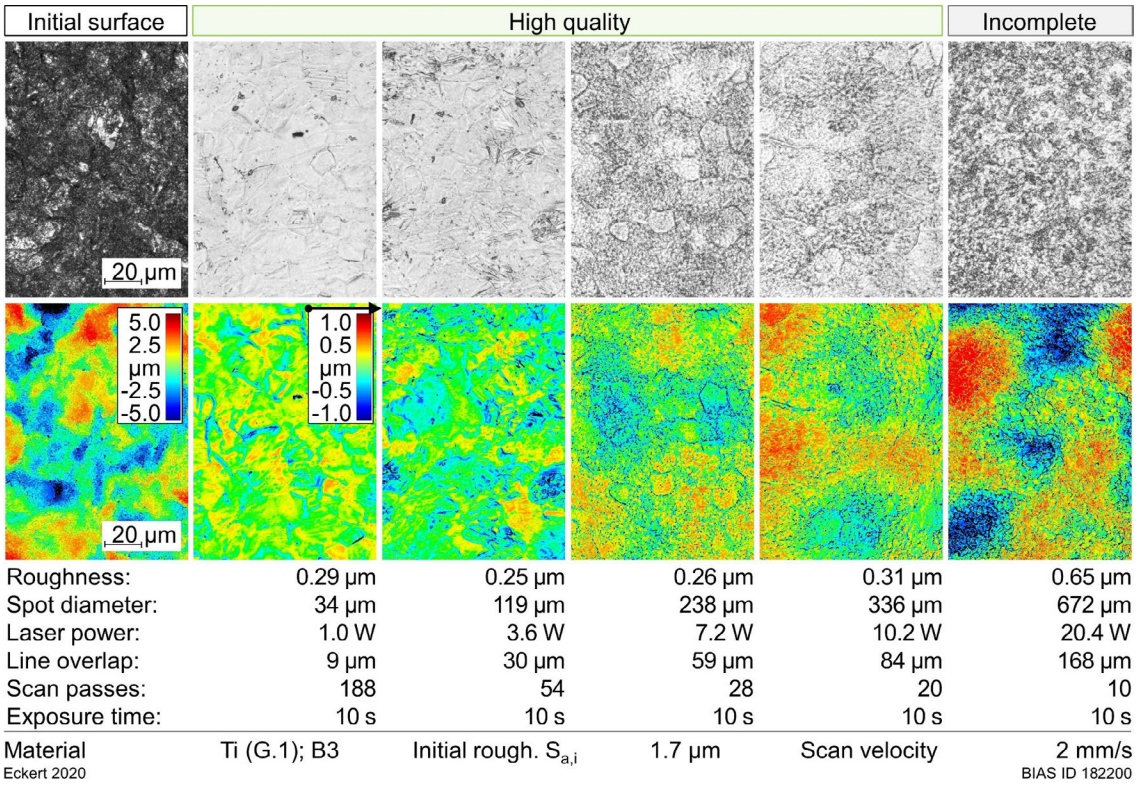

Figure 5.28: Reflected-light images and surface-height data for surface finishes after processing with different spot diameters at an exposure time of 10 s.

5.3 Surface finish limitations

5.3.1 Initial roughness and lower limit

Preprocessing by rolling (B1), abrasive blasting (B2 to B4), grinding (T1) and turning (T2 to T4) induces characteristic surface features that are reflected in the roughness spectra, as shown by the dashed lines in **Figure 5.29** for B1 to B4 and **Figure 5.30** for T1 to T4 (semi-logarithmic scale). Over all wavelength regimes, the spectral roughness $S_{a,\lambda}$ was higher the longer the initially rolled surface was abrasive-blasted. The initial rolled surface had a spectral roughness below 0.2 µm for all wavelengths. The 6 s abrasive-blasted surface (B4) showed a mesoroughness of more than 1 µm and a microroughness of approximately 0.6 µm.

The turned surfaces T2 through T4 exhibited microroughnesses of approximately 0.2 µm, and the ground surface T1 exhibited microroughness of less than 0.1 µm. T3 showed a local maximum at a wavelength of 15 µm and an absolute maximum at 120 µm. T4 also showed a maximum at 120 µm.

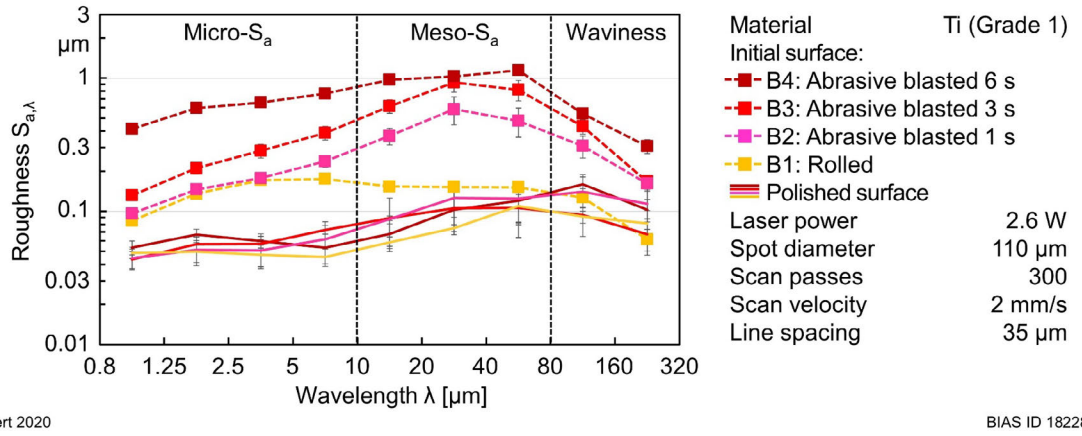

Figure 5.29: Roughness of the preprocessed (dashed lines) and polished (continuous lines) surfaces of samples B1 through B4.

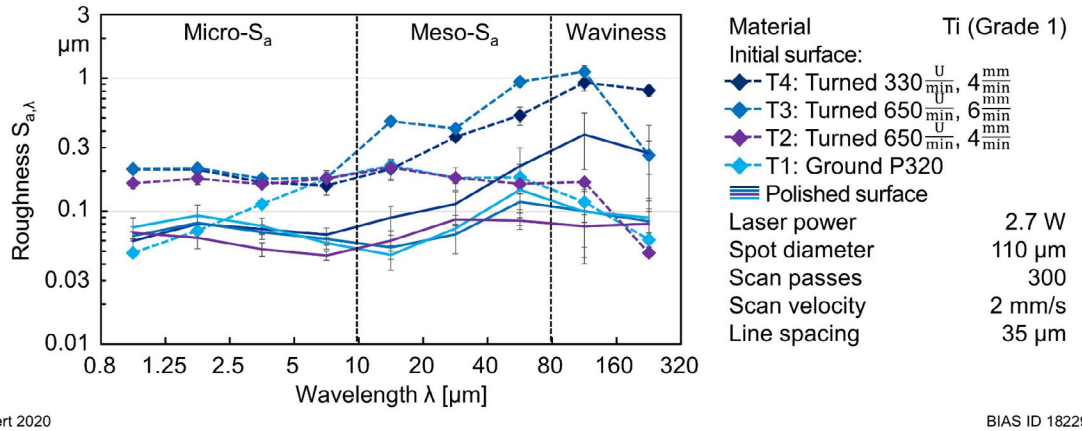

Figure 5.30: Roughness of the preprocessed (dashed lines) and polished (continuous lines) surfaces of samples T1 through T4.

Polishing with a laser power between 2.6 W and 2.7 W and 300 passes significantly reduced the spectral roughness at all wavelengths to a microroughness below 0.1 µm and a mesoroughness and waviness of approximately 0.1 µm, as shown by the continuous lines in the figures. The zigzag scan trajectory gave the roughness spectrum of the final surface the characteristic s-curve. Only the surface turned at 4 mm/s (T4) showed a higher residual waviness under these laser powers and pass numbers.

Figure 5.31 shows reflected-light images and surface-height data of the corresponding surface finishes after 300 passes. The microstructures of the turned surfaces showed more dislocations within the grains, which might result from the preprocessing approach. Regardless of the preprocessing approach and initial surface roughness, the final roughness was between 0.15 µm and 0.28 µm, except for the surface that had been turned at 4 mm/s (T4), which showed a final roughness of 0.45 µm and did not reach the stable lower limit after 300 passes.

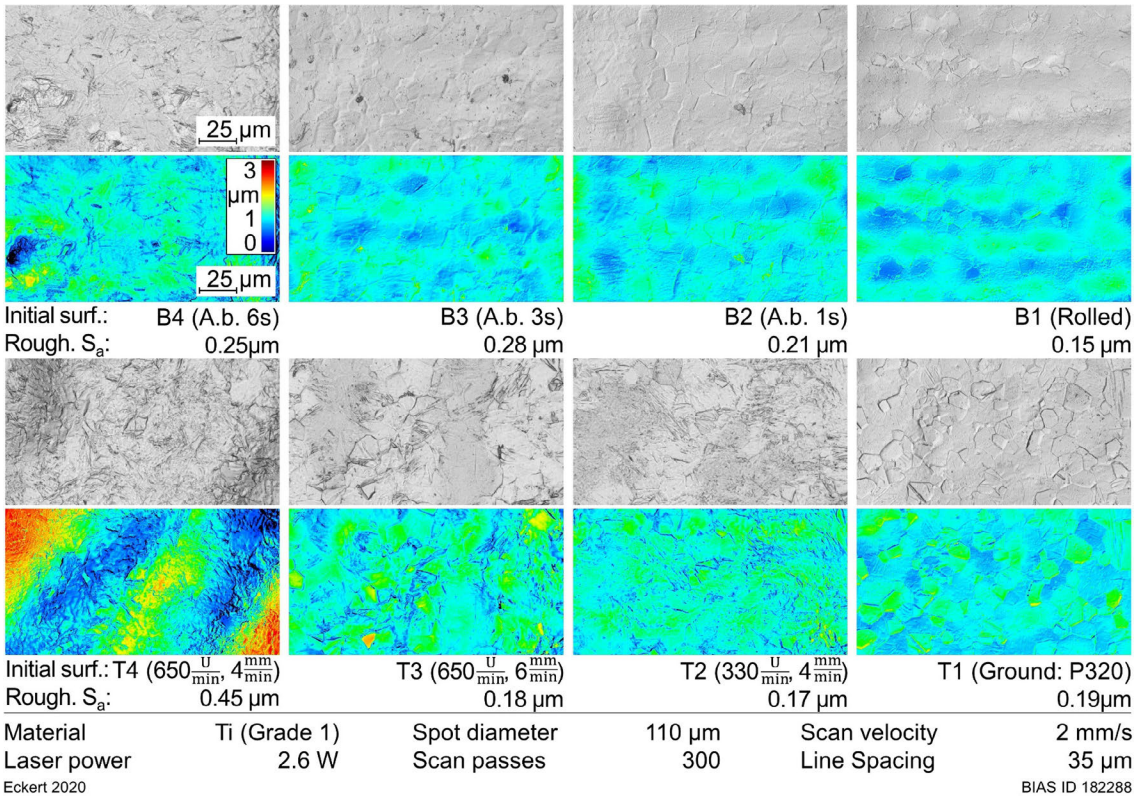

Figure 5.31: Images of the surface finishes of different preprocessed surfaces after 300 passes.

Figure 5.32 shows the average roughnesses, as a function of the number of passes, of the initial surfaces of samples B1 through B4, with average roughness values of 0.6, 1.4, 2.3 and 3.2 µm, respectively. Smoothing these initial surfaces to the stable lower limit, with a minimum roughness of $S_{a,f} \approx 0.2$ µm, required 25, 50, 100 and 150 passes. Thus, smoothing takes longer when the initial roughness and average wavelength are greater. No further surface improvement was observed after processing with up to 300 passes.

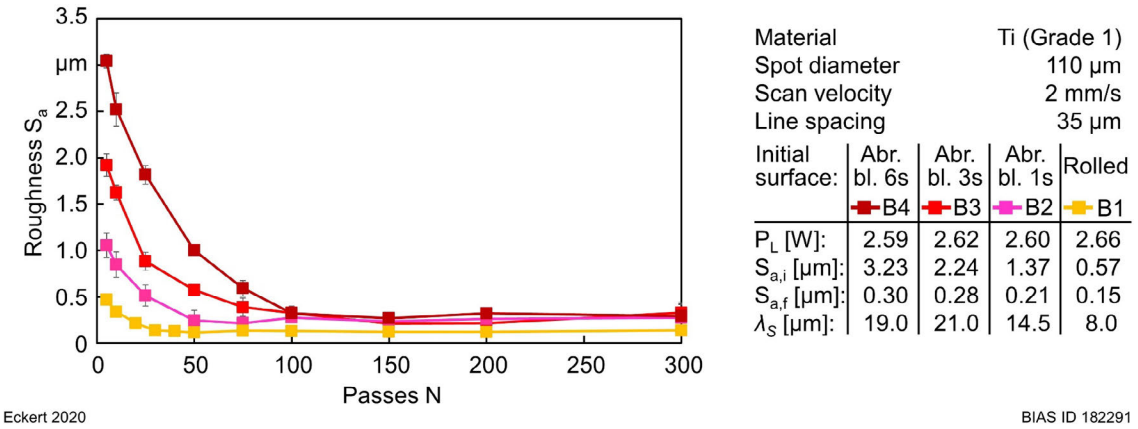

Figure 5.32: Average roughness of rolled and abrasive-blasted surfaces after multiple passes.

Figure 5.33 shows the roughness as a function of the number of passes for five laser powers. The roughness decreased faster the higher the laser power, and for powers of 2.86, 2.59, 2.28 and 2.19 W, the lower limit of approximately 0.3 µm was attained after 50, 100, 200 and 250 passes, respectively. With the laser power of 1.82 W, the roughness decreased during the first 75 passes and then stayed relatively high without further improvement. The initial smoothing was presumed to reduce the absorbed laser power to below the power threshold necessary for material removal, halting the smoothing process.

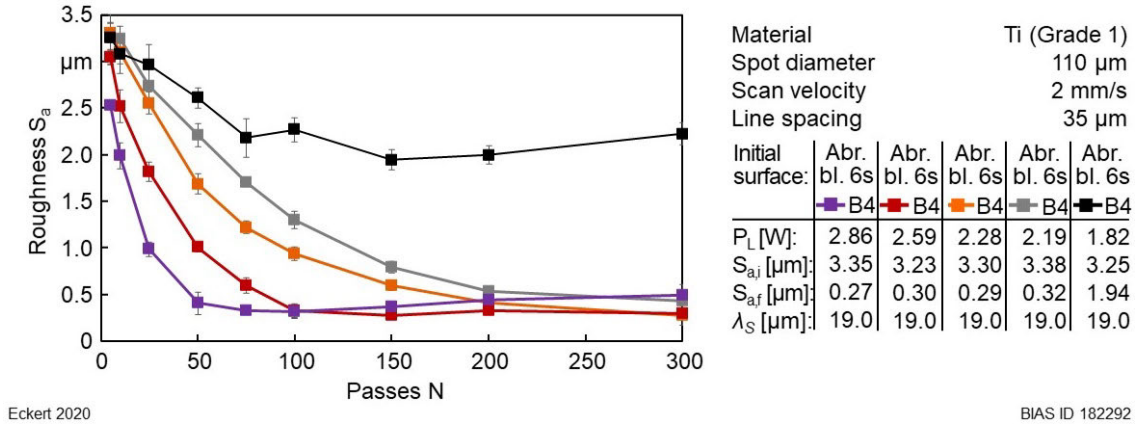

Figure 5.33: Roughness as a function of number of passes for five different laser powers.

Figure 5.34 shows the average roughnesses of the 3 s abrasive-blasted sample (B3), the ground surface T1 and the turned surfaces T2 through T4 over an increasing number of passes. The surfaces B3, T3 and T4 had similar initial average roughnesses but different average wavelengths of 21.0, 22.8 and 50.6 µm. The 4 mm/min turned (T4) surface was smoothed half as fast as the 3 s abrasive-blasted (B3) and 6 mm/min turned surfaces (T3). The two latter samples attained their lower limits of 0.28 µm and 0.18 µm after 100 passes, whereas the 4 mm/min turned surface attained 0.48 µm after 200 passes.

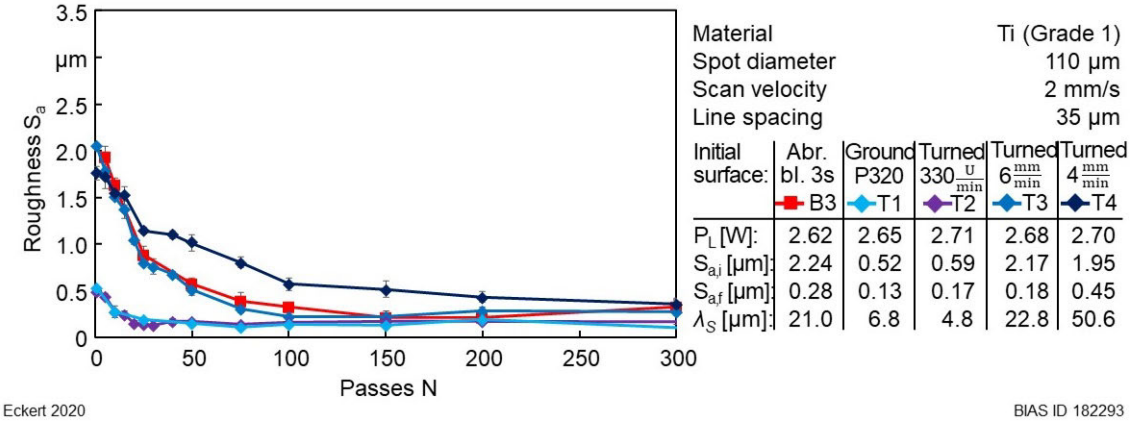

Figure 5.34: Roughness as a function of number of passes for abrasive-blasted and turned surfaces, and the process parameters, at right.

The minimum roughness achieved for the 4 mm/min turned surface (T4) was significantly larger compared with the other two, and did not reach a stable lower limit even after 300 scan passes. **Figure 5.35** shows the roughness spectra and surface-height data for the 3 s abrasive-blasted sample (B3) and the turned surfaces T3 and T4 under different numbers of passes. The roughness spectra reflect the average height and wavelength of the surface features induced by the preprocessing treatment.

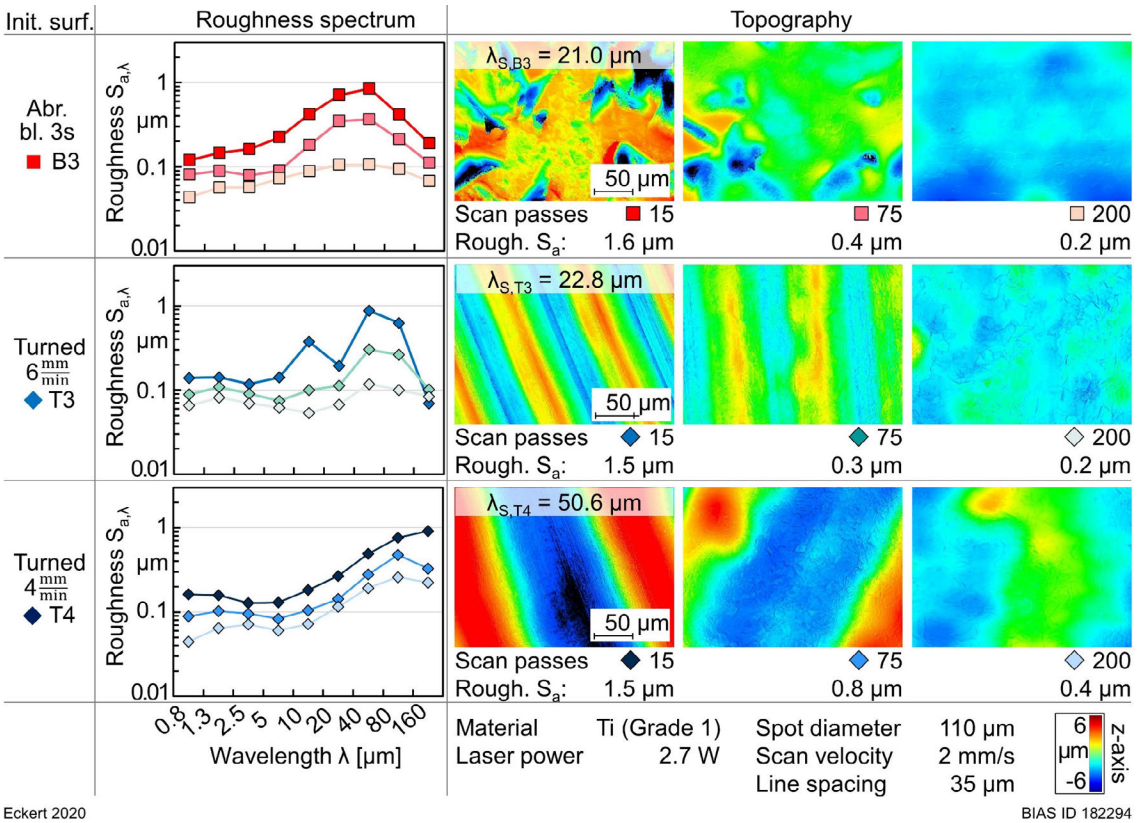

Figure 5.35: Roughness spectra of the abrasive-blasted (B3) and turned (T3 and T4) surfaces after multiple passes 15, 75 and 200 passes, and the corresponding topographic images.

Both the abrasive-blasted (B3) and turned (T3) surfaces initially showed maxima in the mesoroughness regime, at wavelengths between 10 µm and 80 µm. In both cases, within 200 passes, LCP reduced the spectral roughness $S_{a,\lambda}$ below 0.1 µm for all wavelengths. The anisotropy of the initial turned surface T3 did not decisively influence the smoothing process compared with the abrasive-blasted surface B3. The turned surface T4 showed a maximum roughness at a wavelength of 120 µm. After 200 passes, a relatively high residual mesoroughness and waviness remained, although the microroughness was the same as for B3 and T3. The surface-height data show the remaining elevations due to the turning ridges. The data presented here indicate that smoothing is slower with larger initial average wavelengths. An initial surface with large roughness mainly at shorter wavelengths, in the microroughness regime, reaches the stable lower limit much faster. This trend can be seen by comparing the rolled and turned surfaces B1 and T2 to the surfaces B3 and T3, which exhibited roughness maxima at wavelengths in the mesoroughness regime, or even the surface T4, which showed a maximum in the waviness regime. These analyses further support that initial surfaces with lower average roughness and shorter average wavelength are smoothed faster.

To summarize, the average roughness S_a decreased rapidly with increasing numbers of passes. The rate of decrease was influenced by the laser power P_L, initial average roughness $S_{a,i}$ and average wavelength λ_S. However, the stable lower roughness limit of the finished surfaces was independent of these influences.

5.3.2 Influence of the material

Figure 5.36 shows the surface roughness as a function of the number of passes for titanium, Ti6Al4V, Nitinol, Stellite 21 and metallic glass under different laser powers. The reflected-light images show typical disturbances occurring at higher laser powers. The roughnesses of these materials can be significantly reduced (by > 90 %) with certain process parameters. The laser power threshold $P_{L,th}$ necessary for thermochemical material removal depends on the material. For example, Ti6Al4V can be polished sufficiently at 1.03 W (orange triangles), whereas titanium required 2.32 W (red triangles) for a comparable roughness decrease. In general, the roughness decayed exponentially with the number of passes to a minimum value between 0.1 µm and 0.3 µm. For higher laser powers, the decay occurred faster. Two exceptions to these general trends were observed: First, the surface finish was incomplete when titanium and Nitinol were treated with the lowest laser power (indicated by the open circles in their plots in the figure), and second, for Nitinol, Stellite 21 and metallic glass treated with higher laser powers, corrosion and secondary chemical disturbances occurred (purple, blue, and green filled circles in the figure). The entire surface can be covered by the structures resulting from these disturbances, as shown in the reflected-light images.

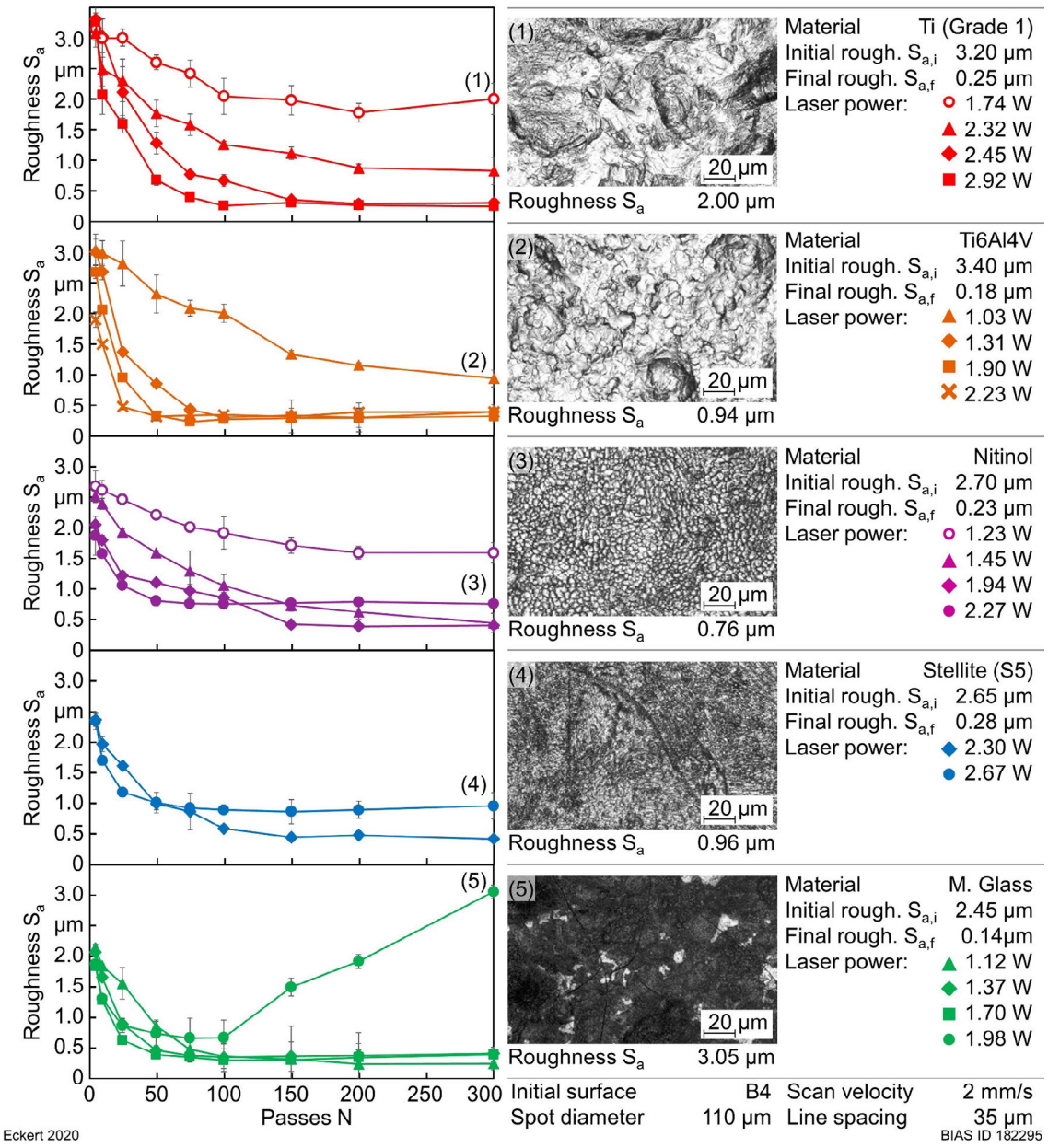

Figure 5.36: Surface roughness as a function of the number of passes for different materials (left side) and corresponding reflected-light images of process disturbances (right side).

In these instances, further LCP treatment did not continue to improve smoothing, and roughness increased. The optimal power range for polishing therefore lies between the removal threshold power $P_{L,th}$ and the disturbance threshold power at $P_{L,dist}$. These two values depend on the specific material-electrolyte combination.

5.3.3 Dependence on microstructure

The focus in this section was on the correlation between the roughness minimum and the microstructure of the materials in order to test the third research hypothesis. **Figure 5.37** shows the roughness spectra of the initial surfaces (dashed lines) and those of the polished titanium (Grade 2), Ti6Al4V, Nitinol, Stellite 21 (S1) and metallic glass surfaces. The minimum roughnesses $S_{a,f}$ lay between 0.28 µm (Stellite 21) and 0.14 µm (metallic glass).

The roughness spectra showed significant decreases between the initial surface (dashed lines) and the polished surface (solid lines) for all materials and almost all wavelengths. Surface features caused by grain and phase boundaries, which have lateral dimensions below 10 µm, had a dominant influence on the microroughness.

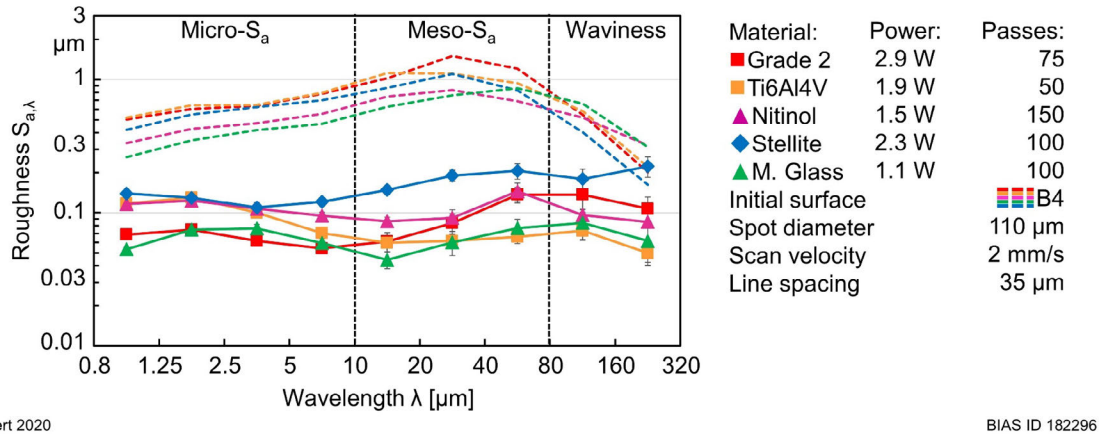

Figure 5.37: Roughness spectra of the materials before (dashed lines) and after polishing (solid lines).

Therefore, the alloys Ti6Al4V, Nitinol and Stellite 21 exhibited up to two times higher microroughnesses compared with titanium (Grade 2) or metallic glass. The higher deviations of Stellite 21 in the mesoroughness and waviness regimes may have been related to inhomogeneities of the sample material (produced by selective laser melting).

Figure 5.38 shows reflected-light images and height data as well as profile lines for polished titanium (Grades 1 and 2), Ti6Al4V, Nitinol and metallic glass. In the reflected-light images, grain boundaries and material phases are visible, except in the metallic glass images, because of this material's amorphous character. The profile lines of titanium (Grades 1 and 2) show discontinuities at grain boundaries. On grain facets, the roughness was significantly lower than the roughness of the entire surface. A finer grain structure or more finely dispersed phases (as in Ti6Al4V) exhibited more discontinuities, whereas coarser (Grade 2) or amorphous structures (metallic glass) exhibited fewer discontinuities or none at all. Thus, the microroughness increased with decreases in microstructural grain size. These results indicate that microroughness is significantly increased by irregular material removal at the grain boundaries and the different chemical dissolution rates of the phases. Because of the chemical nature of the material removal process, different material phases can be expected to dissolve at different rates. The resulting surface finishes showed structures of different heights remaining due to isotropic etching, possibly because titanium grains dissolved faster than aluminum and vanadium components. Those differences in the dissolution rate determine the residual roughness and final surface finish and therefore support the third research hypothesis for the materials investigated here.

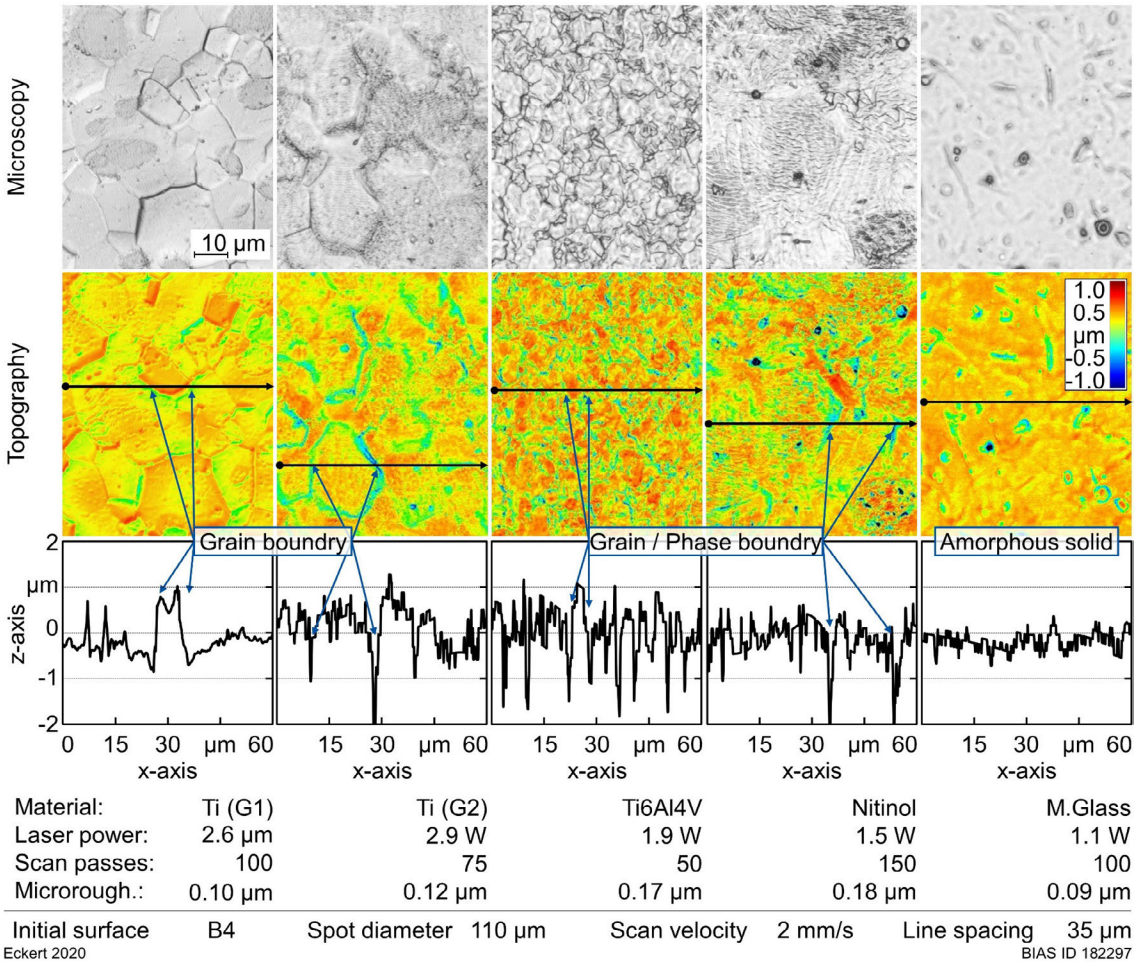

Figure 5.38: Reflected-light images, surface-height data and profile lines for different materials after LCP.

Figure 5.39 shows reflected-light images and height data as well as profile lines for the polished Stellite 21 samples S1 through S5 (Table 2). The polishing result depended significantly on the microstructure of the sample and therefore on the manufacturing process. The grain sizes ranged from 10 µm to 20 µm for S1 to very fine grains of 1 µm to 5 µm for S4 and S5. The profile lines showed discontinuities at grain and phase boundaries, although across individual grains or phases, the roughness was comparably low (S2). For finer-grained structures, such as S3 (S_a = 0.91 µm) and S4 (S_a = 0.56 µm), discontinuities occurred more frequently.

Figure 5.40 shows roughness spectra of the surface finishes for samples S1 to S5. For all samples, the laser process parameters were almost the same. Minimum surface roughnesses S_a from 1.9 µm for S1 to 0.3 µm for S5 were achieved. The spectral roughnesses $S_{a,\lambda}$ of the samples did not show a clear trend but were reduced for almost all wavelengths compared with the initial roughness (black dashed line).

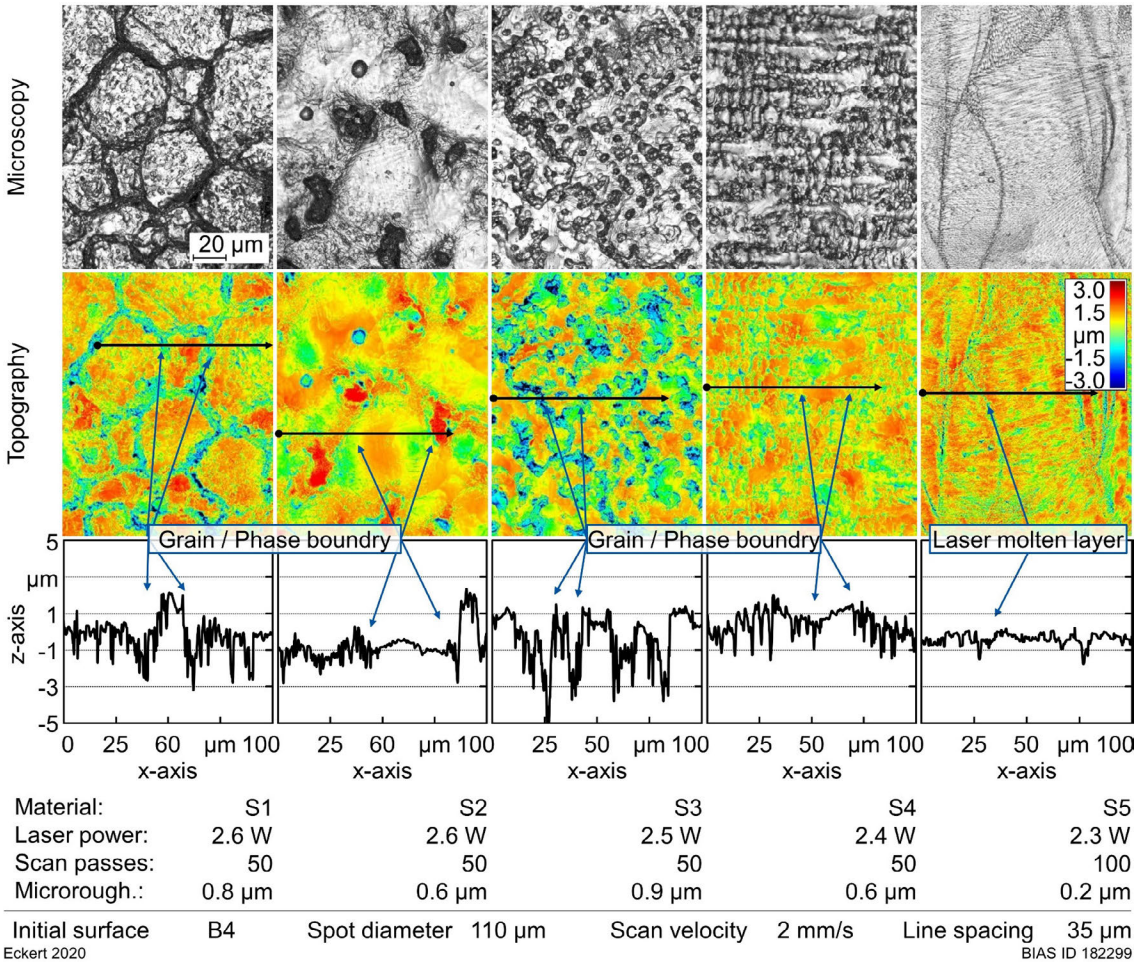

Figure 5.39: Reflected-light images, surface-height data and profile lines for the polished Stellite 21 samples S1–S5.

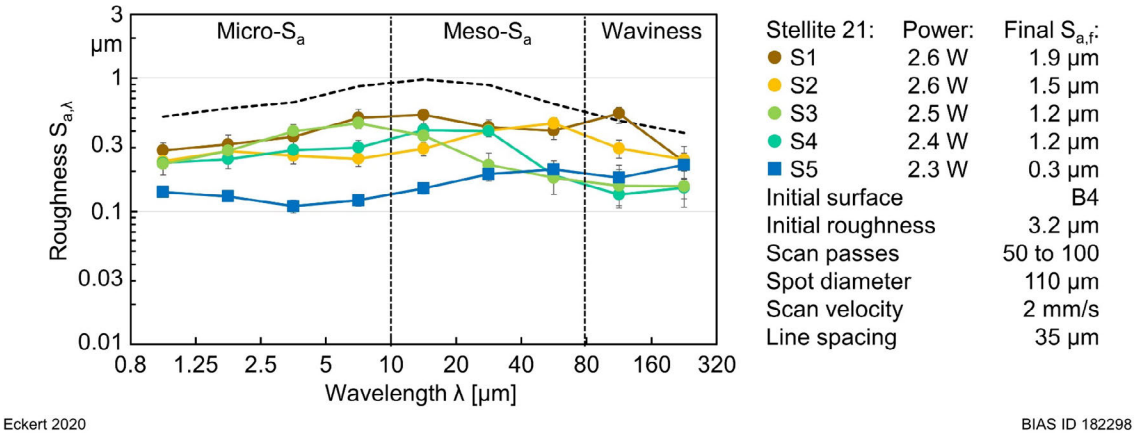

Figure 5.40: Roughness spectrum of Stellite 21 samples before (dashed line) and after polishing (solid lines).

5.3.4 Periodic surface structures

Figure 5.41 shows the surface finish of a titanium (Grade 1) sample, polished with a spot diameter of 31 µm and laser power of 0.98 W, after 100 and 500 passes. The surface was smoothed to 0.24 µm after 100 passes. On this sample, laser-induced, periodic surface

nanostructures in the form of ripples appeared sporadically on the grain facets. After 500 passes, almost all grain facets were covered evenly by ripples, as shown in the SEM image.

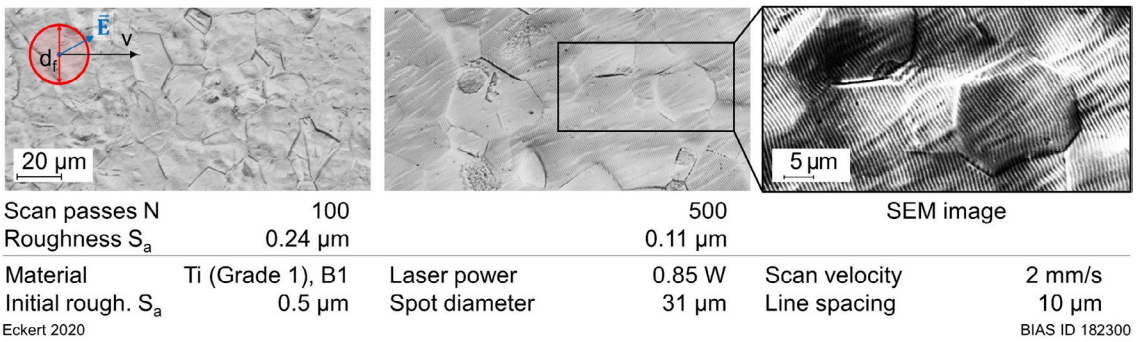

Figure 5.41: Reflected-light images of periodic nanostructures emerging during LCP.

Figure 5.42 shows the profile line along one grain facet. The ripple structure is between 10 nm and 80 nm deep. Its periodicity is interrupted at the grain boundary (red curve) but then continues after the boundary in the same way as before. Averaged over 20 periods, the structure spacing was $\Lambda = 0.714$ µm. This corresponds to the theoretical predicted ripple spacing of $\Lambda = 0.732$ µm calculated with Equation (2.17). The angle of incidence was assumed to be 1.25° ($NA = 0.03$) and the refractive index was assumed to be 1.43 (for 30 % phosphoric acid [Saf08]). Because of its small depth of 80 nm, the contribution of the ripple structure to the overall roughness was of secondary importance. However, its function as a reflection grating has a macroscopic effect on the polished surface, as shown in Chapter 9.

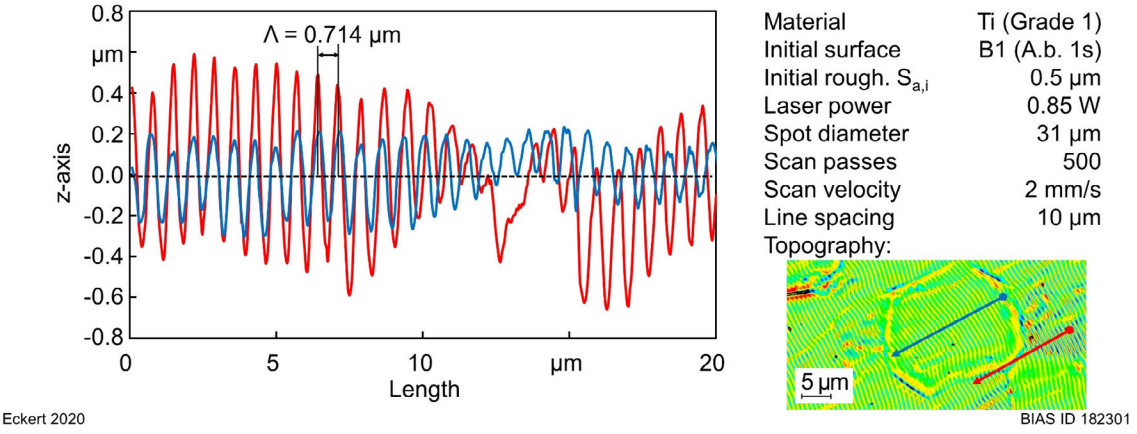

Figure 5.42: Profile lines of the periodic nanostructure along a titanium-grain facet.

In summary, the results presented in Section 5.3 have shown a strong correlation between the achieved surface finish and the microstructure (Section 5.3.3), regardless of the initial surface (Section 5.3.1). These results give confirmation to the third central research hypothesis on a qualitative basis. In order to identify a quantitative correlation between the minimum roughness $S_{a,f}$ and the microstructure of the material, further experimental work is necessary.

5.4 Polishing kinetics

5.4.1 Evolution of the surface finish

Figure 5.43 shows reflected-light images of the same area on the titanium surface (B4) after passes incrementally increased to 550. The initial sand-blasted surface, with a roughness of 2.4 µm, was smoothed with each additional pass. After 70 passes, the average roughness was reduced to half of the initial value and was characterized mostly by bright areas with scattered indented, darker valleys. After 350 passes, the surface was polished and had reached its stable lower roughness limit at 0.2 µm, with the exception of a few defects. Most valleys were leveled out of the surface finish.

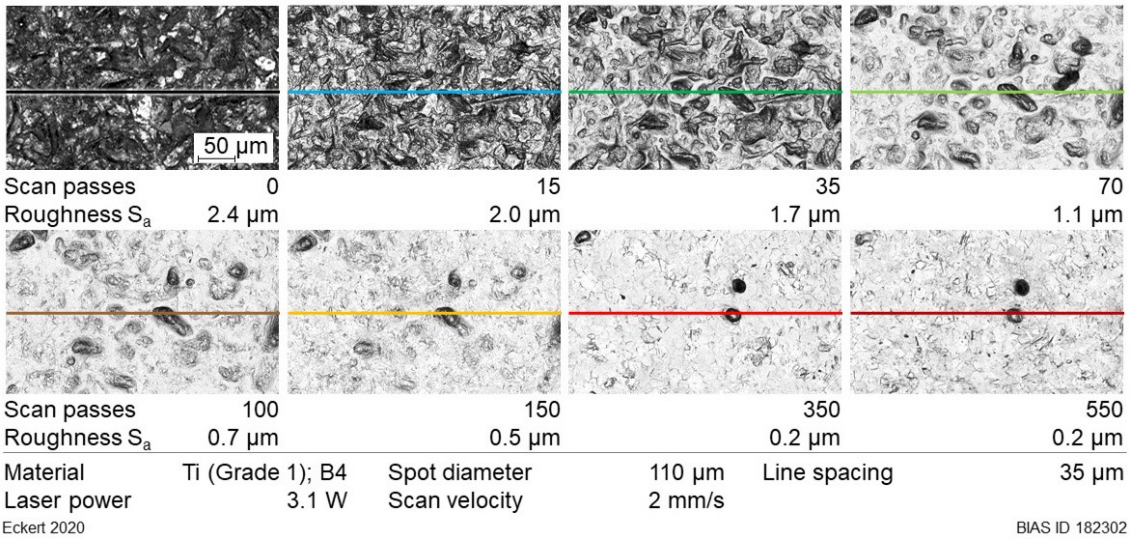

Figure 5.43: Reflected-light images of a single surface region after increasing numbers of scan passes.

The profile lines corresponding to these images are shown in **Figure 5.44**. The polishing continuously deepened the removal depth, down to 38 µm after 550 passes. The general trend of smoothing was interrupted when defects were uncovered, which were then levelled in subsequent passes by the incremental removal of the material around them.

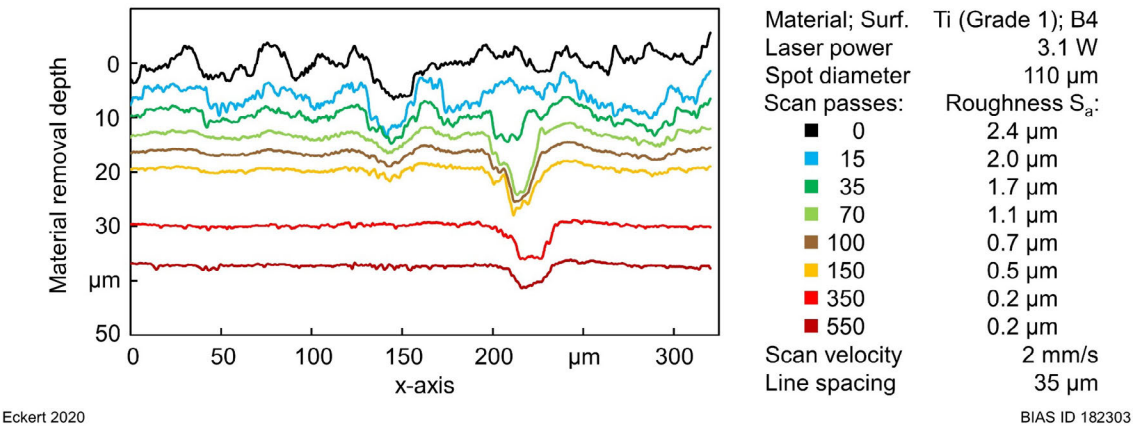

Figure 5.44: Traced profile lines of one surface region after an increasing number of passes.

As an example, this process can be observed for one defect between the transmission from 35 (green line) to 150 scan passes (yellow line).

Figure 5.45 shows the surface roughness S_a and removal depth $|h_s|$ as functions of the number of passes. Similar to the results in **Figure 5.23**, the removal depth increased in an approximately linear pattern, but shows a faster increase during the first 100 passes. The laser powers differed for these two experiments (3.1 W compared with 2.5 W), and the laser power determines the slope at which the removal depth increases. Moreover, the initial roughness of 2.4 µm for the abrasive-blasted surface (B4) used in this experiment differed from the 0.5 µm roughness of the rolled surface (B1) used to generate the data in Section 5.2.4. The higher initial roughness allowed greater absorptivity of the laser radiation on the surface: Table 3 showed that the absorptivity of 63 % for the abrasive-blasted surface (B4) differed by 20 % from the absorptivity of 43 % of the rolled surface (B1). Within the first 100 passes, where the roughness decreased from 2.4 µm to 0.7 µm and the surface was visually brightened, the amount of absorbed laser radiation would be expected to decrease. As a result, the smoothing could cease completely if the applied laser power is only slightly above the power threshold, as observed in **Figure 5.33**. However, the surface roughness was reduced to 0.2 µm after 200 passes and reached its stable lower limit.

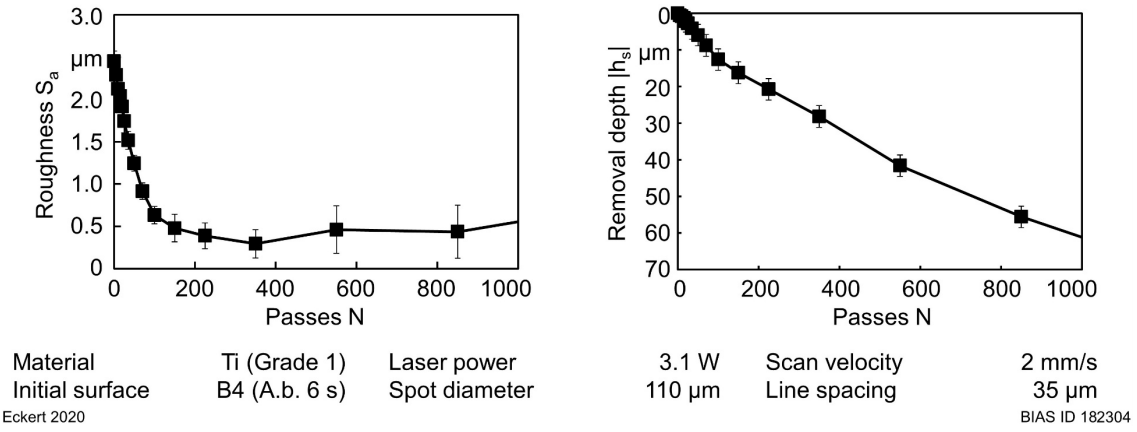

Figure 5.45: Surface roughness and removal depth as functions of the number of passes.

Figure 5.46 shows the evolution of the surface-height data and the height distribution of sample B4 after 35, 70, 150 and 350 passes. The initial surface showed a symmetrical height distribution of surface features up to 8 µm above (peaks) and surface features up to 8 µm below (valleys) the average surface plane. After 70 passes, the peaks were significantly reduced in size, whereas the valleys largely remained, resulting in an asymmetric distribution. The surface-height distribution showed few roughness peaks exceeding 2 µm, but 8 µm deep valleys remained. With further processing, the average surface plane receded further in depth, thus levelling the remaining valleys. The height distribution of the polished surface became symmetric again, and 90 % of all average

height data were found to be within 1 µm of the average height. These results show that the roughness peaks are removed first, and the valleys are then levelled by further recessing of the average surface plane.

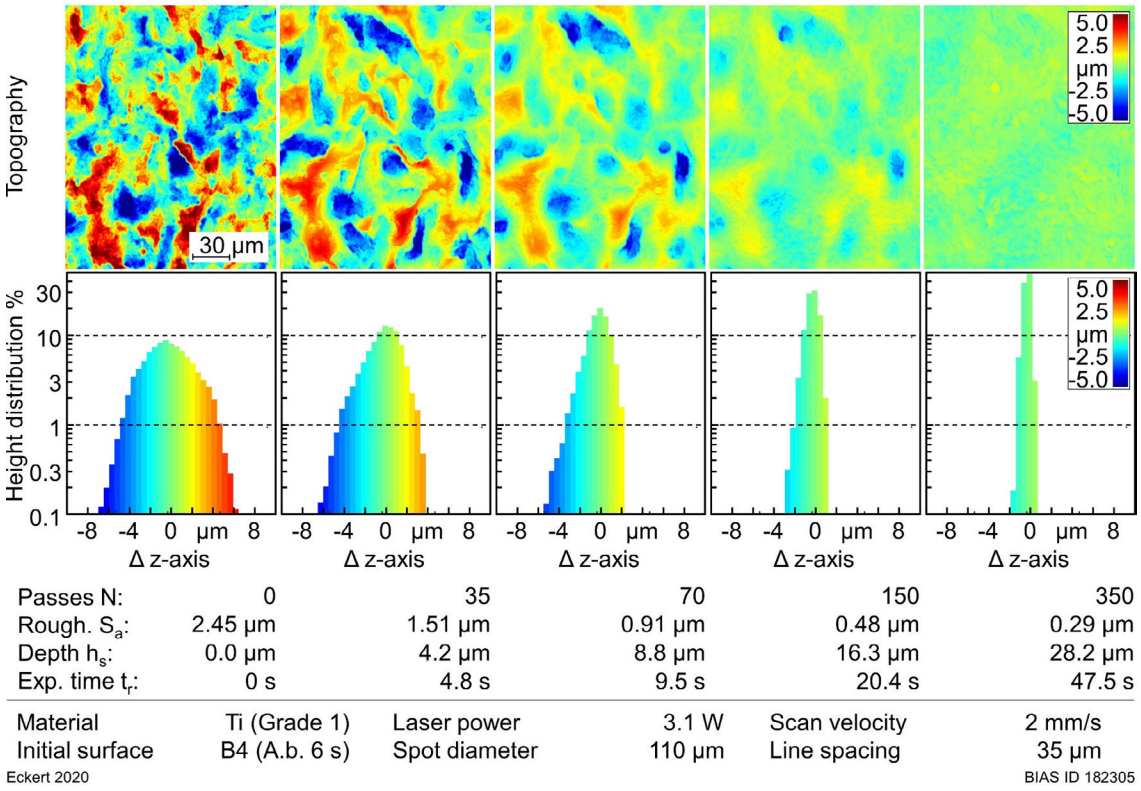

Figure 5.46: Surface-height data and height distributions after multiple passes.

5.4.2 Peak and valley removal

Figure 5.47 shows the removal depth h_s and the derivation $\Delta|h_s|/\Delta N$ as a function of the number of passes on a logarithmic plot. As expected in the previous section, during the first 100 passes, the removal depth of the abrasive-blasted surface (B4) shows a nonlinear characteristic as readily recognized by the non-constant derivation. The derivation, describes the removal velocity, decreased from approximately 0.5 µm/N (black curve, mean surface) and approached a constant value of 0.01 µm/N after 100 passes.

Furthermore, the surface-height data were separated into average height levels that predominantly contributed to the roughness peaks and valleys, as shown in the legend. The peak and valley levels were defined as the average height planes of the highest 16 % (red symbols) and lowest 16 % (blue symbols) of surface-height data. The initial distance between peak level and valley level was approximately 12 µm. With polishing, this distance between the level heights decreased continuously. This process was driven by the removal velocity of the peaks, which was up to four times faster than that of the valleys. After 100 passes, the distinction between peak and valley removal velocities became obsolete.

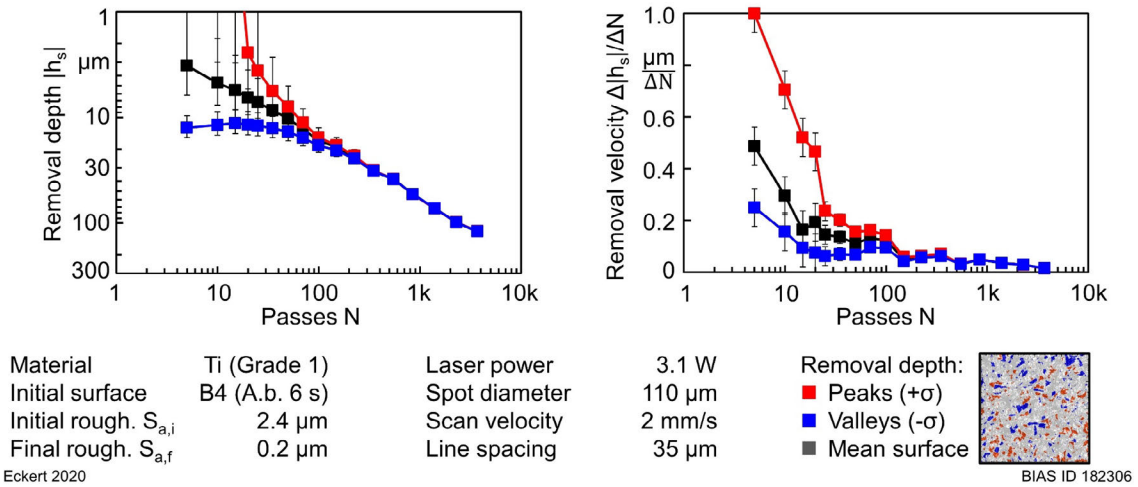

Figure 5.47: (a) Removal depth as a function of the number of passes for the average surface plane (black curve), its power function fit (light blue), the average peak level (red curve) and average valley level (blue curve) and (b) of the removal velocity.

These observations were also reflected in the roughness spectra shown in **Figure 5.48**. The initial surface had the highest spectral roughness, with a maximum of 1.2 µm in the mesoroughness regime. During smoothing, the roughness spectra showed two salient characteristics. First, the microroughness decreased down to 0.1 µm after 100 passes (brown curve). This was accompanied by surface brightening and reduction of the average roughness S_a by 65 %. The microroughness then remained constant during further processing.

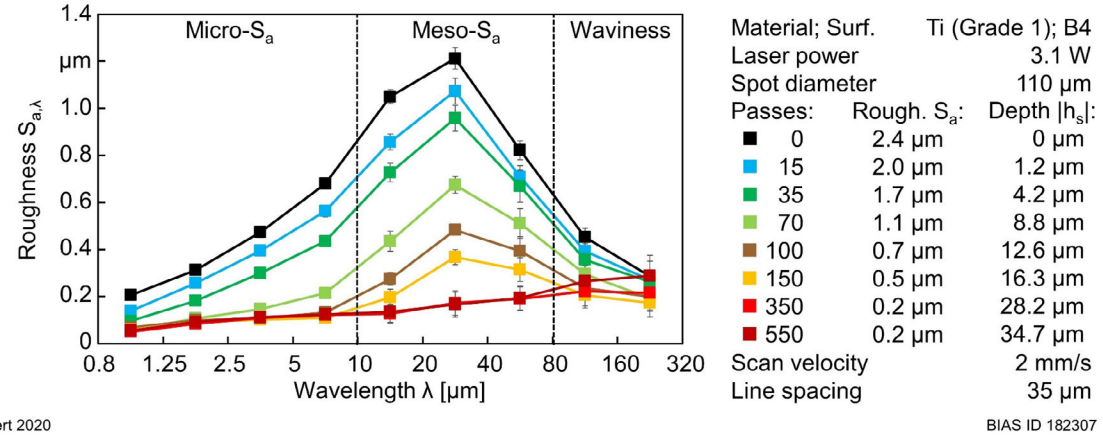

Figure 5.48: Roughness spectra of sample B4 after different numbers of passes.

Second, the mesoroughness decreased to 0.4 µm after 100 passes and to 0.14 µm after 350 passes. The roughness was not further improved by further processing (dark red curve). Considering the previous observations, surface features with a lateral dimension in the microroughness regime were removed significantly faster at the beginning of the polishing process. By contrast, remaining surface features with a lateral dimension in the mesoroughness regime were further smoothed at a later stage of the process. These remaining surface features were mainly valleys, as shown in the reflected-light images

(**Figure 5.43**). Valleys are smoothed by being levelled into the receding surface. The smoothing process seems to have only an insignificant influence on surface features with a lateral dimension in the waviness regime.

The experimental results showed that at the beginning of the process (first 100 passes) the smoothing is caused by a higher material removal rate of elevated surface parts (mostly microroughness) compared with depressed parts (mesoroughness). Once the microroughness is removed, surface roughness is further improved by reduction of the mesoroughness.

6 Fundamental Process Parameters

Exposure time and thermal load

As presented in Section 2.5, it is often advantageous and desired to describe the influence of a machining process on the material modification by more general variables such as intensity, temperature distribution, etc. Previous studies on LCM have shown a correlation between the removal geometry and the temperature distribution [Mes17]. In contrast, LCP leverages spatial and temporal averaging because each part of the surface is irradiated multiple times and exposed to varying thermal loads. In Section 4.6 it was proposed to describe the thermal impact during LCP by using the averaged variables of the thermal load T_L and exposure time t_r, according to Equation (4.7) and Equation (4.4). The aim of the following discussion is to test the first research hypothesis, that the material modification can be described by these more fundamental parameters.

The exposure time describes the duration over which each surface part was in average illuminated after multiple passes. For line cavities (Section 5.1.3) with a minimum line spacing of $b = d_f$, Equation (4.2) can be simplified to $t_r = (\pi/4) \cdot (d_f/v) \cdot N$. This describes the duration required for the laser spot to traverse distance d_f. **Figure 6.1** shows the removal depth as a function of the average exposure time for the results presented in **Figure 5.10**. Line cavities structured with increasing scan velocities reach the same depths as those structured under slower velocities when the number of passes is increased proportionally. The linear correlation after hundreds of passes shows, first, that the material removal is little influenced by changes in cavity geometry, and second, that mass transport limitations, such as saturation, do not decrease the material removal rate with increasing depth.

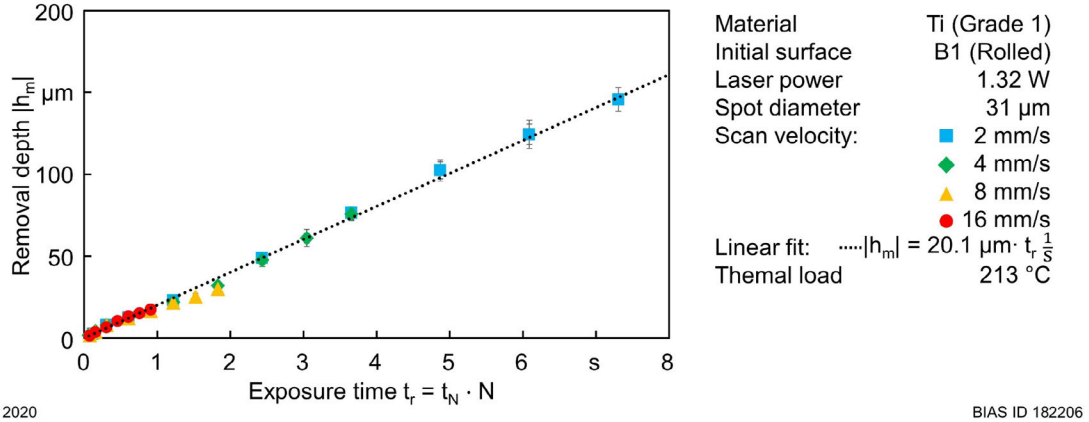

Figure 6.1: Removal depth as a function of exposure time t_r for different scan velocities.

Figure 6.2 shows the roughness results presented in **Figure 5.25** as a function of the exposure time. Scan velocities of up to 200 mm/s and up to 100,000 passes were

investigated. As before, only the effective duration of the active chemical reaction appears relevant to the decrease in roughness. The number of passes must be increased in proportion to the scan velocity in order to achieve similar surface finishes.

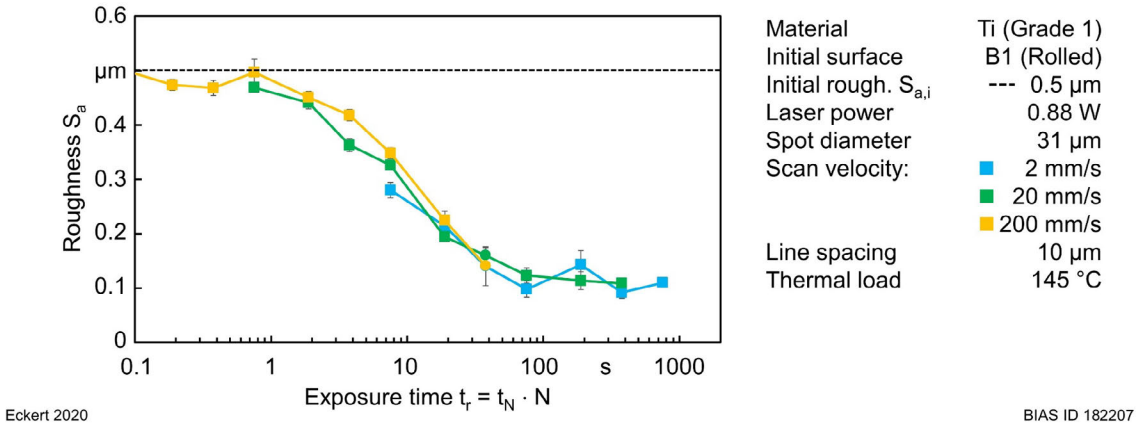

Figure 6.2: Roughness S_a as a function of exposure time for three selected scan velocities.

The influence of the process parameters on the material removal rate and quality can be generalized based on the thermal load. **Figure 6.3** shows the maximum removal velocity (cavity center depth h_c divided by the exposure time t_r) as a function of thermal load for the results presented in **Figure 5.5**. Regardless of the spot diameter and laser power, the removal velocity shows an approximately linear increase with increasing thermal load, until the removal velocity drops abruptly at a characteristic thermal load threshold $T_{th,dist} \approx 190$ °C. At this threshold, disturbances occur in the cavity center, caused by emerging gas [Meh13] or material deposition (**Figure 5.2**). The x-intercept of the linear regression (dotted line) determines the thermal threshold $T_{th} = 111$ °C that defines the onset of laser-induced thermochemical material removal.

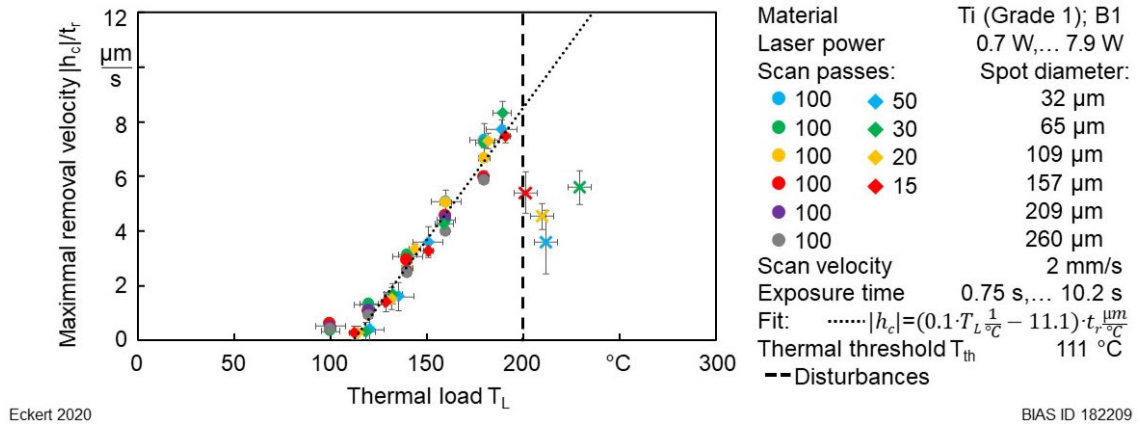

Figure 6.3: Removal velocity as a function of thermal load T_L for six different spot diameters.

This threshold is related to the activation energy $E_a = R \cdot T_{th}$ of the chemical reaction according to the Arrhenius Equation (7.10), although that equation describes the reaction rate as related to an exponential decrease in the temperature and thereby has no real

"starting point" except absolute zero temperature. From the Arrhenius plot for the LCP system, the thermal threshold is the temperature at which the average material removal velocity is 0.2 µm/s, as shown in Appendix A.4. The activation energy of the laser-induced thermochemical material removal investigated here was determined to be 55.7 kJ/mol, which is in the typical range between 20 kJ/mol and 80 kJ/mol observed for most chemical reactions [Job11], although this value is specific to the material-electrolyte combination and must be determined empirically. However, in the interval between the upper and lower thermal limit, a surface finish of high quality and low roughness is achievable.

Although the removal velocity does not depend on the spot diameter, the absolute depth per single scan pass is deeper as the spot diameter increases. **Figure 6.4** illustrates this relationship, with a larger spot diameter exposing the surface along the scanned line for a longer period of time during each scan. Although the three cavities were structured in the same overall processing time, the cavity depth increases with the spot diameter, and the cavity width also increases significantly. Because polishing depends on the removal depth, the process generally becomes faster with larger spot diameters.

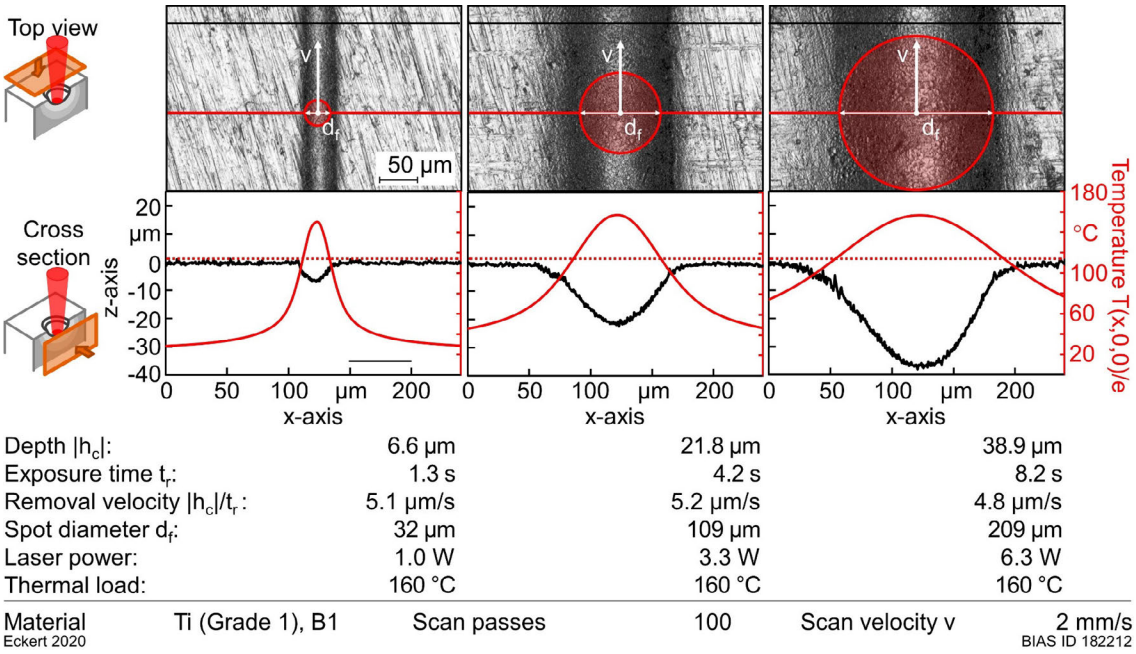

Figure 6.4: Influence of temperature distribution on the cavity depth for three different spot diameters.

Figure 6.5 shows the cavity width w_c as a function of thermal load for the results presented in **Figure 5.6**. Although the cavity width slightly increased with the thermal load, the width was mostly governed by the spot diameter. Thus, increased width can be understood by considering the laser-induced temperature distribution.

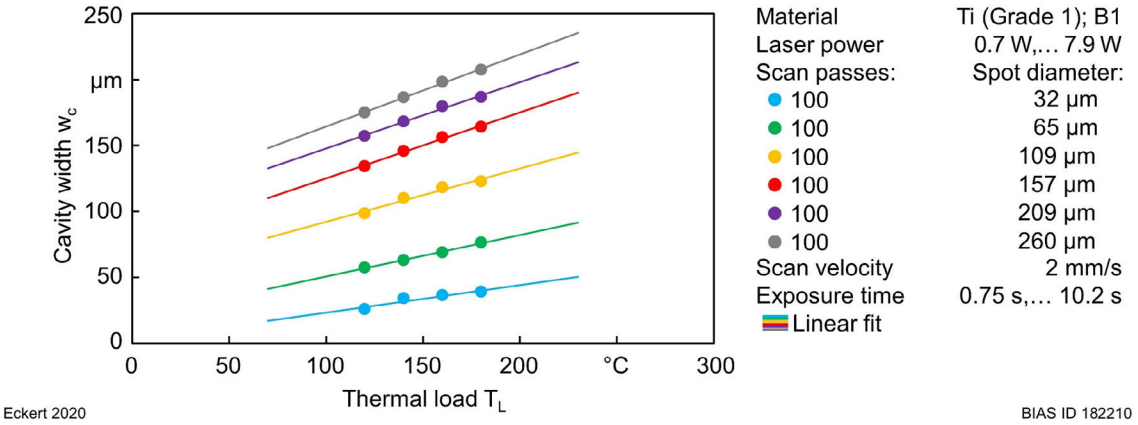

Figure 6.5: Line cavity width as a function of thermal load for different spot diameters.

Figure 6.6 shows the temperature distribution $T(x,0,0)/e$ and the temperature gradient $\partial T(x,0,0)/\partial x/e$ along the x-axis as numerically calculated by Equation (A.10) for the laser parameters shown in **Figure 6.5**. The blue lines show the temperature distribution for a spot diameter of 32 µm and increasing laser power, and accordingly increased thermal load. With increasing laser power, the center temperature increases, and the distribution slightly widens. This explains the observed increase in removal depth (**Figure 6.3**) and slight increase in the cavity width (**Figure 6.5**). The rest of the lines show the temperature distribution for a constant thermal load of 180°C and increasing spot diameters, which increased the width of the temperature distribution in approximate proportion.

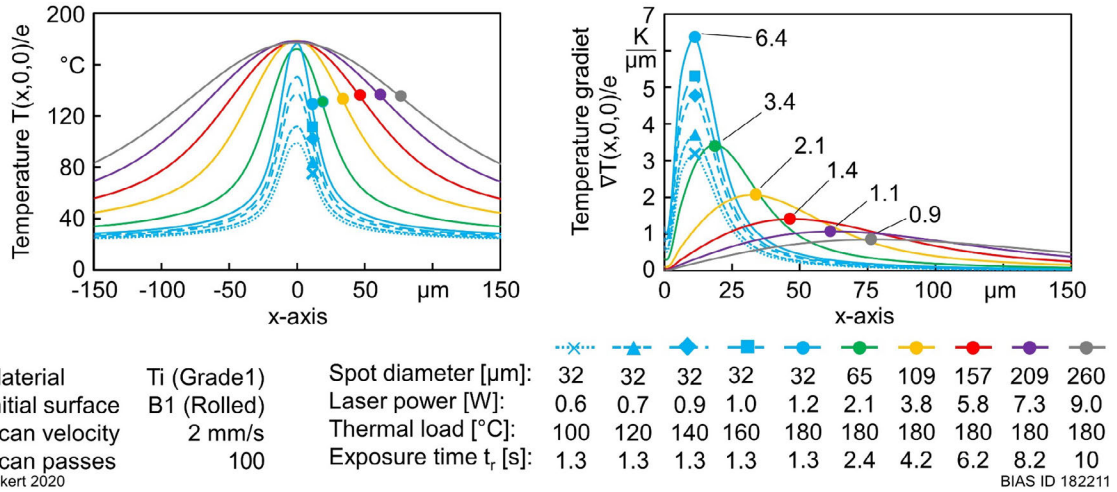

Figure 6.6: Laser-induced temperature distribution and temperature gradient along the x-axis for different laser powers and spot diameters.

This analysis explains the observed step-wise increase in the cavity width apparent in **Figure 6.5** along with the constant depth removal rate shown in **Figure 6.3**. The figure also shows that the maximum temperature gradient was reduced for larger spot diameters. Because the product of the maximum temperature gradient and the average exposure time is almost constant, at approximately 8.6 (K·s)/m, and the removal depth increases in proportion to the spot diameter (**Figure 6.4**), the findings of this analysis support the first

hypothesis that guided this research: that thermochemical material removal can be described by the fundamental parameters of the laser-induced thermal load and the average exposure time.

Figure 6.7 qualitatively compares the induced temperature distribution along the *x*-axis with cross-sections of the surface-height profiles for three line spacings. Without line overlap ($u < 0$ %), single line cavities are structured. Small lateral overlaps ($u \leq 30$ %) result in an inhomogeneous wavy surface finish, as more material is removed from the cavity centers compared with the periphery. Lateral overlaps ($u \geq 66$ %) achieve uniform polishing because the influence of the nonuniform temperature distribution is averaged under this condition. In such cases, the averaged value of the thermal load T_L is sufficient to describe the expected polishing characteristics.

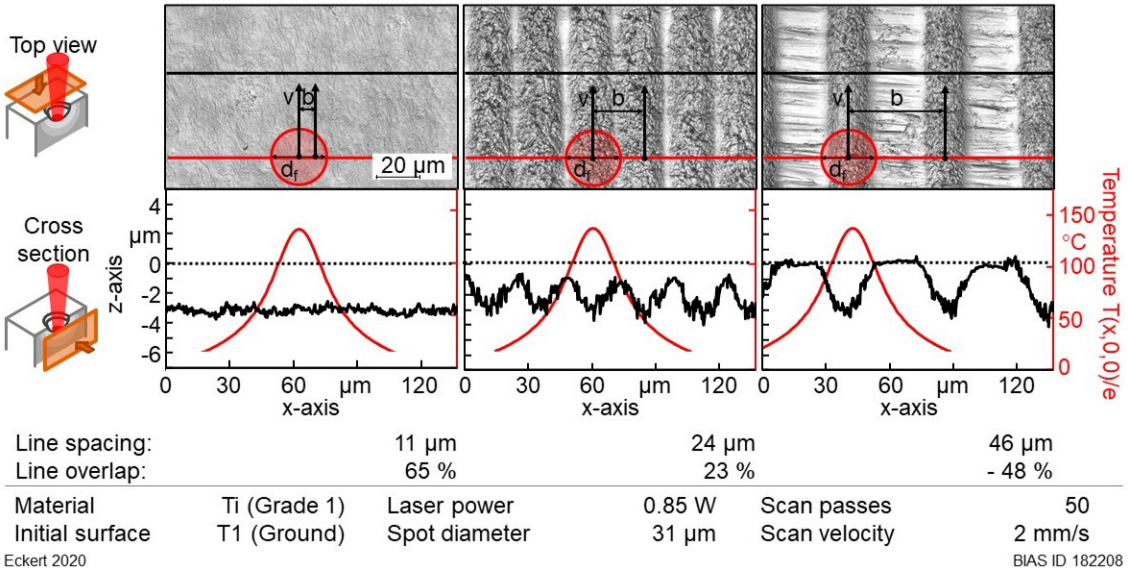

Figure 6.7: Influence of temperature distribution on the surface finish for three line spacings.

Formalism for multicycle process signatures

The concept of process signatures outlined in Section 2.5 aims to describe the modification M as a function of the material load L according to Equation (2.2). The experimental results described in Chapter 5 indicated correlations of type A (**Figure 2.11**) between material modifications and the process parameters. Changes in material removal, chemical composition, porosity and roughness were identified as material modifications. In accord with the previous section, the laser-induced thermal load and exposure time were confirmed to be the main internal material loads. Applied to LCP in terms of roughness and thermal load, Equation (2.2) appears as:

$$M_{Sa} = f_{Sa}(T_L, t_N) \tag{6.1}$$

where M_{Sa} is the modification in roughness after one scan pass and f_{Sa} is the constituting functional relation. The modification M_{Sa} is generally very small because of the short exposure time $t_N \ll 1$ s and material removal rates of several µm/s. For this reason, polishing requires multiple scan passes N. The N-fold modification $\widetilde{M}_{Sa}$ is an N-fold composition of the functions f_{Sa}, as follows.

$$\widetilde{M}_{Sa} = \underbrace{f_{Sa}(T_L, t_N) \cdot f_{Sa}(T_L, t_N) \cdot \ldots \cdot f_{Sa}(T_L, t_N)}_{N\ times} = f_{Sa}(T_L, t_N)^N \tag{6.2}$$

$$= f_{Sa}(T_L, t_N \cdot N) = f_{Sa}(T_L, t_r) \tag{6.3}$$

Equation (6.2) can be transformed to Equation (6.3) as long as f_{Sa} is a power function. The N-fold modification $\widetilde{M}_{Sa}$ ultimately resembles the single-pass modification M_{Sa}, but with an N-fold exposure time $t_r = t_N \cdot N$. By differentiating Equation (6.2) with respect to N [Bro01], one obtains the following ordinary differential equation for the multipass correlation:

$$\frac{d\widetilde{M}_{Sa}}{dN} = \underbrace{ln\big(f_{Sa}(T_L, t_N)\big)}_{:= c} \cdot \underbrace{f_{Sa}(T_L, t_N)^N}_{= \widetilde{M}_{Sa}} = c \cdot \widetilde{M}_{Sa} \tag{6.4}$$

This ordinary differential equation is solved by any exponential function of the form

$$\widetilde{M}_{Sa} = a \cdot e^{-c \cdot N} + b \tag{6.5}$$

as can be readily recognized by taking the derivation with respect to the number of passes N.

Conclusion

The results showed, in accordance with the first hypothesis, that the average exposure time and thermal load, which are expressed by Equation (4.4) and Equation (4.7), can be used as fundamental variables to describe the material removal in a multipass LCM process. The material removal velocity was shown to be independent of the spot diameter or scan velocity. Material removal starts at a characteristic thermal threshold T_{th}, which is defined by a visible material removal within the irradiation time. Thermal loads above the disturbance threshold lead to an abruptly drops of the removal velocity.

7 Mechanisms and Model of Polishing

Extended thermobattery approach

Chapter 2 described previous studies on LCM that focused on reliably shaping metallic microparts of prescribed tolerance and quality, and Section 2.3 summarized how the laser-induced material dissolution can be explained within the framework of the thermobattery model. To date, the surface roughness produced by LCM and its application as a micropolishing process has not been reported elsewhere. In this work, the experiments described in Section 5.2 identified process conditions and suitable scan trajectories for achieving a uniformly polished surface. From the results reported in Section 5.4, smoothing is evidently the result of a higher removal rate of roughness peaks compared to valleys. The physical and chemical mechanisms that govern the smoothing process are currently unknown.

Therefore, this chapter will show that LCP can be explained by means of geometric levelling. First, chemical, thermal, electric and fluid mechanical aspects of the roughness and levelling will be discussed within the framework of the thermobattery approach, focusing on how the thermobattery conditions might influence roughness peaks and valleys in different ways. Second, laser-induced thermochemical smoothing can be described by a model based on geometric levelling according to Equation (2.16). Third, a model of an ideal thermal-based smoothing process will be presented. A formula will be derived for the decrease of the average roughness S_a as a function of time, roughness parameters, material properties, and the thermal impact of the laser radiation.

Figure 7.1 illustrates the laser-induced thermobattery, as described in Section 2.3.1, on an ideal sine-wave profile of wavelength λ and amplitude ψ. The laser-induced temperature shifts the corrosion potential in the center of the irradiated spot and generates a local electric cell with an anodic zone inside and a cathodic zone outside the radiated area. A temperature increase of approximately 100 K can generate a potential difference of 0.5 V and cause material dissolution in the center. Although this voltage is very small, the electric field strengths are very high because of the small dimensions of the battery [Bäu11]. In order to maintain charge neutrality, the current within the solution (positive ion) must flow towards the periphery, and within the metal towards the center.

The material dissolution is therefore influenced by the laser-induced temperature, the subsequently generated electric potential and the concentration of reactants near the surface. Thus, differences in the dissolution rates of surface features such as peaks and valleys are governed by thermal conduction, electric conduction and diffusion. In

addition, the exchange of electrolyte and reactants is influenced by laser-induced convective flows or external flow dynamics.

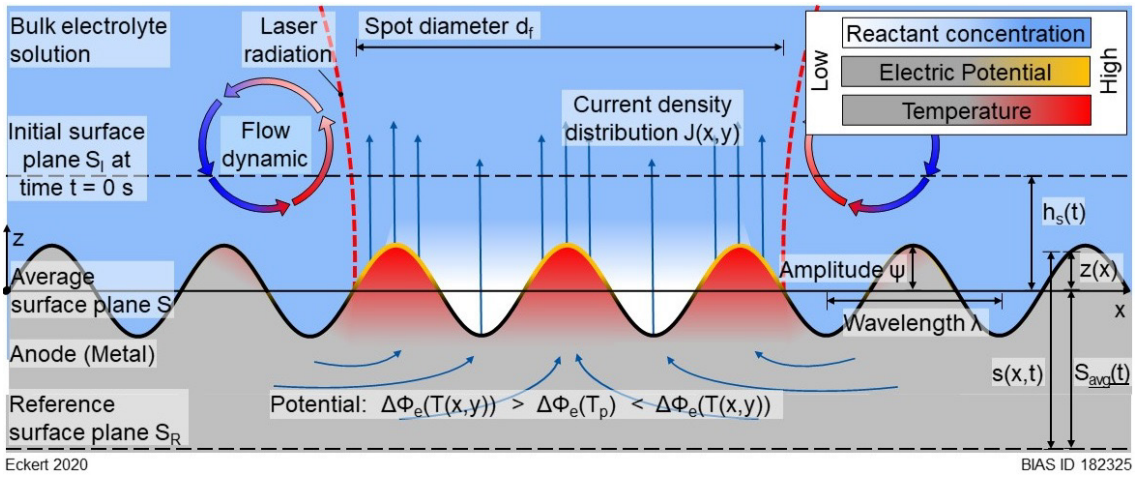

Figure 7.1: Illustration of the thermobattery model augmented with roughness-related aspects.

In the following, thermal conduction, electric conduction, and diffusion are assumed to proceed independently of each other. If the dimensions λ and ψ are much smaller than the spot diameter d_f, the induced temperature T, electric potential Φ and reactant concentration c are approximately constant within the spot area in the x- and y-directions. Furthermore, if convective flows and forced flow dynamics are neglected and stationary conditions given, the boundary value problem of geometric levelling described in Section 2.2.4 can be applied inside the spot area according to:

$$\begin{matrix} T = T_0 \\ \Phi = \Phi_0 \\ c = 0 \end{matrix} \qquad \text{at} \qquad z = \psi \sin\left(\frac{2\pi x}{\lambda}\right) \tag{7.1}$$

In order to determine T, Φ or c, the heat, Laplace's, or diffusion equation must be solved. Thus, Wagner's approach holds inside the spot area and we can apply his particular solution for the concentration (Equation (2.4)) and the formulas derived from it to describe smoothing during LCP [Wag54]. Therefore, the amplitude ψ is expected to decrease exponentially as a function of the distance $h_s(t)$ of the receding average surface plane S from the initial surface plane S_I (material removal depth) and wavelength, according to Equation (2.16). A direct consequence of these considerations is that microroughness must disappear faster than meso- or macroroughness. This result is observed for LCP as summarized in **Figure 7.2** by (a) reflected-light images, (b) removal depth and (c) relative roughness $(S_a - S_{a,f})/\Delta S_a$. Removing the microroughness significantly brightens the surface, similar to anodic brightening as described in Section 2.2.5 for electropolishing. The remaining valleys, which contribute to the mesoroughness, are then further planed into the receding average surface plane S. The resulting surface finish reveals the distinct crystal planes of the titanium microstructure.

In electropolishing, the occurrence of distinct etching patterns indicates material dissolution in the active or transpassive regime in the absence of transport limitation.

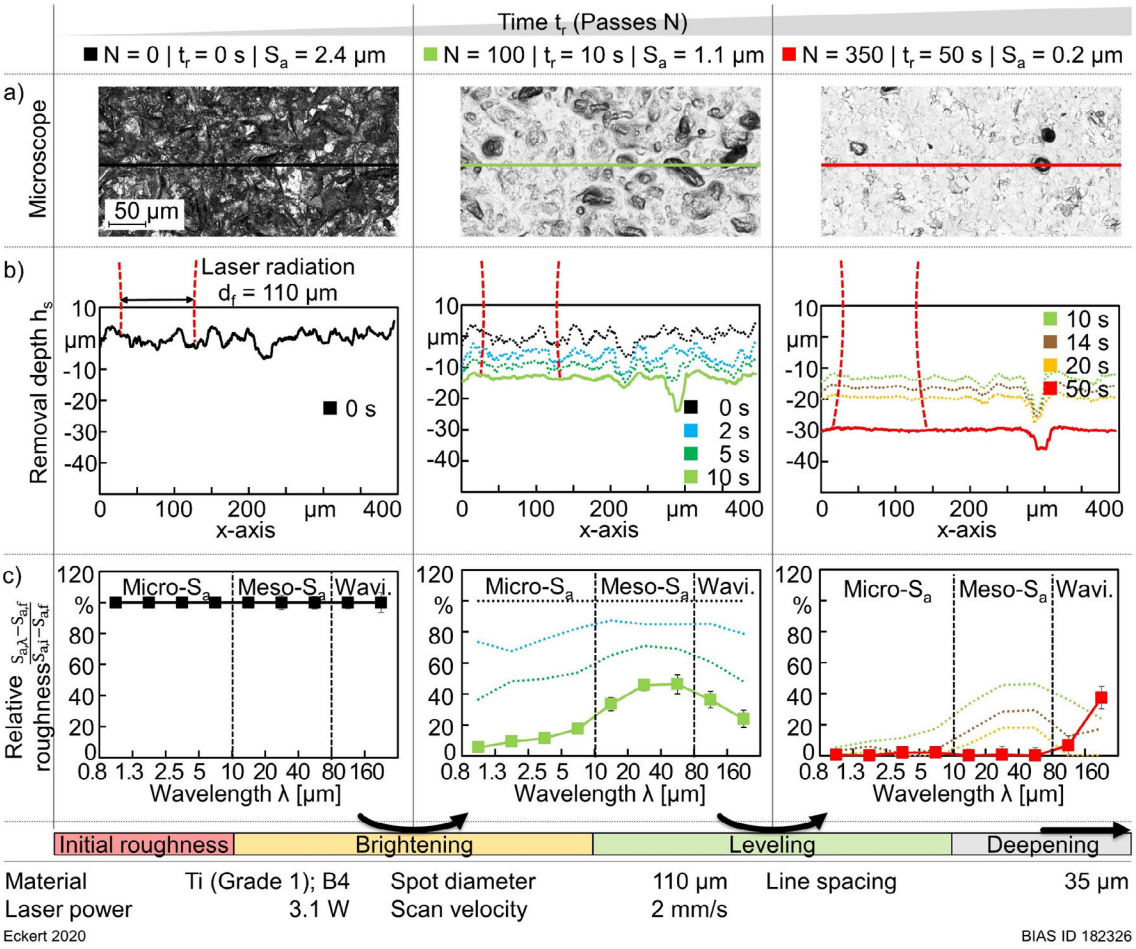

Figure 7.2: (a) Reflected-light images, (b) surface-height profiles and (c) relative roughness after multiple passes.

Polishing effects can be categorized as follows.

1. *Brightening*: Sharp peaks with heights of more than 4 µm and lateral dimensions between 1 µm and 10 µm (micro-S_a) are reduced down to 5 % of their initial value. The surface finish is visually brightened, but more than 40 % of the initial mesoroughness remains.
2. *Leveling*: The remaining valleys with depths of up to 8 µm and lateral dimensions between 10 µm and 80 µm (meso-S_a) are planed into the continuous receding surface plane. This leads to an even and uniform surface finish. The roughness is reduced by more than 95 % at all wavelengths except for $\lambda > 160$ µm.
3. *Deepening*: The surface is leveled without any further improvement in roughness.

Polishing is a continuous process with steady transitions between these three regimes. To test whether the geometric levelling model provides a suitable description of these

processes, the following section analyzes the surface-height data acquired during LCP in comparison to the predictions of geometric levelling according to Equation (2.16).

Polishing by geometric levelling

Two-dimensional Fourier analysis is used in order to test if the observed polishing kinetics from Section 5.4 is subjected to geometric levelling as described in Section 2.2.4. The mathematical procedure is similar to models presented by Stout [Sto00] or Vadali for pulsed laser micropolishing [Vad12]. Equation (2.16) describes geometric levelling as an exponential decay of one particular amplitude ψ and spatial frequency $f = 1/\lambda$ as a function of the average removal depth h_s, regardless of any process parameters. Geometric levelling in the formulation of Equation (2.16) is independent of the process parameters, because a change of the process parameters always affects both the smoothing of the roughness and deepening of the average surface plane (material removal depth).

The levelling of any arbitrary surface topography can be generalized by applying Equation (2.16) to each spatial Fourier component. Therefore, the initial surface-height data must be Fourier-transformed to the frequency domain. This transforms the primary height data $s(x,y)$ into discrete spatial Fourier components of spatial frequencies f and amplitudes $|\psi^*(f_x,f_y)|$:

$$s(x,y) \xrightarrow{FFT} \psi^*(f_x,f_y) \tag{7.2}$$

The levelling of any surface is achieved by the geometric levelling of all its amplitudes, according to:

$$\psi^*(f_x,f_y) = \psi_0^*(f_x,f_y) \cdot e^{-2\pi \cdot \sqrt{f_x^2+f_y^2} \cdot h_s} \tag{7.3}$$

Figure 7.3 shows representative initial surface-height data from Section 5.4 and the corresponding Fourier components in a two-dimensional visualisation of the initial amplitudes $|\psi_0^*(f_x,f_y)|$, as well as the amplitudes $|\psi_0^*(f_x,0)|$ and $|\psi_0^*(0,f_y)|$ along the positive f_x- and f_y-directions. Spatial frequencies $f = 1/\lambda$ above 100 mm^{-1} correspond to wavelengths smaller than 10 µm, and thus to the microroughness regime. Frequencies between 12.5 mm^{-1} and 100 mm^{-1} correspond to the mesoroughness regime, and those below 12.5 mm^{-1} correspond to the waviness regime. In the following, only the positive quadrant of the two-dimensional spectral analysis is shown because the negative spatial frequencies are only computationally significant [Vad12]. From a technical perspective, Equation (7.3) applies a point-symmetrical spatial low-pass filtering process to the initial amplitude distribution $|\psi_0^*(f_x,f_y)|$.

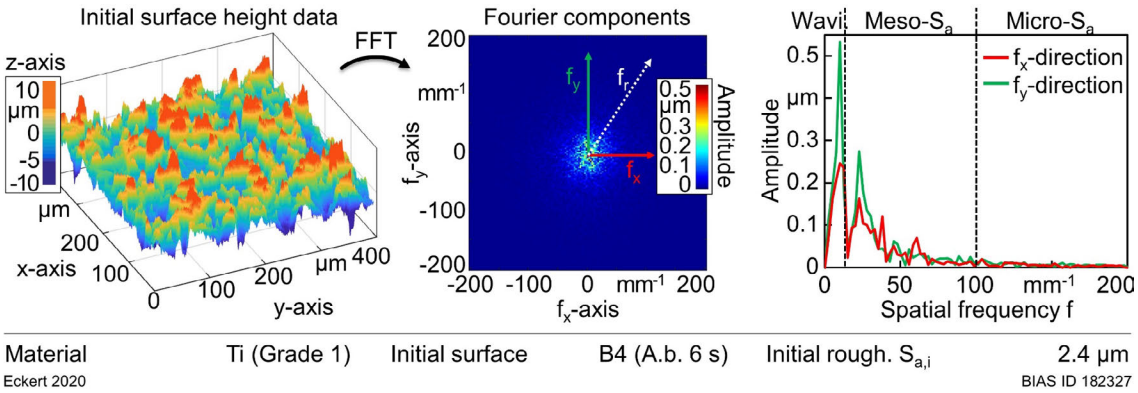

Figure 7.3: Surface-height data, two-dimensional amplitude distribution of the spatial Fourier components and amplitudes in the f_x- and f_y-directions of the initial surface topography data presented in Section 5.4.

Figure 7.4 shows the transmission characteristic of the two-dimensional spatial filter as a function of the spatial frequencies and the corresponding projection along the f_x-direction (straight red line) for a material removal depth of $h_s = 2$ µm. The filter describes the transmission as a two-dimensional exponential decay of f_x and f_y. The contour lines in **Figure 7.4a** mark spatial frequencies of equal transmission separated by increments of 10 %. **Figure 7.4b** projects the transmission for material removal depths of 1, 5 and 40 µm. The projections show that 5 µm of material removal reduces the microroughness by over 95 % and 40 µm of material removal reduces the microroughness and the mesoroughness by over 95 %. In comparison, pulsed laser micropolishing can be described by a Gaussian-like low-pass filter in which higher percentages of low spatial frequencies are transmitted [Vad12].

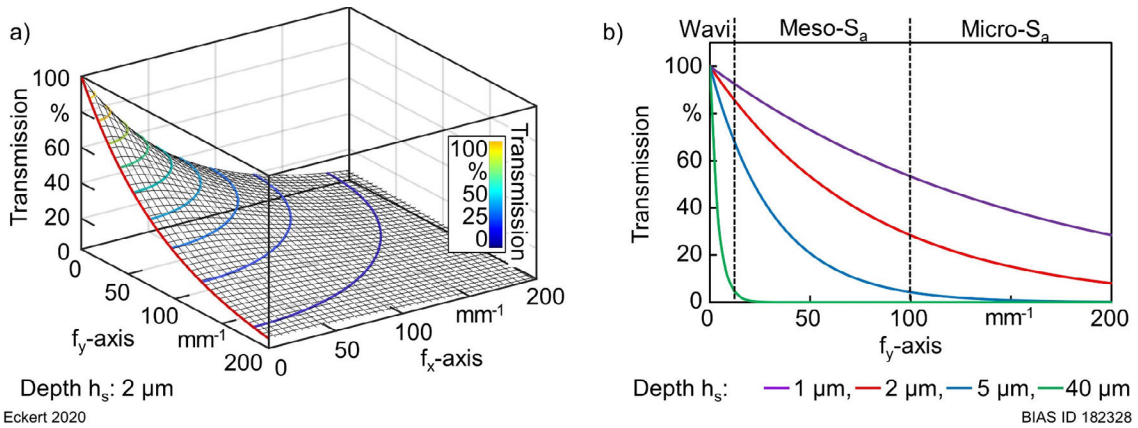

Figure 7.4: Visualization of the two-dimensional low-pass filter described in Equation (7.3) for positive spatial frequencies and the corresponding projection onto the vertical plane along the f_x-direction for different removal depths h_s.

Applying Equation (7.3) to the initial amplitudes $|\psi_0^*(f_x,f_y)|$ gives the predicted spatial frequency content of the surface after the levelling of h_s. Subsequent inverse Fourier transformation of the predicted spatial frequencies yields the corresponding predicted surface-height data. **Figure 7.5** shows the predicted height data and distribution after

material removal of 4.2, 8.8, 16.3 and 28.2 µm, in direct comparison to the measured data shown in **Figure 5.46**. The figure clearly shows the close agreement between the measurement and prediction. The surface-height data can be characterized using any roughness parameter according to ISO 27178 [ISO12]. Here, the average roughness S_a was calculated from the predicted data, which yielded roughness reductions from an initial value of 2.45 µm to 1.34, 0.87, 0.52 and 0.27 µm, respective of the material removal amounts listed above. These values correspond to the measurement data within an error of ~10 %.

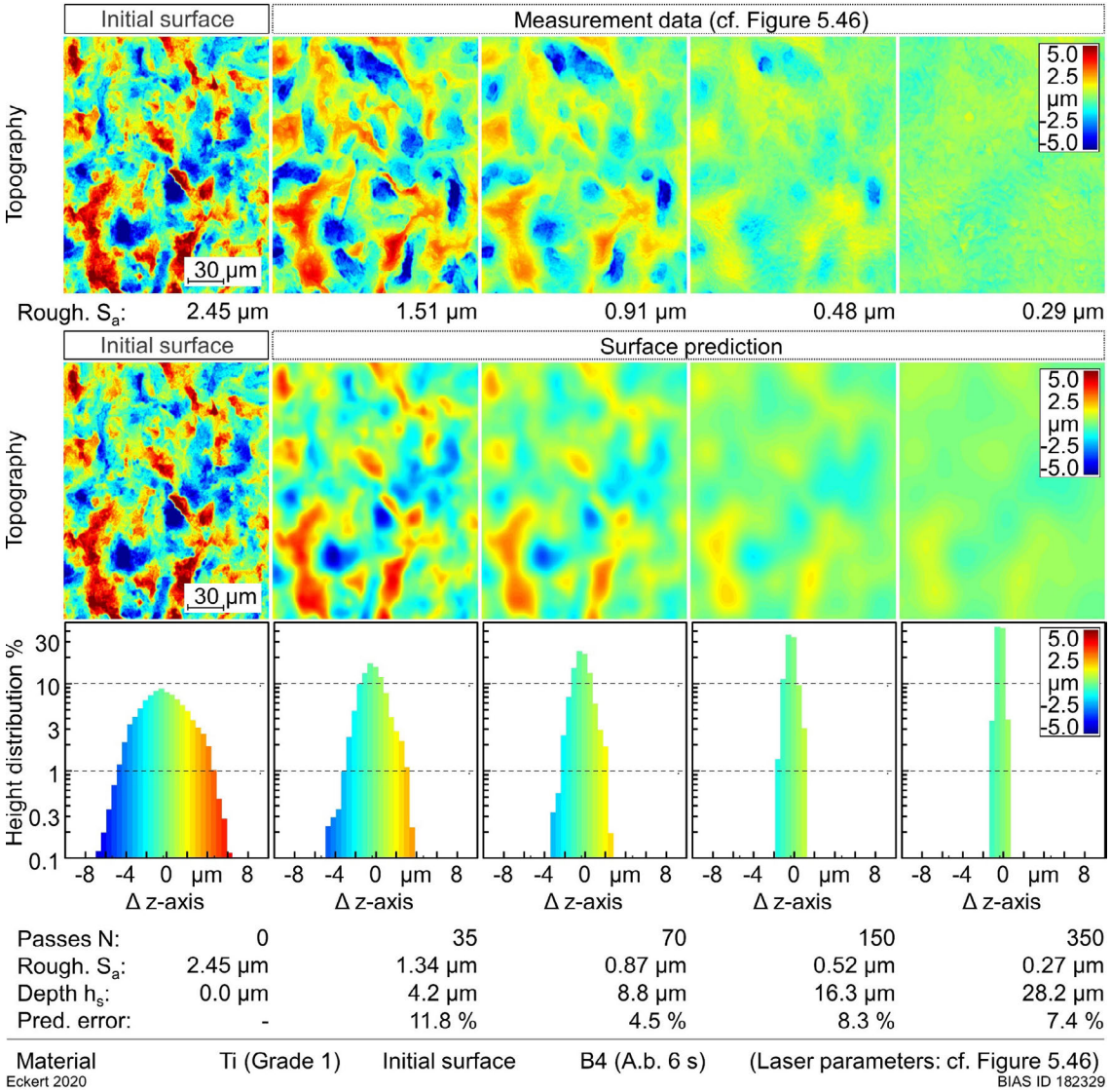

Figure 7.5: Comparision of the measured (Figure 5.46) and predicted surface-height data and the predicted height distributions for various removal depths.

Figure 7.6 shows the measured roughness S_a from **Figure 5.45** as a function of removal depth and the corresponding predicted surface roughness (red line). The experimental and predicted data are consistent within the measurement accuracy. The average roughness of the initially abrasive-blasted surface (B4) decreased exponentially as a function of the

removal depth. The presented prediction methodology confirms that the surface finish and roughness S_a during LCP can be predicted by geometric levelling of the initial Fourier components.

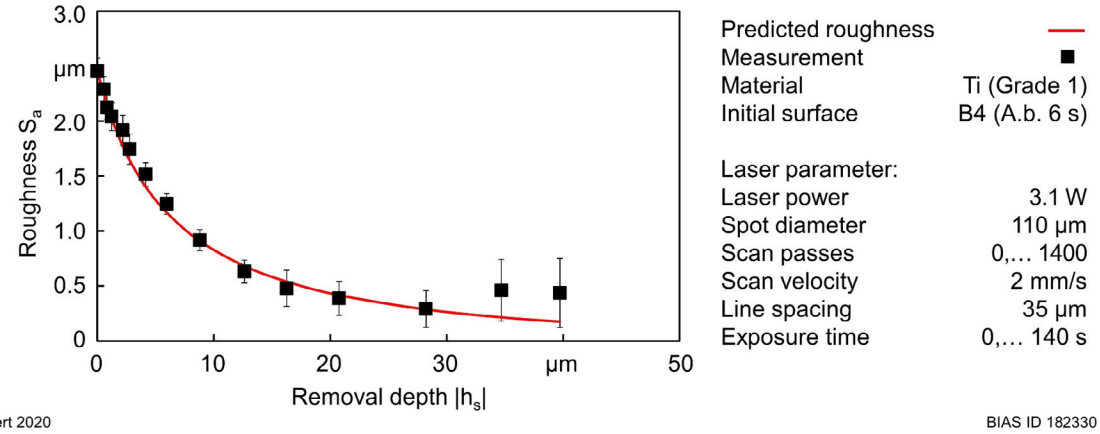

Figure 7.6: Average roughness as a function of the removal depth (measurement data from Figure 5.45) and the corresponding predicted roughness.

The faster removal of microroughness compared to mesoroughness and waviness is also accurately predicted, as shown by the roughness spectra of the predicted surfaces in **Figure 7.7**. The predicted microroughness decreased from an initial value of 0.68 µm to almost 0.06 µm after 8.8 µm of material removal, and the maximum predicted mesoroughness decreased from 1.21 µm to 0.55 µm, and further down to 0.05 µm after 28.2 µm of material removal. However, in contrast to the experimental data shown in **Figure 5.48**, the predicted spectral roughness approaches zero for large removal depths. Thus, the geometric levelling approach does not predict the experimentally observed stable lower limit of the roughness of the surface finish with ever-increasing removal depths, because the approach does not consider effects such as anisotropic etching, which fundamentally limit the surface finish.

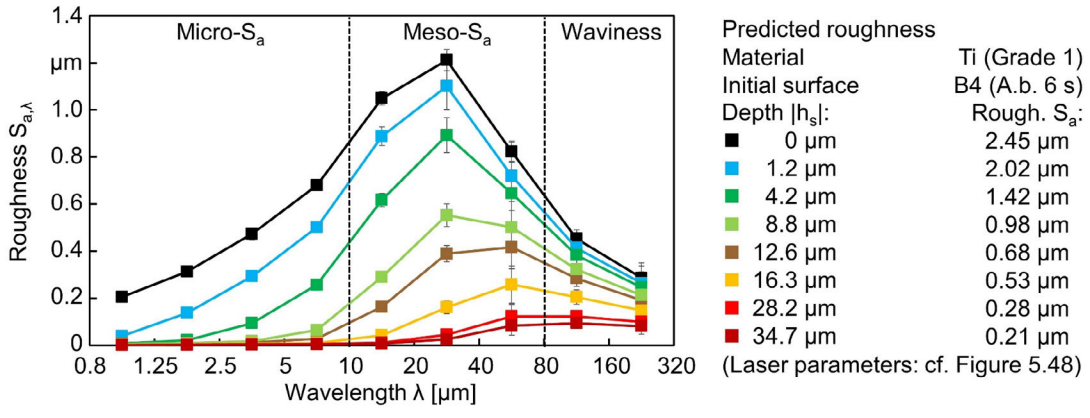

Figure 7.7: Predicted roughness spectra for different removal depths (cf. Figure 5.48).

Appendix A.3 shows additional surface finish predictions for the initial rolled material (B1) (**Figure A.8**), as well as the ground (T1) (**Figure A.10**) and abrasive-blasted (B2) (**Figure A.12**) surfaces. These data validate the application of the spatial Fourier filtering methodology to predicting surface-height data, average roughness and roughness spectra for different initial topographies under LCP. Laser spot diameters of 31, 110 and 336 µm, with corresponding laser powers of 1.05, 2.46 and 10.2 W were used. The predicted results match the experimental measurements in most cases with accuracies of more than 90 %. The presented prediction methodology is based on the assumption that the smoothing process is governed by geometric levelling according to Equation (2.16), and therefore the validation shows that the mechanism of geometric levelling governs the polishing process, which confirms the second research hypothesis. This finding is independent of the driving force that causes geometric levelling, whether it is thermal conduction, electric conduction or diffusion. However, under certain process conditions, other mechanisms can dominate the smoothing and lead to different results, as discussed in the following section.

Electrochemical and fluid mechanical aspects

As mentioned in Section 2.2.5, the best surface qualities achieved by electropolishing occur by anodic levelling in the passive regime under transport limitation. Under these conditions, the diffusion layer (typically between 1 µm and 100 µm thickness) is understood to suppress anisotropic etching effects caused by the orientations of the lattice plane, material phases, pitting corrosion or fluid-mechanically induced inhomogeneities [Lan87]. Conversely, the appearance of anisotropic etching indicates that the diffusion layer is very thin and unable to suppress those effects. The effective thickness δ_c of the diffusion layer is generally strongly influenced by the local flow conditions. If δ_c is smaller than or in the order of the dimensions ψ and λ, the boundary value problem for the concentration according to Equation (2.1) and Equation (2.2) no longer applies. Thus, geometric levelling cannot be caused by local concentration differences.

Furthermore, although Wagner mathematically compared the diffusion equation and Laplace's equation (see Section 2.2.4), he concluded that because of polarization, the effective potential gradient must be more uniform than calculated and thus cannot cause geometric levelling in electropolishing processes [Wag51]. However, LCP presents a different processing environment because the small dimensions of the thermobattery can be expected to cause strong electric fields [Bäu11], and the laser radiation induces strong local convective flow dynamics. The induced electric field strengths may be strong enough to locally break the passive film and polarization, and the material removal would then occur in the transpassive regime, where three general types of dissolution behavior can be observed: First, uniform transpassive dissolution at potentials below that of oxygen

formation, second, localized dissolution by pitting, and third, high-rate transpassive dissolution above the potential of oxygen formation [Lan07].

The following results and considerations indicate that material dissolution during LCP occurs in the active or transpassive regime rather than under mass transport limitations.

First, the effective thickness δ_c of the diffusion layer during LCP is considered to be thin compared to the average roughness. This assertion is supported by the following experimental results. **Figure 5.25** showed that polishing can be achieved with scan velocities of 2, 20 or 200 mm/s after a proportionally increased number of passes and appropriate adjustments of the time lapse between passes. For example, with a spot diameter of 31 µm, a scan velocity of 20 mm/s and a polishing area of 1 mm^2, polishing was achieved with a 5 s lapse between scan passes. On average, the laser radiation exposes each part of the surface for only 1.2 ms (Equation (4.4)), and with a typical material removal velocity of 5 µm/s (**Figure 5.1**), the average surface plane would deepen by only 6 nm on each scan pass, such that dozens to hundreds of scan passes are necessary to achieve the removal depth required for polishing. Based on these results, the time lapse between scans is considered to allow the electrolyte to exchange completely because the concentration of reactants will decrease rapidly to the bulk level of the electrolyte. Since the removed material of 6 nm is much smaller than the average roughness of 0.5 µm, the diffusion layer thickness δ_c is expected to be smaller than the dimension of the roughness S_a and of the amplitude ψ. The necessary assumption $\delta_c \gg \psi$ for the derivation of Equation (2.16) is violated (see Section 2.2.4). Thus, the observed geometric levelling cannot be based on local differences in concentration.

Second, the fluid dynamics in the interaction zone may inhibit stable layer formation. The fluid dynamics are influenced by the external electrolyte flow (with a velocity of v_f = 2 m/s), laser-induced convective currents and emerging gas bubbles. The electrolyte flushing reduces or suppresses layer formation, thereby permitting anisotropic etching patterns on the microstructure. For example, the etching pattern on titanium reveals distinct crystal (hexagonal close-packed) planes [Lan87] of random orientation, as shown in **Figure 5.38**. This is a typical result for a surface finish produced by uniform active or transpassive dissolution. Therefore, LCP is expected to insufficiently suppress inhomogeneous etching, which fundamentally limits the surface quality as shown in Section 5.3.3.

Third, **Figure 7.8b** magnifies the surface finish shown in **Figure 5.17**, which was covered with small nanoporous cavities. The cavity structure appeared above a certain laser power and increased the microroughness. Such structures are interpreted as pitting corrosion, which occurs at the transition from uniform to localized material dissolution under higher laser powers. The structures originate at local defects with increased absorptance, which

in turn increases the induced thermal load and leads to further pitting corrosion. This feedback effect results in the entire surface becoming covered with nanoporous cavities. Pitting occurs in the transpassive regime, above U_b, by localized dissolution due to the breakdown of the passive layer [Lan07]. The formation of pitting is intensified by the presence of certain anions [Fra98], increased gas formation and high temperatures.

Finally, alloys show inhomogeneous material dissolution of individual phase components. **Figure 7.8a** magnifies the discontinuities at grain and phase boundaries in the Ti6Al4V profile line observed in **Figure 5.38**. These discontinuities occur under material dissolution in the transpassive regime governed by inhomogeneous crystallographic factors, as observed during electrochemical machining [Klo16].

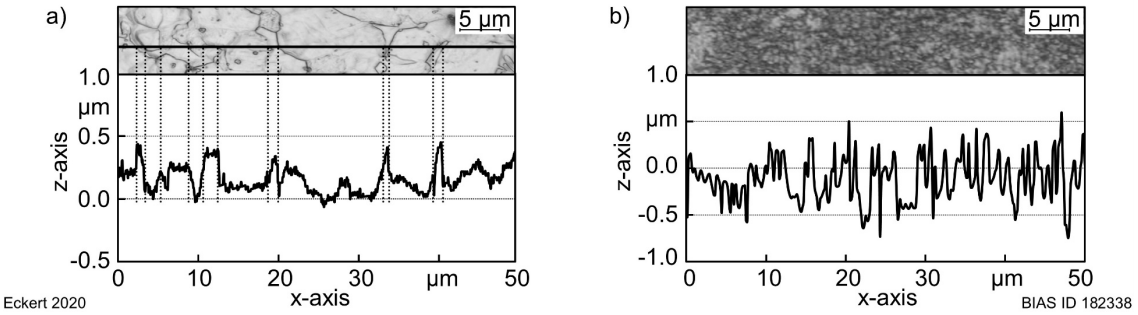

Figure 7.8: Surface finishes limited by (a) inhomogenous material dissolution and (b) pitting corrosion.

Thus, none of the experimental observations indicate a decisive influence of the concentration gradient during LCP. Instead, the experimental results of Section 5.3.1 have shown that independent of the initial roughness, stable low roughness limits were reached. Due to the material dissolution in the active or transpassive regime the lower limit of the surface finish roughness is governed by inhomogeneous etching or pitting. This explains the microstructural influences on the surface finish, which were observed in all experimental data in Section 5.3.3 and qualitatively confirms the third hypothesis for the materials investigated in this thesis. Consequently, geometric levelling must be caused by the laser-induced thermal and electrodynamic aspects described herein, rather than the concentration gradient and diffusion.

LCP-Model of geometric levelling

In contrast to electropolishing, LCP subjects materials to a considerable thermal influence due to the laser-induced surface heating that initiates the chemical dissolution. As outlined in Chapter 6, the thermal load and the exposure time can be used as fundamental variables to describe the laser-induced thermochemical material modifications. Furthermore, the preceding analysis verified that the mechanism of geometric levelling governs the surface polishing. In the following, these two findings are used to develop a laser-thermal model of geometric levelling and to derive a formula that predicts the

surface roughness S_a as a function of the thermal load and exposure time. Therefore, a third mathematical approach is presented by comparing Wagner's analysis, which is based on Fick's first and second laws, with Fourier's law of thermal conduction and the heat equation.

A boundary value problem analogous to that presented in Section 2.2.4 is structured by assuming the sine-wave surface profile has dimensions $\psi \ll \lambda$ and $\lambda \ll d_f$, i.e., the three-dimensional problem can be reduced to a two-dimensional problem as depicted in **Figure 7.9**. Therefore, the heat source can be approximated as transverse-infinite. The material is assumed to be isotropic with temperature-independent material parameters. The following boundary conditions should apply for the temperature $T(x,z)$:

$$\begin{aligned} T &= T_L && \text{at} && z = \psi \cdot sin(2\pi x/\lambda) \\ T &\to 0 && \text{for} && z \to \infty \end{aligned} \tag{7.4}$$

Here, z is the distance from the average surface plane of the anode and x is the coordinate on the axis parallel to the average surface plane.

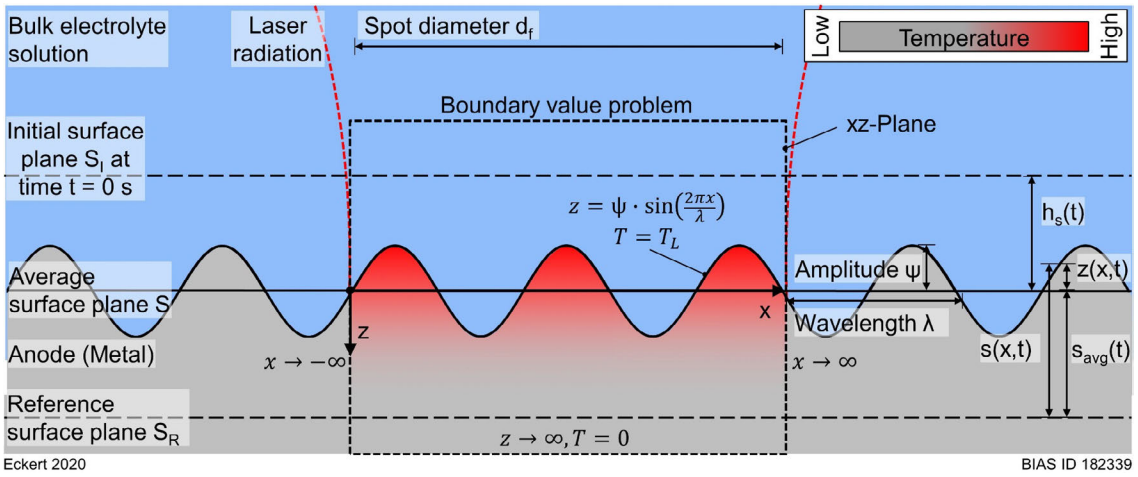

Figure 7.9: Illustration of the boundry-value problem of thermal geometric levelling.

The evolution of the temperature in time and space is described by the heat equation. The stationary heat equation reads according to Equation (4.6), without an external source:

$$\frac{\partial T}{\partial t} = D_T \left(\frac{\partial^2 T}{\partial x^2} + \frac{\partial^2 T}{\partial z^2} \right) = 0 \tag{7.5}$$

Here, D_T is the thermal diffusivity defined by $D_T = K/\rho c_p$, where c_p is the specific heat capacity. The heat equation shows the same mathematical form for the temperature and thermal diffusivity as Fick's second law for the concentration and diffusion coefficient. Therefore, the particular solution given by Equation (2.4) also solves the heat equation, but must be modified by a constant T_L in order to satisfy the boundary condition in Equation (7.4). The solution, satisfying the boundary condition only for $\psi \ll \lambda$, reads:

$$T(x,z) = T_L - B\left(z - \psi \cdot e^{-2\pi z/\lambda} \cdot \sin(2\pi x/\lambda)\right) \tag{7.6}$$

where B is a constant. Differentiation of Equation (7.6) with respect to z describes the temperature gradient according to:

$$\frac{\partial T}{\partial z} = B\left(1 - (2\pi\psi/\lambda) \cdot e^{-2\pi z/\lambda} \cdot sin(2\pi x/\lambda)\right) \tag{7.7}$$

In contrast to the presumed constant concentration gradient (cf. Section 2.2.4), Equations (7.6) and (7.7) presume a constant temperature gradient at some distance $z \gg \lambda$. This is appropriate because for large z values, the exponential term approaches zero, and the temperature gradient becomes equal to the constant B, independent of x and z. Thus, the constant B describes the average temperature gradient $(\partial T/\partial z)_{avg}$ in the z-direction.

In general, the laser-induced temperature gradient $\partial T(x,y,z)/\partial z$ of a Gaussian beam has a three-dimensional distribution in the x-, y- and z-directions, which can be calculated numerically. However, Section 4.6 showed that for LCP, a constant temperature gradient according to Equation (4.9) can be assumed inside the thermal boundary layer δ_{th}. Thus, a necessary condition for applying Equations (7.6) and (7.7) to describe LCP is that the effective thickness of the thermal layer must be larger than the wavelength of the sine-wave profile $\delta_{th} > \lambda$. From Equation (4.10), the spot diameter must also be larger than the wavelength. Therefore, for sufficiently large laser spot diameters and small wavelengths, the boundary value problem is applicable to LCP, despite the Gaussian-shaped intensity distribution of the laser radiation. Typical results presented in Section 5.2.3 had values of ψ (approximated by S_a) = 0.5 µm < λ (approximated by λ_S) = 8 µm < $d_f/3$ = 37 µm ≈ δ_{th}.

Based on Equation (7.7), the exponential function can be expanded to the first term of its Taylor series to obtain the temperature gradient at the surface according to:

$$\frac{\partial T}{\partial z} = \left(\frac{\partial T}{\partial z}\right)_{avg} (1 + (2\pi\psi/\lambda) \cdot sin(2\pi x/\lambda)) \tag{7.8}$$

This equation has an analogous form to that of the concentration gradient given by Equation (2.6).

Next, the change of the surface shape will be described as a function of time t. The surface-height data $s(x,t)$ describe the distance of a point at the surface from the reference plane S_R and can be separated into the sum of the distance $s_{avg}(t)$ of the average surface plane from the reference plane S_R and the distance $z(x)$ from the average surface plane to a point on the surface (**Figure 7.9**), analogous to Equations (2.10) and (2.11). The depth of a point at the surface decreases per unit time in the z-direction because of the material dissolution. This material dissolution is inhomogeneous depending on the position at the

surface. The local and average dissolution rates are assumed to be proportional to the local and average temperature gradients at the surface. Thus, the heat flux density through the surface, described by Fourier's law [Lie81], should be proportional to the energy change caused by the number of dissolved particles n with activation energy E_a, across the surface dA per time unit dt:

$$J_T = -K\frac{\partial T}{\partial z} = \frac{c_a E_a dn}{dA dt} \tag{7.9}$$

where c_a is a constant factor. The amount of substance n that dissolves from the surface is determined according to Equation (2.8). The activation energy E_a of a particle can be interpreted in the context of the Arrhenius equation [Pel12] as the specific activation energy necessary to initiate the chemical reaction. The Arrhenius equation reads:

$$k = A_a \cdot exp\left(\frac{-E_a}{R\,T}\right) \tag{7.10}$$

where k is the reaction rate, T is the absolute temperature in kelvin, A_a is the pre-exponential factor and R is the universal gas constant. In other words, only particles with a sufficient thermal energy E_a will dissolve into the electrolyte. Substituting Equations (2.8) and (7.8) in Equation (7.9) and rearranging to ds/dt yields the following:

$$\frac{ds(x,t)}{dt} = -\underbrace{\frac{m_M\,K}{\rho\,E_a c_a}\left(\frac{\partial T}{\partial z}\right)_{avg}}_{:=\,c_T} \cdot \left(1 + \frac{2\pi\psi}{\lambda} \cdot sin(2\pi x/\lambda)\right) \tag{7.11}$$

Except for the adjustments to the constant, here represented by c_T, such that the average material dissolution velocity, describes the linear decrease of the distance s_{avg} of the average surface plane S from the reference plane S_R, this equation is the same as Equation (2.9). With the reasoning presented in Section 2.2.4, Equation (2.10) to Equation (2.16) will still apply with the constant c_T instead of c_D. Equation (2.16) represents the amplitude as a function of the removal depth, and therefore the presented prediction methodology will hold. The thermal approach of Equation (7.11) provides an alternative explanation for the observed polishing in terms of geometric levelling governed by local differences of the temperature gradient. Heat dissipation and cooling occur faster in surface valleys because they are embedded in the metallic material. This leads to locally different chemical reaction rates, and a faster removal of roughness peaks compared to valleys.

Last, an approximation for the change of the average roughness S_a as a function of time is derived. Substituting Equation (2.10) and (2.11) in Equation (7.11), and separating the variables yields the following analogue to Equation (2.14), with c_T:

$$\frac{1}{z(x)}dz(x) = -\frac{2\pi}{\lambda}c_T dt \tag{7.12}$$

The solution is acquired upon integrating with an integration constant of $z_0 = \psi_0 \sin(2\pi x/\lambda)$ according to:

$$z(x,t) = \psi_0 \, sin\left(\frac{2\pi}{\lambda}x\right) exp\left(-\frac{2\pi}{\lambda}c_T \, t\right) \tag{7.13}$$

where ψ_0 is the amplitude of the initial surface profile at the time $t = 0$ s. The solution $z(x,t)$ describes the surface-height data of the sine-wave profile as a function of time t. The profile roughness R_a in the x-direction can be calculated by the arithmetical mean deviation of the profile $z(x,t)$ [ISO97] (cf. Equation (4.1)) as:

$$R_a(t) = R_{a,0} \, exp\left(-\frac{2\pi}{\lambda}c_T \, t\right) \qquad \text{with} \qquad c_T = \frac{m_M \, K}{\rho \, E_a c_a}\left(\frac{\partial T}{\partial z}\right)_{avg} \tag{7.14}$$

where $R_{a,0} = 2\psi_0/\pi$ is the initial roughness at $t = 0$ s. Equation (7.14) predicts the decrease of the roughness of the sine-wave profile as an exponential decay based on the laser-induced thermal impact and the wavelength of the profile. As mentioned in Section 2.2.4, a proper mathematical extension to an arbitrary two-dimensional surface profile usually requires the application of numerical methods as for example previously presented by the surface prediction model in this chapter.

As a simple approximation, Equation (7.14) can be extended to any two-dimensional surface profile by substituting the variables with their two-dimensional expected values. In particular, the roughness R_a must be replaced with the average roughness S_a, and the wavelength λ with the average wavelength λ_S. Additionally, in order to apply the formula on LCP, the temperature gradient has to be substituted by Equation (4.9) and the time by Equation (4.4) (exposure time t_r), as follows:

$$S_a(t_r) = \underbrace{(S_{a,i} - S_{a,f})}_{\Delta S_a} \, exp\left(-\frac{2\pi}{\lambda_S} \cdot \underbrace{\frac{m_M \, K}{\rho \, E_a c_a}}_{=c_M} \cdot \underbrace{\frac{\Delta T}{d_f}}_{=c_L} \cdot t_r\right) + S_{a,f} \tag{7.15}$$

where:

- S_a [m] is the average roughness
- $S_{a,i}$ [m] is the average roughness of the initial surface ($t = 0$ s)
- λ_S [m] is the average wavelength of the initial surface (cf. Section 4.3.2)
- $S_{a,f}$ [m] is the residual average roughness of the surface finish
- m_M [kg] is the atomic mass (average atomic mass for alloys)
- K [W/(m·K)] is the thermal conductivity
- ρ [kg/m^3] is the mass density
- E_a [J/mol] is the activation energy

- ΔT [K] is the thermal load difference
- d_f [m] is the laser spot diameter
- c_a [--] is the constant factor (of 10^3; see Appendix A.5)

Thus, S refers to surface roughness parameters, c_M [m^2/(K·s)] summarizes material-related parameters and c_L [K/m] summarizes process-related parameters. Equation (7.15) is expected to be applicable if the boundary condition $S_a \ll \lambda_S \ll d_f/3 \approx \delta_{th}$ is satisfied.

For small exposure times ($t_r \to 0$), the average roughness equals the initial roughness. Smoothing can reduce the roughness by the maximum amount of ΔS_a (roughness amplitude), which is defined as the difference of the initial roughness and the residual roughness $S_{a,f}$. The term for the residual roughness $S_{a,f}$ was added to describe the stable lower limit (as $t_r \to \infty$) of the roughness of the surface finish. This limit is governed by inhomogeneous etching (as previously discussed) and cannot be reduced any further by geometric levelling. In this context, the lower roughness limit is a specific constant that must be determined for every material-electrolyte combination. The average temperature gradient in the z-direction $(\partial T/\partial z)_{avg}$ is approximated by Equation (4.9) in terms of the ratio $\Delta T/d_f$. As shown in Chapter 6, considering the thermal load difference $\Delta T = (T_L - T_{th})$, only the difference between thermal load T_L and thermal material removal threshold T_{th} contribute to polishing. However, considering the absorptivity α and thereby the laser-induced thermal load to be constant over time is a simplification because the absorptivity depends on the surface profile itself and can change during polishing.

The constant factor c_a can be determined by the recess of the distance s_{avg}, which is proportional to the constant c_T (cf. Equation (2.13)) and related to the material removal depth by $dh_s = -\, ds_{avg}$ (see **Figure 7.9**). The comparison of the measured material removal depth with the calculated one based on c_T, yields a constant factor of $c_a = 10^3$ as shown in the Appendix A.5

Note, that apart from the constant $S_{a,f}$, Equation (7.15) solves the ordinary differential Equation (6.4), as can be readily recognized by substitution of Equation (4.4) for the exposure time and derivation with respect to the number of passes N. In this context, Equation (7.15) can be interpreted as the multicycle process signature of LCP.

The following chapter presents tests of Equation (7.15) by comparing the experimental results with the roughness predictions depending on the initial surface topography ($S_{a,i}$ and λ_S), different material and electrolyte combinations (m_M, ρ, K and T_{th}) and the thermal impact of the laser radiation ($T_L \sim P_L/d_f$).

Conclusion

This chapter demonstrated that LCP can be described by geometric levelling based on a two-dimensional prediction model, and therefore confirms the second research hypothesis. The surface roughness is predicted to decrease exponentially as a function of material removal depth in accordance with the experimental data. The frequency dependence of geometric levelling explains the faster removal of microroughness at the start of the smoothing, in the brightening stage. None of the experimental observations indicated a considerable influence of the concentration gradient and diffusion. Therefore, the surface finish is governed by inhomogeneous etching during the deepening stage, which gives reason for the third hypothesis. An alternative formula has been derived and approximated that explains geometric levelling based on local temperature differences between roughness peaks and valleys.

8 Evaluation of the LCP-Model

Validation of the model

The formula (Equation (7.15)) derived in Chapter 7 predicts the decrease of the average roughness S_a as a function of exposure time and thermal load and thus the process parameters. In this form Equation (7.15) constitutes the first research hypothesis for the surface roughness in a testable manner. The aim of the following discussion is the evaluation of Equation (7.15) as a suitable approach to predicting the average roughness during polishing. This chapter will show, first, that the experimental data shown in Section 5.3 correlate with the predicted average roughness, and second, that the formula allows to predict the surface roughness and the time required for polishing accurately.

Besides the thermal load and average exposure time, Equation (7.15) depends on the surface parameters $S_{a,I}$ and λ_S, the spot diameter d_f and material properties. The exposure time is given by Equation (4.4) and depends on the parameters N, b, v and d_f, and the thermal load is given by Equation (4.7), depending on P_L and d_f. All of these parameters can be determined experimentally. Table 4 summarizes the experimental parameters analyzed in Section 5.3.1, which are used to validate the prediction of the roughness S_a.

Table 5: Overview of the process parameters analyzed in Section 5.3.1 and used for the prediction and coefficient of determination between the experimental and predicted results.

Marker		Surface			Process parameters							Material parameters				Results
			$S_{a,i}$	$S_{\lambda a}$	P_L	d_f	T_L	b	v	N	t_r		$S_{a,f}$	E_a	T_{th}	R^2
			[µm]	[µm]	[W]	[µm]	[°C]	[µm]	[mm/s]	[1]	[s]		[µm]	[kJ/mol]	[°C]	[1]
Figure 5.32	■	B4	3.30	19.0	2.64	110	134	35	2	-	-	Titanium (Grade 1) (cf. Table 1)	0.2	55.7	111	0.98
	■	B3	2.24	21.0												0.99
	■	B2	1.37	14.5												0.97
	■	B1	0.57	8.0												0.93
Figure 5.34	◆	T4	1.95	50.6												0.96
	◆	T3	2.17	22.8												0.98
	◆	T2	0.59	4.8												0.92
	◆	T1	0.53	6.8												0.88
Figure 5.33	■	B4	3.30	19.0	2.86	110	143	35	2	-	-					0.90
	■				2.45		126									0.98
	■				2.29		119									0.99
	■				2.19		116									0.99
Figure 5.26	●	B3	1.73	21.0	1.0	34	160	9	2	-	-					0.59
	●				1.8	60		15								0.68
	●				2.6	84		21								0.78
	●				3.6	119		30								0.97
	●				5.1	168		42								0.98
	●				7.2	238		59								0.99
	●				10.2	336		84								0.99
	●				14.4	475		119								0.99
	●				20.4	672		168								0.96
	●				28.8	950		238								0.85

First, Equation (7.15) is tested with regard to the dependency on the initial surface topography. **Figure 8.1** shows the average roughness as a function of the exposure time for eight different prepared surfaces (cf. **Figure 5.32** and **Figure 5.34**) and the predicted average roughness (solid lines) according to Equation (7.15). The initial average roughness ranged from 0.53 µm to 3.30 µm and the average roughness wavelength from 4.8 µm to 50.6 µm. All process-related parameters were essentially constant, and therefore the dependency between $S_{a,i}$ and λ_S was tested according to:

$$S_a(t_r) = (S_{a,i} - 0.2\mu m)\, e^{-\left(\frac{2\pi}{\lambda_S} \cdot c \cdot t_r\right)} + 0.2\mu m \qquad \text{with} \quad c = c_M c_L \approx 1\,\frac{\mu m}{s} \qquad (8.1)$$

The process parameters listed in Table 4 were used to calculate c_M and c_L. The predicted data show trends similar to those of the measurements. First, polishing was predicted to take longer for surfaces with higher initial roughness but similar average wavelengths (B3 and B4). Second, smoothing was slower for similar initial roughnesses but larger average wavelengths (T3 and T4). Third, no significant differences were observed when the initial roughness and average wavelength both had similar values (B3 and T3).

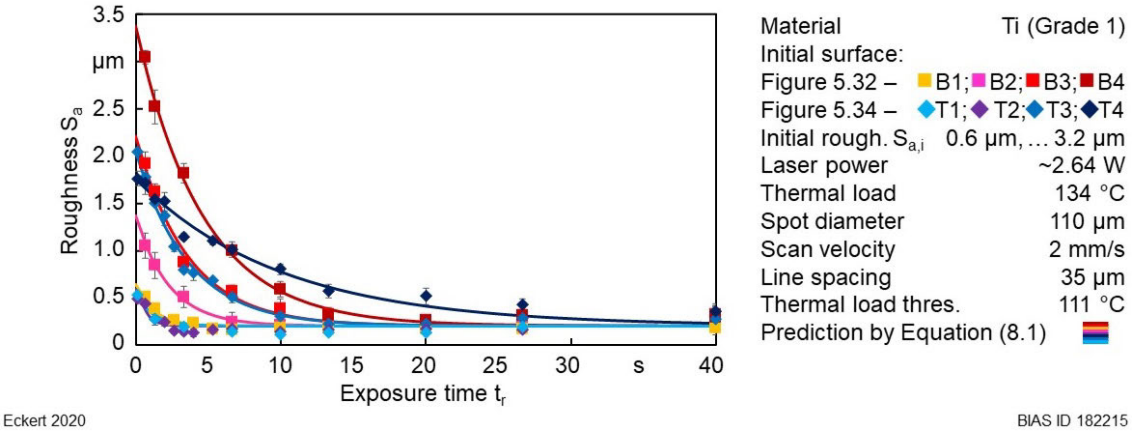

Figure 8.1: Experimental and predicted average roughness as a function of average exposure time for different prepared surfaces.

The residuals between the measurements and predictions were mostly within ± 0.1 µm and thereby within the variation of the roughness measurement, as shown in **Figure 8.2**. The sum of squared residuals (SSR) and the total sum of squares (SST) were used to calculate the coefficient of determination $R^2 = 1 - (\text{SSR/SST})$ [Gar85]. The results are shown in Table 5, with R^2 values ranging between 0.88 and 0.99. The large R^2 values show that the prediction model accounts for the majority of the observed data. The R^2 values are smaller for B1, T1 and T2 because on the one hand, the total variation (SST) was smaller in these cases, and on the other hand, the proportion of variation around the residual roughness $S_{a,f}$ was larger. Mechanisms causing the residual roughness are not considered by the prediction model. Therefore, the prediction cannot account for the

variation in the experimental data in the range of $S_{a,f}$, and the prediction is less accurate for small average roughnesses near the observed lower limit.

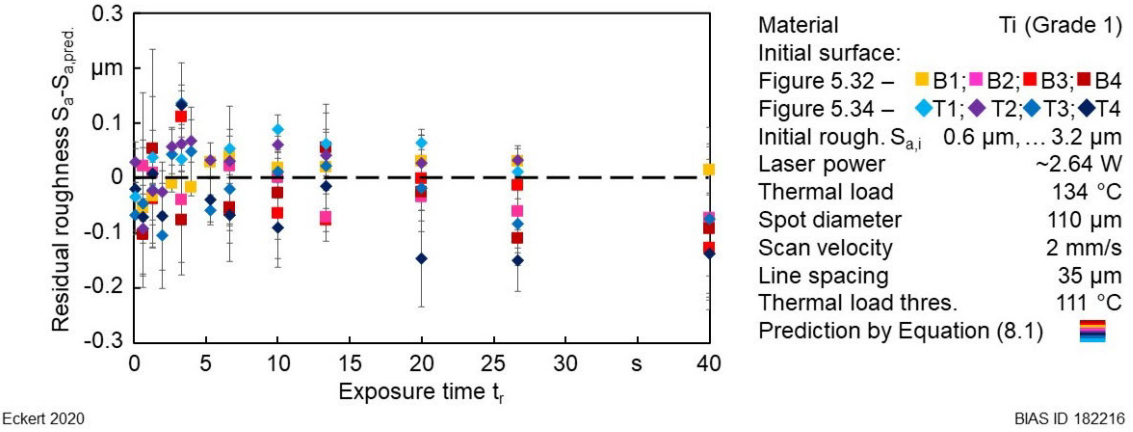

Figure 8.2: Residuals of the measured (S_a) and predicted average roughness ($S_{a,pred.}$) as a function of exposure time. The predicted roughness was calcualted according to Equation (8.1).

Next, Equation (7.15) is tested with regard to the thermal gradient in the z-direction. In Chapter 7, the gradient $(\partial T/\partial z)_{avg}$ during LCP was approximated by the formula $(T_L - T_{th})/d_f$. Thus, the influence of the gradient on the surface roughness can be tested either by varying the thermal load T_L or the spot diameter d_f. First, the influence of the laser power, i.e., the thermal load, is analyzed with otherwise constant process and surface parameters. With the parameters given in Table 4 and **Figure 5.33**, Equation (7.15) becomes:

$$S_a(t_r) = (S_{a,i} - 0.2\mu m)\, e^{-c\cdot(T_L - T_{th})\cdot t_r} + 0.2\mu m \quad \text{with} \quad c \approx 14.32\,\frac{10^{-3}}{K\cdot s} \qquad (8.2)$$

where T_{th} is the thermal threshold of titanium. **Figure 8.3** shows the measured and predicted (solid lines) average roughness as a function of the exposure time for five different thermal loads of 143, 126, 119, 116 and 99 °C, and the residuals between the measurements and predictions. The predictions correctly reflected the faster smoothing with higher thermal loads, with two exceptions.

First, for a laser power of 1.82 W, the thermal load of 99 °C was below the thermal threshold of 111 °C, and the exponent of the e-function changed its sign. In this case, Equation (7.15) no longer provides a useful prediction because the roughness increases over time. As mentioned in Section 5.3.1, the smoothing stops because the absorbed laser power, and thus thermal load, decrease below T_{th} during smoothing. Second, higher laser powers, such as 2.86 W (purple data points), deepen the surface plane and thereby increases the aspect ratio and, as shown in Section 5.2.4, the waviness. Therefore, the roughness and residuals steadily increase slightly over time. This effect will occur at any laser power after a certain period of time because it depends only on the aspect ratio. However, aside from these two exceptions, the residuals between the measurements and

predictions were within ± 0.1 µm, with a coefficient of determination of above 0.98 (Table 5).

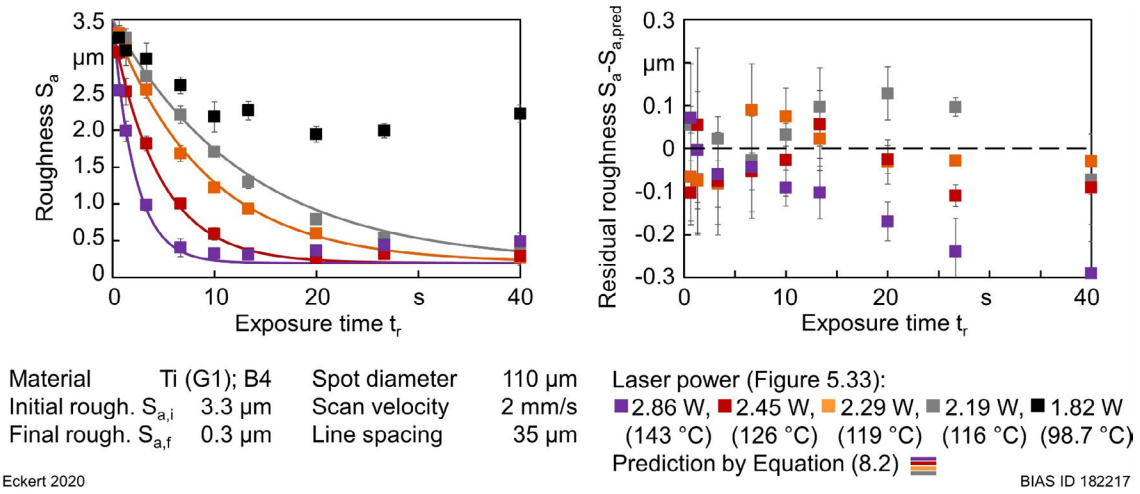

Figure 8.3: Experimental and predicted average roughness as functions of average exposure time for different thermal loads and the corresponding residuals.

Last, Equation (7.15) is tested with regard to the dependency of the thermal gradient $(T_L - T_{th})/d_f$ on the spot diameter d_f, i.e., whether different pairs of spot diameter and laser power are correctly predicted, with each pair inducing the same constant thermal load. Because neither the initial surface parameters nor the thermal load varied, the experimental data were described by:

$$S_a(t_r) = (S_{a,i} - 0.2\mu m)\, e^{-\left(\frac{c}{d_f} \cdot t_r\right)} + 0.2\mu m \qquad \text{with} \qquad c = 73.7\,\frac{\mu m}{s} \tag{8.3}$$

From Equation (8.3), surface polishing should take longer for larger spot diameters and faster for smaller ones. This seems to contradict the results shown in **Figure 5.26** because a higher number of scan passes was required for smoothing with a smaller spot diameter. However, according to Equation (4.4), the average exposure time increases in proportion to the square of the spot diameter. Therefore, by using a larger spot diameter, each part of the surface is exposed for a longer time to the laser radiation. The relationship revealed by Equation (8.3) is more evident from a plot of the average roughness data from **Figure 5.26** as a function of the exposure time, as shown in **Figure 8.4**. As predicted, for larger spot diameters, the smoothing takes place slower, i.e., a longer exposure to the laser radiation is necessary for the same roughness reduction. That does not necessarily mean that the processing time (Equation (4.5)) required to smooth a specific area will take longer.

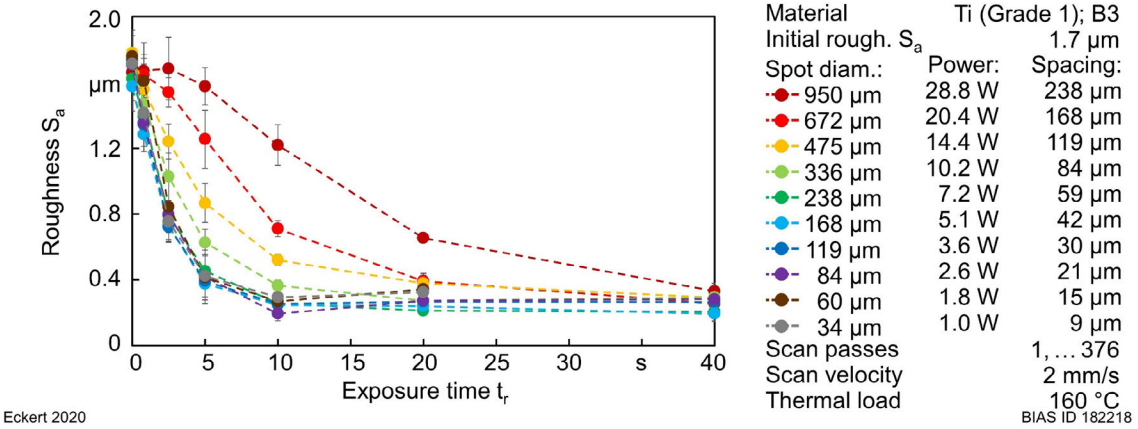

Figure 8.4: Average roughness S_a as a function of exposure time for different pairs of spot diameters and laser powers adjusted so that each case has the same thermal load.

Figure 8.5 compares the measured average roughness on the *y*-axis with the predicted roughness (Equation (8.3)) on the *x*-axis, calculated with the parameters shown in Table 4 and **Figure 5.26**. If the results were to match, with $R^2 = 1$, all data points would follow the straight black line exactly. Therefore, Equation (8.3) predicts the roughness quite accurately for spot diameters between 119 µm and 672 µm. For those spot diameters, the R^2 is equal to or larger than 0.95.

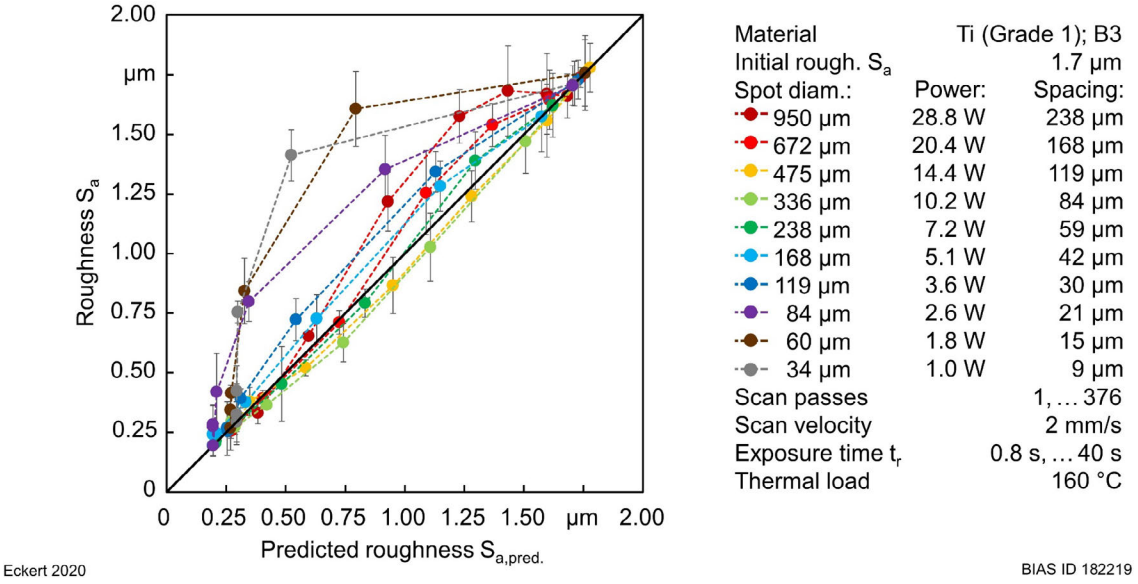

Figure 8.5: Experimentally measured average roughness as a function of the predicted roughness for different spot diameters.

For spot diameters of 84 µm and below, the R^2 deceases down to 0.57, and the measured roughness is up to almost 0.9 µm larger than the predicted value. These deviations cannot be explained by statistical variations. However, in these cases, the necessary conditions for Equation (7.15) of $\lambda s \ll d_f/3$ (Chapter 7) no longer applied because for such small spot diameters, with an average wavelength of approximately 21 µm and a spot diameter of 84 µm, the values are within the same order of magnitude. Thus, smoothing is not

accurately described by thermally governed geometric levelling under these conditions. Nonetheless, the results shown in Section 5.2.1 were achieved under polishing with a spot diameter of 31 µm on the ground surface T1 with an average wavelength of 6.8 µm, and therefore satisfied at least $\lambda_S < d_f/3$.

For spot diameters of 950 µm, the R^2 deceases down to 0.85, and the measured roughness is at some points up to almost 0.3 µm larger than the predicted value. This deviation is probably attributed to the fact that Equations (7.15) and (4.7) presuppose a semi-infinite boundary value problem, with a small spot diameter compared to the sample dimensions. However, the titanium sheets had thicknesses of $L_z = 0.8$ mm and were embedded in a polymer, such that the calculated thermal load and gradient deviated from the actual values. Thus, Equation (7.15) no longer applied because the spot diameter was above the size range of the sample thickness.

The analysis in this section has shown that the derived Equation (7.15) and the developed model of thermal geometric levelling explains most of the experimental observations and their variation, confirming the first research hypothesis. The dependencies of surface parameters and process parameters were verified for titanium in 5.0 M phosphoric acid. Significant mismatches between the experimental and predicted values occurred among others under process conditions outside the ranges specified in the development of the thermal geometric levelling model, which could be extended to such cases by further development of the model to include additional mechanisms and/or boundary conditions. Furthermore, the model does not take into account effects like corrosion, deposition, or emerging gas occurring at high thermal loads as shown in the next paragraph.

Transfer to other passive metals

In order to apply Equation (7.15) to other materials, their activation energy E_a and thermal thresholds T_{th} must be determined. The activation energy can be interpreted as the amount of energy necessary to transform the reactants into products and the thermal threshold as the temperature required to dispel passivation [Now95]. Both values depend on the particular chemical reactions occurring in the system and represent characteristic properties of the material-electrolyte system. They are currently best seen as empirical values [Con90] and can be determined experimentally with the Arrhenius equation, as shown for titanium in Appendix A.4. Alternatively, E_a and T_{th} can be determined by fitting Equation (7.15) to the experimental data. This can be done computationally in MATLAB by using a customized model based on Equation (7.15) with the independent variables E_a and T_{th}. In this work, the variables were optimized with a least-squares method and starting points of 50 kJ/mol and 100 °C. All parameters are given in Table 6. **Figure 8.6** exemplifies the results of the least-squares fit, with an R^2 of 0.97 for the

experimental data from Ti6Al4V. The activation energy and thermal threshold were determined to be 64.1 kJ/mol and 142 °C, respectively.

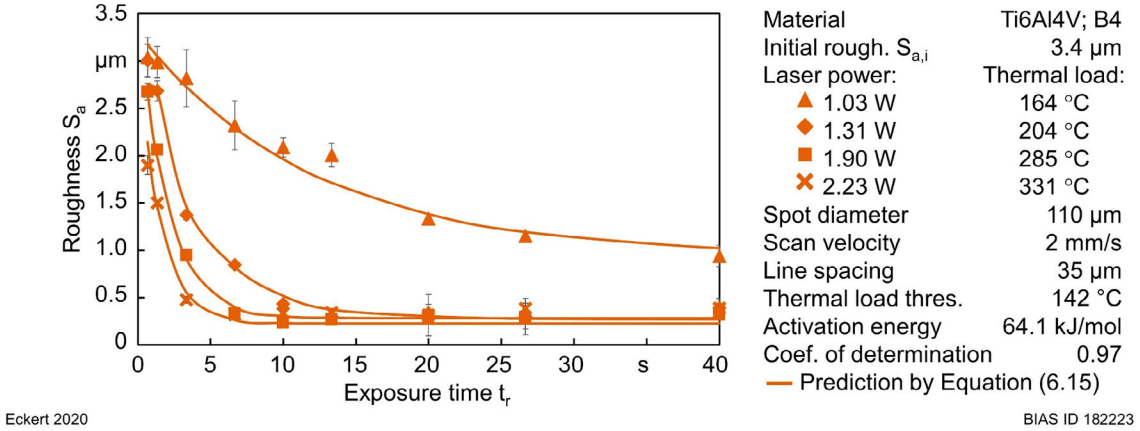

Figure 8.6: Experimental and fitted average roughness as a function of exposure time for Ti6Al4V.

Table 6 summarizes the results for the activation energies and thermal thresholds for the different materials presented in Table 1 and Section 5.3.2. For all materials, the coefficients of determination exceeded 0.95. The activation energies ranged from 45.9 kJ/mol for metallic glass to 131.3 kJ/mol for Nitinol, and the thermal thresholds ranged from 59 °C for metallic glass to 142 °C for Ti6Al4V.

Table 6: Overview of the process parameters for the materials analysis presented in Section 5.3.2 and the fitting results for the material's activation energies and thermal thresholds.

Marker		Surface			Process parameters							Material		Results		
			$S_{a,i}$	$S_{\lambda a}$	P_L	d_f	T_L	b	v	N	t_r		$S_{a,f}$	E_a	T_{th}	R^2
			[µm]	[µm]	[W]	[µm]	[°C]	[µm]	[mm/s]	[1]	[s]		[µm]	[kJ/mol]	[°C]	[1]
Figure 5.36	○	B4	3.20	22.6	1.74	110	93	35	2	-	-	Titanium (G2)	0.20	76.1	106	0.98
	▲				2.32		116									
	◆				2.45		123									
	■				2.92		141									
	▲	B4	3.40	18.8	1.03	110	164	35	2	-	-	Ti6Al4V	0.21	64.1	142	0.97
	◆				1.31		204									
	■				1.90		285									
	✖				2.23		332									
	○	B4	2.70	18.5	1.23	110	104	35	2	-	-	Nitinol	0.29	131.3	92	0.99
	▲				1.45		136									
	◆				1.94		175									
	●				2.27		202									
	◆	B4	2.65	18.0	2.30	110	129	35	2	-	-	Sellite 21	0.38	59.7	88	0.98
	●				2.67		147									
	▲	B4	2.45	16.6	1.12	110	81	35	2	-	-	Metallic Glass	0.14	45.9	59	0.96
	◆				1.37		94									
	■				1.70		112									
	●				1.98		127									

Figure 8.7 shows the measured average roughness on the *y*-axis as a function of the predicted roughness using the parameters given in Table 6. Incorporating the specific

thermal threshold and activation energy in the predictions for each material, produces close agreement with the experimental data. The dashed black line shows a perfect correlation of $R^2 = 1$. These results show that the thermal geometric levelling model derived in Chapter 7 can be successfully applied and generalized to other material-electrolyte systems.

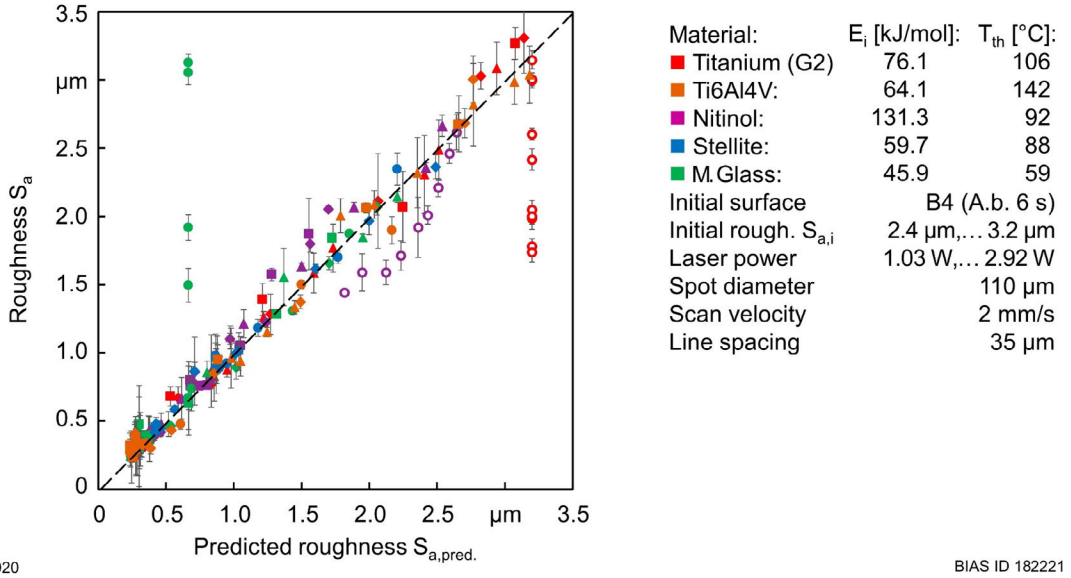

Figure 8.7: Experimentally measured average roughness as a function of the predicted roughness for different materials. The shapes used for each point are defined in Table 6.

Two types of mismatch between the experimental data and the predictions indicate the influence of as-yet unconsidered mechanisms. First, the open red and purple circles in **Figure 8.7** correspond to the cases of incomplete polishing due to the change of the surface absorptivity during the polishing process. Although the absorptivity is always affected by the roughness, in these two cases the laser-induced temperature drops below the thermal threshold and polishing stops completely. Second, the closed green circles in the figure correspond to increases in both roughness and absorptivity resulting from process disturbances that can be induced under higher thermal loads. In these cases, after initial polishing, sporadic pitting corrosion or material deposition became more frequent, and the entire surface was gradually covered with micro- and nanocavities or chemical byproducts, as shown in the reflected-light images in **Figure 5.36**. Despite these mismatches, the results presented here demonstrate that a residue-free surface finish can be achieved and predicted within the optimum power range.

Application for roughness prediction

Equation (7.15) can be used to predict the average roughness for any given set of process parameters within the range listed in Table 5 and Table 6. **Figure 8.8** shows the average roughness data from **Figure 5.21** and the corresponding prediction in a two-dimensional colormap with the thermal load on the *y*-axis and average exposure time on the *x*-axis.

The roughness was accurately predicted, albeit with deviations at higher thermal loads above the disturbance threshold ($T_{th,dist} \approx 200$ °C). Disturbances such as pitting corrosion, material deposition and aspect-ratio-related waviness (Section 5.2.4) are not accounted for by Equation (7.15).

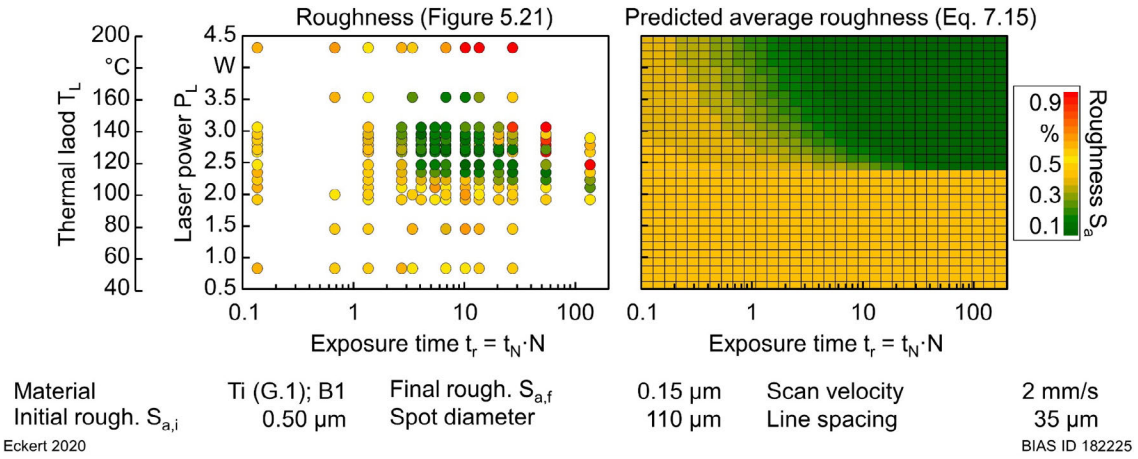

Figure 8.8: Comparision of experimental and predicted average roughness as a function of the thermal load and average exposure time.

In the same manner, **Figure 8.9** shows the average roughness results from **Figure 5.27** and the corresponding prediction in a two-dimensional colormap in relation to the spot diameter and average exposure time. The thermal load had a constant value of 160 °C because the laser power and spot diameter were adjusted proportionally. The experimentally observed slower smoothing for larger spot diameters was accounted for by the prediction.

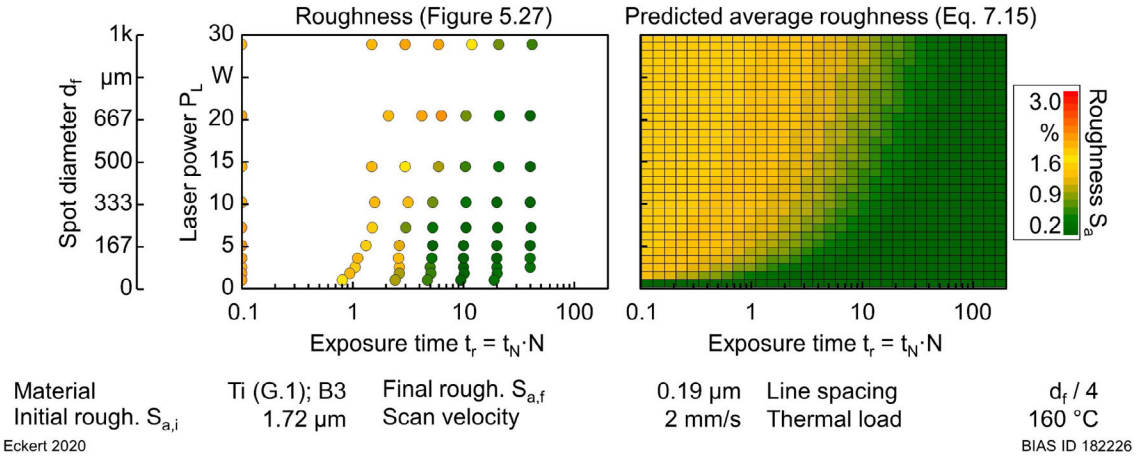

Figure 8.9: Comparision of experimental and predicted average roughness as a function of the spot diameter and average exposure time.

With respect to the thermal threshold and activation energy given in Table 6, the average roughnesses of other materials can be predicted, as shown in **Figure 8.10**. The upper limit of the thermal load is determined by the experimentally observed occurrence of disturbances (dashed red line). Optimal conditions of a high-quality surface finish are in

the range of 111 °C to 200 °C for titanium, 142 °C to > 332 °C for Ti6Al4V, 92 °C to 200 °C for Nitinol, 88 °C to 146 °C for Stellite 21 and 59 °C to 126 °C for metallic glass.

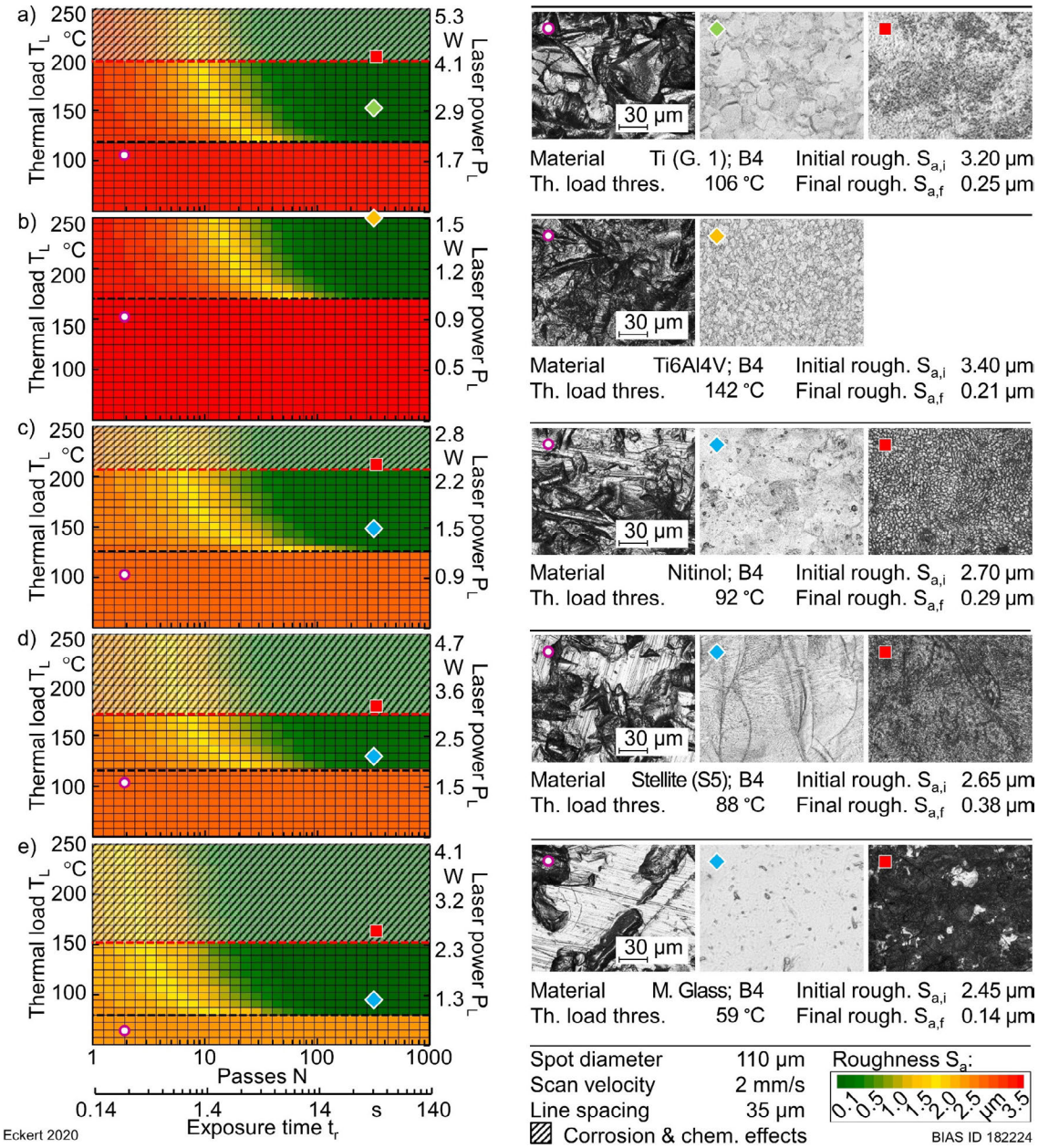

Figure 8.10: (a)–(e) Predicted average roughness for different materials and characteristic reflected-light images of the initial, polished and disturbed surface finishes.

Implications for the polishing time

In the following, Equation (7.15) is used to derive a formula for the so-called polishing time, which describes how long a surface must be machined to achieve the lower roughness limit. Equation (7.15) describes the decrease of the initial roughness as an exponential decay with exposure time. The reciprocal of the exponential coefficient during an exponential decay can be interpreted as the mean lifetime τ_{Sa} of the average roughness, so that Equation (7.15) yields:

$$S_a(t_r) = \Delta S_a \, exp\left(-\frac{t_r}{\tau_{S_a}}\right) + S_{a,f} \quad \text{with} \quad \tau_{S_a} = \left(\frac{2\pi}{\lambda_S} \cdot \frac{m_M K}{\rho E_a} \cdot \frac{(T_L - T_{th})}{d_f}\right)^{-1} \tag{8.4}$$

At time $t_r = \tau_{Sa}$, $2 \cdot \tau_{Sa}$ and $3 \cdot \tau_{Sa}$, the average roughness S_a is reduced to e^{-1}, e^{-2} and e^{-3}, approximately 0.37, 0.13 and 0.05 times its initial value, respectively, and so on. For long exposure times the exponential term approaches zero and the stable lower roughness limit is given by $S_{a,f}$. The reduction of the initial roughness to 5 % of its value after an exposure time of $t_r = 3 \cdot \tau_{Sa}$, is used as criterion to define the polishing time t_p, because after this time the surface has been almost completely polished. Upon substituting $t_r = 3 \cdot \tau_{Sa}$ in the processing time given by Equation (4.5), the time required to polish an area A is given by:

$$t_p\left(d_f, T_L\right) = \frac{6}{\pi^2} \cdot \frac{\lambda_S}{c_M} \cdot \frac{A}{d_f \cdot (T_L - T_{th})} \quad \text{with} \quad c_M = \frac{m_M K}{\rho E_a} \tag{8.5}$$

From Equation (8.5), one can readily recognize first, that surfaces with smaller average wavelength λ_S (microroughness) will be polished faster, and second, that the polishing time can be reduced only by increasing the spot diameter d_f or the thermal load T_L. The former implication can be observed experimentally from, for example, the turned surfaces T3 and T4 in **Figure 8.1**. The latter implication is illustrated in **Figure 8.11** by the polishing time per unit area as a two-dimensional function of the thermal load and spot diameter, according to Equation (8.5), for a common set of process parameters.

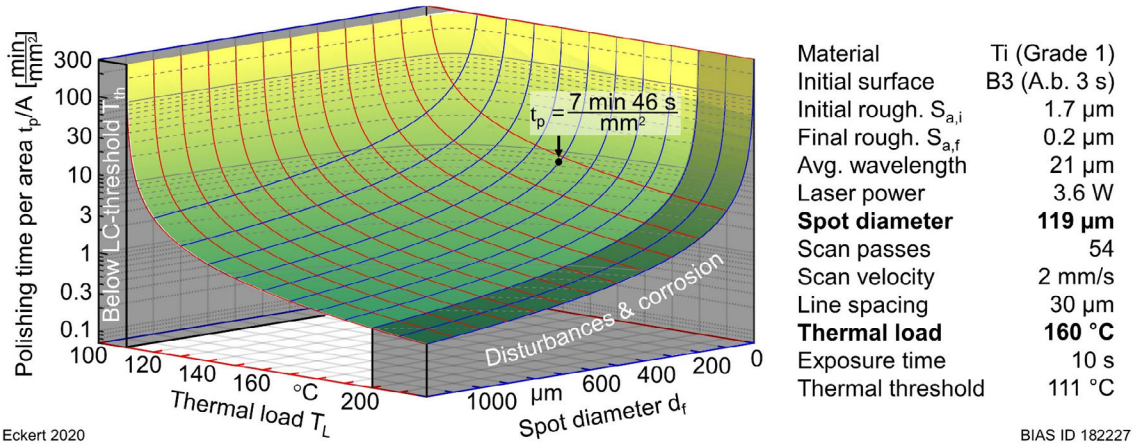

Figure 8.11: Polishing time as a function of thermal load and spot diameter.

To polish a surface area of 1 mm² with a spot diameter of 119 µm and thermal load of 160 °C is predicted to take $t_p = 7$ min 46 s. Doubling the difference $\Delta T = (T_L - T_{th})$ from 24 K to 48 K, or doubling the spot diameter to 238 µm, halves the polishing time. However, increasing the laser power and thereby the thermal load above 200 °C results in undesired process disturbances and increasing the spot diameter while maintaining a constant laser power reduces the thermal load. In order to keep the thermal load constant, the laser power must be increased in proportion to the spot diameter. The laser power and

the number of passes for a specific spot diameter can be calculated by rearranging Equations (4.7) and (4.4) (with $b = d_f/3$):

$$P_L = \frac{\sqrt{\pi} \cdot e}{\sqrt{2}} \frac{K}{\alpha} \cdot d_f \cdot T_L \qquad \text{and} \qquad N = \frac{4}{3\pi} \cdot v \cdot d_f^{-1} \cdot t_r \tag{8.6}$$

The average roughness for proportionally increased spot diameters and laser powers, i.e., constant thermal load, is shown in **Figure 8.9** as a function of the average exposure time. Thus, the relevant time parameters for LCP can be summarized:

- The exposure time t_r (Equation (4.4)) describes the period of time that the surface is actually exposed to the laser radiation.
- The processing time t_A (Equation (4.2)) describes the actual time that a given surface is machined.
- The polishing time t_p (Equation (8.5)) describes the processing time required to reach the lower roughness limit.

The following discussion addresses how these three parameters relate to the achieved surface roughness. **Figure 8.12** plots the average roughness data (blue circles, secondary *y*-axis) from **Figure 8.9** with an exposure time of 10 s along with the corresponding processing time (black circles, primary *y*-axis) and the caluclated polishing time (black dashed line) for a 1 mm^2 surface, all as functions of the spot diameter. Up to a spot diameter of 237 µm, the observed surface finish achieved the stable lower roughness limit below 0.25 µm, and then the roughness steadily increased up to 1.18 µm for a spot diameter of 950 µm. The observed roughness was below 0.25 µm as long as the processing time was longer than the predicted polishing time. These times were the same (intersection point) for the spot diameter of 238 µm, and for larger spot diameters, the roughness is higher because the processing time is too short to reach the stable lower limit. The difference between the processing time and the predicted polishing time is a measure of whether the surface finishing has already reached its stable lower roughness limit ($t_A > t_p$) or was stopped before ($t_A < t_p$). For example, with a spot diameter of 119 µm, the processing time of one square millimeter was 15 min, which is almost twice as longer as the predicted 7 min 46 s to achieve the stable lower limit, whereas for a spot diameter of 672 µm, the processing time was 28 s, which is 54 s shorter than the predicted polishing time of 1 min 22 s.

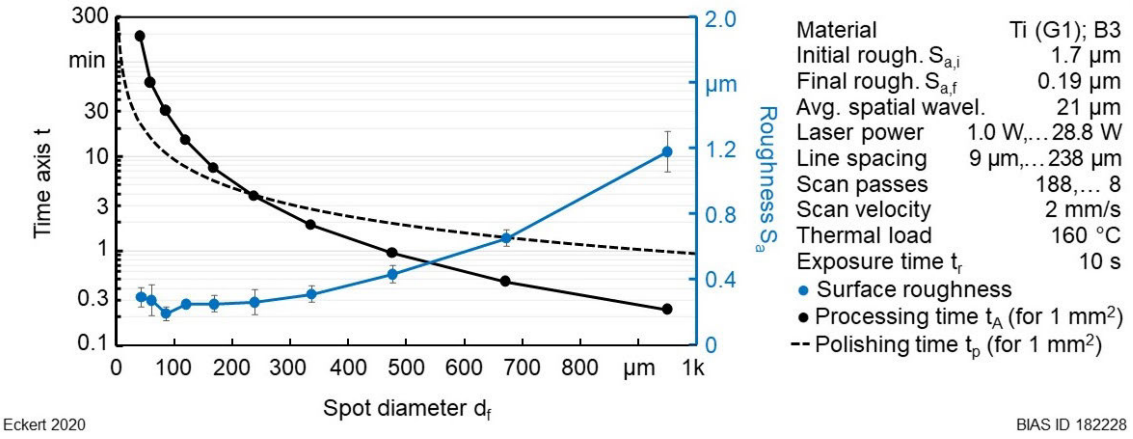

Figure 8.12: Processing time (solid black line), polishing time (dashed black line) and experimentally measured average roughness (blue line) as functions of the spot diameter.

Figure 8.13 shows the processing time and average roughness as a function of the spot diameter after a shorter average exposure time of 5 s (square symbols) and a longer average exposure time of 40 s (diamond symbols). With the shorter exposure time, the intersection between the processing and polishing times shifted to a shorter spot diameter of 120 µm. Thus, the stable lower roughness limit was just achieved with the spot diameter of 119 µm. The average roughness gradually increased for spot diameters above 120 µm because the processing time was shorter than the required polishing time, and the time deficit increased with the spot diameter.

With the longer exposure time, the intersection shifted to a larger spot diameter of 952 µm. The processing time was longer than the required polishing time, and thus the lower roughness limit was achieved for almost all spot diameters, except for 950 µm. Therefore, in order to execute the polishing process as quickly and with as little material removal as possible, the processing time should not significantly exceed the predicted polishing time.

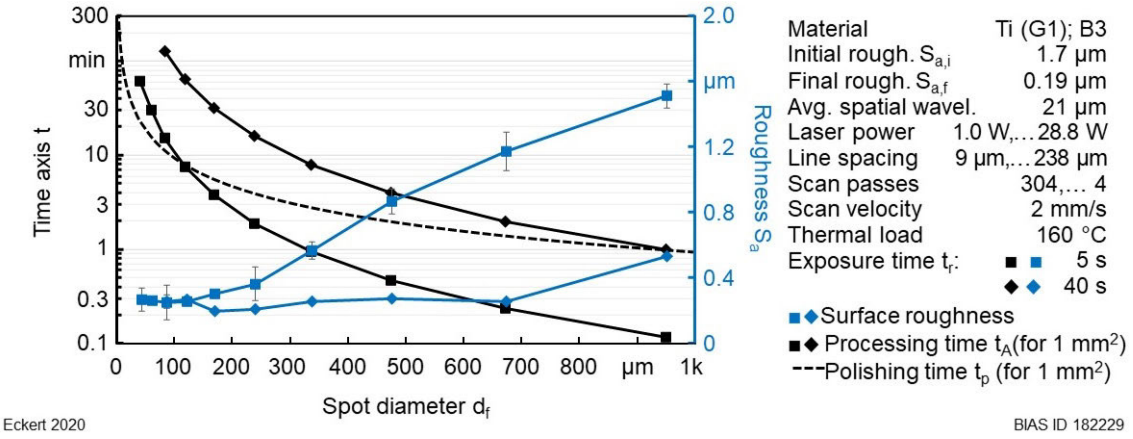

Figure 8.13: Processing times (solid black), predicted polishing time (dashed black) and measured roughness (blue lines) as functions of the spot diameter for two different exposure times.

Figure 8.14 shows the roughness as a function of the processing time t_A divided by the polishing time t_p for the different spot diameters. The horizontal dashed black line indicates the criterion for the polished surface with the 95 % reduction in initial roughness with respect to the lower roughness limit. Typically, the surface roughness reaches the lower roughness limit after a processing time of about the polishing time (t_A / t_p = 1). However, for spot diameters about $d_f \lesssim 3 \cdot \lambda_S = 63$ µm and $d_f \gtrsim L_z$, the predicted polishing times were increasingly inaccurate because the necessary conditions for Equation (7.15) and thereby Equation (8.5) were not satisfied.

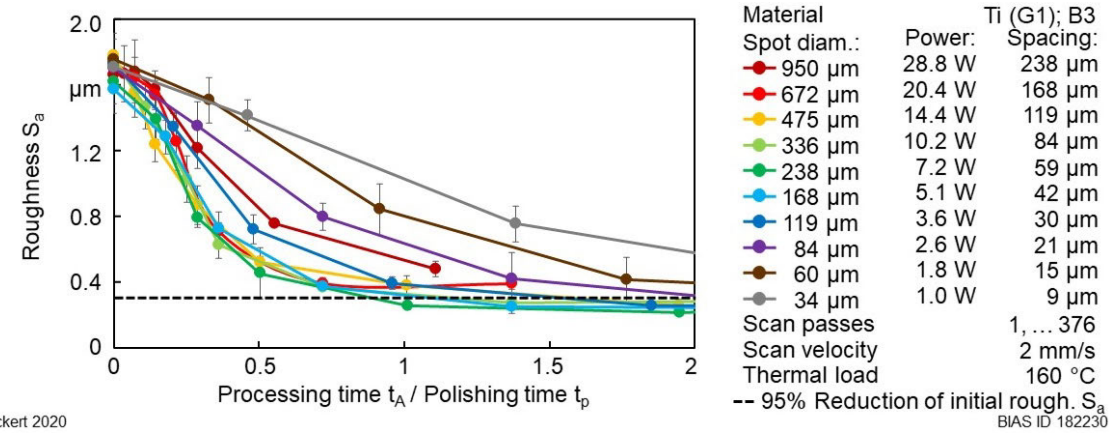

Figure 8.14: Average roughness S_a as a function of the quotient of processing and polishing time for different spot diameters.

In fact, with a spot diameter of 34 µm, it takes more than twice as long as predicted to reach the stable lower roughness limit. Nevertheless, within its range of validity, Equation (8.5) describes the reduction of the polishing time per square millimeter decreasing from 7 min 46 s down to 1 min 22 s, and is reversely proportional to the spot diameter, which was increased from 119 µm to 672 µm.

Conclusion

The first hypotheses that guided this research was verified. The thermal load T_L and the average exposure time t_r were verified to be fundamental parameters that control roughness during LCP. The approximation of thermal geometric levelling model by Equation (7.15), was verified to predict the average roughness S_a as an exponential decay over time, as long as the equation's boundary conditions were fulfilled such that other mechanisms like corrosion, deposition, or emerging gas were of negligible importance. Taking the respective thermal thresholds T_{th} and activation energy E_a into account, Equation (7.15) can be applied to other materials, as shown for Ti6Al4V, Nitinol, Stellite 21 and metallic glass. Thus, the proposed model is an effective tool for calculating and scaling suitable process parameters for precise roughness control.

9 Polishing Examples

The LCP process developed in this work allows selective, direct and gentle polishing of passive metal workpieces. The scanner-based experimental setup allows flexible beam guidance and the adjustment of the relevant process parameters to achieve macroscopic polishing with microscopic precision. In the following, several examples illustrate the previously discussed possibilities and limitations of this technology.

Figure 9.1 shows a top view of two polished 5 mm × 5 mm tiled patterns on a ground titanium surface (T1) with an initial roughness of 0.5 µm. In the positive pattern, the tile area was polished and the tile joints were left unpolished, versus the reverse for the negative pattern. In both cases, the polished area showed a bright surface finish with a minimum roughness of 0.16 µm. The laser spot diameter of 31 µm allowed polishing tile joints with lateral dimensions of 60 µm. Only a small amount of material was removed by the polishing process, and therefore the waviness of the polished surface was not increased.

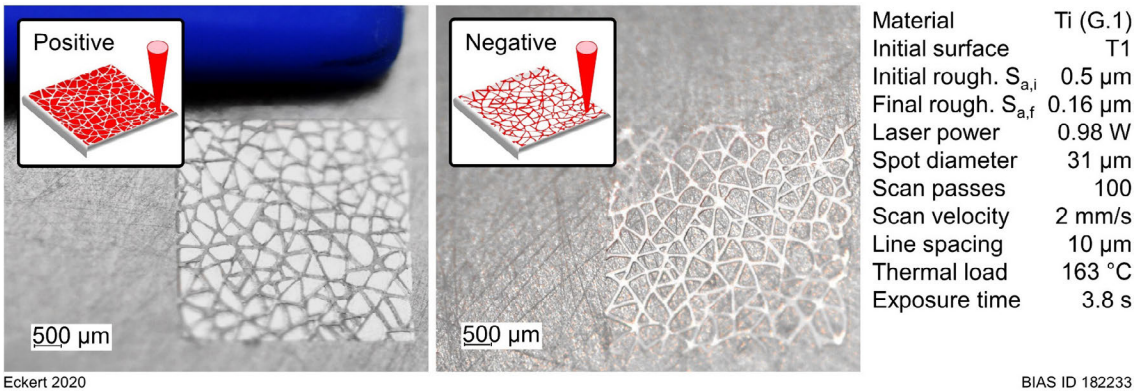

Figure 9.1: Example of micropolishing on a macroscopic scale for a 5 mm × 5 mm tiled pattern.

Figure 9.2 shows the polishing result for an image of the Bremen Town Musicians on a previously abrasive-blasted surface (B4) with an initial roughness of 2.8 µm. Because of the high initial roughness, the average surface plane must be levelled by approximately 30 µm in depth in order to achieve the stable lower roughness limit. Because of the small lateral dimensions of the structure, the aspect ratio was larger than 0.03 and caused shape deviation and increased waviness on the bottom surface plane. This removal depth may be acceptable for larger areas, when the aspect ratio is much smaller than 0.03.

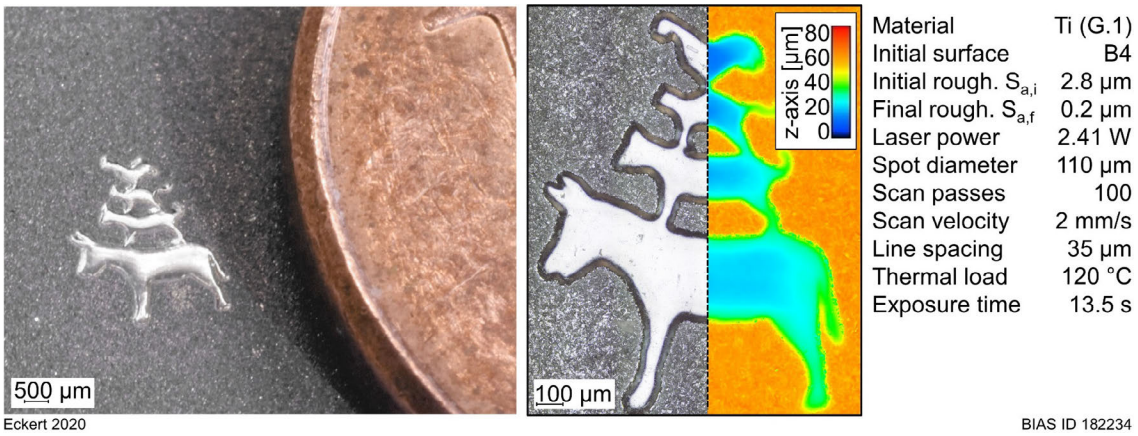

Figure 9.2: Micropolishing of an image of the Bremen Town Musicians on an abrasive-blasted surface.

LCP can also be applied to polish thin foils selectively because no mechanical forces are applied to the workpiece and the laser-induced thermal load is far below the melting or phase-transformation temperature. **Figure 9.3** shows a matrix of 7 × 20 polished squares of decreasing sizes on a 16 µm thin titanium foil. In the first row, the squares have sizes of 500 µm × 500 µm, and the sizes are reduced by 20 µm in each subsequent row to a minimum of 100 µm × 100 µm. Although the initial roughness was only 0.3 µm, LCP reduced the surface roughness further to 0.18 µm. During this process, the average surface plane was levelled by 3 µm. The microstructure is not visible, because on such thin foils single grains can be stretched over several tens of micrometers in *x*- and *y*-direction.

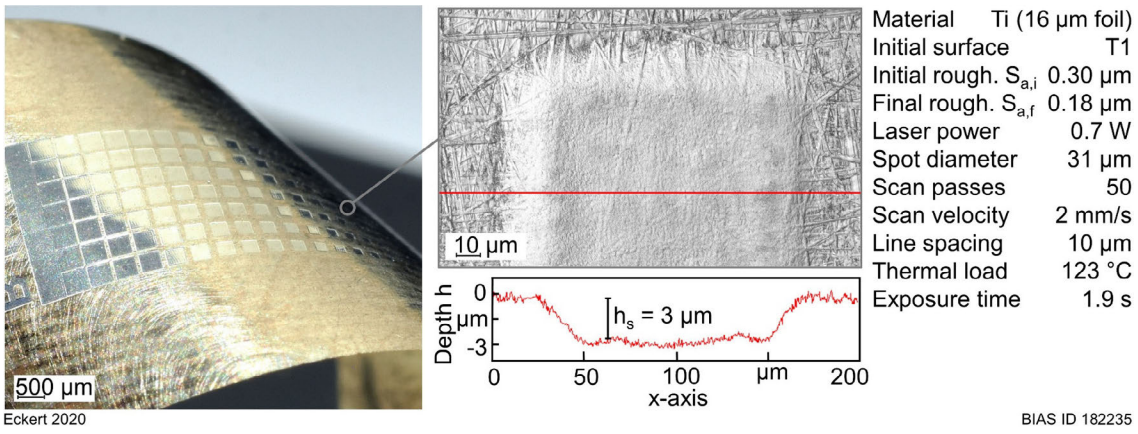

Figure 9.3: Polished squares of decreasing sizes on a 16-µm-thin titanium foil.

The same matrix pattern was also polished on a 0.8 mm thick titanium (Grade 1) sheet. **Figure 9.4** shows images of the structure, taken under slightly different angles. The colored impressions were created by laser-induced periodic ripple nanostructures, which can occur during the polishing process as shown in Section 5.3.4. These structures can cover a macroscopic area homogeneously, creating a reflection grating on the surface. The incident light interacts with the grating structure and is diffracted into its spectral components, because the pattern's periodicity of 714 nm lies in the visible light spectrum.

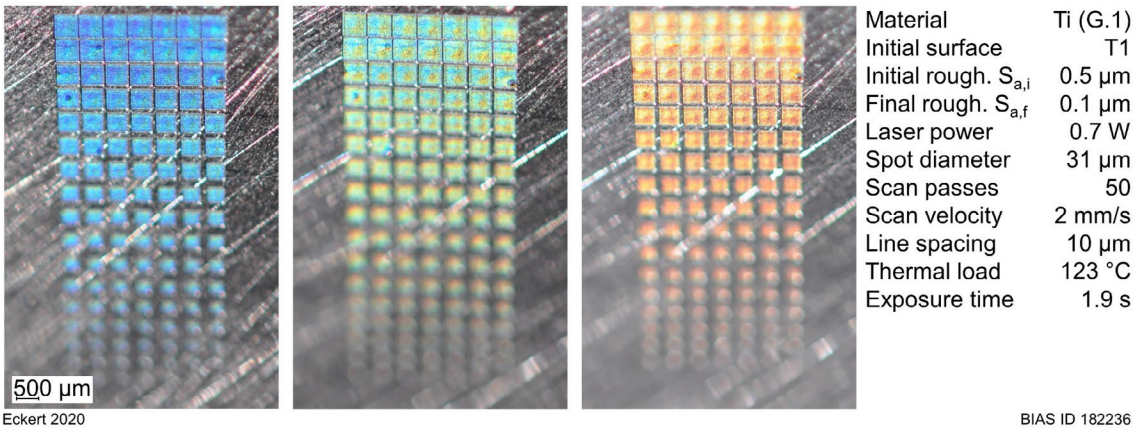

Figure 9.4: Formation of laser-induced periodic surface structures with a spacing of $\Lambda = 0.714$ µm, creating a reflection grating on a titanium (Grade 1) surface.

LCP can also be used for precise deburring of cut edges of thin foils or microparts. This is illustrated by the SEM image in **Figure 9.5**. The left side of the picture shows an edge cut by a pulsed (20 µs) modulated continuous wave laser, and the right side shows the same edge after LCP. For this purpose, the center of the laser spot was offset 25 µm from the workpiece, so that only a fraction of the laser beam was absorbed at the edge. The chemical reaction removed ablated material, residual debris and roughness peaks, resulting in a clean, smoothed cut edge. Both processing steps were performed with the same laser setup without demounting the sample. In the first step, the reaction chamber was flooded with argon, and in the second step, with phosphoric acid (H_3PO_4).

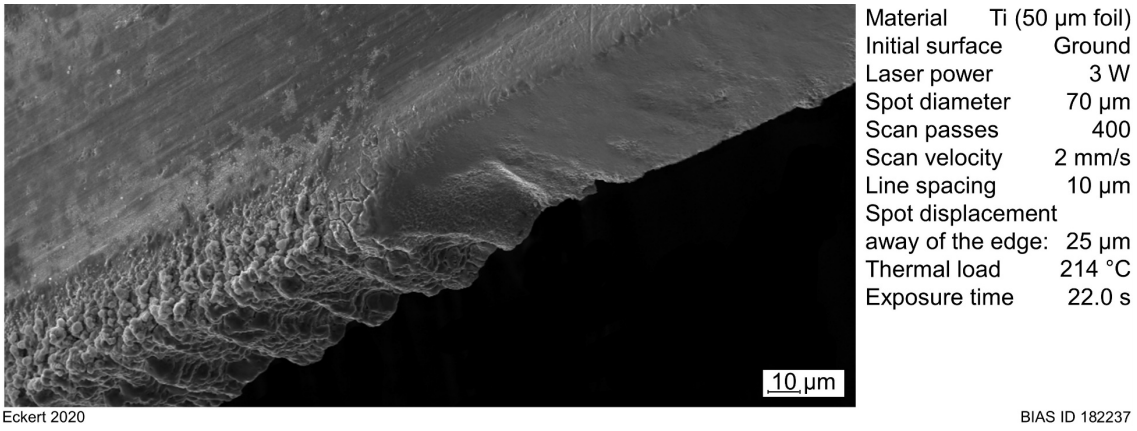

Figure 9.5: SEM image of a laser-thermochemically deburred cut edge.

Macroscopically large surfaces of a few cm^2 can be polished in a manageable time by using larger spot diameters. **Figure 9.6** shows an LCP-treated surface in the shape of a world map on a micro- and 76 times larger macro-scale on a 0.8 mm thick Ti6Al4V sheet. The surfaces of bordering countries were polished with different exposure times in order to achieve the desired average roughness and optical gloss effect. Thus, either a mirror-like surface finish with a roughness of $S_a = 0.2$ µm or a matt effect with a roughness of $S_a = 1.2$ µm can be produced. The average exposure times to achieve the lower roughness

limits are shorter for Ti6Al4V compared to titanium (Grade 2), i.e., polishing occurs faster for the former than the latter (cf. **Figure 5.36**). The larger map was polished with a spot diameter of 311 µm and the smaller one with a spot diameter of 34 µm.

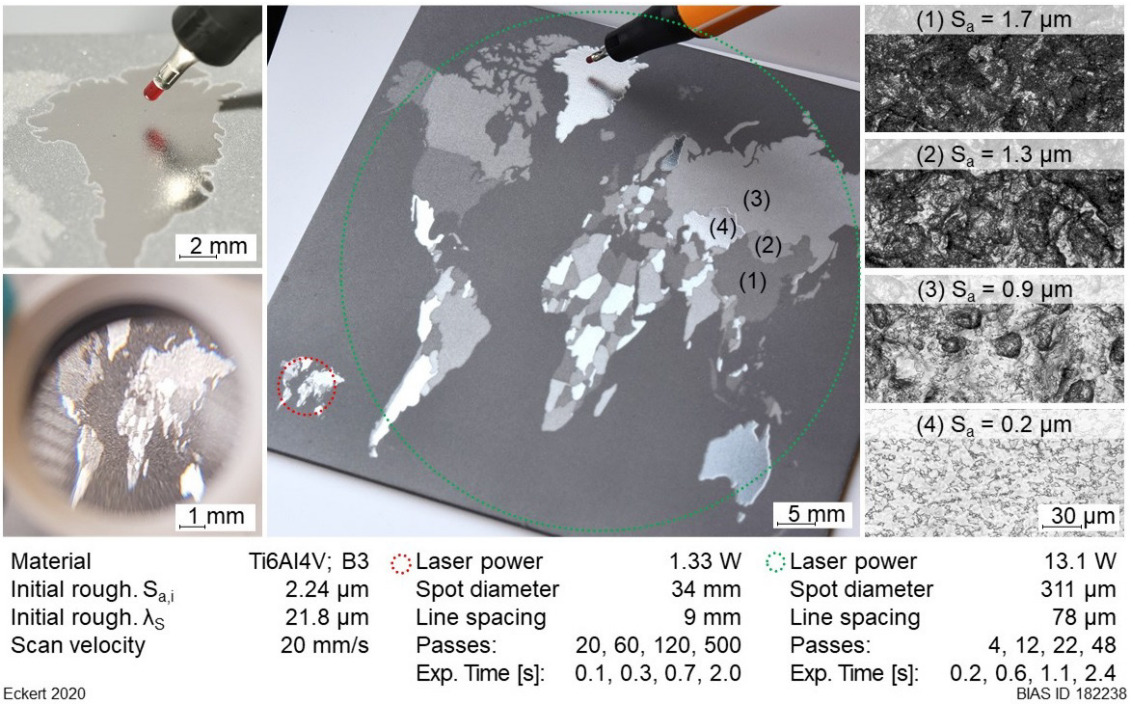

Figure 9.6: LCP-treated surface in the shape of a world map on a micro- and 76 times larger macro-scale.

10 Summary

Conventional finishing methods have limited capacity to improve the surface quality of free-form surfaces, cavity interiors or selective areas to a desired roughness level, especially for metallic microparts, and these limitations motivate the development of new finishing technologies. Therefore, the aims of this work were to study the application of laser-induced thermochemical machining for selective micropolishing applications, to understand the mechanisms of laser-induced thermochemical polishing and to develop methods to predict surface finishes.

Laser-induced thermochemical material removal was demonstrated to achieve favorable surface finish results in the selective polishing of passive metals. The surface roughness was reduced by N-fold recurring millisecond exposures t_N to laser radiation. During each exposure, anodic sub-micrometer material dissolution occurred at the metal-electrolyte interface. The recurring exposure allowed very precise control of the roughness level in the sub-µm range. In order to characterize the influence of the process parameters on the surface finish, the overall roughness was separated into microroughness, mesoroughness and waviness wavelength regimes. Suitable values for laser power, spot diameter, scan velocity, line spacing, number of passes and inter-pass rotation angle were identified to create a uniform surface finish.

The results showed, regardless of the initial roughness, which was between 0.5 µm and 3.4 µm, after several to hundreds scan passes, the surface finish approached a stable lower roughness limit with a minimum average surface roughness. Smoothing was caused by the higher material removal rate of roughness peaks as compared to valleys. The microroughness disappeared faster than the mesoroughness and waviness. Further levelling of the remaining valleys followed as the average surface plane receded. Once the lower roughness limit was achieved, the surface did not improve further. Laser-induced thermochemical polishing was verified for titanium (Grades 1 and 2), Ti6Al4V, Nitinol, Stellite 21 and metallic glass in a 5 M phosphoric acid solution. Based on the experimental results, it was possible to draw the following conclusions.

First, two fundamental variables, the thermal load T_L and the exposure time t_r, were identified to describe the average laser-induced impact on the surface. The influence of the process parameters on the material removal and roughness was shown to be generalized by these two variables. Depending on the material and thermal load, after an average exposure time between 2 s and 30 s, the surface finish approached its stable lower roughness limit. For the mentioned materials, material dissolution started at thermal thresholds of T_{th} = 111, 142, 92, 88 and 59 °C, respectively, and minimum surface

roughnesses of $S_{a,f}$ = 0.11, 0.18, 0.23, 0.28 and 0.14 µm were achieved. Depending on the material, the optimal thermal range for a high-quality surface finish was between 58 K to 190 K wide and was limited by the occurrence of pitting corrosion, material deposition or other secondary chemical effects. The lower roughness limit was primarily determined by discontinuities at grain and phase boundaries due to inhomogeneous etching.

Second, the mechanism of geometric levelling was shown to govern the observed smoothing. This mechanism is based on the exponential decrease of the surface amplitude as a function of the spatial frequency and the recess of the initial surface plane, measured by the material removal depth. A spatial filtering method was applied that attenuates the amplitudes of a Fourier-transformed surface depending on the removal depth. With this method, two-dimensional surface-height data can be predicted. Comparisons between the predicted and experimental results matched with accuracies above 90 %. Furthermore, a model of an ideal LCP process was presented, which implements geometric levelling based on local differences of the laser-induced thermal gradient in the direction perpendicular to the surface. A formula was derived for the decrease of the average roughness S_a as a function of average wavelength, laser-induced thermal gradient and average exposure time.

Third, the derived formula was verified to predict the average roughness S_a as an exponential decay over time consistent with the experimental results. The vast majority of the residuals between the predictions and experimental data were below 0.1 µm and within the error limits of the roughness measurements. High coefficients of determination of $R^2 > 0.95$ implied that more than 95 % of the variability of the experimental data was accounted for by the prediction formula. By applying the formula, the polishing time was shown to be inversely proportional to the spot diameter and thermal load, and was verified to decrease from 7 min 46 s to 1 min 22 s per square millimeter for spot diameters between 119 µm to 672 µm.

The presented model and derived formula provided accurate results as long as its boundary conditions were fulfilled, such that other mechanisms were of negligible importance. Not considered are effects associated to, first, significant changes of the absorptivity α during polishing, second, corrosion, deposition, or emerging gas occurring at high thermal loads, and third, discontinuities at grain and phase boundaries due to inhomogeneous etching.

Finally, the capabilities of the polishing process were demonstrated with several examples of polished surfaces and edges. Laser-induced thermochemical polishing allows selective processing of macroscopic surfaces (cm^2) with microscopic precision (µm).

References

[Alv12] Alvarez, E.; Vinciguerra, J.: The effect of a novel CoCr electropolishing technique on CoCr-UHMWPE bearing frictional performance for total joint replacements. In Tribology International, 2012, 47; pp. 204–211.

[Bar07] Barbour, M. E.; O'Sullivan, D. J.; Jenkinson, H. F.; Jagger, D. C.: The effects of polishing methods on surface morphology, roughness and bacterial colonisation of titanium abutments. In Journal of Materials Science. Materials in Medicine, 2007, 18; pp. 1439–1447.

[Bäu11] Bäuerle, D.: Laser Processing and Chemistry. Springer Berlin Heidelberg, Berlin, Heidelberg, 2011; pp. 477–487.

[Bir65] Birnbaum, M.: Semiconductor surface damage produced by ruby lasers. In Journal of Applied Physics, 1965, 36; pp. 3688–3689.

[Bon17] Bonse, J.; Hohm, S.; Kirner, S. V.; Rosenfeld, A.; Kruger, J.: Laser-induced periodic surface structures— a scientific evergreen. In IEEE Journal of Selected Topics in Quantum Electronics, 2017, 23.

[Bri11] Brinksmeier, E.; Gläbe, R.; Klocke, F.; Lucca, D. A.: Process signatures – an alternative approach to predicting functional workpiece properties. In Procedia Engineering, 2011, 19; pp. 44–52.

[Bri18a] Brinksmeier, E.; Reese, S.; Klink, A.; Langenhorst, L.; Lübben, T.; Meinke, M.; Meyer, D.; Riemer, O.; Sölter, J.: Underlying mechanisms for developing process signatures in manufacturing. In Nanomanufacturing and Metrology, 2018, 1; pp. 193–208.

[Bri18b] Brinksmeier, E.; Meyer, D.; Heinzel, C.; Lübben, T.; Sölter, J.; Langenhorst, L.; Frerichs, F.; Kämmler, J.; Kohls, E.; Kuschel, S.: Process signatures - the missing link to predict surface integrity in machining. In Procedia CIRP, 2018, 71; pp. 3–10.

[Bro01] Bronstein; Bronštejn, I. N.; Semendjaev, K. A.: Taschenbuch der Mathematik. Deutsch, Thun, 2001.

[Buc17] Buchkremer, S.; Klocke, F.: Compilation of a thermodynamics based process signature for the formation of residual surface stresses in metal cutting. In Wear, 2017, 376-377; pp. 1156–1163.

[Buh05] Buhlert, M.: Zur Dynamik des elektrochemischen Metallabtrags. Dissertation, 2005.

[Buh15] Buhlert, M.: Electropolishing. Electrolytic brightening, smoothing and deburring of stainless steel, steel, brass, copper, aluminium, titanium and magnesium. Leuze Verlag, Bad Saulgau, 2015; pp. 13–33.

[Car59] Carlslaw, H. S.; Jaeger, J. C.: Conduction of Heat in Solids. Oxford Univ. Press, Oxford, 1959;v pp. 50–80, 353–387.

[Cle84] Clerc, C.; Datta, M.; Landolt, D.: On the theory of anodic levelling: model experiments with triangular nickel profiles in chloride solution. In Electrochimica Acta, 1984, 29; pp. 1477–1486.

[Con90] Connors, K. A.: Chemical Kinetics: The Study of Reaction Rates in Solution. VCH, 1990; pp. 187–200, 245–261.

[Dat00] Datta, M.; Landolt, D.: Fundamental aspects and applications of electrochemical microfabrication. In Electrochimica Acta, 2000, 45; pp. 2535–2558.

[Dat87] Datta, M.; Romankiw, L. T.; Vigliotti, D. R.; Gutfeld, R. J. von: Laser etching of metals in neutral salt solutions. In Applied Physics Letters, 1987, 51; pp. 2040–2042.

[Dav11] Davis, V.; Edmonds, M. R.: Stone axe studies. III. Oxbow, Oxford, 2011; pp. 39–54.

[Del07] Delgado, A. V.; González-Caballero, F.; Hunter, R. J.; Koopal, L. K.; Lyklema, J.: Measurement and interpretation of electrokinetic phenomena. In Journal of Colloid and Interface Science, 2007, 309; pp. 194–224.

[Des04] Desilva, A.K.M.; Pajak, P. T.; Harrison, D. K.; McGeough, J. A.: Modelling and experimental investigation of laser assisted jet electrochemical machining. In CIRP Annals, 2004, 53; pp. 179–182.

[Edw51] Edwards, J.: An experimental study of electropolishing. In Transactions of the IMF, 1951, 28; pp. 133–154.

[Epp95] Eppinger, S. D.; Huber, C. D.; van Pham, H.: A methodology for manufacturing process signature analysis. In Journal of Manufacturing Systems, 1995, 14; pp. 20–34.

[Fan98] Fang, T.; Jafari, M. A.; Bakhadyrov, I.; Safari, A.; Danforth, S.; Langrana, N.: Online defect detection in layered manufacturing using process signature: 1998 IEEE International Conference on Systems, Man and Cybernetics. IEEE, Piscataway, 1998; pp. 4373–4378.

[Fra98] Frankel, G. S.: Pitting corrosion of metals. In Journal of The Electrochemical Society, 1998, 145; p. 2186.

[Fre18] Frerichs, F.; Lübben, T.: Development of process signatures for manufacturing processes with thermal loads without and with hardening. In Procedia CIRP, 2018, 71; pp. 418–423.

[Fri98] Frigo, M.; Johnson, S. G.: FFTW: an adaptive software architecture for the FFT. In Proceedings of the 1998 IEEE International Conference on Acoustics, Speech, and Signal Processing. IEEE, 1998; pp. 1381–1384.

[Gab72] Gabe, D. R.: Toward a universal electropolishing solution. In Metallography, 1972, 5; pp. 415–421.

[Gar85] Gardiner, C. W.: Handbook of Stochastic Methods for Physics, Chemistry and the Natural Sciences. Springer, Berlin, London, 1985.

[Ger02] Gerlach, C.: Räumliche und zeitliche Instabilitäten in einem technischen Prozess, Elektropolieren von Messing. Universität Bremen; FB2 Biologie/Chemie, 2002.

[Guo82] Guosheng, Z.; Fauchet, P. M.; Siegman, A. E.: Growth of spontaneous periodic surface structures on solids during laser illumination. In Physical Review B, Condensed Matter, 1982, 26; pp. 5366–5381.

[Gut87] Gutfeld, R. J. von: Laser-enhanced patterning using photothermal effects: maskless plating and etching. In Journal of the Optical Society of America B, 1987, 4; p. 272.

[Gut88] Gutfeld, R. J. von; Vigliotti, D. R.; Datta, M.: Laser chemical etching of metals in sodium nitrate solution. In Applied Physics Letters, 1988, 64; pp. 5197–5200.

[Hac12] Hackert-Oschätzchen, M.; Meichsner, G.; Zinecker, M.; Martin, A.; Schubert, A.: Micro machining with continuous electrolytic free jet. In Precision Engineering, 2012, 36; pp. 612–619.

[Huo03] Huo, J.; Solanki, R.; McAndrew, J.: Electrochemical polishing of copper for microelectronic applications. In Surface Engineering, 2003, 19; pp. 11–16.

[ISO97] International Organization for Standardization: ISO 4287 Geometrical Product Specifications (GPS)—surface texture: profile method, terms, definitions and surface texture parameters. In Geneve: International Organization for Standardization, 1997, 32; pp. 313–320.

[ISO12] International Organization for Standardization: ISO 25178, Geometrical product specifications (GPS) — surface texture: areal. https://www.iso.org/obp/ui/#iso:std:iso:25178:-2:ed-1:v1:en, accessed 6/22/2020.

[Jac36] Jacquet, P. A.: On the anodic behavior of copper in aqueous solutions of orthophosphoric acid. In Transactions of The Electrochemical Society, 1936, 69; p. 629.

[Jac56] Jacquet, P. A.: Electrolytic and chemical polishing. In Metallurgical Reviews, 1956, 1; pp. 157–238.

[Job11] Job, G.; Rüffler, R.: Physikalische Chemie. Eine Einführung nach neuem Konzept mit zahlreichen Experimenten. Springer Verlag, 2011.

[Kar89] Karima, M.; Chandrasekaran, N.; Tse, W.: Process signatures in metal stamping: basic concepts. In Journal of Materials Shaping Technology, 1989, 7; pp. 169–183.

[Kaw14] Kawanaka, T.; Kato, S.; Kunieda, M.; Murray, J. W.; Clare, A. T.: Selective surface texturing using electrolyte jet machining. In Procedia CIRP, 2014, 13; pp. 345–349.

[Kaw15] Kawanaka, T.; Kunieda, M.: Mirror-like finishing by electrolyte jet machining. In CIRP Annals, 2015, 64; pp. 237–240.

[Klo12] Klocke, F.; Zeis, M.; Klink, A.: Technological and economical capabilities of manufacturing titanium- and nickel-based alloys via electrochemical machining (ECM). In Key Engineering Materials, 2012, 504-506; pp. 1237–1242.

[Klo14] Klocke, F.; Klink, A.; Veselovac, D.; Aspinwall, D. K.; Soo, S. L.; Schmidt, M.; Schilp, J.; Levy, G.; Kruth, J.-P.: Turbomachinery component manufacture by application of electrochemical, electro-physical and photonic processes. In CIRP Annals, 2014, 63; pp. 703–726.

[Klo16] Klocke, F.; Vollertsen, F.; Harst, S.; Eckert, S.; Zeis, M.; Klink, A.; Mehrafsun, S.: Comparison of material modification occurring in laserchemical and electrochemical machining. In Proceedings INSECT 2016, 2016; pp. 57–64.

[Klo18] Klocke, F.; Harst, S.; Zeis, M.; Klink, A.: Modeling and simulation of the microstructure evolution of 42CrMo4 steel during electrochemical machining. In Procedia CIRP, 2018, 68; pp. 505–510.

[Kou12] Kouřil, M.; Christensen, E.; Eriksen, S.; Gillesberg, B.: Corrosion rate of construction materials in hot phosphoric acid with the contribution of anodic polarization. In Materials and Corrosion, 2012, 63; pp. 310–316.

[Küg19] Kügler, H.: Effects of short-term laser beam heating on the absorptivity of steel sheets. In Journal of Manufacturing and Materials Processing, 2019, 3; p. 41.

[Lai84] Laidler, K. J.: The development of the Arrhenius equation. In Journal of Chemical Education, 1984, 61; p. 494.

[Lan03] Landolt, D.; Chauvy, P.-F.; Zinger, O.: Electrochemical micromachining, polishing and surface structuring of metals: fundamental aspects and new developments. In Electrochimica Acta, 2003, 48; pp. 3185–3201.

[Lan07] Landolt, D.: Corrosion and Surface Chemistry of Metals. CRC Press, Lausanne, Boca Raton, 2007; pp. 119–179, 227–331.

[Lan87] Landolt, D.: Fundamental aspects of electropolishing. In Electrochimica Acta, 1987, 32; pp. 1–11.

[Lee06] Lee, D. E.; Hwang, I.; Valente, C. M. O.; Oliveira, J. F. G.; Dornfeld, D. A.: Precision manufacturing process monitoring with acoustic emission. In: Condition Monitoring and Control for Intelligent Manufacturing. Springer-Verlag London Limited, London, 2006; pp. 33–54.

[Lie81] Lienhard IV, J. H.; Lienhard V; John H.: A Heat Transfer Textbook. Philogiston Press, Cambridge, MA, 1981.

[Liu15] Liu, J.; Alfantazi, A.; Asselin, E.: The anodic passivity of titanium in mixed sulfate-chloride solutions. In Journal of The Electrochemical Society, 2015, 162; pp. 289–295.

[Mar99] Marx, D.: Protonenwanderung im virtuellen Labor. In Spektrum der Wissenschaft, 1999; pp. 21–25.

[Meh12] Mehrafsun, S.; Zhang, P.; Vollertsen, F.; Goch, G.: Laser-chemical precision machining of micro forming tools at low laser powers. In: Laser-based Micro- and Nanopackaging and Assembly VI. SPIE, 2012; 82440K; pp. 148-154.

[Meh13] Mehrafsun, S.; Vollertsen, F.: Disturbance of material removal in laser-chemical machining by emerging gas. In CIRP Annals, 2013, 62; pp. 195–198.

[Meh18] Mehrafsun, S.; Messaoudi, H.: Dynamic process behavior in laser chemical micro machining of metals. In Journal of Manufacturing and Materials Processing, 2018, 2; p. 54.

[Mes17] Messaoudi, H.; Eckert, S.; Vollertsen, F.: Thermal analysis of laser chemical machining part I: static irradiation. In Materials Sciences and Applications, 2017, 08; pp. 685–707.

[Mes18] Messaoudi, H.; Böhmermann, F.; Mikulewitsch, M.; Freyberg, A. von; Fischer, A.; Riemer, O.; Vollertsen, F.: Chances and limitations in the application of laser chemical machining for the manufacture of micro forming dies. In MATEC Web of Conferences, 2018, 190; p. 15010.

[Mey16] Meyer, D.; Kämmler, J.: Surface integrity of AISI 4140 after deep rolling with varied external and internal loads. In Procedia CIRP, 2016, 45; pp. 363–366.

[Mor05] Mora, A.; Haase, M.; Rabbow, T.; Plath, P. J.: Discrete model for laser driven etching and microstructuring of metallic surfaces. In Physical Review E Statistical, 2005, 72; p. 61604.

[Now95] Nowak, R.; Metev, S.; Sepold, G.: Nd:YAG-laser-induced wet chemical etching of titanium and stainless steel. In Sensors and Actuators A: Physical, 1995, 51; pp. 41–45.

[Now96] Nowak, R.; Metev, S.: Thermochemical laser etching of stainless steel and titanium in liquids. In Applied Physics A Materials Science & Processing, 1996, 63; pp. 133–138.

[Oka73] Okamoto, G.: Passive film of 18-8 stainless steel structure and its function. In Corrosion Science, 1973, 13; pp. 471–489.

[Oli07] Oliveira, N. T.C.; Aleixo, G.; Caram, R.; Guastaldi, A. C.: Development of Ti–Mo alloys for biomedical applications: microstructure and electrochemical characterization. In Materials Science and Engineering A, 2007, 452-453; pp. 727–731.

[Paj06] Pajak, P. T.; Desilva, A.K.M.; Harrison, D. K.; McGeough, J. A.: Precision and efficiency of laser assisted jet electrochemical machining. In Precision Engineering, 2006, 30; pp. 288–298.

[Pel12] Peleg, M.; Normand, M. D.; Corradini, M. G.: The Arrhenius equation revisited. In Critical Reviews in Food Science and Nutrition, 2012, 52; pp. 830–851.

[Per09] Perry, T. L.; Werschmoeller, D.; Li, X.; Pfefferkorn, F. E.; Duffie, N. A.: Pulsed laser polishing of micro-milled Ti6Al4V samples. In Journal of Manufacturing Processes, 2009, 11; pp. 74–81.

[Pet80] Fedkiw, P.: Primary current distribution on a sinusoidal profile. In Journal of The Electrochemical Society, 1980, 127; p. 1304.

[Pfe13] Pfefferkorn, F. E.; Duffie, N. A.; Li, X.; Vadali, M.; Ma, C.: Improving surface finish in pulsed laser micro polishing using thermocapillary flow. In CIRP Annals, 2013, 62; pp. 203–206.

[Pop11] Poprawe, R. Ed.: Tailored Light 2: Laser Application Technology. Springer-Verlag Berlin Heidelberg, Berlin, Heidelberg, 2011; pp. 43–62.

[Pui81] Puippe, J. C.; Acosta, R. E.; Gutfeld, R. J. von: Investigation of laser-enhanced electroplating mechanisms. In Journal of The Electrochemical Society, 1981, 128; pp. 2539–2545.

[Rab07] Rabbow, T.: Strukturbildung beim Mikrostrukturieren von Metallen in sauren Ätzmitteln mit dem Laser-Jet-Verfahren, 2007.

[Röm10] Römer, G.R.B.E.; Huis in ’t Veld, A. J.: Matlab Laser Toolbox. International Congress on Applications of Lasers & Electro-Optics. 2010, 1; pp. 523–529.

[Saf08] Safonova, L. P.; Pryahin, A. A.; Fadeeva, J. A.; Shmukler, L. E.: Viscosities, refractive indexes, and conductivities of phosphoric acid in N,N-dimethylformamide + water mixtures. In Journal of Chemical & Engineering Data, 2008, 53; pp. 1381–1386.

[Sch01] Scheffer, C.; Heyns, P. S.: Wear monitoring in turning operations using vibration and strain measurments. In Mechanical Systems and Signal Processing, 2001, 15; pp. 1185–1202.

[Sea16] Sealy, M. P.; Liu, Z. Y.; Guo, Y. B.; Liu, Z. Q.: Energy based process signature for surface integrity in hard milling. In Journal of Materials Processing Technology, 2016, 238; pp. 284–289.

[Sha08] Shabalovskaya, S.; Anderegg, J.; van Humbeeck, J.: Critical overview of Nitinol surfaces and their modifications for medical applications. In Acta Biomaterialia, 2008, 4; pp. 447–467.

[Sil11] Silva, A.K.M. de; Pajak, P. T.; McGeough, J. A.; Harrison, D. K.: Thermal effects in laser assisted jet electrochemical machining. In CIRP Annals, 2011, 60; pp. 243–246.

[Sip83] Sipe, J. E.; Young, J. F.; Preston, J. S.; van Driel, H. M.: Laser-induced periodic surface structure I: Theory. In Physical Review B, 1983, 27; pp. 1141–1154.

[Spi13] Spieser, A.; Ivanov, A.: Recent developments and research challenges in electrochemical micromachining (µECM). In The International Journal of Advanced Manufacturing Technology, 2013, 69; pp. 563–581.

[Ste02] Stephen, A.; Lilienkamp, T.; Metev, S.: Laser-assisted chemical micromachining of metals and alloys, 2002; pp. 56–63.

[Ste04] Stephen, A.; Sepold, G.; Metev, S.; Vollertsen, F.: Laser-induced liquid-phase jet-chemical etching of metals. In Journal of Materials Processing Technology, 2004, 149; pp. 536–540.

[Ste10] Stephen, A.; Vollertsen, F.: Mechanisms and processing limits in laser thermochemical machining. In CIRP Annals, 2010, 59; pp. 251–254.

[Ste11] Stephen, A.; Gerhard, C.; Vollertsen, F.: Laser-chemical finishing of micro forming tools: laser-based micro- and nanopackaging and assembly V. SPIE, 2011; 79210J; pp. 135-140.

[Ste13] Stenberg, N.; Proudian, J.: Numerical modelling of turning to find residual stresses. In Procedia CIRP, 2013, 8; pp. 258–264.

[Sto00] Stout, K.; Blunt, L.: Three-Dimensional Surface Topography. Elsevier, 2000; pp. 98–142.

[Swa10] Swain, J.: The “then and now” of electropolishing. In Surface World, 2010; pp. 30–36.

[Tou70a] Touloukian, Y. S.; Liley, P. E.; Saxena, S. C.: Thermophysical properties of matter-the TPRC data series. Volume 3. Thermal conductivity - nonmetallic liquids and gases. Thermophysical and Electronic Properties Information Analysis Center Lafayette In, 1970.

[Tou70b] Touloukian, Y. S.; Powell, R. W.; Ho, C. Y.; Klemens, P. G.: Thermophysical properties of matter-the TPRC data series. Volume 1. Thermal conductivity-metallic elements and alloys. Thermophysical and Electronic Properties Information Analysis Center Lafayette In, 1970.

[Vad12] Vadali, M.; Ma, C.; Duffie, N. A.; Li, X.; Pfefferkorn, F. E.: Pulsed laser micro polishing: surface prediction model. In Journal of Manufacturing Processes, 2012, 14; pp. 307–315.

[Vad13] Vadali, V. M.: Advanced Study of Pulsed Laser Micro Polishing. Dissertation, The University of Wisconsin-Madison, 2013.

[Wag54] Wagner, C.: Contribution to the theory of electropolishing. In Journal of The Electrochemical Society, 1954, 101; p. 225.

[Wan17] Wang, J.; Zhang, D.; Wu, B.; Luo, M.: Numerical and empirical modelling of machining-induced residual stresses in ball end milling of Inconel 718. In Procedia CIRP, 2017, 58; pp. 7–12.

[Wil03] Willenborg, E.; Wissenbach, K.; Poprawe, R.: Polishing by laser radiation. In Proceedings of the Second International WLT-Conference on Lasers in Manufacturing, 2003; pp. 297–300.

[Wil06] Willenborg, E.: Polieren von Werkzeugstählen mit Laserstrahlung. Zugl.: Aachen, Techn. Hochsch., Diss., 2005. Shaker, Aachen, 2006.

[Yan17] Yang, G.; Wang, B.; Tawfiq, K.; Wei, H.; Zhou, S.; Chen, G.: Electropolishing of surfaces: theory and applications. In Surface Engineering, 2017, 33; pp. 149–166.

[Yan18] Yang, S.; Li, W.: Surface Quality and Finishing Technology. In (Yang, S.; Li, W. Eds.): Surface finishing theory and new technology. Springer, Berlin, Germany, 2018; pp. 1–64.

[Zha15] Zhang, P.; Goch, G.: A quality controlled laser-chemical process for micro metal machining. In Production Engineering, 2015, 9; pp. 577–583.

Appendix

A.1 Temperature model

A.1.1 The boundary-value problem

The laser-induced temperature distribution and gradients are described by the heat equation as follows. The material substrate is assumed to be isotropic in all spatial dimensions, such that all temperature dependencies of the density ρ, specific heat capacity c_p, thermal conductivity K and thermal diffusivity $D_T = K/(\rho \cdot c_p)$ can be ignored. Furthermore, phase transformations between gases, liquids, and solids and chemical reaction enthalpies are disregarded, and fluid mechanical heat transfer into the electrolyte is not considered. The local temperature rise $\Delta T(x,y,z)$, is then described by the linear three-dimensional heat equation:

$$\rho c_p \left(\frac{\partial T}{\partial t} + v \cdot \nabla T \right) = K \nabla^2 T + Q \tag{A.1}$$

with the heat source Q and the laser beam velocity v. This heat equation is formulated in reference to the laser beam (if the heat source Q is time-independent), and is therefore stationary with respect to the conductive heat term $v \cdot \nabla T$ [Pop11]. A rectangular coordinate system fixed on the laser beam is used, with the origin directly beneath the beam center. The xy-plane is the substrate surface and the positive z-axis points into the material. The laser beam interacts on the surface at $z = 0$. **Figure A.1** shows the initial configuration.

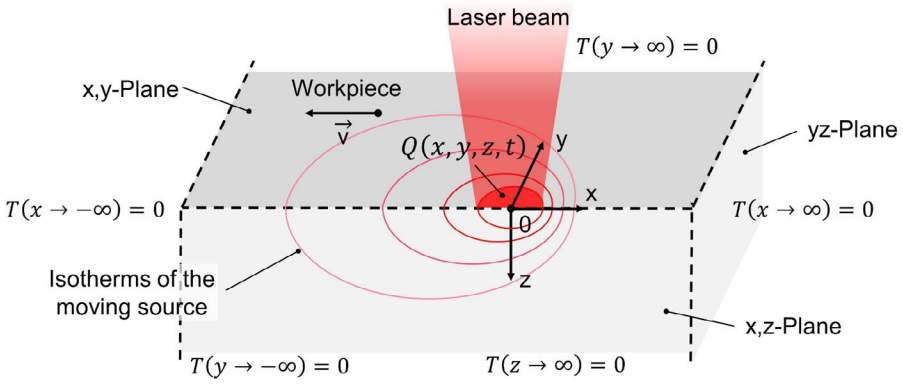

Figure A.1: Schematic of the boundry-value problem.

The source term in the heat equation is defined by the absorbed laser-light intensity $I_a = \alpha \cdot I_0$ within the medium and can be written in the form:

$$Q(x,y,z,t) = \alpha \cdot I(x,y) \cdot f(z) \cdot q(t) \tag{A.2}$$

where $I(x,y)$ describes the laser-intensity distribution on the surface, $f(z)$ describes the attenuation of the laser-light in z-direction and $q(t)$ is the temporal dependency (for modulated laser radiation). The laser-light intensity can be described by the Gaussian-shaped (TEM_{00} mode) intensity distribution:

$$I(x,y) = I_0 \cdot exp\left(-\frac{x^2+y^2}{w_0^2}\right) \tag{A.3}$$

with w_0 as the distance of the laser beam defined by $I(w_0) = I_0/e$, in contrast to the beam radius w_r, defined by $I(w_r) = I_0/e^2$, and the beam diameter, defined by $d_f = 2w_r$. Thus, $w_r = \sqrt{2}\cdot w_0$ or $w_0 = d_f/\sqrt{8}$. The laser power P_L results after integration over x and y:

$$P_L = 2\pi \int_{-\infty}^{\infty}\int_{-\infty}^{\infty} I(x,y)\,dxdy = \pi w_0^2 I_0 = \frac{\pi}{8} d_f^2 I_0 \tag{A.4}$$

For metals irradiated with laser radiation within the near-ultraviolet to near-infrared spectral range, the absorption typically occurs on the scale of the skin depth, which is small compared to the heat diffusion length or beam diameter. Therefore, the laser-light intensity that penetrates the material can be ignored, and the intensity is considered to be completely absorbed at the surface. The attenuation can be described by the delta function:

$$f(z) = 2 \cdot \delta(z) \tag{A.5}$$

Furthermore, for a static continuous wave laser beam (not modulated in time), the temporal dependency of the laser-intensity distribution is constant, with:

$$q(t) = 1 \tag{A.6}$$

A.1.2 General solution with the method of Green's functions

A general solution for the boundary problem with spatially infinite dimensions is provided by Green's functions. The initial conditions are defined as follows.

$$T(x,y,z,t=0) = 0 \qquad\qquad T \to 0 \text{ for } x,y,z \to \pm\infty \tag{A.7}$$

Using Green's functions, the resulting temperature distribution is given by a linear superposition of the temperature distribution of a point source. A detailed explanation can be found in Carslaw and Jaeger [Car59]. For the time-independent case ($q(t) = 1$), the Green function G of the heat equation with a Dirac delta source ($Q = \delta(x,y,z)$) reads [Pop11]:

$$G(\vec{r},\vec{r}') = \frac{1}{4\pi\kappa}\frac{1}{|\vec{r}-\vec{r}\prime|} exp\left(\frac{\vec{v}\cdot(\vec{r}-\vec{r}\prime)}{2\kappa}\right) exp\left(-\frac{|\vec{v}||\vec{r}-\vec{r}\prime|}{2\kappa}\right) \tag{A.8}$$

with the vector $\vec{r} = (x, z, y)$ and $\vec{r}' = (x', z', y')$. The general solution for a given source distribution $Q(x,y,z)$ can be calculated as a convolution of Green's functions:

$$T(x,y,z) = \int_{-\infty}^{\infty}\int_{-\infty}^{\infty}\int_{-\infty}^{\infty}\frac{Q(x',y',z\prime)}{\rho c_p} G(x,y,z,x',y',z')\,dx'dy'dz' \tag{A.9}$$

A.1.3 Boundary and initial conditions

The boundary problem for a uniform semi-infinite workpiece that is irradiated by a continuous wave laser beam focused on the surface can be derived from the solution of the entire space by mirroring the source at the plane that separates the two half-spaces. This is already account for in the source term by the factor 2 in Equation (A.5).

Thermal convection into the ambient electrolyte is neglected because the thermal conductivity of liquids such as water (K = 0.556 W/(m·K) [Tou70a]) or sulfuric acid (K = 0.544 W/(m·K) [Tou70a]) is at least one order of magnitude smaller than the thermal conductivity of most metals, such as titanium (K = 25 W/(m·K), Table 1) or stainless steel (K = 15 W/(m·K) [Tou70b]). Previous works have shown that heat losses into the electrolyte in LCM setups are below 10 K for beam diameters between 31 µm and 110 µm [Mes17]. Heat losses by thermal radiation are also neglected.

From the general solution of Equation (A.9), the solution of a semi-infinite substrate with a surface heat source $Q(x',y',z') = 2\alpha I(x,y)\delta(z)$ moving at a constant velocity $\vec{v}$ in the x-direction relative to the surface is as follows.

$$T(x,y,z) = \int_{-\infty}^{\infty}\int_{-\infty}^{\infty}\frac{\alpha I(x\prime,y\prime)}{2\pi K}\frac{exp\left(-\frac{v}{2\kappa}\left(x\text{-}x'+\sqrt{(x\text{-}x\prime)^2+(y\text{-}y\prime)^2+z^2}\right)\right)}{\sqrt{(x\text{-}x\prime)^2+(y\text{-}y\prime)^2+z^2}}dx'dy' \tag{A.10}$$

This expression can be evaluated numerically by FFT because the temperature is given by $T = \alpha I * G$, where * denotes the convolution operator [Röm10]. Applying the two-dimensional Fourier transform $F_2\{\cdot\}$ leads to:

$$F_2\{T\} = F_2\{\alpha I * G\} = \alpha F_2\{I\}F_2\{G\} \tag{A.11}$$

and inverse Fourier transformation yields:

$$T = \alpha F_2^{-1}\left\{F_2\{I\}F_2\{G\}\right\} \tag{A.12}$$

Using this method and replacing the continuous convolution by discrete convolutions, the temperature distribution of Equation (A.10) can be calculated numerically in $O(N^2)$ operations. A detailed explanation is given by Römer [Röm10].

A.1.4 Center temperature rise

The influence of the scan velocity on the temperature during LCM is negligible for velocities between 2 mm/s and 20 mm/s because the temperature decreases less than approximately 2 % compared to the static center temperature rise. **Figure A.2a** shows the center temperature rise $T(0,0,0)$ calculated with Equation (A.10) as a function of the scan velocity on a logarithmic scale. For scan velocities up to 100 mm/s, the center temperature rise is approximately constant. **Figure A.2b** shows, on a double logarithmic scale, the percentage deviation $T(v)/T(v = 0)\cdot 100$ of the moving center temperature rise compared to the static center temperature as a function of the scan velocity.

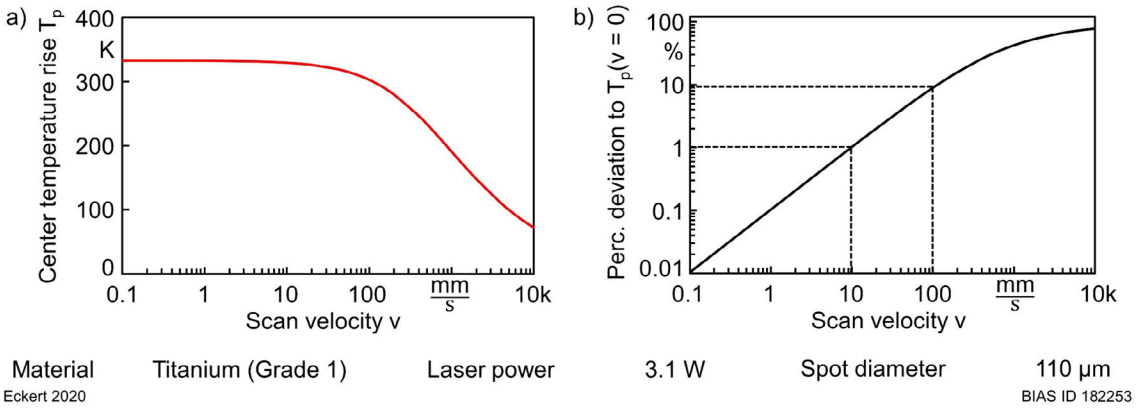

Figure A.2: Center temperature rise on titanium for a moving laser beam according to Equation (A.10).

As an approximation, $v = 0$ can be set for LCM. Thus, from Equation (A.10) with the surface temperature at $z = 0$:

$$\begin{aligned} T(x,y,0) &= \frac{\alpha}{2\pi K}\int_{-\infty}^{\infty}\int_{-\infty}^{\infty}\frac{I(x\prime,y\prime)}{\sqrt{(x-x\prime)^2+(y-y\prime)^2}}dx'dy' \\ &= \frac{\alpha I_0}{2\pi K}\int_{-\infty}^{\infty}\int_{-\infty}^{\infty}\frac{exp\left(-\left(x\prime^2+y\prime^2/w_0^2\right)\right)}{\sqrt{(x-x\prime)^2+(y-y\prime)^2}}dx'dy' \end{aligned} \tag{A.13}$$

The surface temperature increase in the center of the beam T_c at $x = 0$ and $y = 0$ is given by:

$$T_c := T(0,0,0) = \frac{\alpha I_0}{2\pi K}\underbrace{\int_{-\infty}^{\infty}\int_{-\infty}^{\infty}\frac{exp\left(-\left(x\prime^2+y\prime^2/w_0^2\right)\right)}{\sqrt{x\prime^2+y\prime^2}}dx'dy'}_{=\pi\sqrt{\pi}\,w_0} \tag{A.14}$$

This integral can be calculated analytically. The temperature increase in the center of the stationary Gauss beam is given by the simple linear relation:

$$T_p = \frac{2\cdot P_L\cdot\alpha}{\sqrt{2\pi}\cdot K\cdot d_f} \tag{A.15}$$

A.1.5 Temperature decrease in *z*-direction near the surface

The center temperature increase in the *z*-direction T(0,0,*z*) can be calculated analytically based on Equation (A.10) for $v = 0$ mm/s by solving the following (e.g., with WolframAlpha):

$$\begin{aligned} T(0,0,z) &= \frac{\alpha I_0}{2\pi K} \int_{-\infty}^{\infty} \int_{-\infty}^{\infty} \frac{exp\left(-\left(x'^2+y'^2/w_0^2\right)\right)}{\sqrt{x'^2+y'^2+z^2}} dx'dy' \\ &= \frac{\alpha I_0}{2\pi K} \left(\sqrt{\pi^3} \cdot w_0 \cdot exp\left(\frac{z^2}{w_0^2}\right) \cdot \left(1 - erf\left(\frac{z}{w_0}\right)\right)\right) \end{aligned} \tag{A.16}$$

Close to the surface ($z = 0$), the exponential and error functions can be approximated by the first term of their Taylor series according to:

$$T(0,0,z) = \frac{\alpha I_0}{2\pi K} \left(\sqrt{\pi}^3 \cdot w_0 \cdot \left(1 - \frac{2}{\sqrt{\pi}} \frac{z}{w_0}\right)\right) \tag{A.17}$$

Inserting Equation (A.4) and $w_0 = d_f/\sqrt{8}$ into the above yields:

$$T(0,0,z) = \frac{\sqrt{2}}{\sqrt{\pi}} \frac{\alpha P_L}{K d_f} - \frac{8}{\pi} \frac{\alpha P_L}{K d_f^2} \cdot z \tag{A.18}$$

The temperature gradient at $z = 0$ µm follows by calculating the derivative:

$$\frac{dT(0,0,0)}{dz} = \frac{8}{\pi} \frac{\alpha P_L}{K d_f^2} \tag{A.19}$$

A.2 Additional surface finish and removal depth results

Figure A.3 shows reflected-light images and height data for an initially ground surface (B1) after finishing with a laser power of 1.05 W and a spot diameter of 31 µm with an increasing number of passes. After 60 passes, the surface was visually smoothed, showing the globular titanium (Grade 1) microstructure. Further processing did not further improve the surface quality but increased the waviness.

Figure A.4 shows the average roughness S_a and removal depth h_s as functions of the number of passes. The roughness decreased rapidly from 0.57 µm down to 0.17 µm within 30 scan passes. Above 60 passes, the roughness increased slightly, due to the induced waviness. The removal depth increased linearly as a function of the number of passes.

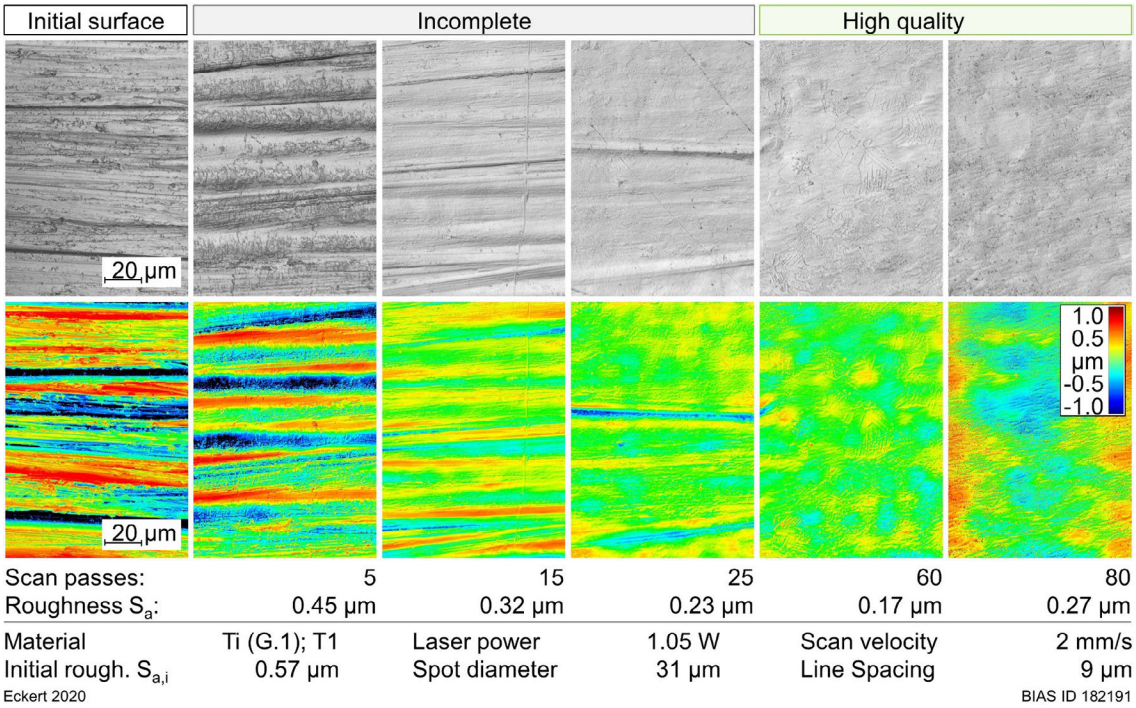

Figure A.3: Reflected-light images and surface-height data for an initally ground surface after finishing with an increasing number of scan passes.

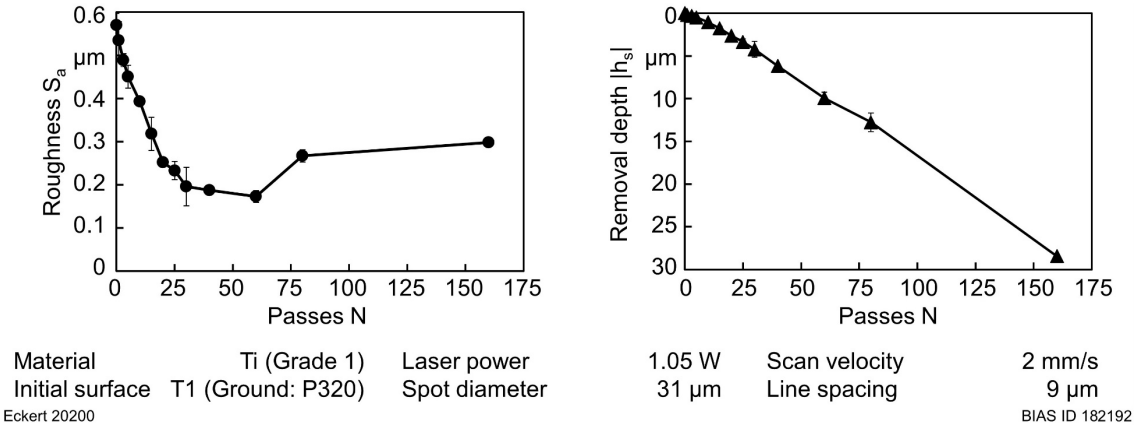

Figure A.4: Surface roughness and removal depth as functions of the number of passes.

Figure A.5 shows reflected-light images and height data for an initially abrasive-blasted surface (B3) after finishing with a laser power of 10.2 W and a spot diameter of 336 µm. The number of scan passes increased from 1 to 19, corresponding to exposure time from 0.8 s to 20 s. With increasing number of passes the average roughness decreased from 1.76 µm down to 0.27 µm. After 19 passes the surface was visually smoothed.

Figure A.6 shows the roughness S_a and the removal depth h_s as functions of the number of passes. Within the first 10 passes, the average roughness decreased rapidly and almost reached its lower limit with respect to the number of passes. The removal depth increased faster during the first 10 passes, after which the depth continued to increase linearly.

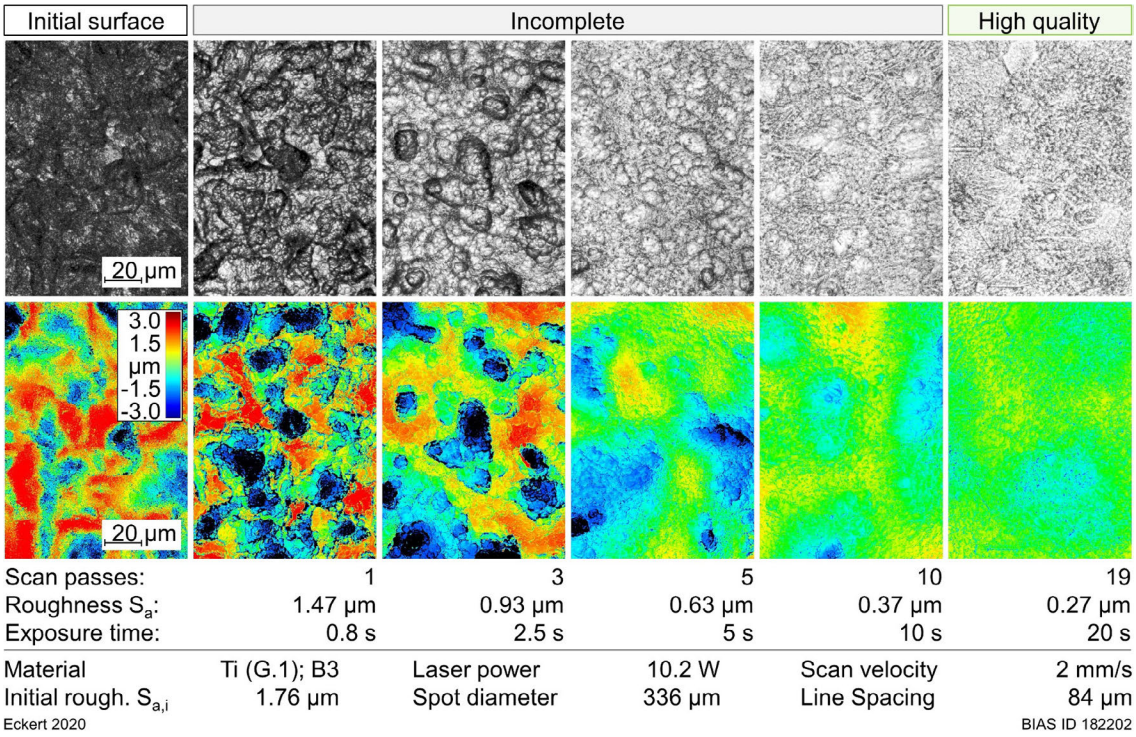

Figure A.5: Reflected-light images and surface-height data for surface finishes after processing with an increasing number of scan passes.

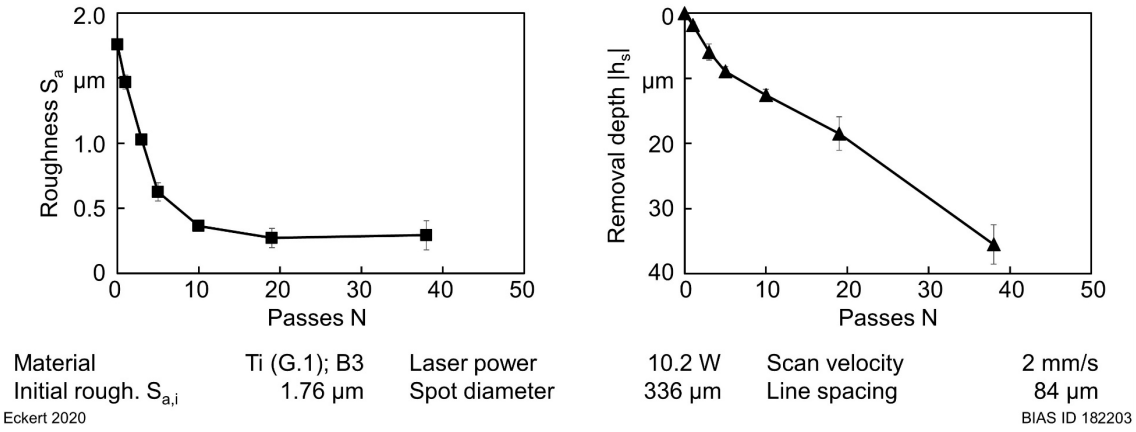

Figure A.6: Surface roughness and removal depth as functions of the number of passes.

Figure A.7 shows the reflected-light images and surface-height data for surface finishes processed with spot diameters of 60, 84, 168, 475 and 950 µm and, respectively, 108, 76, 38, 14 and 8 scan passes. These parameters were chosen so that the average exposure time was approximately 10 s in each case. For spot diameters below 475 µm, the surface roughness was significantly reduced to approximately 15 % of the initial value. For larger spot diameters, 475 µm and 950 µm, the surface roughnesses were reduced to only 25 % and 69 % of the initial value, respectively. The surface-height data show remnants from the initial roughness.

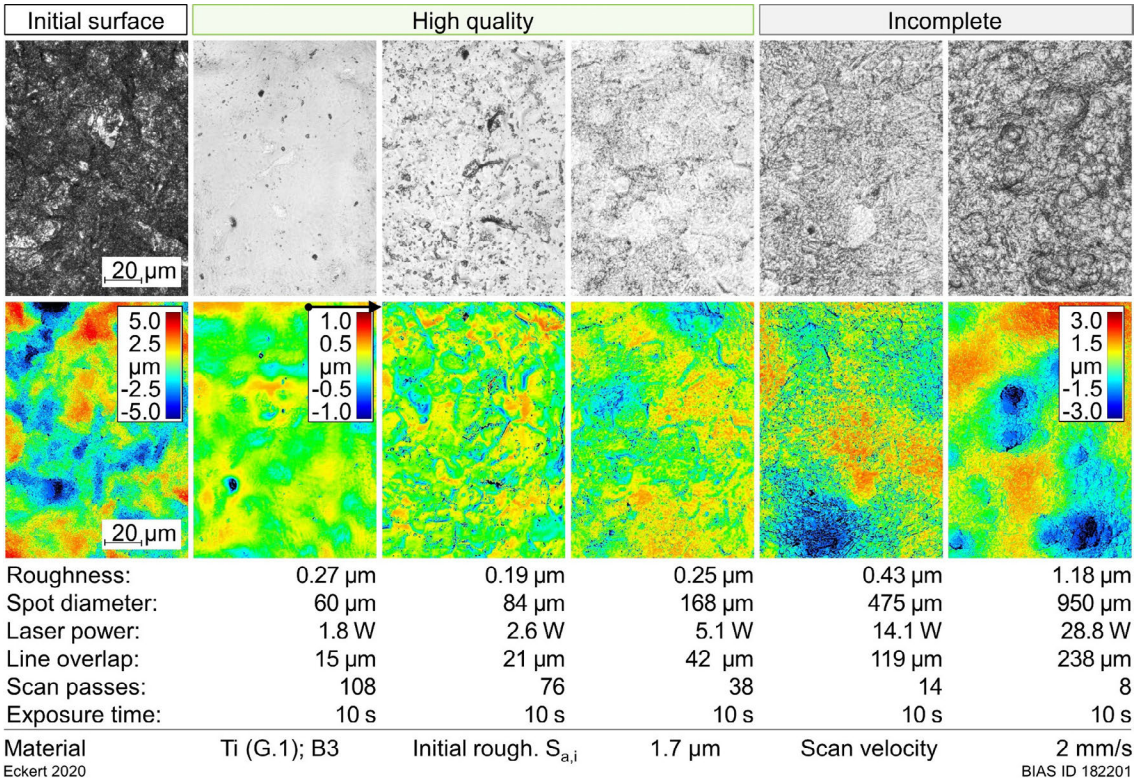

Figure A.7: Reflected-light images and surface-height data of surface finishes after processing with different spot diameters at an exposure time of 10 s.

A.3 Additional surface prediction data

Figure A.8 shows the predicted surface-height data for an initially rolled surface (B1) after 1.3, 3.5, 6.3, 14.9 and 30.3 µm of material removal. These predictions correspond to the experimental measurements shown in **Figure 5.19**. The experimental data were polished with a spot diameter of 110 µm, laser power of 2.46 W and line spacing of 35 µm. The measurements and predictions show a similar surface finish. Note that the measurements are made at different locations on the sample. Except for removal depths greater than or equal to 14.9 µm, the average roughness of the measurements and predictions agree within an error of approximately 7 %.

Figure A.9a shows the measured roughness S_a from **Figure 5.20a** of a rolled surface as a function of its removal depth (**Figure 5.23**) and the corresponding average roughness predicted from the surface-height data (red line). The experimental and predicted data are consistent within the measurement accuracy, except for removal depths larger than 10 µm. The predicted average roughness decreases exponentially with the removal depth, as does the measured roughness. The faster levelling of microroughness compared to mesoroughness and waviness is predicted, as shown in the predicted roughness spectra in **Figure A.9b**, which shows a similar change as the experimental results in **Figure 5.20b**.

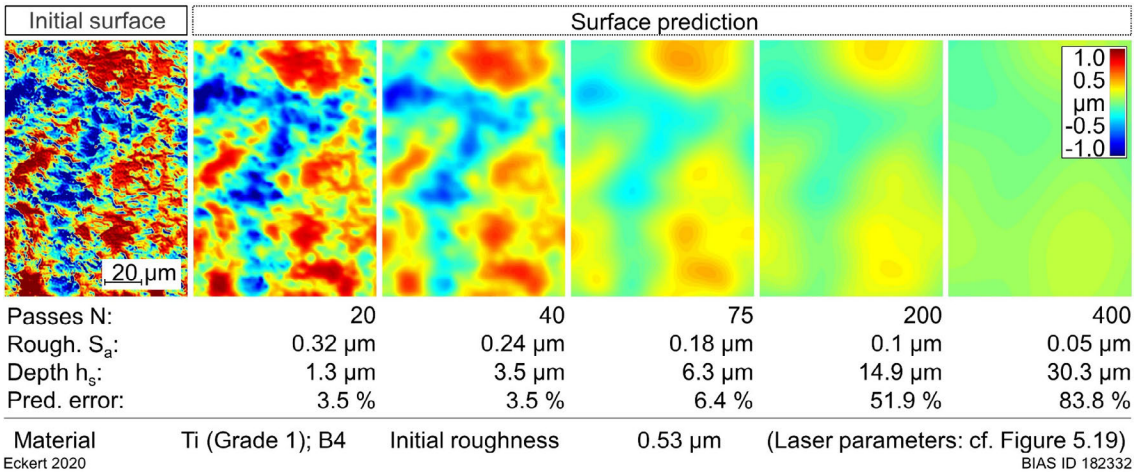

Figure A.8: Predicted surface-height data for various removal depths (cf. Figure 5.19).

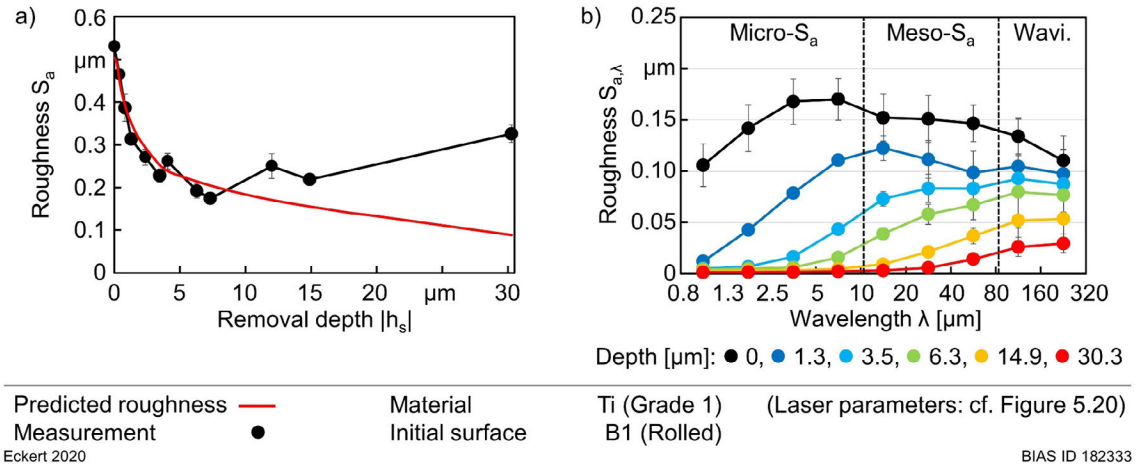

Figure A.9: (a) Measured (in black) and predicted (in red) average roughness as a function of the removal depth (cf. Figure 5.20) and (b) the predicted roughness spectra for different removal depths.

Figure A.10 shows the predicted surface-height data for an initially ground surface (T1) after 0.5, 1.8, 3.4, 9.9 and 12.8 µm of material removal. These surface-height data correspond to the experimental measurements shown in **Figure A.3**. The experimental data were acquired with polishing under a spot diameter of 31 µm, laser power of 1.05 W and line spacing of 9 µm. The measurements and predictions agree within an error of approximately 7 % for average roughnesses above the stable lower limit.

Figure A.11 shows the experimentally measured surface roughness S_a from **Figure A.4** as a function of its removal depth and the corresponding average roughness predicted from the surface-height data (red line). The experimental and predicted data are consistent within the measurement accuracy, except for removal depths larger 10 µm. The predicted average roughness of the initially ground surface (T1) decreases exponentially with the removal depth, as observed experimentally.

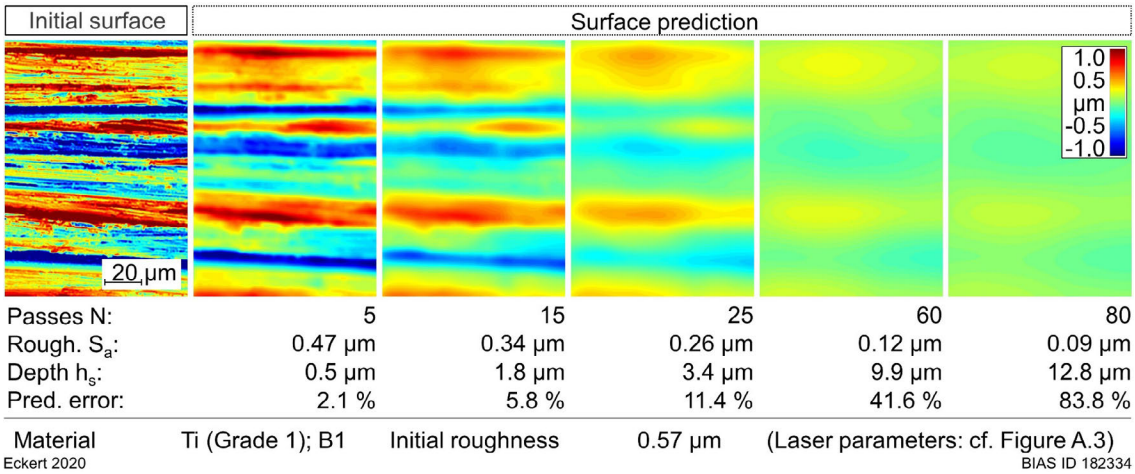

Figure A.10: Predicted surface-height data for various removal depths (cf. Figure A.3).

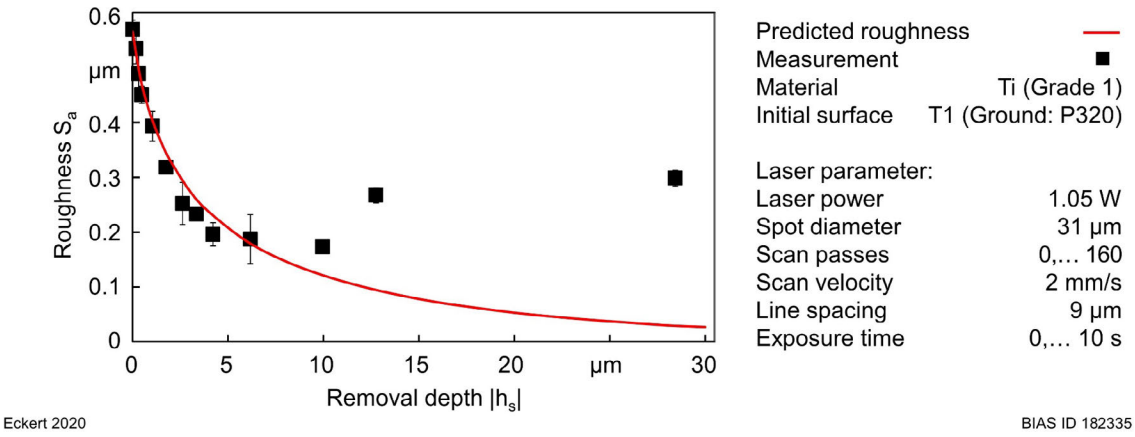

Figure A.11: Predicted (red line) and measured average roughness as a function of the removal depth (cf. Figure A.4).

Figure A.12 shows the predicted surface-height data of an initially sand blasted surface (B3) after 1.0, 2.9, 6.8, 12.6 and 35.5 µm of material removal. These surface-height data correspond to the experimental measurements shown in **Figure A.5**. The experimental data were acquired under polishing with a spot diameter of 336 µm, laser power of 10.5 W and line spacing of 84 µm. The predictions and measurements show a very similar smoothed surface finish, even though the measured surface-height data were taken at different locations on the sample surface, and a significantly larger spot diameter was used than for the predictions shown in **Figure A.8** and **Figure A.10**.

Figure A.13 shows the measured roughness S_a from **Figure A.6** as a function of removal depth and the corresponding average roughness predicted from the surface-height data (red line). Even for a spot diameter of 336 µm and laser power of 10.5 W, the experimental and predicted data are consistent within the measurement accuracy.

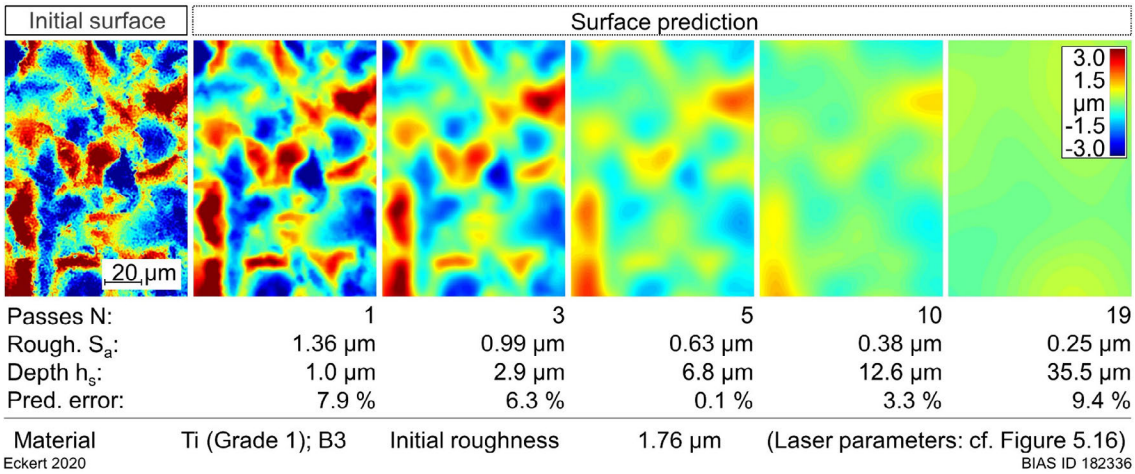

Figure A.12: Predicted surface-height data for various removal depths (cf. **Figure 5.26**).

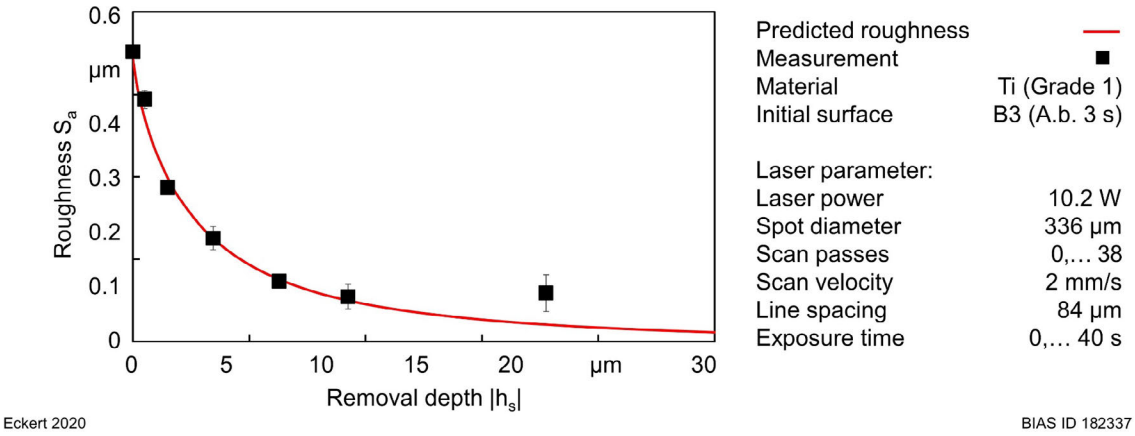

Figure A.13: Average roughness as a function of the removal depth (cf. Figure 5.27) and the corresponding predicted roughness.

A.4 LCP activation energy of titanium in H_3PO_4

The Arrhenius Equation (7.10) describes the (reaction) rate constant k as a function of temperature in kelvin. It can be used to determine the activation energy E_a and chemical reaction rates, or to model temperature dependencies of various chemical processes, such as creep rates, diffusion coefficients, etc. [Lai84]. For chemical reactions that occur in the volume of a solution, the rate constant is expressed in units of $m^3/(mol \cdot s)$ and describes the frequency of collisions in a specific volume per mole of substance. For reactions that occur at an interface, the surface area (instead of the molar concentration) determines the rate constant, which is then expressed in units of $m^3/(m^2 \cdot s)$ [Con90]. Thus, the rate constant during LCP is given by the average exposure time t_r and the cavity volume V_c divided by the irradiated area (the cavity width w_c times its length L_c). In this context, the rate constant is expressed in units of m/s and is equal to the average removal velocity. **Figure A.14** shows the logarithm of the average removal velocity calculated based on the results shown in **Figure 5.6** and **Figure 5.7** as a function of the inverse thermal load $1/(T_L+294\ K)$ (Equation (A.15)) in kelvin.

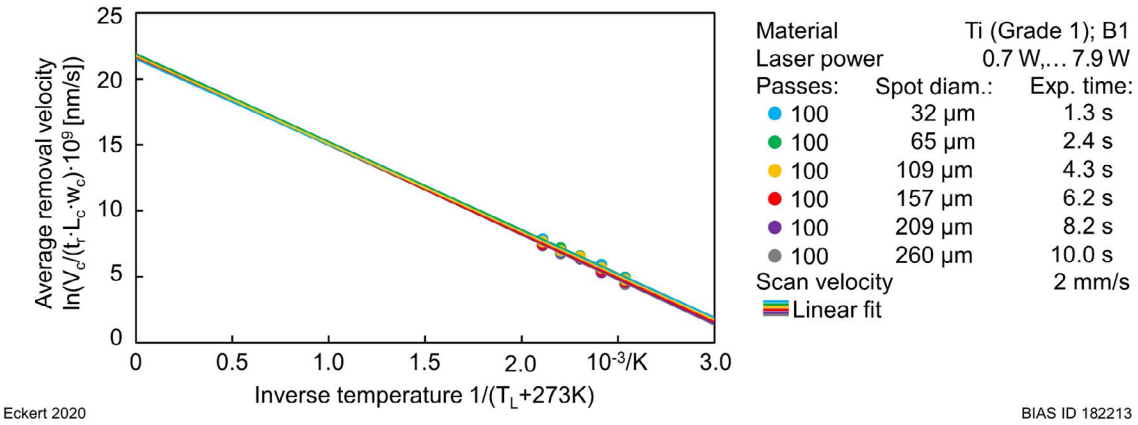

Figure A.14: Arrhenius plot of the average removal rate as a function of the inverse center temperature calculated based on the experimental results from Figure 5.6 and Figure 5.7.

Data points for each spot diameter were fitted by a linear regression according to:

$$\ln\left(\frac{V_c}{w_c L_c t_r}\right) = \ln(A_a) - \frac{E_a}{R}\left(\frac{1}{T_p}\right) \tag{A.20}$$

where R is the universal gas constant and A_a is the pre-exponential factor. The fit parameters for $\ln(A_a)$ and E_a/R are summarized in Table A.7.

Table A.7: Fit parameters from the linear regression on the Arrhenius plot.

Spot diameter d_f [µm]	34	62	109	158	209	260	Average
Fit parameter E_a/R [kK]	6.53	6.67	6.67	6.69	6.78	6.82	6.69
Activation energy E_a [kJ/mol]	54.3	55.4	55.5	44.6	56.4	56.7	55.7
Fit parameter $\ln(A_a)$ [nm/s]	21.5	21.9	21.7	21.6	21.8	21.8	21.7
pre-exponential factor A_a [m/s]	2.19	3.29	2.77	2.56	2.88	2.91	2.77

The straight lines have almost the same slope E_a/R and interception with the y-axis. Thus, the activation energy is independent of the spot diameter, determined by the average value of $E_a = 55.7$ kJ/mol and the pre-exponential factor of $A_a = 2.77$ m/s. With these parameters, the Arrhenius equation can be used to calculate the average removal velocity. For $T = T_{th} + 294$ K = 405 K, an average material removal of 0.2 µm would result at the thermal threshold after an exposure time of 1 s. This value is within the range of the order of magnitude of the optical measurement resolution, and thereby gives reason to the definition of the thermal threshold. **Figure A.15** shows, on the primary y-axis, the experimental results for the removal velocity (**Figure 6.3**) as a function of the thermal load, and on the secondary y-axis the average removal velocity calculated with the Arrhenius equation using the averaged fit parameters from Table A.7. Due to the Gaussian-like removal cavity, the average removal velocity calculated with the Arrhenius equation is supposed to be much smaller than that seen in the cavity center (from the measurement data). The activation energy in the Arrhenius equation can be interpreted as the energy required to initiate the chemical reaction and determines the increase in the

reaction rate. A 20 % higher activation energy shifts the removal velocity to higher thermal loads (dashed blue line) and a 20 % smaller activation energy shifts the removal velocity to lower thermal loads (dotted blue line).

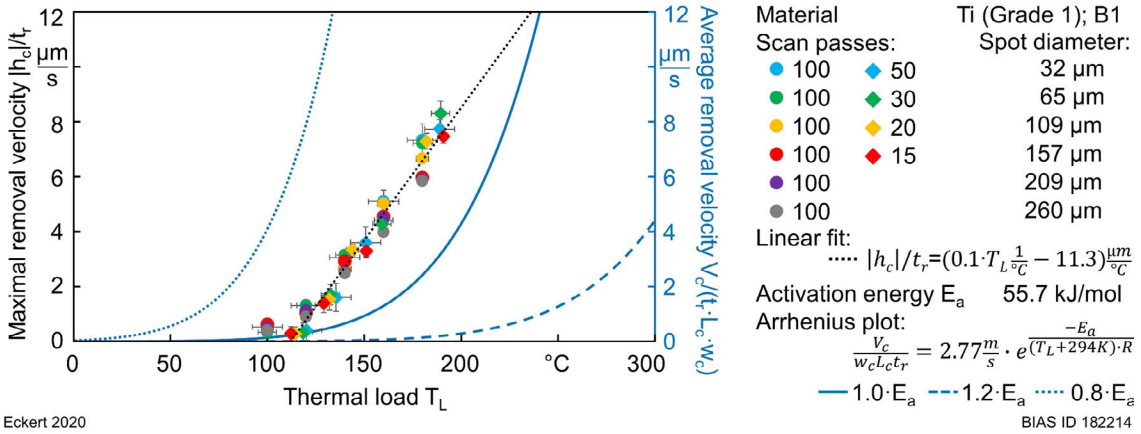

Figure A.15: Removal velocity as a function of thermal load T_L for six different spot diameters and the corresponding Arrhenius plot.

A.5 Determination of the factor c_a

The material removal depth can be calculated with Equation (2.13) with the constant c_T instead of c_D and the relation $dh_s = -ds_{avg}$ as follows:

$$\mathrm{d}h_s = c_T dt = \frac{m_M K}{\rho E_a c_a} \cdot \frac{(T_L - T_{th})}{d_f} dt \tag{A.21}$$

Integration of Equation (A.21) and substitution of the exposure time t_r (Equation (4.4)), yields:

$$h_s = \frac{\pi}{4} \frac{m_M K}{\rho E_a} \cdot \frac{(T_L - T_{th})}{d_f} \cdot \frac{d_f^2}{b \cdot v} \cdot \frac{1}{c_a} N \tag{A.22}$$

All parameters except the constant c_a are known in Equation (A.22). The equation can therefore be used to determine the constant c_a by comparison with the experimental data. **Figure A.16** shows the material removal depth as a function of the scan passes for the experimental data (black data points) from **Figure 5.45** and the calculated removal depth (red line) according to Equation (A.22). The calculated data correctly describe the approximately linear material removal increase. Thereby, the constant factor was assumed to be $c_a = 10^3$. Deviations from the calculated linear progression could be related to the changing absorption during polishing in the process beginnings.

In the same way, **Figure A.17** shows the material removal depth (black data points) of **Figure 5.23** as a function of scan passes as well as the calculated removal depth (red line) according to Equation (A.22). With a constant factor of $c_a = 10^3$, Equation (A.22) described the experimental data correct.

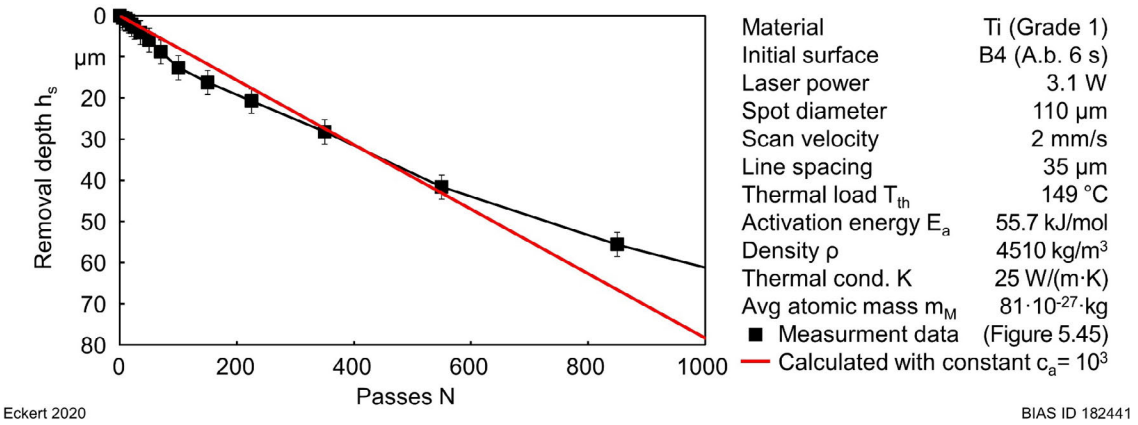

Figure A.16: Measured (Figure 5.45) and calculated removal depth h_s and as a function of the number of passes for a initially 6 s abrasive blasted surface.

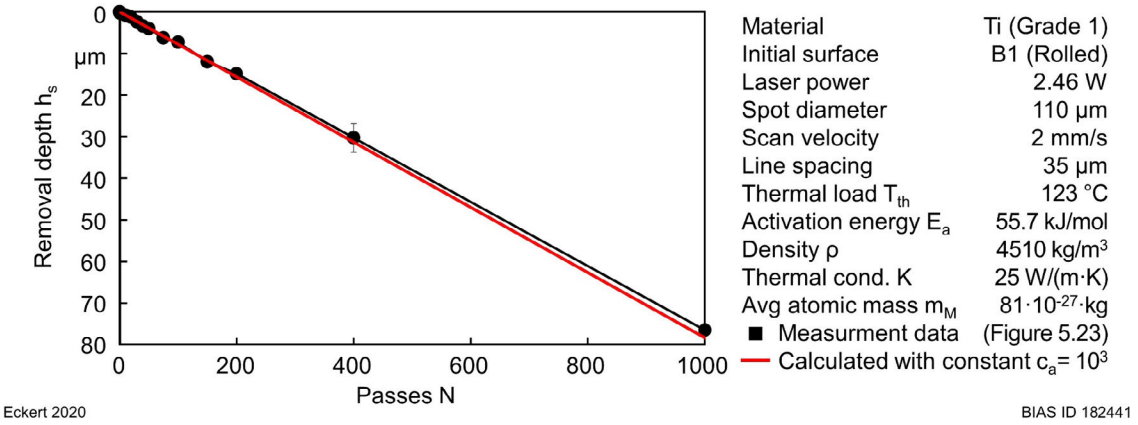

Figure A.17: Measured (Figure 5.23) and calculated removal depth h_s and as a function of the number of passes for a initially rolled surface.

These results confirm the assumed value of 10^3 for the proportionality constant c_a in Equation (7.15).

Publication List

Articles in journals with peer review (contributing to this work)

Eckert, S.: Multi-Cycle process signature of laser-induced thermochemical polishing. In Journal of Manufacturing and Materials Processing, 2019, 3; p. 90.

Eckert, S.; Vollertsen, F.: Mechanisms and processing limits of surface finish using laser-thermochemical polishing. In CIRP Annals, 2018, 67; pp. 201–204.

Messaoudi, H.; Eckert, S.; Vollertsen, F.: Thermal analysis of laser chemical machining part I: static irradiation. In Materials Sciences and Applications, 2017, 08; pp. 685–707.

Eckert, S.; Messaoudi, H.; Mehrafsun, S.; Vollertsen, F.: Laser-thermochemical induced micro-structures on titanium. In Journal of Materials Science & Surface Engineering, 2016; pp. 685–691.

Articles in journals with peer review

Borchers, F.; Clausen, B.; Eckert, S.; Ehle, L.; Epp, J.; Harst, S.; Hettig, M.; Klink, A.; Kohls, E.; Meyer, H.; Meurer, M.: Comparison of Different Manufacturing Processes of AISI 4140 Steel with Regard to Surface Modification and Its Influencing Depth. Metals, 10(7), p. 895.

Articles in journals without peer review

Eckert, S.; Vollertsen, F.: Prozessbeschleunigung beim laserchemischen Polieren. Laser Magazin, 2020, 2; pp. 20-23

Zhao, T.; Eckert, S.; Vollertsen, F.: Recast zone and unmelted zone of the white layer induced by microsecond pulsed laser surface processing of 42CrMo4 alloy steel. In Lasers in Engineering (Old City Publishing), 2018; pp. 349–358.

Contributions at conferences with peer review

Mehrafsun, S.; Harst, S.; Hauser, O.; Eckert, S.; Klink, A.; Klocke, F.; Vollertsen, F.: Energy-based analysis of material dissolution behavior for laser-chemical and electrochemical machining. In Procedia CIRP, 2016, 45; pp. 347–350.

Contributions at conferences

Klink, A.; Rommes, B.; Zander, D.; Schupp, A.; Vollertsen, F.; Eckert, S.: Mechanism-based classification of electrochemical machining processes. In International Symposium on Electrochemical Machining Technology, 2019.

Eckert, S.; Gadeschi, G. B.; Meinke, M.; Vollertsen, F.; Schröder, W.: Comparison of laser-induced thermal heat impact on 42CrMo4 in gaseous and liquid ambient. In International Symposium on Electrochemical Machining Technology 2018, 2018.

Eckert, S.; Köhnsen, A.; Vollertsen, F.: Surface finish using laser-thermochemical machining. In Lasers in Manufacturing Conference 2017, 2017.

Klocke, F.; Vollertsen, F.; Harst, S.; Eckert, S.; Zeis, M.; Klink, A.; Mehrafsun, S.: Comparison of material modification occurring in laserchemical and electrochemical machining. In International Symposium on Electrochemical Machining Technology, 2016.

Student Works

The present work contains results that were produced in the context of the supervision of subsequent student theses:

Köhnsen, A.: Einfluss des Gefüges auf die Oberflächenrauheit beim laserchemischen Polieren, Masterarbeit, März 2017

Köhnsen, A.; Niemeier, T.; Hövermann, W.: Entwicklung und Erprobung einer Prozesszelle für die Laserbearbeitung in reaktiven Medien, Masterprojektarbeit, Juni 2016.

Reihe Strahltechnik im BIAS Verlag

Bisher erschienen:

Herausgegeben von Frank Vollertsen, Ralf Bergmann

Hannes Freiße
Hartpartikelverstärkte Oberfläche für das Trockentiefziehen eines hochlegierten Stahls
Strahltechnik Bd. 72, Bremen, 2020, ISBN 978-3-933762-66-5

Markus Prieske
Eignung von CVD-Diamantschichten für die Trockenumformung von Aluminium
Strahltechnik Bd. 71, Bremen, 2020, ISBN 978-3-933762-65-8

Hamza Messaoudi
Thermal conditions for laser chemical micro processing of metals
Strahltechnik Band 70, Bremen 2020, ISBN 978-3-933762-64-1

Tim Radel
Laserstrahlschweißen von Aluminiumlegierungen mit Schwingungsüberlagerung
Strahltechnik Band 69, Bremen 2020, ISBN 978-3-933762-63-4

Silke Huferath-von Lüpke
Produktionsbegleitende Messeinrichtung basierend auf digitaler Holografie
Strahltechnik Band 68, Bremen 2019, ISBN 978-3-933762-62-7

Salar Mehrafsun
Dynamisches Prozessverhalten bei der laserinduzierten thermochemischen Mikrostrukturierung von Metallen
Strahltechnik Band 67, Bremen 2018, ISBN 978-3-933762-61-0

Vijay V. Parsi Sreenivas
Material modifications due to nonlinear effects created by multiphoton absorption in single crystalline silicon
Strahltechnik Band 66, Bremen 2017, ISBN 978-3-933762-60-3

Peer Woizeschke
Eigenschaften laserstrahlgefügter Mischverbindungen aus Aluminium und Titan in Abhängigkeit der Kantengeometrie und Halbzeugstruktur
Strahltechnik Band 65, Bremen 2017, ISBN 978-3-933762-59-7

Henry Köhler
Schwingfestigkeit laserauftraggeschweißter legierter Stähle
Strahltechnik Band 64, Bremen 2017, ISBN 978-3-933762-58-0

Jörg Volpp
Dynamik und Stabilität der Dampfkapillare beim Laserstrahltiefschweißen
Strahltechnik Band 63, Bremen 2017, ISBN 978-3-933762-57-3

Colin Dankwart
High resolution of wave fields from measurements with unknown sensor positions and unknown phase shifts of the object wave
Strahltechnik Band 61, Bremen 2017, ISBN 978-3-933762-55-9

Edwin N. Kamau
Dynamic wave field synthesis: enabling the generation of field distributions with a large space-bandwidth product
Strahltechnik Band 60, Bremen 2016, ISBN 978-3-933762-54-2

Felix Möller
Wechselwirkung zwischen Lichtbogen und Laserstrahl beim Fügen von Aluminium
Strahltechnik Band 59, Bremen 2016, ISBN 978-3-933762-53-3

Simon Kibben
UV-laserbasierte Oberflächenfluorierung von Polymeren
Strahltechnik Band 58, Bremen 2016, ISBN 978-3-933762-52-8

Heiko Brüning
Prozesscharakteristiken des thermischen Stoffanhäufens in der Mikrofertigung
Strahltechnik Band 57, Bremen 2017, ISBN 978-3-933762-51-1

Michael Schwander
Lokale Diamantsynthese durch einen laserbasierten atmosphärischen CVD-PVD-Prozess
Strahltechnik Band 56, Bremen 2016, ISBN 978-3-933762-50-4

Marius Gatzen
Durchmischung beim Laserstrahltiefschweißen unter dem Einfluss niederfrequenter Magnetfelder
Strahltechnik Band 55, Bremen 2015, ISBN 978-3-933762-49-8

Frank Vollertsen, Hendrik Tetzel (Hrsg.)
Thermal Forming and Welding Distortion, Proceedings of the IWOTE‘14
Strahltechnik Band 54, Bremen 2014, ISBN 978-3-933762-48-1

Zhuo Tang
Heißrissvermeidung beim Schweißen von Aluminiumlegierungen mit einem Scheibenlaser
Strahltechnik Band 53, Bremen 2014, ISBN 978-3-933762-47-4

Martin Grden
Simulation thermischen Biegens mittels Gebietszerlegung
Strahltechnik Band 52, Bremen 2014, ISBN 978-3- 933762-46-7

Jens Sakkiettibutra
Modellierung thermisch bedingter Formänderungen und Eigenspannungen von Stählen zum Aufbau von geregelten Prozessen
Strahltechnik Band 51, Bremen 2013, ISBN 978-3-933762-45-0

Frank Buschenhenke
Prozesskettenübergreifende Verzugsbeherrschung beim Laserstrahlschweißen am Beispiel einer Welle-Nabe-Verbindung
Strahltechnik Band 50, Bremen 2013, ISBN 978-3-933762-44-3

Daniel Reitemeyer
Stabilisierung der Fokuslage beim Schweißen mit Faser- und Scheibenlasern
Strahltechnik Band 49, Bremen 2013, ISBN 978-3-933762-43-6

Steffen Neumann
Einflussanalyse beim single mode Faserlaserschweißen zur Vermeidung des Humping-Phänomens
Strahltechnik Band 48, Bremen 2012, ISBN 978-3-933762-42-9

Mostafa Agour
Determination of the complex amplitude of monochromatic light from a set of intensity observations
Strahltechnik Band 47, Bremen 2011, ISBN 978-3-933762-41-2

Andreas Stephen
Elektrochemisches Laser-Jet-Verfahren zur Mikrostrukturierung von Metallen
Strahltechnik Band 46, Bremen 2011, ISBN 978-3-933762-40-5

Michael Koerdt
Herstellung von integriert-optischen Sensorstrukturen in Polymersubstraten basierend auf Brechzahländerungen durch ultraviolette Laserstrahlung
Strahltechnik Band 45, Bremen 2011, ISBN 978-3-933762-39-9

Hanna Wielage
Hochgeschwindigkeitsumformen durch laserinduzierte Schockwellen
Strahltechnik Band 44, Bremen 2011, ISBN 978-3-933762-38-2

Claus Thomy
Dynamisches Prozessverhalten beim Laserstrahl-MSG-Hybridschweißen
Strahltechnik Band 43, Bremen 2011, ISBN 978-3-933762-37-5

Thomas Seefeld
Laser-Randschichtschmelzen mit erhöhter Prozessgeschwindigkeit am Beispiel von Aluminium-Zylinderlaufbahnen
Strahltechnik Band 42, Bremen 2011, ISBN 978-3-933762-36-8

Frank Vollertsen (Hrsg.)
Thermal Forming and Welding Distortion
Strahltechnik Band 41, Bremen 2011, ISBN 978-3-933762-35-1

Frank Vollertsen, Daniel Reitemeyer (Hrsg.)
Laserstrahlfügen: Prozesse, Systeme, Anwendungen, Trends
Strahltechnik Band 40, Bremen 2010, ISBN 978-3-933762-34-4

Claas Falldorf
Bestimmung der komplexwertigen Amplitude von Wellenfeldern auf Basis des Prinzips der Selbstreferenz
Strahltechnik Band 39, Bremen 2010, ISBN 978-3-933762-33-7

Marc Baumeister
Dynamische Laser-Mikroperforation mit single-mode Faserlaser
Strahltechnik Band 38, Bremen 2009, ISBN 978-3-933762-31-3

Zhenyu Hu
Analyse des tribologischen Größeneffekts beim Blechumformen
Strahltechnik Band 37, Bremen 2009, ISBN 978-3-933762-30-6

Frank Vollertsen, Thomas Seefeld (Eds.)
Laserbearbeitung: Prozesse, Systeme, Anwendungen, Trends
Strahltechnik Band 36, Bremen 2008, ISBN 978-3-933762-28-3

Torsten Baumbach
Untersuchungen zur vergleichenden, digitalen Holografie mit aktiver Wellenfrontmodifikation
Strahltechnik Band 35, Bremen 2008, ISBN 978-3-933762-27-6

Knut Partes
Hochgeschwindigkeitsbeschichten mit dem Laserstrahl
Strahltechnik Band 34, Bremen 2008, ISBN 978-3-933762-26-9

Hendrik Schulze Niehoff
Entwicklung einer hochdynamischen, zweifachwirkenden Mikroumformpresse
Strahltechnik Band 33, Bremen 2008, ISBN 978-3-933762-25-2

Thorsten Bothe
Grundlegende Untersuchungen zur Formerfassung mit einem neuartigen Prinzip der Streifenprojektion und Realisierung in einer kompakten 3D-Kamera
Strahltechnik Band 32, Bremen 2008, ISBN 978-3-933762-24-5

F. Vollertsen, J. Sakkiettibutra (Hrsg.)
Thermal Forming and Welding Distortion
Strahltechnik Band 31, Bremen 2008, ISBN 978-3-933762-23-8

Herausgegeben von Frank Vollertsen

Michael Kreimeyer
Verfahrenstechnische Voraussetzungen zur Integration von Aluminium-Stahl-Mischbauweisen in den Kraftfahrzeugbau
Strahltechnik Band 30, Bremen 2007, ISBN 978-3-933762-20-7

Carsten Wochnowski
UV-laser-basierte Erzeugung von planaren, polymeren Bragg-Multiplexer-Strukturen
Strahltechnik Band 29, Bremen 2007, ISBN 978-3-933762-19-1

Herausgegeben von Frank Vollertsen, Werner Jüptner

Frank Vollertsen, Thomas Seefeld (Hrsg.)
Laserstrahlfügen: Prozesse, Systeme, Anwendungen, Trends
Strahltechnik Band 28, Bremen 2006, ISBN 978-3-933762-18-4

Frank Vollertsen (Hrsg.)
Prozessskalierung
Strahltechnik Band 27, Bremen 2005, ISBN 978-3-933762-17-7

Frank Vollertsen, Thomas Seefeld (Hrsg.)
Thermal Forming
Strahltechnik Band 26, Bremen 2005, ISBN 978-3-933762-16-0

Volker Kebbel
Untersuchung zur Erzeugung und Propagation ultrakurzer optischer Bessel-Impulse
Strahltechnik Band 25, Bremen 2004, ISBN 978-3-933762-15-3

Frank Vollertsen, Ferdinand Hollmann (Ed.)
Process Scaling
Strahltechnik Band 24, Bremen 2003, ISBN 978-3-933762-14-6

Emil Schubert
Untersuchungen zum Leichtbau mit Hilfe lasergestützter Mischbauweise
Strahltechnik Band 23, Bremen 2003, ISBN 978-3-933762-13-9

Christoph von Kopylow
Durchstimmbare Mikrokristall-Laser für die absolute Distanzinterferometrie
Strahltechnik Band 22, Bremen 2003, ISBN 978-3-933762-12-2

Carmen Theiler
Aufbau gradierter Nickelbasis-Chromkarbid-Verbundwerkstoffe durch Laserstrahl-Pulverbeschichten
Strahltechnik Band 21, Bremen 2003, ISBN 978-3-933762-11-5

Herausgegeben von Gerd Sepold, Werner Jüptner

Thomas Kreis (Hrsg.)
Werkzeug Laser – Industrieller Fortschritt durch wissenschaftliche Forschung
Strahltechnik Band 20, Bremen 2002, ISBN 978-3-933762-10-8

Gerd Sepold, Thomas Seefeld (Hrsg.)
Laserstrahlfügen: Prozesse, Systeme, Anwendungen, Trends
Strahltechnik Band 19, Bremen 2002, ISBN 978-3-933762-09-2

Gerd Sepold, Florian Wagner, Jürgen Tobolski
Kurzzeitmetallurgie
Strahltechnik Band 18, Bremen 2002, ISBN 978-3-933762-08-5 (vergriffen)

Frank Elandaloussi
Modellgestützte Detektion und Analyse von Materialfehlern an technischen

Objekten nach dem Prinzip „Erkennung durch Synthese“
Strahltechnik Band 17, Bremen 2002, ISBN 978-3-933762-07-8

Ingo Zerner
Prozessstabilisierung und Ergebnisse für das Laserstrahlfügen von Aluminium-Stahl-Verbindungen
Strahltechnik Band 16, Bremen 2001, ISBN 978-3-933762-05-4

Daniel Holstein
Ortsaufgelöste Charakterisierung von mechanischen Eigenschaften laserstrahlgeschweißter Verbindungen
Strahltechnik Band 15, Bremen 2001, ISBN 978-3-933762-04-7

Bernd Grubert
Untersuchung neuartiger Resonatorkonzepte für koaxiale Wellenleiterlaser
Strahltechnik Band 14, Bremen 2001, ISBN 978-3-933762-03-0

Martin Klassen
Prozessdynamik und resultierende Prozessinstabilitäten beim Laserstrahlschweißen von Aluminiumlegierungen
Strahltechnik Band 13, Bremen 2000, ISBN 978-3-933762-02-3

Ingo Engler
Verfahrenskombination Laserstrahlschweißen und -richten am Beispiel einer Titan-Leichtbaustruktur
Strahltechnik Band 12, Bremen 1999, ISBN 978-3-933762-01-6

Ulrike Mieth
Erscheinungsbild von Materialfehlern in holografischen Interferogrammen
Strahltechnik Band 11, Bremen 1998, ISBN 978-3-933762-00-9

Werner Jüptner (Hrsg.)
Laser von der Wissenschaft zur Anwendung
Strahltechnik Band 10, Bremen 1997, ISBN 978-3-9805011-4-9

Peter Andrä
Ein verallgemeinertes Geometriemodell für das Streifenprojektionsverfahren zur optischen 3D-Koordinatenmessung
Strahltechnik Band 9, Bremen 1998, ISBN 978-3-9805011-9-4

Thomas Franz
Laserstrahlschweißen mit Nd:YAG-Laser unter Wasser
Strahltechnik Band 8, Bremen 1998, ISBN 978-3-9805011-8-7

Sigurd Weise
Heißrissbildung beim Laserstrahlschweißen von Baustählen
Strahltechnik Band 7, Bremen 1998, ISBN 978-3-9805011-7-0

Gerd Sepold, Manfred Geiger (Hrsg.)
Strahl-Stoff-Wechselwirkung bei der Laserstrahlbearbeitung 2
Strahltechnik Band 6, Bremen 1998, ISBN 978-3-9805011-6-3

Werner Jüptner, Gerd Sepold (Hrsg.)
Lasermaterialbearbeitung im Transportwesen
Strahltechnik Band 5, Bremen 1997, ISBN 978-3-9805011-5-6

Carolin Renate Radscheit
Laserstrahlfügen von Aluminium mit Stahl
Strahltechnik Band 4, Bremen 1997, ISBN 978-9805011-3-2

Jürgen Breuer
UV-lasergestütztes Vorbehandlungsverfahren zur gezielten Modifizierung der Oberflächen von Polypropylen
Strahltechnik Band 3, Bremen 1996, ISBN 978-3-9805011-2-5

Bernd Heidenreich
Beitrag zum Laserstrahlbrennschneiden von großen Stahlblechen
Strahltechnik Band 2, Bremen 1995, ISBN 978-3-9805011-1-8

Christian Binroth
Beitrag zur Prozessstabilität beim CO_2-Laserstrahlschweißen von Aluminium mit Zusatzwerkstoffen
Strahltechnik Band 1, Bremen 1995, ISBN 978-3-9805011-0-1